Renormalization-Group Theory of Correlated Electron Systems

by

Michael Hinczewski

Submitted to the Department of Physics
in partial fulfillment of the requirements for the degree of

Doctor of Philosophy

at the

MASSACHUSETTS INSTITUTE OF TECHNOLOGY
[September 2005]
August 2005

Author .....
Department of Physics
August 1, 2005

Certified by .....
A. Nihat Berker
Emeritus Professor
Thesis Supervisor

Accepted by .....
Thomas J. Greytak
Associate Department Head for Education

Renormalization-Group Theory of Correlated Electron Systems

by

Michael Hinczewski

Submitted to the Department of Physics
on August 1, 2005, in partial fulfillment of the
requirements for the degree of
Doctor of Philosophy

Abstract

The thesis applies position-space renormalization-group theory to a variety of correlated electron systems, determining finite-temperature phase diagrams and thermodynamic properties for electron densities both at and away from half-filling.

We begin by assessing the effectiveness of the Suzuki-Takano quantum decimation method on a $d = 1$ Hubbard model in an external magnetic field, where exact results for the specific heat, magnetic and charge susceptibilities are available at various electron densities. We find that our approach converges to the exact values at high temperature, and agrees well even at moderate-to-low temperatures.

We then extend the decimation through the Migdal-Kadanoff procedure to a Hubbard model in $d = 3$. Phase diagrams are calculated for a range of Coulomb couplings, and two new "τ" phases are found for hole-dopings of $10 - 18\%$ and $30 - 35\%$. The electron hopping strength renormalizes to infinity at the τ phase sinks, possibly indicating superconductivity, an interpretation further supported by features of the specific heat.

The next part turns to the tJ model in $d = 3$, where the τ phase was originally observed. In the vicinity of this phase we see a sharp peak in the superfluid weight, and a suppressed low temperature specific heat indicating gap formation. The doping dependence of the free carrier density is similar to that found experimentally in cuprate superconductors.

Since strong anisotropy is a key aspect of high-T_c materials, we also consider a $d = 3$ tJ model with distinct in-plane and out-of-plane couplings. We examine the evolution of the phase diagram as the interplane coupling is weakened, and find that the τ phase persists even in the quasi-two-dimensional regime. The complex lamellar structure of antiferromagnetic and disordered phases that develops between the τ phase and half-filling could be a sign of incommensurate spin ordering. While the pure $d = 2$ tJ model does not exhibit a τ phase, we see pre-signatures of it in the renormalization-group flows, and the phase becomes stabilized with a finite transition temperature upon the addition of even the smallest interplane coupling.

The last part of the thesis looks at renormalization-group techniques for quenched

random systems. As a preliminary step to dealing with disorder in the tJ model, we start with a simpler, yet currently important, classical system, testing a conjecture relating the locations of multicritical points on dual pairs of hierarchical lattice Ising spin glasses. Finally, we incorporate nonmagnetic impurities into the $d = 3$ tJ model. Small concentrations of these impurities rapidly destroy the τ phase and enhance antiferromagnetism, observations that have parallels in Zn-doped cuprates.

Thesis Supervisor: A. Nihat Berker
Title: Emeritus Professor

Acknowledgments

My debt to my advisor, Prof. Nihat Berker, begins with physics, but extends to so many other aspects of my life during these past five years. His motto may be "Hayat zordur," but through his support and encouragement he has had the very opposite effect. Were it not for his insanely fast but compelling IAP course in the winter of 2000, I would have never ended up on a crowded midnight train in the middle of Anatolia two years later, heading to a small farming village in the Taurus Mountains to ask the hand of my future wife. So for all the crazy turns my life has taken recently, I can happily blame his influence.

I'd like to thank the many people at MIT whose teaching and advice I have benefited from: Prof. Mehran Kardar and Prof. John Joannopoulos for their amazing classes, and also Prof. Krishna Rajagopal, Prof. Robert Jaffe, Prof. John Negele, and Prof. Washington Taylor, with whom I worked as a TA and who have been inspirations as teachers. The logistics of TA'ing, academics, jumping between continents has been made much easier through the help of Margaret O'Meara at the CMT, Alicia Duarte, Nancy Savioli, Maria Springer, and Brian Canavan at the Physics Education Office, and Prof. Richard Yamamoto.

For the summers that became semesters that became years on the banks of the Bosphorus, I'm grateful to the kind hospitality of the Feza Gürsey Research Institute and the Physics Department at Istanbul Technical University. Prof. İlhan İkeda's unfailing good humor buoyed my early days at Feza Gürsey, and I always looked forward to conversations with Prof. Cihan Saçlıoğlu on the ferry between Asia and Europe. At İ.T.Ü. there are too many people to thank, but I have to mention Esat, İbrahim, Esra, Ayşe, Sevtap, and Haluk for taking me under their wing that first summer in Istanbul. Aynur, Hakan, and Gürsel have been good friends, and I'm grateful to them for looking out for Dursen when I was gone. Fevzi brought a little piece of İ.T.Ü. to MIT, and brightened our last year in Boston. And a heartfelt thanks to Dursen's parents, who accepted me into their family without reservations, and provided the occasional warm spot by the wood stove where I could sit and run

calculations.

Back at home, life at MIT would not have been the same without J.D. and Ian's companionship, which I have missed now that they are living the good life as post-docs. I've been happy to have some old Mod 3 stalwarts around—Manish during my first years in Boston, Michael O'Kelly during my last. And I'm indebted to Rashad for his close friendship and innumerable long discussions.

I'd like to thank my grandparents for keeping faith in me, and of course Mom, Dad, and my sister Monica, without whose love and support none of this would be possible. Monica, especially in the last few months chatting with you has kept me sane. Finally, to my wonderful wife Durşen: you have been my source of strength during this whole process, patient and understanding through the long nights, a solace at those moments of crisis when a sign error threatened to make the world collapse. At some point in the coming years, when our roles will be reversed, I only hope I can begin to repay you.

This research was supported by the Scientific and Technical Research Council of Turkey (TÜBITAK), by the Academy of Sciences of Turkey, and the U.S. Department of Energy under Grant No. DE-FG02-92ER-45473. We thank H. Nishimori and K. Takeda for useful correspondance on the conjecture discussed in Chapter 6.

Contents

List of Figures

List of Tables

Chapter 1

Introduction

The basic distinctions between metals, insulators, and semiconductors were one of the major successes of the independent electron approximation and the band theory of solids, developed early on in the wake of quantum mechanics. However, theories that neglected or assumed only weak electron-electron interactions could not give a comprehensive explanation of all materials. It was known by the late 1930's that transition-metal oxides, despite having partially-filled d bands, could actually be insulators. The only way to account for this was through strong Coulomb repulsion between two electrons localized on the same ion orbital, so that tunneling onto singly-occupied ions becomes energetically unfavorable. Pioneered by Mott, the study of how these Coulomb interactions affect narrow electronic bands gave birth to a whole new sub-field of solid-state physics: strongly correlated electrons [1].

The modern-day prominence of the subject is largely due to the discovery of high-temperature superconductivity by Bednorz and Müller in 1986. The compounds in which this phenonenon is observed are antiferromagnetic Mott insulators in the absence of doped carriers, but make a transition to the superconducting state at low temperatures with a small amount of doping. Strong correlation effects thus play a central role in these materials, and many theoretical tools like the Hubbard model, first introduced in the context of tight-binding electron bands, have enjoyed a second life in the intense twenty-year effort to crack the high-T_c problem.

The work described in this thesis applies the techniques of position-space renor-

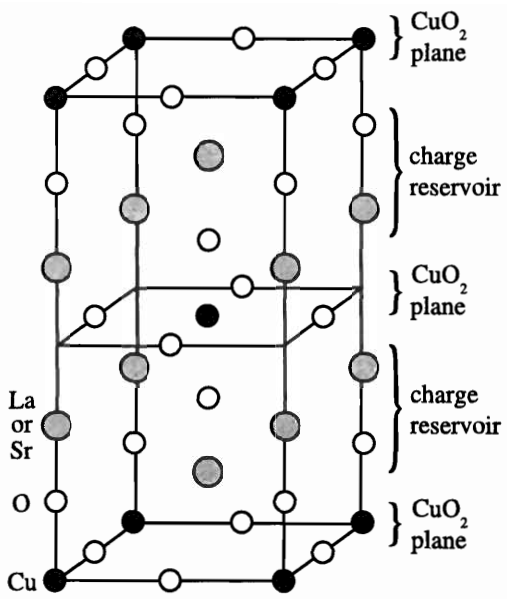

Figure 1-1: Crystal structure of $La_{2-x}Sr_xCuO_4$.

malization-group theory to strongly correlated lattice fermion models, with the ultimate goal of gaining insight into the finite-temperature phase diagram of high-T_c compounds. We begin this introductory chapter with a brief overview of cuprate superconductors, and then turn to the simplified one-band descriptions of lattice electron conduction—the Hubbard and tJ models—that are our primary focus. In the final section, we outline the basic thrust of our research, which has been to gauge the effectiveness of renormalization-group methods applied to these quantum systems, and to progressively add complications—anisotropy, disorder—that may bring the models closer to the real-world materials we hope to understand.

1.1 Electronic Structure and Phase Diagram of the Cuprates

The key structural feature shared by all cuprate superconductors is the CuO_2 plane, one or more of which are sandwiched between layers of other atoms that act as

charge reservoirs[1]. Let us consider the canonical example, La_{2-x} Sr_xCuO_4 (LSCO), illustrated in Fig. 1-1. For the undoped ($x = 0$) crystal, the CuO_2 planes are composed of Cu^{2+} and O^{2-} ions, with each copper atom surrounded by an octahedron of oxygen. The Cu^{2+} ions have a single hole in the $3d$ shell, and thus carry a net spin of $1/2$, while O^{2-} has a completed $2p$ shell. The oxygen octahedra around the copper atoms are slightly elongated in the out-of-plane direction, and this lattice distortion breaks the degeneracy of the d orbitals in such a way that the one at highest energy is $d_{x^2-y^2}$, which is where the hole resides. The lobes of this d orbital overlap with a p orbital on each of the nearest-neighbor oxygens, and the conduction network formed by these hybridized d and p orbitals along the entire CuO_2 plane is where we expect to find the essential physics relating to high-temperature superconductivity.

Every nearest-neighbor pair of copper d orbitals is connected through an oxygen p orbital, and the possibility of d-to-p virtual hopping of holes generates a nearest-neighbor antiferromagnetic coupling between the spins at the copper sites. The unusually large amplitude of this coupling along the CuO_2 plane, $J \sim 0.1$ eV, leads one to expect a Néel temperature $T_N \sim 10^3$ K, but since the system is highly anisotropic, with a much smaller interplane coupling, the actual T_N is an order of magnitude less. Even so, the large in-plane J manifests itself through the strong antiferromagnetic correlations and insulating behavior that persist far above T_N.

The doping process, where La^{3+} ions are replaced with Sr^{2+} in LSCO, adds holes to the CuO_2 planes. Because of the large Coulomb repulsion between two holes at a single copper site, these doped holes are mainly carried by the oxygen p orbitals, and the d-p hybridization means they are mobile. The right-hand side of Fig. 1-2 shows the phase diagram of LSCO in terms of concentration x versus temperature. The antiferromagnetic insulator survives only for very small hole concentrations, and at higher temperatures the system makes a rapid transition to metallic behavior upon doping. At lower temperatures we find the superconducting phase for $0.05 \lesssim x \lesssim 0.30$, and sandwiched between the antiferromagnetic and superconducting regions a spin-

[1]The literature on basic properties of high-T_c materials is vast, and the elementary description in this section is based largely on the reviews in Refs. [1, 2, 3], where additional sources may be found.

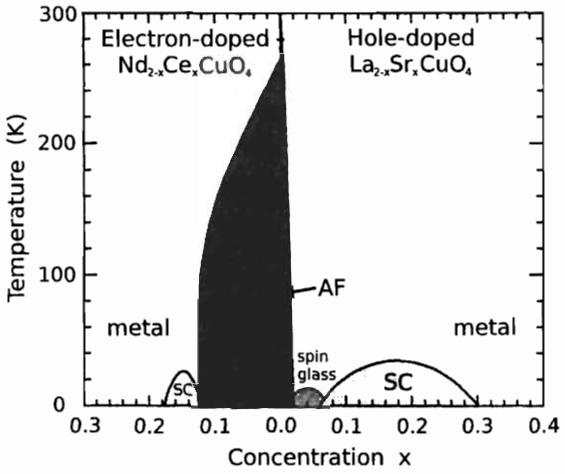

Figure 1-2: Phase diagrams for $Nd_{2-x}Ce_xCuO_4$ and $La_{2-x}Sr_xCuO_4$, taken from Ref. [2].

glass at $0.02 \lesssim x \lesssim 0.05$. For comparison, Fig. 1-2 also shows the phase diagram of $Nd_{2-x}Ce_xCuO_4$, a high-T_c compound where the doped carriers are electrons. In such materials, for reasons not entirely understood, the antiferromagnetism is more stable to doping, and remains up to $x \sim 0.12$. It is possible that the doped electrons are less mobile than the doped holes, and thus less destructive to the antiferromagnetic order.

The doping value at which the superconducting transition temperature T_c is maximum (~ 0.15 in LSCO) is known as optimal doping, and samples in the superconducting range with x smaller or greater than optimal are referred to as underdoped and overdoped respectively. The properties of the normal state above T_c vary dramatically with doping region, despite the fact that there are no clear phase transitions separating underdoped, optimal, and overdoped metals. In the underdoped region near the antiferromagnetic boundary, certain thermodynamic properties like the uniform magnetic susceptibility and specific heat indicate the existence of a "pseudogap"—a partial suppression of the density of low energy excitations. The normal state at optimal doping exhibits a different kind of anomaly: most notably, a resistivity ρ linear in T and a temperature dependent Hall coefficient, both deviations from the standard Fermi-liquid picture, where $\rho \sim T^2$ and the Hall coefficient is approximately constant. Only in the overdoped region does the normal state approach conventional

Fermi-liquid-like behavior, with $\rho \sim T^2$ over a temperature range that widens with increased doping.

1.2 Lattice Models for Electron Conduction

Based on the above description, the natural starting point for a theory of high-T_c materials is to model the holes hopping among the copper d and oxygen p orbitals of the CuO_2 plane. A Hamiltonian can be written down for these holes—the three-band or d-p model [4, 5]—but it is complicated by a large number of parameters describing all the possible interactions in the system. One has to take into account the energy levels of the holes on the copper and oxygen orbitals, the amplitude for d-to-p hopping, the smaller amplitude for direct p-to-p hopping, the on-site Coulomb repulsions for both the d and p orbitals, and the Coulomb repulsion between holes on adjacent sites. The result may be a realistic Hamiltonian, but a fairly intractable problem as far as calculating a phase diagram.

Most theoretical approaches choose to emphasize a few key physical features rather than remain completely faithful to the details of cuprate chemistry. The assumption, not yet entirely borne out, is that simpler models do retain enough of the interesting physics to be to relevant to experimental observations. From this point of view, the simplest system that might yield cuprate-like behavior is the Hubbard model [6], originally introduced to describe electron correlations in narrow bands. The model is derived from a one-band tight-binding approximation where we consider only a single type of orbital at every lattice site. If $c_{i\sigma}^\dagger$ and $c_{i\sigma}$ are creation and destruction operators for an electron of spin σ localized in a Wannier state $\phi_{i\sigma}(\mathbf{r})$ at site i, then we can write the Hamiltonian in second-quantized notation as

$$\mathcal{H} = -t \sum_{\langle ij \rangle, \sigma} (c_{j\sigma}^\dagger c_{i\sigma} + c_{i\sigma}^\dagger c_{j\sigma}) + U \sum_i n_{i\uparrow} n_{i\downarrow} - \mu \sum_i n_i \,, \tag{1.1}$$

where $\langle ij \rangle$ denotes a sum over nearest-neighbor lattice sites, $\sigma = \uparrow$ (spin up) or $\downarrow$ (spin down), $n_{i\sigma} = c_{i\sigma}^\dagger c_{i\sigma}$, and $n_i = n_{i\uparrow} + n_{i\downarrow}$. The first term represents the tunneling of the

electrons between nearest-neighbor orbitals, with an amplitude t proportional to the overlap between Wannier wavefunctions $\phi_{i\sigma}(\mathbf{r})$ and $\phi_{j\sigma}(\mathbf{r})$,

$$t = \int d\mathbf{r}\, \phi^*_{i\sigma}(\mathbf{r}) \frac{\hbar^2}{2m} \nabla^2 \phi_{j\sigma}(\mathbf{r})\,. \tag{1.2}$$

The second term describes the Coulomb repulsion between a pair of spin up and spin down electrons localized on the same orbital, with

$$U = \int d\mathbf{r}\, d\mathbf{r}'\, \phi^*_{i\uparrow}(\mathbf{r}) \phi_{i\uparrow}(\mathbf{r}) \frac{e^2}{|\mathbf{r} - \mathbf{r}'|} \phi^*_{i\downarrow}(\mathbf{r}') \phi_{i\downarrow}(\mathbf{r}')\,, \tag{1.3}$$

and the third term is chemical potential. The apparent simplicity of this Hamiltonian belies the forty years of research that have gone into understanding its properties, and even today we have no exact solutions for $d > 1$.

Since applications to high-temperature superconductivity concentrate on the strongly coupled regime of the Hubbard model, it is instructive to look at the limit $U/t \to \infty$, where double occupation of lattice sites becomes energetically prohibited. Second-order perturbation theory in t/U yields a Hamiltonian known as the tJ model [7, 8],

$$\mathcal{H} = P \left[-t \sum_{\langle ij \rangle, \sigma} \left(c^\dagger_{i\sigma} c_{j\sigma} + c^\dagger_{j\sigma} c_{i\sigma} \right) + J \sum_{\langle ij \rangle} (\vec{S}_i \cdot \vec{S}_j - \frac{1}{4} n_i n_j) \right] P\,, \tag{1.4}$$

where $J = 4t^2/U$ and P is a projection operator excluding double occupation of a lattice site. The perturbation also generates an additional three-site term, not shown, since it is usually ignored under the assumption that it does not change the essential physics of the tJ model.

1.3 Overview of the Thesis

The Hamiltonians of Eqs. (1.1) and (1.4) form the starting points of our theoretical inquiry into the finite-temperature phase structure and thermodynamic properties of lattice fermion models. A position-space renormalization-group transformation can

be constructed for these models based on an approximate quantum decimation first developed by Suzuki and Takano [9, 10]. In Chapter 2, we apply this decimation to a one-dimensional Hubbard model in an external magnetic field. Since we know exact thermodynamic results for this system at various electron densities, we can evaluate the effectiveness of our approximation in determining finite-temperature specific heat, as well as charge and magnetic susceptibilities. We find that our approach converges to the exact results at high temperatures, and remains remarkably accurate even at lower temperatures, despite breaking down near $T = 0$.

The usefulness of our method becomes clear in higher dimensions, since here we have little definite information about Hubbard and tJ systems away from half-filling. In Chapter 3 we extend the one-dimensional Suzuki-Takano decimation to $d > 1$ through the Migdal-Kadanoff procedure, and determine the finite-temperature phase diagram of the $d = 3$ Hubbard model for the entire range of electron densities. Besides the expected antiferromagnetic phase near half-filling, we find two low temperature "τ" phases in the doped system—one present at large U/t, and seen in earlier studies of the tJ model [11, 12], and the other, present at smaller U/t, completely new. These τ phases bear tantalizing indicators of superconductivity, notably an electron hopping amplitude that flows to infinity upon rescaling, and we interpret the specific heat results for the two phases in the framework of a weak-coupling and strong-coupling superconducting transition.

In Chapter 4 we turn to the $d = 3$ tJ model, where the τ phase was originally observed, to investigate in detail the behavior of the system in the vicinity of this phase. By including a small magnetic flux in the Hamiltonian, we are able to calculate superfluid density n_s/m^* through a modified renormalization-group transformation. Around $\langle n_i \rangle \approx 0.63-0.68$, where the τ phase appears, we find a pronounced maximum in n_s/m^*, and the low temperature specific heat shows signs of a gap in the excitation spectrum. The free carrier density, which increases steadily with hole-doping until $\langle n_i \rangle \sim 0.63$, levels off and remains approximately constant as we dope beyond this point, similar to experimental results in the overdoped region in high-T_c compounds.

Up to now we have only considered the phase diagrams of the isotropic $d = 3$

Hubbard and tJ models, but in order to connect the interesting physics we find in these systems to actual materials, we need to take into account one of the crucial aspects of cuprate structure: anisotropy. Chapter 5 presents a renormalization-group approach to a tJ model with distinct in-plane and out-of-plane couplings, allowing us to chart the evolution of the phase diagram from the isotropic to the more realistic quasi-two-dimensional regime. The τ phase, while weakened, survives even for strong anisotropy. In fact, the renormalization-group flows in the purely two-dimensional case show indications of the τ phase, which becomes stabilized with a nonzero transition temperature upon the addition of a finite interplane coupling. In the anisotropic phase diagram we also find markers of incommensurate charge ordering—possibly microscopic stripes—in a region between half-filling and the τ phase characterized by a suppressed chemical potential shift and an intricate lamellar structure of antiferromagnetic and disordered phases.

The last portion of the thesis looks at ways we can study the effects of quenched disorder through the renormalization-group transformation. In particular, we seek to model the behavior of high-T_c compounds with the addition of nonmagnetic impurities like Zn, which are substituted for the Cu atoms in the CuO_2 planes. Even small concentrations of these impurities drastically reduce the superconducting transition temperature. To probe this type of disorder in our lattice fermion systems, we need a new set of renormalization-group techniques, where we calculate the flows of probability distributions associated with the interaction strengths in the Hamiltonian. Before turning to the full problem of quenched randomness in the tJ model, Chapter 6 employs these techniques in a simpler, classical context: hierarchical-lattice Ising spin-glasses. Our renormalization-group transformation is exact for such lattices, and we can precisely test a recent conjecture that relates the locations of multicritical points on dual lattice pairs. Finally in Chapter 7 we consider the $d = 3$ tJ model with a small percentage of random vacancies, to simulate nonmagnetic impurities. The τ phase is rapidly destroyed by the disorder, while antiferromagnetism in the doped system is actually enhanced for small impurity amounts—two features which we relate to experimental observations.

References

[1] M. Imada, A. Fujimori, and Y. Tokura, Rev. Mod. Phys. **70**, 1039 (1998).

[2] E. Dagotto, Rev. Mod. Phys. **66**, 763 (1994).

[3] P.A. Lee, N. Nagaosa, and X.-G. Wen, cond-mat/0410445.

[4] V.J. Emery, Phys. Rev. Lett. **58**, 3759 (1987).

[5] C.M. Varma, S. Schmitt-Rink, and E. Abrahams, Solid State Commun. **62**, 681 (1987).

[6] J. Hubbard, Proc. R. Soc. A **276**, 238 (1963); **277**, 237 (1964); **281**, 401 (1964).

[7] P.W. Anderson, Science **235**, 1196 (1987).

[8] G. Baskaran, Z. Zhou, and P.W. Anderson, Solid State Commun. **63**, 973 (1987).

[9] M. Suzuki and H. Takano, Phys. Lett. A **69**, 426 (1979).

[10] H. Takano and M. Suzuki, J. Stat. Phys. **26**, 635 (1981).

[11] A. Falicov and A.N. Berker, Phys. Rev. B **51**, 12458 (1995).

[12] A. Falicov and A.N. Berker, Turk. J. Phys. **19**, 127 (1995).

Chapter 2

The Hubbard Model in $d = 1$

2.1 Introduction

Before going into the details of the Suzuki-Takano decimation applied to the one-dimensional Hubbard model, let us review the basic idea of decimation through an example of a quantum system where the procedure is exact. Consider a linear chain of spin-1/2 particles with Hamiltonian

$$-\beta\mathcal{H} = J\sum_i \sigma_i^z \sigma_{i+1}^z \,, \tag{2.1}$$

where σ_i^z is the z component Pauli spin operator at site i, and there are two possible states $|m_i = \pm 1\rangle$ at each site, with $\sigma_i^z|m_i\rangle = m_i|m_i\rangle$. The decimation consists of a mapping

$$\begin{aligned}\langle m_1 m_3 m_5 \cdots |e^{-\beta'\mathcal{H}'}|m_1' m_3' m_5' \cdots \rangle \\ = \sum_{m_2, m_4, m_6, \ldots} \langle m_1 m_2 m_3 m_4 m_5 \cdots |e^{-\beta H}|m_1' m_2 m_3' m_4 m_5' \cdots \rangle \,.\end{aligned} \tag{2.2}$$

The Hamiltonian $-\beta'\mathcal{H}'$ defined through Eq. (2.2) depends only on the states at the odd-numbered sites, and its partition function Z' is equal to that of the original system, Z. Since the terms in the Hamiltonian $\mathcal{H}$ mutually commute, $[\sigma_i^z\sigma_{i+1}^z, \sigma_j^z\sigma_{j+1}^z] = 0$ for all i, j, we can find a basis in which $e^{-\beta H}$ is diagonal (in fact this is just the

$|m_1 m_2 m_3 \ldots\rangle$ basis). The problem becomes identical to a classical Ising model, and we can carry out the partial trace on the right-hand side of Eq. (2.2) exactly,

$$\begin{aligned}
&\sum_{m_2,m_4,m_6,\ldots} \langle m_1 m_2 m_3 m_4 m_5 \cdots | e^{-\beta H} | m_1' m_2 m_3' m_4 m_5' \cdots \rangle \\
&\qquad = \sum_{m_2,m_4,m_6,\ldots} e^{J\sum_i m_i m_{i+1}} \prod_i^{\text{odd}} \delta_{m_i,m_i'} \\
&\qquad = \prod_i^{\text{odd}} \sum_{m_{i+1}} e^{Jm_i m_{i+1} + Jm_{i+1} m_{i+2}} \delta_{m_i,m_i'} \\
&\qquad = \prod_i^{\text{odd}} \left(e^{Jm_i + Jm_{i+2}} + e^{-Jm_i - Jm_{i+2}} \right) \delta_{m_i,m_i'} .
\end{aligned} \tag{2.3}$$

If we express the renormalized Hamiltonian as $-\beta' \mathcal{H}' = J' \sum_i^{\text{odd}} \sigma_i^z \sigma_{i+2}^z + G'$, then the left-hand side of Eq. (2.2) becomes

$$\begin{aligned}
&\langle m_1 m_3 m_5 \cdots | e^{-\beta' \mathcal{H}'} | m_1' m_3' m_5' \cdots \rangle \\
&\qquad = e^{J' \sum_i^{\text{odd}} m_i m_{i+2} + G'} \prod_i^{\text{odd}} \delta_{m_i,m_i'} \\
&\qquad = \prod_i^{\text{odd}} e^{J' m_i m_{i+2} + G'} \delta_{m_i,m_i'} .
\end{aligned} \tag{2.4}$$

Comparing Eqs. (2.3) and (2.4) we find the recursion relations $J' = \frac{1}{2} \ln(\cosh 2J)$ and $G' = \frac{1}{2} \ln(4 \cosh 2J)$.

Note that this exact decimation was only possible because the original Hamiltonian was composed of mutually commuting terms. Unfortunately this is not the case for the Hubbard model, and thus to construct a renormalization-group transformation we resort to the Suzuki-Takano approximation described in the next section.

2.2 Thermodynamics of the One-Dimensional Hubbard Model: An Assessment of the Suzuki-Takano Quantum Decimation Technique

Michael Hinczewski and A. Nihat Berker
Department of Physics, Istanbul Technical University,
Maslak 34469, Istanbul, Turkey,
Department of Physics, Massachusetts Institute of Technology,
Cambridge, Massachusetts 02139, U.S.A.,
Feza Gürsey Research Institute, TÜBITAK - Bosphorus University,
Çengelköy 81220, Istanbul, Turkey

Abstract

Position-space renormalization-group transformations based on the Suzuki-Takano decimation method have been used for years in the study of spin and electron conduction models. Lack of extensive information about finite-temperature thermodynamic properties for many quantum models has hampered past efforts to gauge the accuracy of this approximation. We investigate the Suzuki-Takano method in the context of the one-dimensional Hubbard model in an external magnetic field, where reliable numerical results for specific heat, magnetic and charge susceptibilities at a variety of electron densities have been determined from the quantum transfer matrix method. Both at and away from half-filling, we find the corresponding thermodynamic quantities calculated using the renormalization-group transformation converge to the exact values at high temperature, and agree well even at moderate-to-low temperatures, particularly in the strongly-coupled regime. As reflected in the specific heat results, the approximation captures qualitatively the variation in the spin and charge excitation properties of the system with doping level and Coulomb coupling.

PACS numbers: 74.72.-h, 71.10.Fd, 05.30.Fk, 74.25.Dw

2.2.1 Introduction

The approximate quantum decimation technique of Suzuki and Takano [1, 2] has been used to construct position-space renormalization-group transformations for a wide variety of spin and correlated electron systems. Originally introduced in the context of the anisotropic Heisenberg and XY models [1, 2], it has since been applied to the Heisenberg model on kagomé, squagome, and fractal lattices [3, 4, 5], the Hubbard model at half-filling in $d=1$ [6] and $d=2,3$ [7, 8], as well as away from half-filling in $d=2,3$ [9]. In conjunction with Migdal-Kadanoff procedure, it has allowed the calculation of global finite-temperature phase diagrams for the tJ model in d=2, 3 [10, 11], and more recently phase diagrams and thermodynamic properties for the $d=3$ Hubbard model [12], superfluid weight, free carrier densities for the $d=3$ tJ model [13], and the evolution of the anisotropic tJ model from the quasi-two-dimensional to three-dimensional limits [14]. This combination of the Migdal-Kadanoff and Suzuki-Takano methods is particularly attractive for studying the finite-temperature physics of lattice electron conduction systems, since it yields closed-form recursion relations whose renormalization-group flows can be exactly calculated for the entire range of chemical potentials, thus describing the system at arbitrary electron densities. The basic approach in Refs. [10, 11, 12, 13, 14] has been to derive an approximate decimation for the one-dimensional system, and generalize this to higher dimensions through the Migdal-Kadanoff method. Since the one-dimensional Suzuki-Takano decimation is the starting point in this procedure, it is crucial to evaluate the effectiveness of this step by itself. The ideal testing ground is the one-dimensional Hubbard model.

Unfortunately, when Suzuki and Takano originally applied their technique to the d=1 Hubbard model in 1981 [6], there were few reliable finite-temperature thermodynamic results available for comparison. Their study was confined to half-filling, where they calculated specific heat, entropy, and local moments. At high temperatures, these were found to agree well with numerical results based on extrapolation from two- to six-site lattices [15, 16]. At lower temperatures, the differences from the

finite lattice values were greater, but the Suzuki-Takano results still captured many of the qualitative features of the half-filled system.

In the intervening quarter century, our understanding of the one-dimensional Hubbard model has dramatically increased. In fact, soon after the ground state of the model was originally found through the Bethe ansatz [17], thermodynamic Bethe ansatz equations were proposed that in principle describe the exact finite-temperature properties of the system [18]. However, since this description consisted of an infinite number of coupled integral equations for an infinite number of unknown functions, deriving numerical results was only possible approximately by truncating the number of equations [19, 20]. The situation improved after Shastry demonstrated the integrability of the one-dimensional Hubbard model [21, 22, 23]. Exploiting the mapping between a d-dimensional quantum system at finite temperatures and a d+1-dimensional classical model, it became possible to evaluate the Hubbard free energy through the quantum transfer matrix method [24, 25, 26, 27]. Thus we now have a set of exact numerical results for specific heat, magnetic and charge susceptibilities, calculated at various electron densities [26, 27].

Taking these results as a basis for comparison, the present study seeks to assess the Suzuki-Takano decimation method applied to a one-dimensional Hubbard model in the presence of an external magnetic field. Specific heat, charge and magnetic susceptibilities are calculated for a range of Coulomb couplings and electron densities. It is found that the renormalization-group method gives exact results at high temperatures, and performs quite well even at relatively lower temperatures, where the interesting structure relating to charge and spin excitations appears in the thermodynamic results. Excellent numerical agreement with the quantum transfer matrix values is found for the charge and magnetic susceptibilities, and the qualitative evolution of the specific heat with increasing Coulomb repulsion is correctly described both around half-filling and for lower electron densities. There are clear discrepancies near zero temperature, but this is exactly where the approximation is expected to break down. As a whole, the results give support to the further use of the Suzuki-Takano approximation as a tool for investigating the finite-temperature properties of

correlated electron systems along the whole range of electron densities, particularly in higher dimensions where the phase structure of lattice conduction systems remains an intensely active area of inquiry.

2.2.2 The Hubbard Model

The one-dimensional Hubbard model coupled to an external magnetic field in the z direction has the Hamiltonian

$$-\beta\mathcal{H} = -t\sum_{i,\sigma}\left(c^{\dagger}_{i\sigma}c_{i+1\sigma} + c^{\dagger}_{i+1\sigma}c_{i\sigma}\right) - U_0\sum_i n_{i\uparrow}n_{i\downarrow} + \mu_0\sum_i n_i + H_0\sum_i S^z_i\ , \quad (2.5)$$

where $\beta = 1/kT$, $c^{\dagger}_{i\sigma}$ and $c_{i\sigma}$ are creation and annihilation operators, obeying anti-commutation rules, for an electron with spin $\sigma = \uparrow$ or $\downarrow$ at the site i of the lattice, $n_{i\sigma} = c^{\dagger}_{i\sigma}c_{i\sigma}$, $n_i = n_{i\uparrow} + n_{i\downarrow}$ are electron number operators, and $\vec{S}_i = \frac{1}{2}\sum_{\sigma,\bar{\sigma}} c^{\dagger}_{i\sigma}\vec{s}_{\sigma\bar{\sigma}}c_{i\bar{\sigma}}$, with $\vec{s}_{\sigma\bar{\sigma}}$ the vector of Pauli spin matrices, is the spin operator at site i with z-component operator S^z_i. Each lattice site can accommodate up to two electrons with opposite spins. The four terms of this Hamiltonian correspond to kinetic energy (parametrized by the electron hopping strength t), on-site Coulomb repulsion (with coefficient $U_0 > 0$), chemical potential μ_0, and magnetic field H_0. It is convenient for our purposes to rearrange Eq.(2.5) into an equivalent Hamiltonian:

$$\begin{aligned} -\beta\mathcal{H} = &\sum_i\Bigg\{-t\sum_{\sigma}\left(c^{\dagger}_{i\sigma}c_{i+1\sigma} + c^{\dagger}_{i+1\sigma}c_{i\sigma}\right) - U\left(n_{i\uparrow}n_{i\downarrow} + n_{i+1\uparrow}n_{i+1\downarrow}\right) \\ &+ \mu\left(n_i + n_{i+1}\right) + H(S^z_i + S^z_{i+1})\Bigg\} \\ \equiv &\sum_i\left\{-\beta\mathcal{H}(i,i+1)\right\}\ . \end{aligned} \quad (2.6)$$

The new interaction constants are $U = U_0/2, \mu = \mu_0/2$, $H = H_0/2$, and we have hereby defined the nearest-neighbor pair Hamiltonian $-\beta\mathcal{H}(i,j)$.

2.2.3 Renormalization-Group Transformation

2.2.3.1 Quantum Decimation

For the Hamiltonian in Eq.(2.6), an exact renormalization-group transformation can be formulated. In terms of matrix elements, this transformation is [10]

$$\langle u_1 u_3 u_5 \cdots | e^{-\beta' \mathcal{H}'} | v_1 v_3 v_5 \cdots \rangle = \sum_{w_2, w_4, w_6, \ldots} \langle u_1 w_2 u_3 w_4 u_5 w_6 \cdots | e^{-\beta \mathcal{H}} | v_1 w_2 v_3 w_4 v_5 w_6 \cdots \rangle \,, \quad (2.7)$$

where u_i, v_i, and w_i are state variables for lattice site i. These variables range over the set $\{\circ, \uparrow, \downarrow, \Updownarrow\}$, by which we represent the no electron, a single electron with spin up, a single electron with spin down, and doubly occupied states. Here and below, the quantities referring to the renormalized (rescaled) system are denoted with a prime. The decimation in Eq.(2.7) eliminates half of the degrees of freedom in the system, while exactly preserving the partition function ($Z' = Z$). However, because the operators in the Hamiltonian do not commute, this transformation cannot be directly implemented.

We thus use the approximate decimation of Suzuki and Takano [1, 2]:

$$\begin{aligned} \mathrm{Tr}_{\mathrm{even}} e^{-\beta \mathcal{H}} =& \mathrm{Tr}_{\mathrm{even}} e^{\sum_i \{-\beta \mathcal{H}(i,i+1)\}} \\ =& \mathrm{Tr}_{\mathrm{even}} e^{\sum_i^{\mathrm{even}} \{-\beta \mathcal{H}(i-1,i) - \beta \mathcal{H}(i,i+1)\}} \\ \simeq& \prod_i^{\mathrm{even}} \mathrm{Tr}_i e^{\{-\beta \mathcal{H}(i-1,i) - \beta \mathcal{H}(i,i+1)\}} \\ =& \prod_i^{\mathrm{even}} e^{-\beta' \mathcal{H}'(i-1,i+1)} \\ \simeq& e^{\sum_i^{\mathrm{even}} \{-\beta' \mathcal{H}'(i-1,i+1)\}} = e^{-\beta' \mathcal{H}'} . \end{aligned} \quad (2.8)$$

In the two approximate steps, marked by $\simeq$ in Eq.(2.8), we ignore the non-commutation of operators separated beyond three consecutive sites of the unrenormalized system. Since each of these two steps involves the same approximation but in opposite directions, some mutual compensation can be expected.

The algebraic content of the renormalization-group mapping can be extracted from Eq.(2.8) as

$$e^{-\beta'\mathcal{H}'(i,k)} = \mathrm{Tr}_j e^{-\beta\mathcal{H}(i,j)-\beta\mathcal{H}(j,k)}, \tag{2.9}$$

where i, j, k are three consecutive sites of the unrenormalized system. The operators $-\beta'\mathcal{H}'(i,k)$ and $-\beta\mathcal{H}(i,j)-\beta\mathcal{H}(j,k)$ act on the space of two-site and three-site states respectively, so that, in terms of matrix elements,

$$\langle u_i v_k|e^{-\beta'\mathcal{H}'(i,k)}|\bar{u}_i\bar{v}_k\rangle = \sum_{w_j}\langle u_i\, w_j\, v_k|e^{-\beta\mathcal{H}(i,j)-\beta\mathcal{H}(j,k)}|\bar{u}_i\, w_j\, \bar{v}_k\rangle\,, \tag{2.10}$$

where $u_i, w_j, v_k, \bar{u}_i, \bar{v}_k$ are single-site state variables. Eq.(2.10) indicates the contraction of a 64×64 matrix on the right into a 16×16 matrix on the left. This is greatly simplified by the use of two- and three-site basis states that block-diagonalize respectively the left and right sides of Eq.(2.10). These basis states are the eigenstates of total particle number, total spin magnitude, total spin z-component, and parity. We denote the set of 16 two-site eigenstates by $\{|\phi_p\rangle\}$ and the set of 64 three-site eigenstates by $\{|\psi_q\rangle\}$, and list them in Tables 2.1 and 2.2. Eq.(2.10) is rewritten as

$$\langle\phi_p|e^{-\beta'\mathcal{H}'(i,k)}|\phi_{\bar{p}}\rangle = \sum_{\substack{u,v,\bar{u},\\ \bar{v},w}}\sum_{q,\bar{q}}\langle\phi_p|u_iv_k\rangle\langle u_iw_jv_k|\psi_q\rangle\langle\psi_q|e^{-\beta\mathcal{H}(i,j)-\beta\mathcal{H}(j,k)}|\psi_{\bar{q}}\rangle\langle\psi_{\bar{q}}|\bar{u}_iw_j\bar{v}_k\rangle\langle\bar{u}_i\bar{v}_k|\phi_{\bar{p}}\rangle\,. \tag{2.11}$$

In the above equation, with the eigenstates shown in Tables 2.1 and 2.2, the largest blocks in $\langle\phi_p|e^{-\beta'\mathcal{H}'(i,k)}|\phi_{\bar{p}}\rangle$ are 2×2 and the largest blocks in $\langle\psi_q|e^{-\beta\mathcal{H}(i,j)-\beta\mathcal{H}(j,k)}|\psi_{\bar{q}}\rangle$ are 5×5. Eq.(2.11) yields 18 independent elements for the matrix $\langle\phi_p|e^{-\beta'\mathcal{H}'(i,k)}|\phi_{\bar{p}}\rangle$ of the renormalized system. These we label γ_p as follows:

$$\begin{aligned}
\gamma_p &= \langle\phi_p|e^{-\beta'\mathcal{H}'(i,k)}|\phi_p\rangle\,, \quad p = 1,\ldots,16\,,\\
\gamma_{17} &= \langle\phi_6|e^{-\beta'\mathcal{H}'(i,k)}|\phi_8\rangle\,,\\
\gamma_{18} &= \langle\phi_7|e^{-\beta'\mathcal{H}'(i,k)}|\phi_{10}\rangle\,.
\end{aligned} \tag{2.12}$$

The values of the γ_p in terms of the matrix elements of the unrenormalized system,

dictated by the right-hand side of Eq.(2.11), are listed below. In the following equations, $\langle\psi_q||\psi_{\bar{q}}\rangle$ denotes $\langle\psi_q|e^{-\beta\mathcal{H}(i,j)-\beta\mathcal{H}(j,k)}|\psi_{\bar{q}}\rangle$:

$$
\begin{aligned}
\gamma_1 =&\langle\psi_1||\psi_1\rangle+\langle\psi_2||\psi_2\rangle+\langle\psi_4||\psi_4\rangle+\langle\psi_9||\psi_9\rangle,\\
\gamma_2 =&\langle\psi_3||\psi_3\rangle+\frac{1}{2}\langle\psi_8||\psi_8\rangle-\langle\psi_8||\psi_{16}\rangle+\langle\psi_{15}||\psi_{15}\rangle+\frac{1}{2}\langle\psi_{16}||\psi_{16}\rangle+\langle\psi_{24}||\psi_{24}\rangle,\\
\gamma_3 =&\langle\psi_5||\psi_5\rangle+\frac{1}{2}\langle\psi_8||\psi_8\rangle+\langle\psi_8||\psi_{16}\rangle+\frac{1}{2}\langle\psi_{16}||\psi_{16}\rangle+\langle\psi_{19}||\psi_{19}\rangle+\langle\psi_{28}||\psi_{28}\rangle,\\
\gamma_4 =&\langle\psi_6||\psi_6\rangle+\frac{1}{2}\langle\psi_{11}||\psi_{11}\rangle-\langle\psi_{11}||\psi_{21}\rangle+\langle\psi_{20}||\psi_{20}\rangle+\frac{1}{2}\langle\psi_{21}||\psi_{21}\rangle+\langle\psi_{32}||\psi_{32}\rangle,\\
\gamma_5 =&\langle\psi_7||\psi_7\rangle+\frac{1}{2}\langle\psi_{11}||\psi_{11}\rangle+\langle\psi_{11}||\psi_{21}\rangle+\frac{1}{2}\langle\psi_{21}||\psi_{21}\rangle+\langle\psi_{22}||\psi_{22}\rangle+\langle\psi_{36}||\psi_{36}\rangle,\\
\gamma_6 =&\langle\psi_{10}||\psi_{10}\rangle+\langle\psi_{26}||\psi_{26}\rangle+\langle\psi_{30}||\psi_{30}\rangle+\langle\psi_{44}||\psi_{44}\rangle,\\
\gamma_7 =&\langle\psi_{13}||\psi_{13}\rangle+\langle\psi_{34}||\psi_{34}\rangle+\langle\psi_{38}||\psi_{38}\rangle+\langle\psi_{48}||\psi_{48}\rangle,\\
\gamma_8 =&\langle\psi_{12}||\psi_{12}\rangle+\langle\psi_{31}||\psi_{31}\rangle+\langle\psi_{35}||\psi_{35}\rangle+\langle\psi_{47}||\psi_{47}\rangle,\\
\gamma_9 =&\langle\psi_{14}||\psi_{14}\rangle+\frac{2}{3}\langle\psi_{23}||\psi_{23}\rangle-\frac{2\sqrt{2}}{3}\langle\psi_{23}||\psi_{40}\rangle+\langle\psi_{39}||\psi_{39}\rangle+\frac{1}{3}\langle\psi_{40}||\psi_{40}\rangle+\langle\psi_{49}||\psi_{49}\rangle,\\
\gamma_{10} =&\langle\psi_{17}||\psi_{17}\rangle+\frac{1}{3}\langle\psi_{23}||\psi_{23}\rangle+\frac{2\sqrt{2}}{3}\langle\psi_{23}||\psi_{40}\rangle+\frac{1}{3}\langle\psi_{27}||\psi_{27}\rangle+\frac{2\sqrt{2}}{3}\langle\psi_{27}||\psi_{42}\rangle\\
&+\frac{2}{3}\langle\psi_{40}||\psi_{40}\rangle+\frac{2}{3}\langle\psi_{42}||\psi_{42}\rangle+\langle\psi_{52}||\psi_{52}\rangle,\\
\gamma_{11} =&\langle\psi_{18}||\psi_{18}\rangle+\frac{2}{3}\langle\psi_{27}||\psi_{27}\rangle-\frac{2\sqrt{2}}{3}\langle\psi_{27}||\psi_{42}\rangle+\langle\psi_{41}||\psi_{41}\rangle+\frac{1}{3}\langle\psi_{42}||\psi_{42}\rangle+\langle\psi_{53}||\psi_{53}\rangle,\\
\gamma_{12} =&\langle\psi_{25}||\psi_{25}\rangle+\frac{1}{2}\langle\psi_{45}||\psi_{45}\rangle-\langle\psi_{45}||\psi_{51}\rangle+\langle\psi_{50}||\psi_{50}\rangle+\frac{1}{2}\langle\psi_{51}||\psi_{51}\rangle+\langle\psi_{59}||\psi_{59}\rangle,\\
\gamma_{13} =&\langle\psi_{29}||\psi_{29}\rangle+\frac{1}{2}\langle\psi_{45}||\psi_{45}\rangle+\langle\psi_{45}||\psi_{51}\rangle+\frac{1}{2}\langle\psi_{51}||\psi_{51}\rangle+\langle\psi_{54}||\psi_{54}\rangle+\langle\psi_{61}||\psi_{61}\rangle,\\
\gamma_{14} =&\langle\psi_{33}||\psi_{33}\rangle+\frac{1}{2}\langle\psi_{46}||\psi_{46}\rangle-\langle\psi_{46}||\psi_{56}\rangle+\langle\psi_{55}||\psi_{55}\rangle+\frac{1}{2}\langle\psi_{56}||\psi_{56}\rangle+\langle\psi_{62}||\psi_{62}\rangle,\\
\gamma_{15} =&\langle\psi_{37}||\psi_{37}\rangle+\frac{1}{2}\langle\psi_{46}||\psi_{46}\rangle+\langle\psi_{46}||\psi_{56}\rangle+\frac{1}{2}\langle\psi_{56}||\psi_{56}\rangle+\langle\psi_{57}||\psi_{57}\rangle+\langle\psi_{63}||\psi_{63}\rangle,\\
\gamma_{16} =&\langle\psi_{43}||\psi_{43}\rangle+\langle\psi_{58}||\psi_{58}\rangle+\langle\psi_{60}||\psi_{60}\rangle+\langle\psi_{64}||\psi_{64}\rangle,\\
\gamma_{17} \equiv&\langle\phi_6|e^{-\beta'\mathcal{H}'(i,k)}|\phi_8\rangle\\
=&\langle\psi_{10}||\psi_{12}\rangle+\langle\psi_{26}||\psi_{31}\rangle+\langle\psi_{30}||\psi_{35}\rangle+\langle\psi_{44}||\psi_{47}\rangle,\\
\gamma_{18} \equiv&\langle\phi_7|e^{-\beta'\mathcal{H}'(i,k)}|\phi_{10}\rangle\\
=&-\langle\psi_{13}||\psi_{17}\rangle-\frac{1}{\sqrt{3}}\langle\psi_{23}||\psi_{34}\rangle-\frac{1}{\sqrt{3}}\langle\psi_{27}||\psi_{38}\rangle\\
&-\sqrt{\frac{2}{3}}\langle\psi_{34}||\psi_{40}\rangle-\sqrt{\frac{2}{3}}\langle\psi_{38}||\psi_{42}\rangle-\langle\psi_{48}||\psi_{52}\rangle\,.
\end{aligned}
\tag{2.13}
$$

n	p	s	m_s	Two-site basis states
0	+	0	0	$\|\phi_1\rangle = \|\circ\circ\rangle$
1	+	1/2	1/2	$\|\phi_2\rangle = \frac{1}{\sqrt{2}}\{\|\uparrow\circ\rangle + \|\circ\uparrow\rangle\}$
1	−	1/2	1/2	$\|\phi_4\rangle = \frac{1}{\sqrt{2}}\{\|\uparrow\circ\rangle - \|\circ\uparrow\rangle\}$
2	+	0	0	$\|\phi_6\rangle = \frac{1}{\sqrt{2}}\{\|\updownarrow\circ\rangle + \|\circ\updownarrow\rangle\}$
2	−	0	0	$\|\phi_7\rangle = \frac{1}{\sqrt{2}}\{\|\updownarrow\circ\rangle - \|\circ\updownarrow\rangle\}$, $\|\phi_8\rangle = \frac{1}{\sqrt{2}}\{\|\uparrow\downarrow\rangle - \|\downarrow\uparrow\rangle\}$
2	+	1	1	$\|\phi_9\rangle = \|\uparrow\uparrow\rangle$
2	+	1	0	$\|\phi_{10}\rangle = \frac{1}{\sqrt{2}}\{\|\uparrow\downarrow\rangle + \|\downarrow\uparrow\rangle\}$
3	+	1/2	1/2	$\|\phi_{12}\rangle = \frac{1}{\sqrt{2}}\{\|\updownarrow\uparrow\rangle + \|\uparrow\updownarrow\rangle\}$
3	−	1/2	1/2	$\|\phi_{14}\rangle = \frac{1}{\sqrt{2}}\{\|\updownarrow\uparrow\rangle - \|\uparrow\updownarrow\rangle\}$
4	+	0	0	$\|\phi_{16}\rangle = \|\updownarrow\updownarrow\rangle$

Table 2.1: The two-site basis states used in the derivation of the recursion relations, in Eq.(2.11). In these basis states, $e^{-\beta'\mathcal{H}'(i,k)}$ is diagonal, with the exception of two 2×2 blocks involving $|\phi_6\rangle$, $|\phi_8\rangle$ and $|\phi_7\rangle$, $|\phi_{10}\rangle$ respectively. The corresponding particle number (n), parity (p), total spin (s), and total spin z-component (m_s) quantum numbers are also given. The states $|\phi_3\rangle$, $|\phi_5\rangle$, $|\phi_{11}\rangle$, $|\phi_{13}\rangle$, $|\phi_{15}\rangle$ are obtained by spin reversal from $|\phi_2\rangle$, $|\phi_4\rangle$, $|\phi_9\rangle$, $|\phi_{12}\rangle$, $|\phi_{14}\rangle$, respectively.

2.2.3.2 Hamiltonian Closed Form under the Renormalization-Group Transformation

Since 18 interaction strengths can be independently fixed by the 18 γ_p, the Hamiltonian $-\beta'\mathcal{H}'$ has a more general form than that of the Hubbard Hamiltonian in Eq.(2.6). This generalized form of the pair Hamiltonian is

$$
\begin{aligned}
-\beta\mathcal{H}(i,j) = \\
&-\sum_{\sigma}\left[t_0\, h_{i-\sigma}h_{j-\sigma} + t_1(h_{i-\sigma}n_{j-\sigma} + n_{i-\sigma}h_{j-\sigma}) + t_2\, n_{i-\sigma}n_{j-\sigma}\right]\left(c^{\dagger}_{i\sigma}c_{j\sigma} + c^{\dagger}_{j\sigma}c_{i\sigma}\right) \\
&- t_x\left(c^{\dagger}_{i\uparrow}c_{j\uparrow}c^{\dagger}_{i\downarrow}c_{j\downarrow} + c^{\dagger}_{j\uparrow}c_{i\uparrow}c^{\dagger}_{j\downarrow}c_{i\downarrow}\right) - U\left(n_{i\uparrow}n_{i\downarrow} + n_{j\uparrow}n_{j\downarrow}\right) + \mu\left(n_i + n_j\right) + J\,\vec{S}_i\cdot\vec{S}_j \\
&+ V_2 n_i n_j + V_3\left(n_{i\uparrow}n_{i\downarrow}n_j + n_i n_{j\uparrow}n_{j\downarrow}\right) + V_4 n_{i\uparrow}n_{i\downarrow}n_{j\uparrow}n_{j\downarrow} + H(S^z_i + S^z_j) \\
&-\sum_{\sigma}\epsilon_{\sigma}\left[u_0\, h_{i-\sigma}h_{j-\sigma} + u_1(h_{i-\sigma}n_{j-\sigma} + n_{i-\sigma}h_{j-\sigma}) + u_2\, n_{i-\sigma}n_{j-\sigma}\right]\left(c^{\dagger}_{i\sigma}c_{j\sigma} + c^{\dagger}_{j\sigma}c_{i\sigma}\right) \\
&+ H_1 S^z_i S^z_j + H_2(n_i S^z_j + S^z_i n_j) + H_3\left(n_{i\uparrow}n_{i\downarrow}S^z_j + S^z_i n_{j\uparrow}n_{j\downarrow}\right) + G\,, \qquad (2.14)
\end{aligned}
$$

where $h_{i\sigma} \equiv 1 - n_{i\sigma}$ is the hole (vacancy) operator and $\epsilon_\sigma = +1$ if $\sigma = \uparrow$, -1 if $\sigma = \downarrow$. The generalized Hamiltonian involves 17 interaction constants, $(t_0, t_1, t_2, t_x, U,$

n	p	s	m_s	Three-site basis states
0	+	0	0	$\|\psi_1\rangle = \|\circ\circ\circ\rangle$
1	+	1/2	1/2	$\|\psi_2\rangle = \|\circ\uparrow\circ\rangle$, $\|\psi_3\rangle = \frac{1}{\sqrt{2}}\{\|\uparrow\circ\circ\rangle + \|\circ\circ\uparrow\rangle\}$
1	−	1/2	1/2	$\|\psi_6\rangle = \frac{1}{\sqrt{2}}\{\|\uparrow\circ\circ\rangle - \|\circ\circ\uparrow\rangle\}$
2	+	0	0	$\|\psi_8\rangle = \frac{1}{2}\{\|\uparrow\downarrow\circ\rangle - \|\downarrow\uparrow\circ\rangle - \|\circ\uparrow\downarrow\rangle + \|\circ\downarrow\uparrow\rangle\}$, $\|\psi_9\rangle = \|\circ\Updownarrow\circ\rangle$, $\|\psi_{10}\rangle = \frac{1}{\sqrt{2}}\{\|\Updownarrow\circ\circ\rangle + \|\circ\circ\Updownarrow\rangle\}$
2	−	0	0	$\|\psi_{11}\rangle = \frac{1}{2}\{\|\uparrow\downarrow\circ\rangle - \|\downarrow\uparrow\circ\rangle + \|\circ\uparrow\downarrow\rangle - \|\circ\downarrow\uparrow\rangle\}$, $\|\psi_{12}\rangle = \frac{1}{\sqrt{2}}\{\|\uparrow\circ\downarrow\rangle - \|\downarrow\circ\uparrow\rangle\}$, $\|\psi_{13}\rangle = \frac{1}{\sqrt{2}}\{\|\Updownarrow\circ\circ\rangle - \|\circ\circ\Updownarrow\rangle\}$
2	+	1	1	$\|\psi_{14}\rangle = \|\uparrow\circ\uparrow\rangle$, $\|\psi_{15}\rangle = \frac{1}{\sqrt{2}}\{\|\uparrow\uparrow\circ\rangle + \|\circ\uparrow\uparrow\rangle\}$
2	+	1	0	$\|\psi_{16}\rangle = \frac{1}{2}\{\|\uparrow\downarrow\circ\rangle + \|\downarrow\uparrow\circ\rangle + \|\circ\uparrow\downarrow\rangle + \|\circ\downarrow\uparrow\rangle\}$, $\|\psi_{17}\rangle = \frac{1}{\sqrt{2}}\{\|\uparrow\circ\downarrow\rangle + \|\downarrow\circ\uparrow\rangle\}$
2	−	1	1	$\|\psi_{20}\rangle = \frac{1}{\sqrt{2}}\{\|\uparrow\uparrow\circ\rangle - \|\circ\uparrow\uparrow\rangle\}$
2	−	1	0	$\|\psi_{21}\rangle = \frac{1}{2}\{\|\uparrow\downarrow\circ\rangle + \|\downarrow\uparrow\circ\rangle - \|\circ\uparrow\downarrow\rangle - \|\circ\downarrow\uparrow\rangle\}$
3	+	1/2	1/2	$\|\psi_{23}\rangle = \frac{1}{\sqrt{6}}\{2\|\uparrow\downarrow\uparrow\rangle - \|\uparrow\uparrow\downarrow\rangle - \|\downarrow\uparrow\uparrow\rangle\}$, $\|\psi_{24}\rangle = \frac{1}{\sqrt{2}}\{\|\uparrow\Updownarrow\circ\rangle + \|\circ\Updownarrow\uparrow\rangle\}$, $\|\psi_{25}\rangle = \frac{1}{\sqrt{2}}\{\|\uparrow\circ\Updownarrow\rangle + \|\Updownarrow\circ\uparrow\rangle\}$, $\|\psi_{26}\rangle = \frac{1}{\sqrt{2}}\{\|\Updownarrow\uparrow\circ\rangle + \|\circ\uparrow\Updownarrow\rangle\}$
3	−	1/2	1/2	$\|\psi_{31}\rangle = \frac{1}{\sqrt{2}}\{\|\uparrow\uparrow\downarrow\rangle - \|\downarrow\uparrow\uparrow\rangle\}$, $\|\psi_{32}\rangle = \frac{1}{\sqrt{2}}\{\|\uparrow\Updownarrow\circ\rangle - \|\circ\Updownarrow\uparrow\rangle\}$, $\|\psi_{33}\rangle = \frac{1}{\sqrt{2}}\{\|\uparrow\circ\Updownarrow\rangle - \|\Updownarrow\circ\uparrow\rangle\}$, $\|\psi_{34}\rangle = \frac{1}{\sqrt{2}}\{\|\Updownarrow\uparrow\circ\rangle - \|\circ\uparrow\Updownarrow\rangle\}$
3	+	3/2	3/2	$\|\psi_{39}\rangle = \|\uparrow\uparrow\uparrow\rangle$
3	+	3/2	1/2	$\|\psi_{40}\rangle = \frac{1}{\sqrt{3}}\{\|\uparrow\downarrow\uparrow\rangle + \|\uparrow\uparrow\downarrow\rangle + \|\downarrow\uparrow\uparrow\rangle\}$
4	+	0	0	$\|\psi_{43}\rangle = \|\Updownarrow\circ\Updownarrow\rangle$, $\|\psi_{44}\rangle = \frac{1}{\sqrt{2}}\{\|\Updownarrow\Updownarrow\circ\rangle + \|\circ\Updownarrow\Updownarrow\rangle\}$, $\|\psi_{45}\rangle = \frac{1}{2}\{\|\uparrow\downarrow\Updownarrow\rangle - \|\downarrow\uparrow\Updownarrow\rangle - \|\Updownarrow\uparrow\downarrow\rangle + \|\Updownarrow\downarrow\uparrow\rangle\}$
4	−	0	0	$\|\psi_{46}\rangle = \frac{1}{2}\{\|\downarrow\uparrow\Updownarrow\rangle - \|\uparrow\downarrow\Updownarrow\rangle - \|\Updownarrow\uparrow\downarrow\rangle + \|\Updownarrow\downarrow\uparrow\rangle\}$, $\|\psi_{47}\rangle = \frac{1}{\sqrt{2}}\{\|\uparrow\Updownarrow\downarrow\rangle - \|\downarrow\Updownarrow\uparrow\rangle\}$, $\|\psi_{48}\rangle = \frac{1}{\sqrt{2}}\{\|\Updownarrow\Updownarrow\circ\rangle - \|\circ\Updownarrow\Updownarrow\rangle\}$
4	+	1	1	$\|\psi_{49}\rangle = \|\uparrow\Updownarrow\uparrow\rangle$, $\|\psi_{50}\rangle = \frac{1}{\sqrt{2}}\{\|\uparrow\uparrow\Updownarrow\rangle + \|\Updownarrow\uparrow\uparrow\rangle\}$
4	+	1	0	$\|\psi_{51}\rangle = \frac{1}{2}\{\|\uparrow\downarrow\Updownarrow\rangle + \|\downarrow\uparrow\Updownarrow\rangle + \|\Updownarrow\uparrow\downarrow\rangle + \|\Updownarrow\downarrow\uparrow\rangle\}$, $\|\psi_{52}\rangle = \frac{1}{\sqrt{2}}\{\|\uparrow\Updownarrow\downarrow\rangle + \|\downarrow\Updownarrow\uparrow\rangle\}$
4	−	1	1	$\|\psi_{55}\rangle = \frac{1}{\sqrt{2}}\{\|\uparrow\uparrow\Updownarrow\rangle - \|\Updownarrow\uparrow\uparrow\rangle\}$
4	−	1	0	$\|\psi_{56}\rangle = \frac{1}{2}\{\|\uparrow\downarrow\Updownarrow\rangle + \|\downarrow\uparrow\Updownarrow\rangle - \|\Updownarrow\uparrow\downarrow\rangle - \|\Updownarrow\downarrow\uparrow\rangle\}$
5	+	1/2	1/2	$\|\psi_{58}\rangle = \|\Updownarrow\uparrow\Updownarrow\rangle$, $\|\psi_{59}\rangle = \frac{1}{\sqrt{2}}\{\|\uparrow\Updownarrow\Updownarrow\rangle + \|\Updownarrow\Updownarrow\uparrow\rangle\}$
5	−	1/2	1/2	$\|\psi_{62}\rangle = \frac{1}{\sqrt{2}}\{\|\Updownarrow\Updownarrow\uparrow\rangle - \|\uparrow\Updownarrow\Updownarrow\rangle\}$
6	+	0	0	$\|\psi_{64}\rangle = \|\Updownarrow\Updownarrow\Updownarrow\rangle$

Table 2.2: The three-site basis states used in the derivation of the recursion relations, in Eq.(2.11). In these basis states, $e^{-\beta\mathcal{H}(i,j)-\beta\mathcal{H}(j,k)}$ is block-diagonal, with the largest blocks being 5×5 (see Table 2.4). The corresponding particle number (n), parity (p), total spin (s), and total spin z-component (m_s) quantum numbers are also given. The states $|\psi_{4-5}\rangle$, $|\psi_7\rangle$, $|\psi_{18-19}\rangle$, $|\psi_{22}\rangle$, $|\psi_{27-30}\rangle$, $|\psi_{35-38}\rangle$, $|\psi_{41-42}\rangle$, $|\psi_{53-54}\rangle$, $|\psi_{57}\rangle$, $|\psi_{60-61}\rangle$, $|\psi_{63}\rangle$ are obtained by spin reversal from $|\psi_{2-3}\rangle$, $|\psi_6\rangle$, $|\psi_{14-15}\rangle$, $|\psi_{20}\rangle$, $|\psi_{23-26}\rangle$, $|\psi_{31-34}\rangle$, $|\psi_{39-40}\rangle$, $|\psi_{49-50}\rangle$, $|\psi_{55}\rangle$, $|\psi_{58-59}\rangle$, $|\psi_{62}\rangle$, respectively.

$\mu, J, V_2, V_3, V_4, u_0, u_1, u_2, H, H_1, H_2, H_3)$, plus an additive constant G which has to included in Eq.(2.16) below in the determination of expectation values. In general, the Hubbard Hamiltonian, after one renormalization-group transformation, maps onto this generalized Hamiltonian, which has a form that stays closed under further renormalization-group transformations.

The matrix elements of the renormalized pair Hamiltonian $-\beta'\mathcal{H}'(i,k)$ are given in Table 2.3 in terms of the renormalized interaction constants. Eq.(2.12) and Table 2.3 allow us to solve for the renormalized interaction constants in terms of the γ_p given in Eq. (2.13):

$$
\begin{aligned}
t_0' &= \frac{1}{4}\ln\frac{\gamma_4\gamma_5}{\gamma_2\gamma_3}, \qquad t_1' = w_1\frac{\gamma_{17}}{\gamma_8-\gamma_6},\\
t_2' &= \frac{1}{4}\ln\frac{\gamma_{12}\gamma_{13}}{\gamma_{14}\gamma_{15}}, \qquad t_x' = \frac{1}{2}\left(-v_1+v_2+w_1-w_2\right),\\
U' &= \frac{1}{2}\ln\frac{\gamma_2\gamma_3\gamma_4\gamma_5}{\gamma_1^2} - \frac{1}{2}\left(v_1+v_2-w_1-w_2\right),\\
\mu' &= \frac{1}{4}\ln\frac{\gamma_2\gamma_3\gamma_4\gamma_5}{\gamma_1^4}, \qquad J' = -v_1+v_2-w_1+w_2,\\
V_2' &= \frac{1}{4}\ln\frac{\gamma_1^4\gamma_9\gamma_{11}}{\gamma_2^2\gamma_3^2\gamma_4^2\gamma_5^2} + \frac{1}{4}\left(v_1+v_2+w_1+w_2\right),\\
V_3' &= \frac{1}{4}\ln\frac{\gamma_2^3\gamma_3^3\gamma_4^3\gamma_5^3\gamma_{12}\gamma_{13}\gamma_{14}\gamma_{15}}{\gamma_1^4\gamma_9^2\gamma_{11}^2} - v_1 - v_2,\\
V_4' &= \ln\frac{\gamma_1\gamma_9\gamma_{11}\gamma_{16}}{\gamma_2\gamma_3\gamma_4\gamma_5\gamma_{12}\gamma_{13}\gamma_{14}\gamma_{15}} + 2v_1 + 2v_2, \qquad G' = \ln\gamma_1,\\
H' &= \frac{1}{2}\ln\frac{\gamma_2\gamma_4}{\gamma_3\gamma_5}, \quad u_0' = \frac{1}{4}\ln\frac{\gamma_3\gamma_4}{\gamma_2\gamma_5}, \quad u_1' = -w_2\frac{\gamma_{18}}{\gamma_{10}-\gamma_7},\\
u_2' &= \frac{1}{4}\ln\frac{\gamma_{13}\gamma_{14}}{\gamma_{12}\gamma_{15}}, \qquad H_1' = \ln\gamma_{11}\gamma_9 - 2(v_2+w_2),\\
H_2' &= \frac{1}{2}\ln\frac{\gamma_3\gamma_5\gamma_9}{\gamma_2\gamma_4\gamma_{11}}, \qquad H_3' = \frac{1}{2}\ln\frac{\gamma_2\gamma_4\gamma_{11}^2\gamma_{12}\gamma_{14}}{\gamma_3\gamma_5\gamma_9^2\gamma_{13}\gamma_{15}},
\end{aligned}
\tag{2.15}
$$

where

$$v_1 = \frac{1}{2}\ln\left(\gamma_6\gamma_8 - \gamma_{17}^2\right), \quad v_2 = \frac{1}{2}\ln\left(\gamma_7\gamma_{10} - \gamma_{18}^2\right),$$
$$w_1 = \frac{\gamma_8 - \gamma_6}{\sqrt{\left(\gamma_8 - \gamma_6\right)^2 + 4\gamma_{17}^2}}\cosh^{-1}\left(\frac{\gamma_8 + \gamma_6}{2e^{v_1}}\right),$$
$$w_2 = \frac{\gamma_{10} - \gamma_7}{\sqrt{\left(\gamma_{10} - \gamma_7\right)^2 + 4\gamma_{18}^2}}\cosh^{-1}\left(\frac{\gamma_{10} + \gamma_7}{2e^{v_2}}\right).$$

Note that when $H = 0$ initially, all odd (under spin reversal) interactions $H' = u_0' = u_1' = u_2' = H_1' = H_2' = H_3' = 0$ for all subsequent iterations, and the renormalization-group flows are closed in the 10-dimensional subspace of even interactions $(t_0, t_1, t_2, t_x,\ U, \mu, J, V_2, V_3, V_4)$. In this case the renormalization-group transformation of Eq.(2.15) reduces to the one derived in an earlier study of the Hubbard model [12].

2.2.3.3 Renormalization-Group Transformation

The decimation described above maps a Hamiltonian with interaction constants $\mathbf{K} = (t_0,\ t_1,\ t_2,\ t_x,\ U,\ \mu,\ J,\ V_2,\ V_3,\ V_4,\ H,\ u_0,\ u_1,\ u_2,\ H_1,\ H_2,\ H_3,\ G)$ onto another Hamiltonian with interaction constants $\mathbf{K}' = \mathbf{R}(\mathbf{K})$. The function $\mathbf{R}$ is calculated as follows: (1) The matrix elements of $-\beta\mathcal{H}(i,j) - \beta\mathcal{H}(j,k)$ are determined in the three-site basis $\{\psi_q\}$ given in Table 2.2. In this basis, this matrix is block-diagonal as shown in Table 2.4, with the largest blocks being 5×5. (2) The above block-diagonal matrix is exponentiated, yielding the matrix elements $\langle\psi_q|e^{-\beta\mathcal{H}(i,j)-\beta\mathcal{H}(j,k)}|\psi_{\bar{q}}\rangle$ which enter on the right-hand side of Eq.(2.11). This in turn yields the 18 γ_p (as given in Eq. (2.13)). (3) Using Eqs.(2.15), the interaction constants of the renormalized Hamiltonian $-\beta'\mathcal{H}'(i,k)$, namely $(t_0',\ t_1',\ t_2',\ t_x',\ U',\ \mu',\ J',\ V_2',\ V_3',\ V_4',\ H',\ u_0',\ u_1',\ u_2',\ H_1',\ H_2',\ H_3',\ G')$ are found.

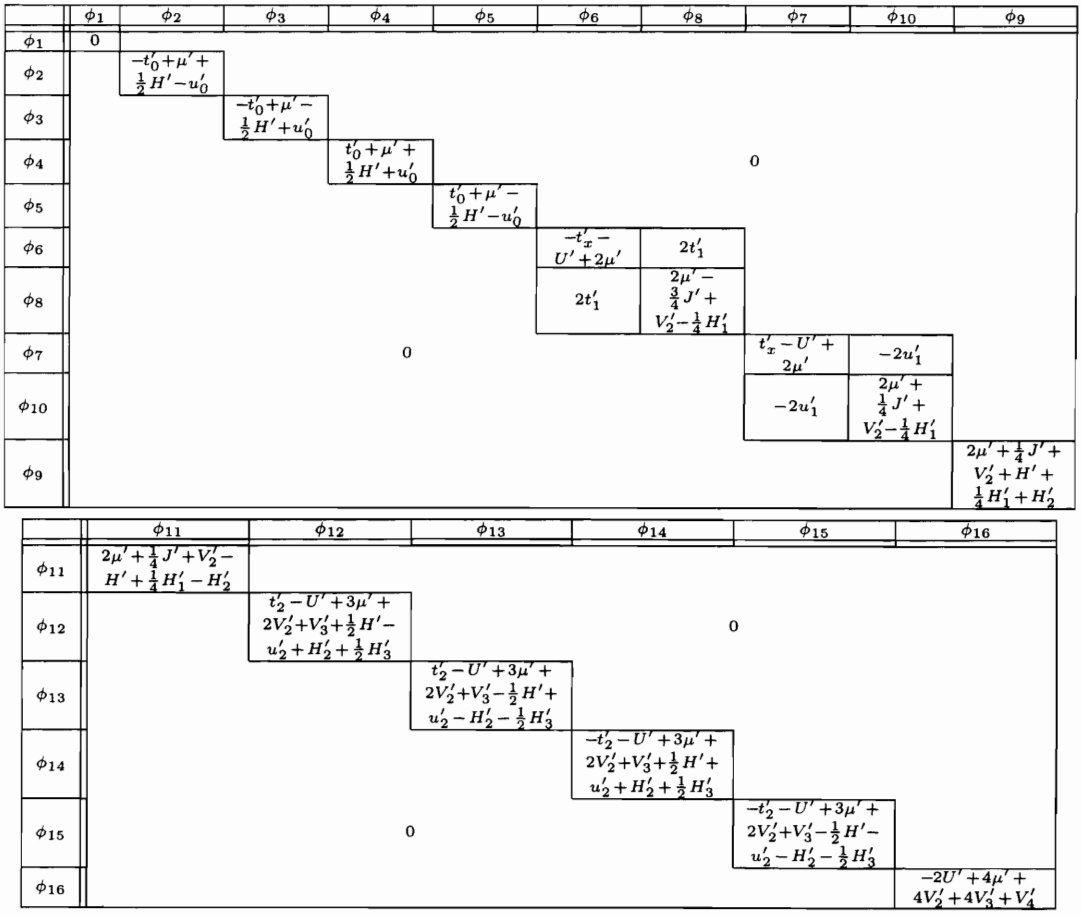

Table 2.3: Block-diagonal matrix of the renormalized two-site Hamiltonian $-\beta'\mathcal{H}'(i,k)$. The additive constant contribution G', occurring at the diagonal terms, is not shown.

2.2.4 Expectation Values from Renormalization-Group Analysis

The renormalization-group transformation specified in the preceding section is implemented numerically, and flows in the 17-dimensional interaction space of the generalized Hamiltonian of Eq.(2.14) are generated for various values of the interaction constants t, U, μ and H in the initial Hubbard Hamiltonian of Eq.(2.6), which in the generalized Hamiltonian correspond to $t_0 = t_1 = t_2 = t$ and all other interaction constants zero except for U, μ, and H. Each interaction constant K_α appearing as a component in the interaction vector $\mathbf{K}$ is the coefficient of a particular operator

	ψ_1
ψ_1	0

	ψ_2	ψ_3
ψ_2	$2\mu + H$	$-\sqrt{2}t_0 - \sqrt{2}u_0$
ψ_3	$-\sqrt{2}t_0 - \sqrt{2}u_0$	$\mu + \frac{1}{2}H$

	ψ_6
ψ_6	$\mu + \frac{1}{2}H$

	ψ_4	ψ_5
ψ_4	$2\mu - H$	$-\sqrt{2}t_0 + \sqrt{2}u_0$
ψ_5	$-\sqrt{2}t_0 + \sqrt{2}u_0$	$\mu - \frac{1}{2}H$

	ψ_7
ψ_7	$\mu - \frac{1}{2}H$

	ψ_8	ψ_{13}	ψ_{16}	ψ_{17}
ψ_8	$3\mu - \frac{3}{4}J + V_2 - \frac{1}{4}H_1$	$\sqrt{2}t_1$	$-\frac{1}{2}H$	$\sqrt{2}u_0$
ψ_{13}	$\sqrt{2}t_1$	$-U + 2\mu$	$-\sqrt{2}u_1$	0
ψ_{16}	$-\frac{1}{2}H$	$-\sqrt{2}u_1$	$3\mu + \frac{1}{4}J + V_2 - \frac{1}{4}H_1$	$-\sqrt{2}t_0$
ψ_{17}	$\sqrt{2}u_0$	0	$-\sqrt{2}t_0$	2μ

	ψ_9	ψ_{10}	ψ_{11}	ψ_{12}	ψ_{21}
ψ_9	$-2U + 4\mu$	$-\sqrt{2}t_x$	$2t_1$	0	$2u_1$
ψ_{10}	$-\sqrt{2}t_x$	$-U + 2\mu$	$\sqrt{2}t_1$	0	$-\sqrt{2}u_1$
ψ_{11}	$2t_1$	$\sqrt{2}t_1$	$3\mu - \frac{3}{4}J + V_2 - \frac{1}{4}H_1$	$-\sqrt{2}t_0$	$-\frac{1}{2}H$
ψ_{12}	0	0	$-\sqrt{2}t_0$	2μ	$\sqrt{2}u_0$
ψ_{21}	$2u_1$	$-\sqrt{2}u_1$	$-\frac{1}{2}H$	$\sqrt{2}u_0$	$3\mu + \frac{1}{4}J + V_2 - \frac{1}{4}H_1$

	ψ_{14}	ψ_{15}
ψ_{14}	$2\mu + H$	$-\sqrt{2}t_0 - \sqrt{2}u_0$
ψ_{15}	$-\sqrt{2}t_0 - \sqrt{2}u_0$	$3\mu + \frac{1}{4}J + V_2 + \frac{3}{2}H + \frac{1}{4}H_1 + H_2$

	ψ_{18}	ψ_{19}
ψ_{18}	$2\mu - H$	$-\sqrt{2}t_0 + \sqrt{2}u_0$
ψ_{19}	$-\sqrt{2}t_0 + \sqrt{2}u_0$	$3\mu + \frac{1}{4}J + V_2 - \frac{3}{2}H + \frac{1}{4}H_1 - H_2$

	ψ_{20}
ψ_{20}	$3\mu + \frac{1}{4}J + V_2 + \frac{3}{2}H + \frac{1}{4}H_1 + H_2$

	ψ_{22}
ψ_{22}	$3\mu + \frac{1}{4}J + V_2 - \frac{3}{2}H + \frac{1}{4}H_1 - H_2$

	ψ_{23}	ψ_{32}	ψ_{33}	ψ_{34}	ψ_{40}
ψ_{23}	$4\mu - J + 2V_2 + \frac{1}{3}H - \frac{1}{3}H_1 + \frac{1}{3}H_2$	$-\sqrt{3}t_1 - \frac{1}{\sqrt{3}}u_1$	$-\sqrt{3}t_1 + \frac{1}{\sqrt{3}}u_1$	0	$-\frac{\sqrt{2}}{3}H - \frac{1}{3\sqrt{2}}H_1 - \frac{\sqrt{2}}{3}H_2$
ψ_{32}	$-\sqrt{3}t_1 - \frac{1}{\sqrt{3}}u_1$	$-2U + 5\mu + 2V_2 + V_3 + \frac{1}{2}H + H_2 + \frac{1}{2}H_3$	$-t_x$	$t_2 - u_2$	$-2\sqrt{\frac{2}{3}}u_1$
ψ_{33}	$-\sqrt{3}t_1 + \frac{1}{\sqrt{3}}u_1$	$-t_x$	$-U + 3\mu + \frac{H}{2}$	$t_0 + u_0$	$2\sqrt{\frac{2}{3}}u_1$
ψ_{34}	0	$t_2 - u_2$	$t_0 + u_0$	$-U + 4\mu + 2V_2 + V_3 + H + H_2 + \frac{1}{2}H_3$	0
ψ_{40}	$-\frac{\sqrt{2}}{3}H - \frac{1}{3\sqrt{2}}H_1 - \frac{\sqrt{2}}{3}H_2$	$-2\sqrt{\frac{2}{3}}u_1$	$2\sqrt{\frac{2}{3}}u_1$	0	$4\mu + \frac{1}{2}J + 2V_2 + \frac{2}{3}H - \frac{1}{6}H_1 + \frac{2}{3}H_2$

	ψ_{24}	ψ_{25}	ψ_{26}	ψ_{31}
ψ_{24}	$-2U + 5\mu + 2V_2 + V_3 + \frac{1}{2}H + H_2 + \frac{1}{2}H_3$	$-t_x$	$t_2 - u_2$	$t_1 - u_1$
ψ_{25}	$-t_x$	$-U + 3\mu + \frac{H}{2}$	$-t_0 - u_0$	$t_1 + u_1$
ψ_{26}	$t_2 - u_2$	$-t_0 - u_0$	$-U + 4\mu + 2V_2 + V_3 + H + H_2 + \frac{1}{2}H_3$	0
ψ_{31}	$t_1 - u_1$	$t_1 + u_1$	0	$4\mu + 2V_2 + H + H_2$

	ψ_{28}	ψ_{29}	ψ_{30}	ψ_{35}
ψ_{28}	$-2U + 5\mu + 2V_2 + V_3 - \frac{1}{2}H - H_2 - \frac{1}{2}H_3$	$-t_x$	$t_2 + u_2$	$-t_1 - u_1$
ψ_{29}	$-t_x$	$-U + 3\mu - \frac{H}{2}$	$-t_0 + u_0$	$-t_1 + u_1$
ψ_{30}	$t_2 + u_2$	$-t_0 + u_0$	$-U + 4\mu + 2V_2 + V_3 - H - H_2 - \frac{1}{2}H_3$	0
ψ_{35}	$-t_1 - u_1$	$-t_1 + u_1$	0	$4\mu + 2V_2 - H - H_2$

Table 2.4: Diagonal matrix blocks of the unrenormalized three-site Hamiltonian $-\beta\mathcal{H}(i,j) - \beta\mathcal{H}(j,k)$. The additive constant contribution $2G$, occurring at the diagonal terms, is not shown. (*Continued on following page.*)

	ψ_{27}	ψ_{36}	ψ_{37}	ψ_{38}	ψ_{42}
ψ_{27}	$4\mu - J + 2V_2 - \frac{1}{3}H - \frac{1}{3}H_1 - \frac{1}{3}H_2$	$\sqrt{3}t_1 - \frac{1}{\sqrt{3}}u_1$	$\sqrt{3}t_1 + \frac{1}{\sqrt{3}}u_1$	0	$\frac{\sqrt{2}}{3}H - \frac{1}{3\sqrt{2}}H_1 + \frac{\sqrt{2}}{3}H_2$
ψ_{36}	$\sqrt{3}t_1 - \frac{1}{\sqrt{3}}u_1$	$-2U + 5\mu + 2V_2 + V_3 - \frac{1}{2}H - H_2 - \frac{1}{2}H_3$	$-t_x$	$t_2 + u_2$	$-2\sqrt{\frac{2}{3}}u_1$
ψ_{37}	$\sqrt{3}t_1 + \frac{1}{\sqrt{3}}u_1$	$-t_x$	$-U + 3\mu - \frac{H}{2}$	$t_0 - u_0$	$2\sqrt{\frac{2}{3}}u_1$
ψ_{38}	0	$t_2 + u_2$	$t_0 - u_0$	$-U + 4\mu + 2V_2 + V_3 - H - H_2 - \frac{1}{2}H_3$	0
ψ_{42}	$\frac{\sqrt{2}}{3}H - \frac{1}{3\sqrt{2}}H_1 + \frac{\sqrt{2}}{3}H_2$	$-2\sqrt{\frac{2}{3}}u_1$	$2\sqrt{\frac{2}{3}}u_1$	0	$4\mu + \frac{1}{2}J + 2V_2 - \frac{2}{3}H - \frac{1}{6}H_1 - \frac{2}{3}H_2$

	ψ_{39}
ψ_{39}	$4\mu + \frac{1}{2}J + 2V_2 + 2H + \frac{1}{2}H_1 + 2H_2$

	ψ_{41}
ψ_{41}	$4\mu + \frac{1}{2}J + 2V_2 - 2H + \frac{1}{2}H_1 - 2H_2$

	ψ_{43}	ψ_{44}	ψ_{46}	ψ_{47}	ψ_{56}
ψ_{43}	$-2U + 4\mu$	$-\sqrt{2}t_x$	$-2t_1$	0	$-2u_1$
ψ_{44}	$-\sqrt{2}t_x$	$-3U + 6\mu + 4V_2 + 4V_3 + V_4$	$-\sqrt{2}t_1$	0	$\sqrt{2}u_1$
ψ_{46}	$-2t_1$	$-\sqrt{2}t_1$	$-U + 5\mu - \frac{3}{4}J + 3V_2 + V_3 - \frac{1}{4}H_1$	$-\sqrt{2}t_2$	$\frac{1}{2}H + H_2 + \frac{1}{2}H_3$
ψ_{47}	0	0	$-\sqrt{2}t_2$	$-2U + 6\mu + 4V_2 + 2V_3$	$\sqrt{2}u_2$
ψ_{56}	$-2u_1$	$\sqrt{2}u_1$	$\frac{1}{2}H + H_2 + \frac{1}{2}H_3$	$\sqrt{2}u_2$	$-U + 5\mu + \frac{1}{4}J + 3V_2 + V_3 - \frac{1}{4}H_1$

	ψ_{45}	ψ_{48}	ψ_{51}	ψ_{52}
ψ_{45}	$-U + 5\mu - \frac{3}{4}J + 3V_2 + V_3 - \frac{1}{4}H_1$	$-\sqrt{2}t_1$	$-\frac{1}{2}H - H_2 - \frac{1}{2}H_3$	$\sqrt{2}u_2$
ψ_{48}	$-\sqrt{2}t_1$	$-3U + 6\mu + 4V_2 + 4V_3 + V_4$	$-\sqrt{2}u_1$	0
ψ_{51}	$-\frac{1}{2}H - H_2 - \frac{1}{2}H_3$	$-\sqrt{2}u_1$	$-U + 5\mu + \frac{1}{4}J + 3V_2 + V_3 - \frac{1}{4}H_1$	$\sqrt{2}t_2$
ψ_{52}	$\sqrt{2}u_2$	0	$\sqrt{2}t_2$	$-2U + 6\mu + 4V_2 + 2V_3$

	ψ_{49}	ψ_{50}
ψ_{49}	$-2U + 6\mu + 4V_2 + 2V_3 + H + 2H_2 + H_3$	$\sqrt{2}t_2 - \sqrt{2}u_2$
ψ_{50}	$\sqrt{2}t_2 - \sqrt{2}u_2$	$-U + 5\mu + \frac{1}{4}J + 3V_2 + V_3 + \frac{3}{2}H + \frac{1}{4}H_1 + 2H_2 + \frac{1}{2}H_3$

	ψ_{53}	ψ_{54}
ψ_{53}	$-2U + 6\mu + 4V_2 + 2V_3 - H - 2H_2 - H_3$	$\sqrt{2}t_2 + \sqrt{2}u_2$
ψ_{54}	$\sqrt{2}t_2 + \sqrt{2}u_2$	$-U + 5\mu + \frac{1}{4}J + 3V_2 + V_3 - \frac{3}{2}H + \frac{1}{4}H_1 - 2H_2 - \frac{1}{2}H_3$

	ψ_{55}
ψ_{55}	$-U + 5\mu + \frac{1}{4}J + 3V_2 + V_3 + \frac{3}{2}H + \frac{1}{4}H_1 + 2H_2 + \frac{1}{2}H_3$

	ψ_{57}
ψ_{57}	$-U + 5\mu + \frac{1}{4}J + 3V_2 + V_3 - \frac{3}{2}H + \frac{1}{4}H_1 - 2H_2 - \frac{1}{2}H_3$

	ψ_{58}	ψ_{59}
ψ_{58}	$-2U + 6\mu + 4V_2 + 2V_3 + H + 2H_2 + H_3$	$\sqrt{2}t_2 - \sqrt{2}u_2$
ψ_{59}	$\sqrt{2}t_2 - \sqrt{2}u_2$	$-3U + 7\mu + 6V_2 + 5V_3 + V_4 + \frac{1}{2}H + H_2 + \frac{1}{2}H_3$

	ψ_{60}	ψ_{61}
ψ_{60}	$-2U + 6\mu + 4V_2 + 2V_3 - H - 2H_2 - H_3$	$\sqrt{2}t_2 + \sqrt{2}u_2$
ψ_{61}	$\sqrt{2}t_2 + \sqrt{2}u_2$	$-3U + 7\mu + 6V_2 + 5V_3 + V_4 - \frac{1}{2}H - H_2 - \frac{1}{2}H_3$

	ψ_{62}
ψ_{62}	$-3U + 7\mu + 6V_2 + 5V_3 + V_4 + \frac{1}{2}H + H_2 + \frac{1}{2}H_3$

	ψ_{63}
ψ_{63}	$-3U + 7\mu + 6V_2 + 5V_3 + V_4 - \frac{1}{2}H - H_2 - \frac{1}{2}H_3$

	ψ_{64}
ψ_{64}	$-4U + 8\mu + 8V_2 + 8V_3 + 2V_4$

Table 2.4: (*continued from previous page*) Diagonal matrix blocks of the unrenormalized three-site Hamiltonian $-\beta\mathcal{H}(i,j) - \beta\mathcal{H}(j,k)$. The additive constant contribution $2G$, occurring at the diagonal terms, is not shown.

in the generalized Hamiltonian, and we calculate the expectation values n_α of these operators through the conjugate recursion relations [28]

$$n_\beta = b^{-d} n'_\alpha T_{\alpha\beta} \,. \tag{2.16}$$

Here summation over the repeated index α is implicit, and the recursion matrix is $T_{\alpha\beta} = \partial K'_\alpha / \partial K_\beta$. This matrix is calculated at each step along a given trajectory until a sink is reached, where the left eigenvector of $T_{\alpha\beta}$ with eigenvalue b^d gives the expectation values at the sink. Working backwards from the sink, Eq.(2.16) is iterated to find the n_α corresponding to the original Hubbard Hamiltonian. In this way expectation values such as the single-site electron occupation number, magnetization, and internal energy per site, can be found for the whole range of initial interaction constants. Specific heat, magnetic and charge susceptibilities are then calculated from the appropriate numerical derivatives of these densities. In the discussion of thermodynamic results below, it is important to remember that the interaction constants in the Hamiltonian of Eq.(2.6) are dimensionless. In particular, $t = \tilde{t}/k_B T$, where $\tilde{t}$ is a constant independent of temperature. Thus we will use $1/t$ as our temperature variable, measured in units of $\tilde{t}/k_B$.

2.2.4.1 Comparison of Renormalization-Group Results with High-Temperature Series Results

Since the approximate quantum decimation in Eq.(2.8) becomes exact in the high-temperature limit, it is worthwhile to verify our approach by comparison to high-temperature series. Starting from a linked cluster expansion in the electron hopping amplitude [29, 30, 31], the grand potential of the Hubbard model can be written as a series in terms of inverse temperature β. We use the results of Takahashi and Shiroishi [32], where the grand potential is given up to order β^6. Figs. 2-1 and 2-2 show the renormalization-group results for the specific heat and the magnetic susceptibility at coupling $U_0/t = 8$ for a range of small inverse temperatures, together with the corresponding curves from high-temperature series. In each case the quantities are

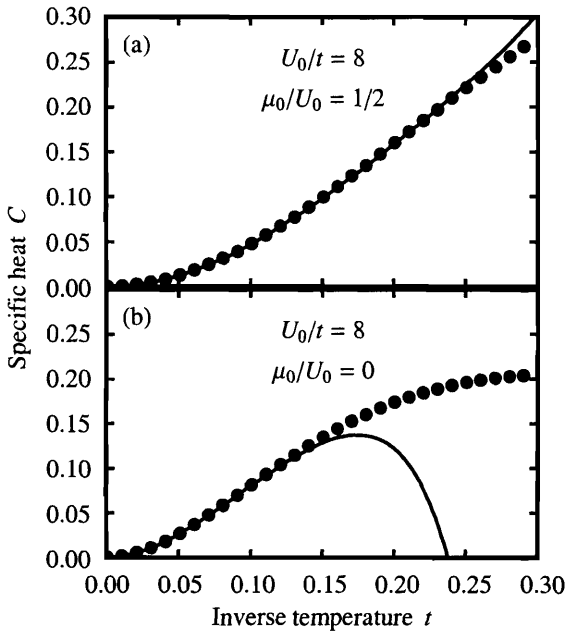

Figure 2-1: Specific heat per site C (in units of k_B) versus inverse temperature t, at zero magnetic field and coupling $U_0/t = 8$. The dots are the results of our renormalization-group calculation, while the solid curve is derived from high-temperature series [32]. In (a) and (b) the specific heat is evaluated at constant chemical potential for two different values of μ_0/U_0, one at half-filling ($\mu_0/U_0 = 1/2$), and the other away from half-filling ($\mu_0/U_0 = 0$).

evaluated at constant chemical potential, both directly at half-filling ($\mu_0/U_0 = 1/2$), and away ($\mu_0/U_0 = 0$). As expected, the renormalization-group results exactly coincide with those of the high-temperature series as $\beta \to 0$.

2.2.4.2 Comparison of Renormalization-Group Results with Quantum Transfer Matrix Results

In order to assess the Suzuki-Takano approximation at lower temperatures, we compare our renormalization-group results with the quantum transfer matrix (QTM) results of Jüttner, Klümper, and Suzuki [26, 27]. For the range of couplings $U_0/t = 4$–8 and at the three electron densities of $\langle n_i \rangle = 0.5$, 0.8, 1.0, we have determined the specific heat, the charge susceptibility $\chi_c = \partial \langle n_i \rangle / \partial \mu_0$, and the magnetic susceptibility $\chi = \partial \langle S_i^z \rangle / \partial H_0$, and plot them in Figs. 2-3–2-5 together with the QTM results (shown as dashed curves) where available.

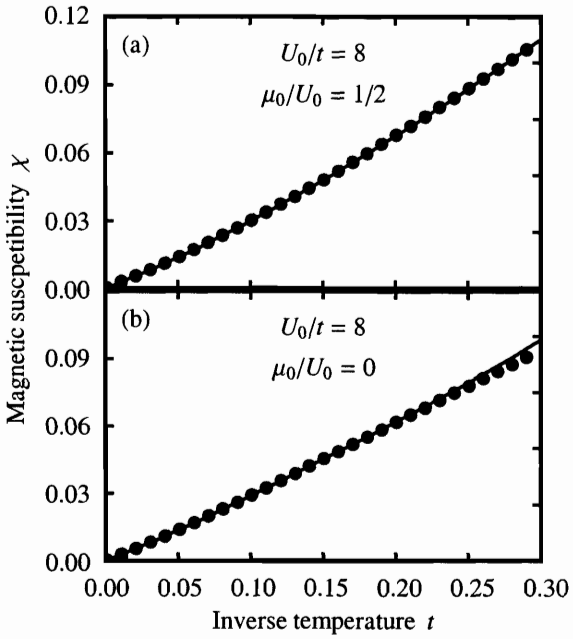

Figure 2-2: Magnetic susceptibility $\chi = \partial\langle S_i^z\rangle/\partial(H_0/t)$ versus inverse temperature t, at zero magnetic field and coupling $U_0/t = 8$. The dots are the results of our renormalization-group calculation, while the solid curve is derived from high-temperature series [32]. In (a) and (b) the magnetic susceptibility is evaluated at constant chemical potential for two different values of μ_0/U_0, one at half-filling ($\mu_0/U_0 = 1/2$), and the other away from half-filling ($\mu_0/U_0 = 0$).

Figs. 2-3 show specific heats C versus temperature $1/t$, evaluated at constant electron density. At half-filling, $\langle n_i\rangle = 1.0$, the single peak in the specific heat at small Coulomb repulsion U_0/t splits into two peaks as U_0/t is increased, with the lower temperature peak corresponding to spin excitations, and the higher temperature peak corresponding to gapped charge excitations. For all coupling strengths in these figures, the agreement between the renormalization-group results and the QTM results is very good both at high and low temperatures, and reasonably good at intermediate temperature. Even where the magnitudes of the peaks differ at intermediate temperature, the renormalization-group approach still quantitatively describes the basic evolution of the system as the coupling strength is increased. This was already noted by Suzuki and Takano in their original renormalization-group study of the $d = 1$ Hubbard model at half-filling [6]. The two-peak structure at large U_0/t persists in the doped system at $\langle n_i\rangle = 0.8$, though the high-temperature peak is reduced and

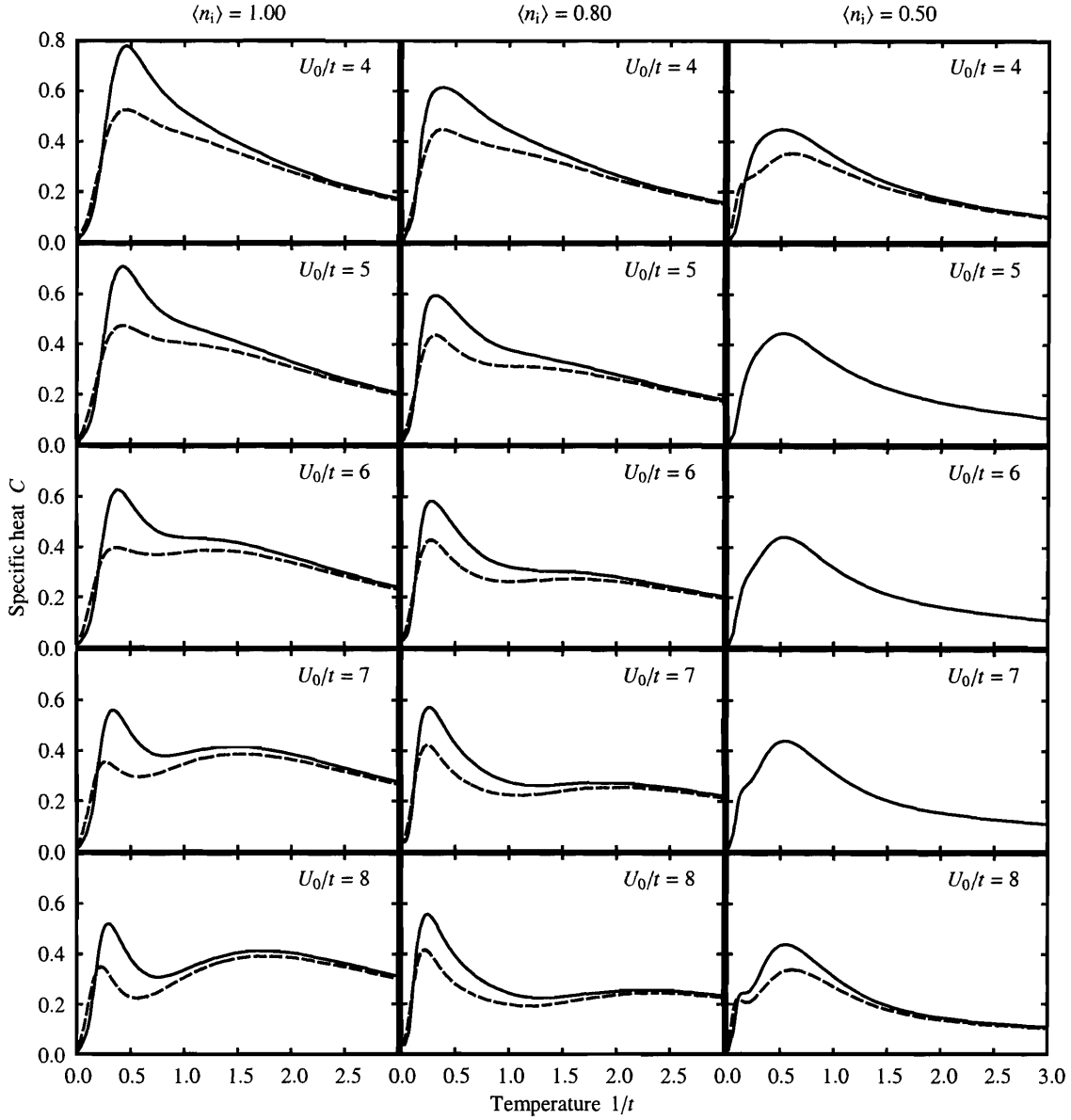

Figure 2-3: Specific heat per site C (in units of k_B) versus temperature $1/t$, at zero magnetic field and the range of couplings $U_0/t = 4$–8. The specific heat is evaluated at the constant electron density of $\langle n_i \rangle = 0.5$, 0.8, or 1.0, shown in the left, middle, and right columns respectively. The solid curves are the results from our renormalization-group calculation, while the dashed curves, where available for comparison, are from the quantum transfer matrix method [26, 27]. The plots for couplings $U_0/t = 5$, 6, 7 at $\langle n_i \rangle = 0.5$ show the renormalization-group results alone.

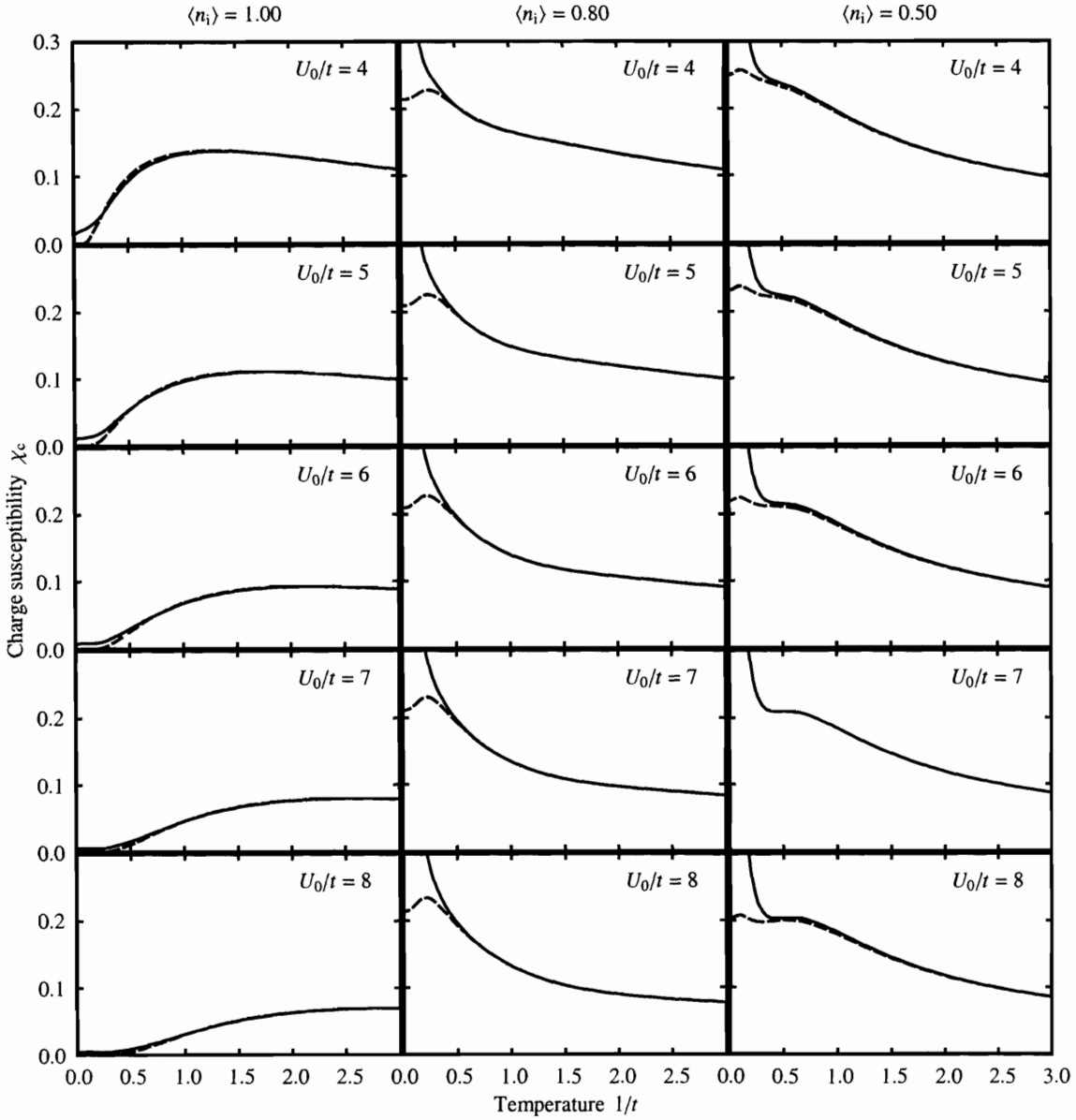

Figure 2-4: Charge susceptibility $\chi_c = \partial\langle n_i\rangle/\partial\mu_0$ versus temperature $1/t$, at zero magnetic field and the range of couplings $U_0/t = 4$–8. The charge susceptibility is evaluated at the constant electron density of $\langle n_i\rangle = 0.5$, 0.8, or 1.0, shown in the left, middle, and right columns respectively. The solid curves are the results from our renormalization-group calculation, while the dashed curves, where available for comparison, are from the quantum transfer matrix method [26, 27]. The plot for coupling $U_0/t = 7$ at $\langle n_i\rangle = 0.5$ shows the renormalization-group result alone.

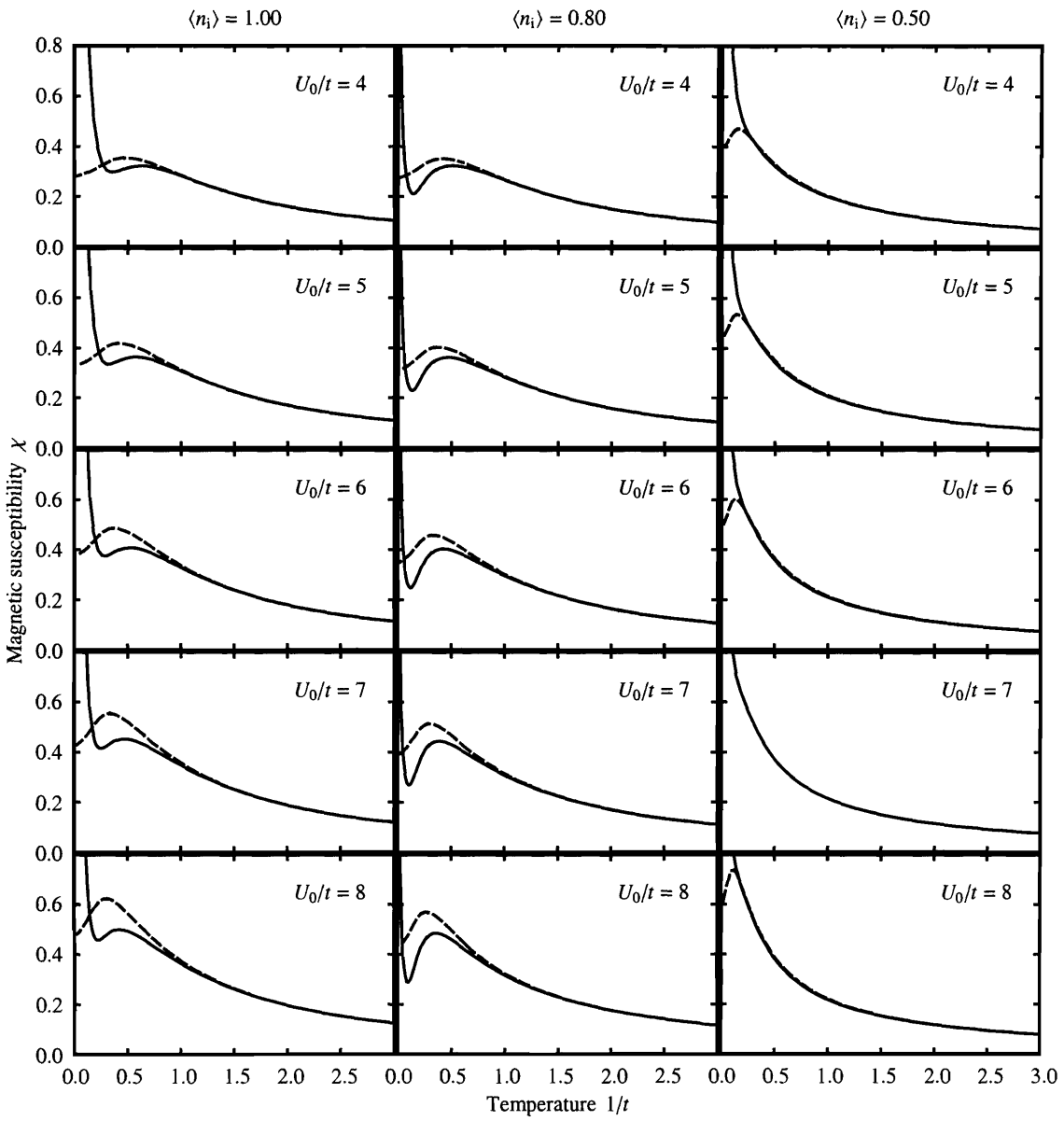

Figure 2-5: Magnetic susceptibility $\chi = \partial\langle S_i^z\rangle/\partial(H_0/t)$ versus temperature $1/t$, at zero magnetic field and for the range of couplings U_0/t = 4–8. The susceptibility is evaluated at the constant electron density of $\langle n_i\rangle$ = 0.5, 0.8, or 1.0, shown in the left, middle, and right columns respectively. The solid curves are the results from our renormalization-group calculation, while the dashed curves, where available for comparison, are from the quantum transfer matrix method [26, 27]. The plot for coupling $U_0/t = 7$ at $\langle n_i\rangle = 0.5$ shows the renormalization-group result alone.

shifted to larger temperatures, while the lower-temperature peak is enhanced by gapless charge excitations which appear upon doping. The behavior at quarter-filling, $\langle n_i \rangle = 0.5$, is precisely that described in Ref. [26] from the QTM data: a broad peak around $1/t \sim 0.6$ which does not change significantly with coupling strength, since the system at lower electron densities is less sensitive to the on-site Coulomb interaction. For $U_0/t = 8$, the renormalization-group result also shows the beginning of a small subsidiary peak near $1/t \sim 0.2$, capturing a feature of the QTM curve even at this low temperature.

For the charge susceptibility χ_c in Fig. 2-4, the two approaches remain in excellent numerical agreement at all U_0/t and electron densities to temperatures as low as $1/t \sim 0.5$. The accuracy achieved is across coupling strength and doping levels: in the worst case, at $U_0/t = 4$ and $\langle n_i \rangle = 1.0$, the renormalization-group and QTM values differed by no more than 5% down to $1/t = 0.6$; in the best, at $U_0/t = 8$ and $\langle n_i \rangle = 0.8$, the difference was smaller than 0.1% down to $1/t = 0.7$. However, there are significant discrepancies in the zero temperature limit. At half-filling, because the system is an incompressible insulator in the ground state, χ_c should be exponentially suppressed at lower temperatures, a behavior approximately reproduced by the renormalization-group calculation, though χ_c goes to a small non-zero constant as $1/t \to 0$. As with the specific heat, the renormalization-group values get closer to the QTM values as U_0/t is increased. For any finite doping near half-filling, the behavior of the charge susceptibility completely changes, with low temperature susceptibility greatly enhanced, and the zero temperature χ_c actually diverging as $1/\delta$, where the doping level is $\delta = 1 - \langle n_i \rangle$ [20]. For both $\langle n_i \rangle = 0.8$ and 0.5, we see that the renormalization-group calculation very precisely describes the increase in χ_c down to $1/t \sim 0.5$, including the formation of a peak with increasing U_0/t for $\langle n_i \rangle = 0.5$, but diverges at zero temperature, whereas the QTM results level off and go to a finite value at zero temperature.

The comparison between renormalization-group and QTM results for the magnetic susceptibility in Fig. 2-5 is similar to that for the charge susceptibility. Depending on coupling strength and doping level, the values from the two methods typically stay

within 7% of one another for temperatures down to $1/t \sim 0.7$ (and in the case of $\langle n_i \rangle = 0.5$, differ by no more than 2.5% down to $1/t = 0.2$), but the renormalization-group curves incorrectly diverge at zero temperature. Despite this, for $\langle n_i \rangle = 1.0$ and 0.8, the renormalization-group calculation still gives a peak structure, and this peak is both enhanced and shifted to lower temperatures as U_0/t increases, which is the expected behavior. For $\langle n_i \rangle = 0.5$ the peak appears at such low temperatures that it does not show up in the renormalization-group results.

Overall, the Suzuki-Takano quantum decimation fares remarkably well even at moderate-to-low temperatures, giving good numerical estimates of the charge and magnetic susceptibilities, as well as quantitatively describing the physical evolution of the system, though unsurprisingly the approximation breaks down near $T = 0$. It thus is a solid candidate for incorporation into higher-dimensional renormalization-group schemes for the Hubbard and other lattice conduction models, where it can yield phase diagram structure and detailed thermodynamic information at finite temperatures and arbitrary electron densities.

References

[1] M. Suzuki and H. Takano, Phys. Lett. A **69**, 426 (1979).
[2] H. Takano and M. Suzuki, J. Stat. Phys. **26**, 635 (1981).
[3] P. Tomczak, Phys. Rev. B **53**, 500R (1996).
[4] P. Tomczak and J. Richter, Phys. Rev. B **54** 9004 (1996).
[5] P. Tomczak and J. Richter, J. Phys A: Math. Gen. **36**, 5399 (2003).
[6] H. Takano and M. Suzuki, Physica A **109**, 618 (1981).
[7] S.A. Cannas, F.A. Tamarit, and C. Tsallis, Solid State Commun. **78**, 685 (1991).
[8] S.A. Cannas, F.A. Tamarit, and C. Tsallis, Phys. Rev. B **45**, 10496 (1992).
[9] S.A. Cannas and C. Tsallis, Z. Phys. **89**, 195 (1992).
[10] A. Falicov and A.N. Berker, Phys. Rev. B **51**, 12458 (1995).
[11] A. Falicov and A.N. Berker, Turk. J. Phys. **19**, 127 (1995).
[12] M. Hinczewski and A.N. Berker, cond-mat/0503226.
[13] M. Hinczewski and A.N. Berker, cond-mat/0503631.
[14] M. Hinczewski and A.N. Berker, cond-mat/0504741.
[15] H. Shiba, Prog. Theor. Phys. **48**, 2171 (1972).
[16] H. Shiba and P.A. Pincus, Phys. Rev. B **5**, 1966 (1972).
[17] E.H. Lieb and F.Y. Wu, Phys. Rev. Lett **20**, 1445 (1968).
[18] M. Takahashi, Prog. Theor. Phys. **47**, 69 (1972).
[19] N. Kawakami, T. Usuki, and A. Okiji, Phys. Lett. A **137**, 287 (1989).
[20] T. Usuki, N. Kawakami, and A. Okiji, J. Phys. Soc. Jpn. **59**, 1357 (1990).
[21] B.S. Shastry, Phys. Rev. Lett. **56**, 1529 (1986).
[22] B.S. Shastry, Phys. Rev. Lett. **56**, 2453 (1986).
[23] B.S. Shastry, J. Stat. Phys. **30**, 57 (1988).
[24] A. Klümper and R.Z. Bariev, Nucl. Phys. B **458**, 623 (1996).
[25] M.J. Martins and P.B. Ramos, Nucl. Phys. B **522**, 413 (1998).
[26] G. Jüttner, A. Klümper, and J. Suzuki, Nucl. Phys. B **522**, 471 (1998).
[27] G. Jüttner, A. Klümper, and J. Suzuki, Physica B **259-261**, 1019 (1999).
[28] A.N. Berker, S. Ostlund, and F.A. Putnam, Phys. Rev. B **17**, 3650 (1978).
[29] K. Kubo, Prog. Theor. Phys. **64**, 758 (1980).
[30] K. Kubo, Suppl. Prog. Theor. Phys. **69**, 290 (1980).
[31] K.L. Liu, Can. J. Phys. **62**, 361 (1984).
[32] M. Takahashi and M. Shiroishi, Phys. Rev. B **65**, 165104 (2002).

Chapter 3

The Hubbard Model in $d = 3$

3.1 Introduction

The results of the last chapter show us that the finite temperature physics of the one-dimensional Hubbard model at arbitrary electron densities can be described quite well using a Suzuki-Takano decimation. The next step is to develop an analogous renormalization-group transformation for the Hubbard model on a d-dimensional hypercubic lattice. Naively, the most straightforward approach is to apply the same procedure used in $d = 1$: divide the lattice into two sublattices, and trace over the spins on one of the sublattices. Unfortunately, for $d > 1$ every iteration of this method will generate new interaction terms in the Hamiltonian, involving ever larger groups of sites. If the original Hamiltonian starts with just on-site and nearest-neighbor terms, the renormalized system will also have further-neighbor and multi-site interactions, and the problem becomes intractable after the first rescaling.

We need to ensure that the form of the Hamiltonian stays closed under repeated renormalization-group transformations. One of the most successful schemes for accomplishing this was developed by Migdal and Kadanoff [1, 2]. An example of the isotropic Migdal-Kadanoff procedure applied to the $d = 3$ cubic lattice is shown in Fig. 3-1. The first step consists of modifying the nearest-neighbor interactions of the original lattice in a process known as "bond-moving"—every deleted interaction between one pair of sites is accompanied by a strengthened interaction between another

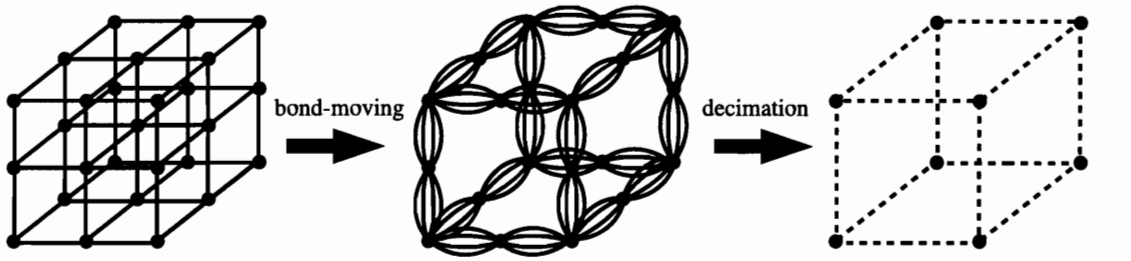

Figure 3-1: An isotropic Migdal-Kadanoff procedure with length rescaling factor $b = 2$ for a cubic lattice.

pair. The result is a new cubic lattice where the nearest-neighbor sites are connected by two consecutive segments of the old lattice. We decimate the middle site connecting these two segments, generating renormalized nearest-neighbor interactions for the new lattice. Alternatively, we could have deleted interactions on the first step, and did the strengthening only after the decimation—the method chosen in the following section. In either variety of the procedure the predicted phase diagram structure remains the same, though the calculated transition temperatures differ.

While the renormalization-group transformation derived from the Migdal-Kadanoff method is approximate for the hypercubic lattice, it is exact on a hierarchical lattice [3, 4, 5] (up to whatever additional approximation is introduced by the decimation). This fact goes a long way towards explaining the effectiveness of the method, since if the transformation can be realized on an actual lattice it must give physically robust results. We will return to the relationship between the Migdal-Kadanoff procedure and hierarchical lattices in Chapters 5 and 6. For now, it is sufficient that we have a simple and reliable way of extending the one-dimensional Suzuki-Takano quantum decimation to $d > 1$. In this chapter we will see the fruits of this approach for the $d = 3$ Hubbard model.

3.2 Two Superconducting Phases in the $d = 3$ Hubbard Model: Phase Diagram and Specific Heat from Renormalization-Group Calculations

Michael Hinczewski and A. Nihat Berker
Department of Physics, Istanbul Technical University, Maslak 34469, Istanbul, Turkey,
Department of Physics, Massachusetts Institute of Technology, Cambridge, Massachusetts 02139, U.S.A.,
Feza Gürsey Research Institute, TÜBITAK - Bosphorus University, Çengelköy 81220, Istanbul, Turkey

Abstract

The phase diagram of the $d = 3$ Hubbard model is calculated as a function of temperature and electron density $\langle n_i \rangle$, in the full range of densities between 0 and 2 electrons per site, using renormalization-group theory. An antiferromagnetic phase occurs at lower temperatures, at and near the half-filling density of $\langle n_i \rangle = 1$. The antiferromagnetic phase is unstable to hole or electron doping of at most 15%, yielding to two distinct "τ" phases: for large coupling U/t, one such phase occurs between 30-35% hole or electron doping, and for small to intermediate coupling U/t another such phase occurs between 10-18% doping. Both τ phases are distinguished by non-zero hole or electron hopping expectation values at all length scales. Under further doping, the τ phases yield to hole- or electron-rich disordered phases. We have calculated the specific heat over the entire phase diagram. The low-temperature specific heat of the weak-coupling τ phase shows a BCS-type exponential decay, indicating a gap in the excitation spectrum, and a cusp singularity at the phase boundary. The strong-coupling τ phase, on the other hand, has characteristics of BEC-type superconductivity, including a critical exponent $\alpha \approx -1$, and an additional peak in the specific heat above the transition temperature indicating pair formation. In the limit of large Coulomb repulsion, the phase diagram of the tJ model is recovered.

PACS numbers: 74.72.-h, 71.10.Fd, 05.30.Fk, 74.25.Dw

arXiv: cond-mat/0503226

3.2.1 Introduction

The Hubbard model [6] is the simplest realistic (in that it retains particulate dynamics) model of electronic conduction systems. This model should constitute a fair description for many real solid-state physics systems and a starting-point description for those systems with added complexities such as quenched randomness, frustration, and/or spatial anisotropy. The first query that comes to mind, in the study of either experimental or model systems, is on the phase diagram, as a function of physical parameters such as temperature and density. Nevertheless, until recently [7], no estimates, let alone (be it approximate) solutions, were ventured on the phase diagram of the Hubbard model at dimensions greater than $d = 1$, at temperatures greater than $T = 0$, and densities away from half-filling.

The first approach to a phase diagram problem, in the past before the advent of renormalization-group theory [8], had been through a mean-field approximation. However, such method is not useful for the Hubbard model, since, where the characteristic phenomena occur away from half-filling, the off-diagonal term in the Hamiltonian plays a determining role, as we shall see below. There is no ready way to deal with such a dominant quantum mechanical effect using mean-field theory. On the other hand, renormalization-group theory, which some time ago has excelled over mean-field theory in phase diagram studies, is effective. Previous renormalization-group calculations have concentrated on studying the Hubbard model in lower dimensions, at zero temperature, or at half-filling: The zero-temperature (ground-state) properties were successfully obtained in $d = 1, 2, 3$.[9, 10] In $d = 1$ at half-filling, the thermodynamic properties were accurately calculated for finite temperatures.[11] In cases where comparison is possible due to the availability of exact results in $d = 1$, the renormalization-group results have proven to be very accurate, coming to within about 1% of the exact results.[10, 11] In $d = 2$ at half filling, it was found that no phase transition occurs as a function of temperature.[12, 13] This result was later extended to other fillings in $d = 2$ [14] and confirmed by quantum Monte Carlo calculations [15]. In $d = 3$ at half filling, an antiferromagnetic phase transition as a function

of temperature was obtained.[13] One calculation done in $d = 3$ at finite temperature and arbitrary chemical potential [14] did not obtain the "τ" phase reported below and in Ref.[7].

The physics of the Hubbard model in the limit of large Coulomb repulsion is believed to be described by the tJ model [16, 17]. Application of renormalization-group theory to the entire density range of the tJ model at finite temperatures in $d = 3$ has yielded [18, 19], between 30-40% vacancies from $\langle n_i \rangle = 1$, a novel (dubbed "τ") phase in which the electron hopping strength in the Hamiltonian renormalizes to infinity under repeated scale changes, while the system remains partially filled. The calculated topology of the phase diagram, including near the τ phase a first-order phase transition that is very narrow (less than 2% jump in the electron density) and an antiferromagnetic phase that is unstable to at most 10% vacancies from $\langle n_i \rangle = 1$, is indeed reminiscent of experimental phase diagram determinations with lanthanide oxides [20].

While the studies above [9, 10, 11, 12, 13, 14, 18, 19] have used position-space renormalization-group approaches, there has recently been a revival of interest in Wilson perturbative renormalization-group methods applied to correlated fermion problems. These methods have long been known to be successful for one-dimensional systems [21, 22] and, in the last few years, for the $d = 2$ Hubbard model, they have yielded antiferromagnetic instabilities near half-filling and superconducting instabilities at smaller densities [23, 24, 25, 26, 27, 28]. Because of the perturbative nature of these treatments, their predictions are strictly valid only in the case of weak coupling. The position-space renormalization-group method presented in this paper appears to work over the entire range of coupling strengths, as seen below, and yields definite phase diagrams and thermodynamic functions.

In fact, our approach makes an interesting prediction for the evolution of the Hubbard phase diagram as coupling is increased. We find two distinct τ phases, one occurring at small to intermediate coupling and the other, inclusive of the tJ model τ phase, occurring at strong coupling. From an analysis of their specific heat behaviors, we find that the two τ phases respectively have characteristic properties of

a weakly-coupled BCS-type and a strongly-coupled BEC-type superconducting phase. Since high-T_c materials share aspects of both limits, and are thought to lie in some intermediate coupling range [29], our prediction for the Hubbard phase diagram may be directly relevant to the physics of high-T_c superconductors.

3.2.2 The Hubbard Model

The Hubbard model is defined by the Hamiltonian

$$-\beta H = -t \sum_{\langle ij \rangle, \sigma} \left(c_{i\sigma}^{\dagger} c_{j\sigma} + c_{j\sigma}^{\dagger} c_{i\sigma} \right) - U_0 \sum_i n_{i\uparrow} n_{i\downarrow} + \mu_0 \sum_i n_i \,, \tag{3.1}$$

with $\beta = 1/kT$, describing electron conduction on a d-dimensional hypercubic lattice. Here $c_{i\sigma}^{\dagger}$ and $c_{i\sigma}$ respectively are creation and annihilation operators, obeying anticommutation rules, for an electron with spin $\sigma = \uparrow$ or $\downarrow$ at the site i of the lattice; $n_{i\sigma} = c_{i\sigma}^{\dagger} c_{i\sigma}$ and $n_i = n_{i\uparrow} + n_{i\downarrow}$ are electron number operators. Each lattice site can accommodate up to two electrons with opposite spins. The index $\langle ij \rangle$ denotes summation over all nearest-neighbor pairs of sites. The three terms of this Hamiltonian respectively incorporate kinetic energy (parametrized by the electron hopping strength t), on-site Coulomb repulsion (with coefficient $U_0 > 0$), and chemical potential μ_0. It is convenient for our purposes to rearrange Eq.(3.1) into an equivalent Hamiltonian by grouping into a single lattice summation:

$$\begin{aligned} -\beta H &= \sum_{\langle ij \rangle} \left\{ -t \sum_{\sigma} \left(c_{i\sigma}^{\dagger} c_{j\sigma} + c_{j\sigma}^{\dagger} c_{i\sigma} \right) - U \left(n_{i\uparrow} n_{i\downarrow} + n_{j\uparrow} n_{j\downarrow} \right) + \mu \left(n_i + n_j \right) \right\} \\ &\equiv \sum_{\langle ij \rangle} \left\{ -\beta H(i,j) \right\} \,. \end{aligned} \tag{3.2}$$

The interaction constants are trivially related by $U = U_0/2d, \mu = \mu_0/2d$, and we have hereby exhibited the individual-pair Hamiltonian $-\beta H(i,j)$.

3.2.3 Renormalization-Group Transformation

3.2.3.1 Exact Formulation in $d = 1$

For $d = 1$ (with lattice sites $i = 1, 2, 3, \ldots$), the Hubbard Hamiltonian in Eq.(3.2) takes the form

$$-\beta H = \sum_i \{-\beta H(i, i+1)\}, \tag{3.3}$$

for which an exact renormalization-group transformation can be formulated. In terms of matrix elements, this exact transformation is [18]

$$\langle u_1 u_3 u_5 \cdots | e^{-\beta' H'} | v_1 v_3 v_5 \cdots \rangle = \sum_{w_2, w_4, w_6, \ldots} \langle u_1 w_2 u_3 w_4 u_5 w_6 \cdots | e^{-\beta H} | v_1 w_2 v_3 w_4 v_5 w_6 \cdots \rangle , \tag{3.4}$$

where u_i, v_i, and w_i are state variables for lattice site i. These variables range over the set $\{\circ, \uparrow, \downarrow, \Updownarrow\}$, by which we represent the no electron, a single electron with spin up, a single electron with spin down, and doubly occupied states. Here and below, the quantities referring to the renormalized (rescaled) system are denoted with a prime. The transformation in Eq.(3.4) eliminates half of the degrees of freedom in the system, while exactly preserving the partition function ($Z' = Z$). However, the transformation cannot be readily implemented, due to the non-commutativity of the operators in the Hamiltonian.

3.2.3.2 Approximation in $d = 1$

The renormalization-group transformation formulated in the previous section is implemented approximately, as follows:

$$\begin{aligned} \mathrm{Tr}_{\mathrm{even}} e^{-\beta H} =& \mathrm{Tr}_{\mathrm{even}} e^{\sum_i \{-\beta H(i,i+1)\}} = \mathrm{Tr}_{\mathrm{even}} e^{\sum_i^{\mathrm{even}} \{-\beta H(i-1,i) - \beta H(i,i+1)\}} \\ \simeq& \prod_i^{\mathrm{even}} \mathrm{Tr}_i e^{\{-\beta H(i-1,i) - \beta H(i,i+1)\}} = \prod_i^{\mathrm{even}} e^{-\beta' H'(i-1,i+1)} \\ \simeq& e^{\sum_i^{\mathrm{even}} \{-\beta' H'(i-1,i+1)\}} = e^{-\beta' H'}. \end{aligned} \tag{3.5}$$

n	p	s	m_s	Two-site basis states
0	+	0	0	$\|\phi_1\rangle = \|\circ\circ\rangle$
1	+	1/2	1/2	$\|\phi_2\rangle = \frac{1}{\sqrt{2}}\{\|\uparrow\circ\rangle + \|\circ\uparrow\rangle\}$
1	−	1/2	1/2	$\|\phi_4\rangle = \frac{1}{\sqrt{2}}\{\|\uparrow\circ\rangle - \|\circ\uparrow\rangle\}$
2	+	0	0	$\|\phi_6\rangle = \frac{1}{\sqrt{2}}\{\|\updownarrow\circ\rangle + \|\circ\updownarrow\rangle\}$
2	−	0	0	$\|\phi_7\rangle = \frac{1}{\sqrt{2}}\{\|\updownarrow\circ\rangle - \|\circ\updownarrow\rangle\}$, $\|\phi_8\rangle = \frac{1}{\sqrt{2}}\{\|\uparrow\downarrow\rangle - \|\downarrow\uparrow\rangle\}$
2	+	1	1	$\|\phi_9\rangle = \|\uparrow\uparrow\rangle$
2	+	1	0	$\|\phi_{10}\rangle = \frac{1}{\sqrt{2}}\{\|\uparrow\downarrow\rangle + \|\downarrow\uparrow\rangle\}$
3	+	1/2	1/2	$\|\phi_{12}\rangle = \frac{1}{\sqrt{2}}\{\|\updownarrow\uparrow\rangle + \|\uparrow\updownarrow\rangle\}$
3	−	1/2	1/2	$\|\phi_{14}\rangle = \frac{1}{\sqrt{2}}\{\|\updownarrow\uparrow\rangle - \|\uparrow\updownarrow\rangle\}$
4	+	0	0	$\|\phi_{16}\rangle = \|\updownarrow\updownarrow\rangle$

Table 3.1: The two-site basis states used in the derivation of the recursion relations, in Eq.(3.8). In these basis states, $e^{-\beta' H'(i,k)}$ is diagonal, with the exception of a 2×2 block involving $|\phi_6\rangle$ and $|\phi_8\rangle$. The corresponding particle number (n), parity (p), total spin (s), and total spin z-component (m_s) quantum numbers are also given. The states $|\phi_3\rangle$, $|\phi_5\rangle$, $|\phi_{11}\rangle$, $|\phi_{13}\rangle$, $|\phi_{15}\rangle$ are obtained by spin reversal from $|\phi_2\rangle$, $|\phi_4\rangle$, $|\phi_9\rangle$, $|\phi_{12}\rangle$, $|\phi_{14}\rangle$, respectively.

In the two approximate steps, marked by $\simeq$ in Eq.(3.5), we ignore the non-commutation of operators separated beyond three consecutive sites of the unrenormalized system. Since each of these two steps involves the same approximation but in opposite directions, some mutual compensation can be expected. The success of this approximation at predicting finite-temperature behavior has been verified in earlier studies of quantum spin systems [30, 31].

The algebraic content of the renormalization-group mapping can be extracted from Eq.(3.5) as

$$e^{-\beta' H'(i,k)} = \mathrm{Tr}_j e^{-\beta H(i,j) - \beta H(j,k)}, \tag{3.6}$$

where i, j, k are three consecutive sites of the unrenormalized system. The operators $-\beta' H'(i,k)$ and $-\beta H(i,j) - \beta H(j,k)$ act on the space of two-site and three-site states respectively, so that, in terms of matrix elements,

$$\langle u_i v_k | e^{-\beta' H'(i,k)} | \bar{u}_i \bar{v}_k \rangle = \sum_{w_j} \langle u_i \, w_j \, v_k | e^{-\beta H(i,j) - \beta H(j,k)} | \bar{u}_i \, w_j \, \bar{v}_k \rangle \, , \tag{3.7}$$

where $u_i, w_j, v_k, \bar{u}_i, \bar{v}_k$ are single-site state variables. Eq.(3.7) indicates the contraction of a 64×64 matrix on the right into a 16×16 matrix on the left. This is

n	p	s	m_s	Three-site basis states
0	+	0	0	$\|\psi_1\rangle = \|\circ\circ\circ\rangle$
1	+	1/2	1/2	$\|\psi_2\rangle = \|\circ\uparrow\circ\rangle$, $\|\psi_3\rangle = \frac{1}{\sqrt{2}}\{\|\uparrow\circ\circ\rangle + \|\circ\circ\uparrow\rangle\}$
1	−	1/2	1/2	$\|\psi_6\rangle = \frac{1}{\sqrt{2}}\{\|\uparrow\circ\circ\rangle - \|\circ\circ\uparrow\rangle\}$
2	+	0	0	$\|\psi_8\rangle = \frac{1}{2}\{\|\uparrow\downarrow\circ\rangle - \|\downarrow\uparrow\circ\rangle - \|\circ\uparrow\downarrow\rangle + \|\circ\downarrow\uparrow\rangle\}$, $\|\psi_9\rangle = \|\circ\updownarrow\circ\rangle$, $\|\psi_{10}\rangle = \frac{1}{\sqrt{2}}\{\|\updownarrow\circ\circ\rangle + \|\circ\circ\updownarrow\rangle\}$
2	−	0	0	$\|\psi_{11}\rangle = \frac{1}{2}\{\|\uparrow\downarrow\circ\rangle - \|\downarrow\uparrow\circ\rangle + \|\circ\uparrow\downarrow\rangle - \|\circ\downarrow\uparrow\rangle\}$, $\|\psi_{12}\rangle = \frac{1}{\sqrt{2}}\{\|\uparrow\circ\downarrow\rangle - \|\downarrow\circ\uparrow\rangle\}$, $\|\psi_{13}\rangle = \frac{1}{\sqrt{2}}\{\|\updownarrow\circ\circ\rangle - \|\circ\circ\updownarrow\rangle\}$
2	+	1	1	$\|\psi_{14}\rangle = \|\uparrow\circ\uparrow\rangle$, $\|\psi_{15}\rangle = \frac{1}{\sqrt{2}}\{\|\uparrow\uparrow\circ\rangle + \|\circ\uparrow\uparrow\rangle\}$
2	+	1	0	$\|\psi_{16}\rangle = \frac{1}{2}\{\|\uparrow\downarrow\circ\rangle + \|\downarrow\uparrow\circ\rangle + \|\circ\uparrow\downarrow\rangle + \|\circ\downarrow\uparrow\rangle\}$, $\|\psi_{17}\rangle = \frac{1}{\sqrt{2}}\{\|\uparrow\circ\downarrow\rangle + \|\downarrow\circ\uparrow\rangle\}$
2	−	1	1	$\|\psi_{20}\rangle = \frac{1}{\sqrt{2}}\{\|\uparrow\uparrow\circ\rangle - \|\circ\uparrow\uparrow\rangle\}$
2	−	1	0	$\|\psi_{21}\rangle = \frac{1}{2}\{\|\uparrow\downarrow\circ\rangle + \|\downarrow\uparrow\circ\rangle - \|\circ\uparrow\downarrow\rangle - \|\circ\downarrow\uparrow\rangle\}$
3	+	1/2	1/2	$\|\psi_{23}\rangle = \frac{1}{\sqrt{6}}\{2\|\uparrow\downarrow\uparrow\rangle - \|\uparrow\uparrow\downarrow\rangle - \|\downarrow\uparrow\uparrow\rangle\}$, $\|\psi_{24}\rangle = \frac{1}{\sqrt{2}}\{\|\uparrow\updownarrow\circ\rangle + \|\circ\updownarrow\uparrow\rangle\}$, $\|\psi_{25}\rangle = \frac{1}{\sqrt{2}}\{\|\uparrow\circ\updownarrow\rangle + \|\updownarrow\circ\uparrow\rangle\}$, $\|\psi_{26}\rangle = \frac{1}{\sqrt{2}}\{\|\updownarrow\uparrow\circ\rangle + \|\circ\uparrow\updownarrow\rangle\}$
3	−	1/2	1/2	$\|\psi_{31}\rangle = \frac{1}{\sqrt{2}}\{\|\uparrow\uparrow\downarrow\rangle - \|\downarrow\uparrow\uparrow\rangle\}$, $\|\psi_{32}\rangle = \frac{1}{\sqrt{2}}\{\|\uparrow\updownarrow\circ\rangle - \|\circ\updownarrow\uparrow\rangle\}$, $\|\psi_{33}\rangle = \frac{1}{\sqrt{2}}\{\|\uparrow\circ\updownarrow\rangle - \|\updownarrow\circ\uparrow\rangle\}$, $\|\psi_{34}\rangle = \frac{1}{\sqrt{2}}\{\|\updownarrow\uparrow\circ\rangle - \|\circ\uparrow\updownarrow\rangle\}$
3	+	3/2	3/2	$\|\psi_{39}\rangle = \|\uparrow\uparrow\uparrow\rangle$
3	+	3/2	1/2	$\|\psi_{40}\rangle = \frac{1}{\sqrt{3}}\{\|\uparrow\downarrow\uparrow\rangle + \|\uparrow\uparrow\downarrow\rangle + \|\downarrow\uparrow\uparrow\rangle\}$
4	+	0	0	$\|\psi_{43}\rangle = \|\updownarrow\circ\updownarrow\rangle$, $\|\psi_{44}\rangle = \frac{1}{\sqrt{2}}\{\|\updownarrow\updownarrow\circ\rangle + \|\circ\updownarrow\updownarrow\rangle\}$, $\|\psi_{45}\rangle = \frac{1}{2}\{\|\uparrow\downarrow\updownarrow\rangle - \|\downarrow\uparrow\updownarrow\rangle - \|\updownarrow\uparrow\downarrow\rangle + \|\updownarrow\downarrow\uparrow\rangle\}$
4	−	0	0	$\|\psi_{46}\rangle = \frac{1}{2}\{\|\downarrow\uparrow\updownarrow\rangle - \|\uparrow\downarrow\updownarrow\rangle - \|\updownarrow\uparrow\downarrow\rangle + \|\updownarrow\downarrow\uparrow\rangle\}$, $\|\psi_{47}\rangle = \frac{1}{\sqrt{2}}\{\|\uparrow\updownarrow\downarrow\rangle - \|\downarrow\updownarrow\uparrow\rangle\}$, $\|\psi_{48}\rangle = \frac{1}{\sqrt{2}}\{\|\updownarrow\updownarrow\circ\rangle - \|\circ\updownarrow\updownarrow\rangle\}$
4	+	1	1	$\|\psi_{49}\rangle = \|\uparrow\updownarrow\uparrow\rangle$, $\|\psi_{50}\rangle = \frac{1}{\sqrt{2}}\{\|\uparrow\uparrow\updownarrow\rangle + \|\updownarrow\uparrow\uparrow\rangle\}$
4	+	1	0	$\|\psi_{51}\rangle = \frac{1}{2}\{\|\uparrow\downarrow\updownarrow\rangle + \|\downarrow\uparrow\updownarrow\rangle + \|\updownarrow\uparrow\downarrow\rangle + \|\updownarrow\downarrow\uparrow\rangle\}$, $\|\psi_{52}\rangle = \frac{1}{\sqrt{2}}\{\|\uparrow\updownarrow\downarrow\rangle + \|\downarrow\updownarrow\uparrow\rangle\}$
4	−	1	1	$\|\psi_{55}\rangle = \frac{1}{\sqrt{2}}\{\|\uparrow\uparrow\updownarrow\rangle - \|\updownarrow\uparrow\uparrow\rangle\}$
4	−	1	0	$\|\psi_{56}\rangle = \frac{1}{2}\{\|\uparrow\downarrow\updownarrow\rangle + \|\downarrow\uparrow\updownarrow\rangle - \|\updownarrow\uparrow\downarrow\rangle - \|\updownarrow\downarrow\uparrow\rangle\}$
5	+	1/2	1/2	$\|\psi_{58}\rangle = \|\updownarrow\uparrow\updownarrow\rangle$, $\|\psi_{59}\rangle = \frac{1}{\sqrt{2}}\{\|\uparrow\updownarrow\updownarrow\rangle + \|\updownarrow\updownarrow\uparrow\rangle\}$
5	−	1/2	1/2	$\|\psi_{62}\rangle = \frac{1}{\sqrt{2}}\{\|\updownarrow\updownarrow\uparrow\rangle - \|\uparrow\updownarrow\updownarrow\rangle\}$
6	+	0	0	$\|\psi_{64}\rangle = \|\updownarrow\updownarrow\updownarrow\rangle$

Table 3.2: The three-site basis states used in the derivation of the recursion relations, in Eq.(3.8). In these basis states, $e^{-\beta H(i,j)-\beta H(j,k)}$ is block-diagonal, with the largest blocks being 4×4 (see Table IV). The corresponding particle number (n), parity (p), total spin (s), and total spin z-component (m_s) quantum numbers are also given. The states $|\psi_{4-5}\rangle$, $|\psi_7\rangle$, $|\psi_{18-19}\rangle$, $|\psi_{22}\rangle$, $|\psi_{27-30}\rangle$, $|\psi_{35-38}\rangle$, $|\psi_{41-42}\rangle$, $|\psi_{53-54}\rangle$, $|\psi_{57}\rangle$, $|\psi_{60-61}\rangle$, $|\psi_{63}\rangle$ are obtained by spin reversal from $|\psi_{2-3}\rangle$, $|\psi_6\rangle$, $|\psi_{14-15}\rangle$, $|\psi_{20}\rangle$, $|\psi_{23-26}\rangle$, $|\psi_{31-34}\rangle$, $|\psi_{39-40}\rangle$, $|\psi_{49-50}\rangle$, $|\psi_{55}\rangle$, $|\psi_{58-59}\rangle$, $|\psi_{62}\rangle$, respectively.

greatly simplified by the use of two- and three-site basis states that block-diagonalize respectively the left and right sides of Eq.(3.7). These basis states are the eigenstates of total particle number, total spin magnitude, total spin z-component, and parity. We denote the set of 16 two-site eigenstates by $\{|\phi_p\rangle\}$ and the set of 64 three-site eigenstates by $\{|\psi_q\rangle\}$, and list them in Tables 3.1 and 3.2. Eq.(3.7) is rewritten as

$$\langle\phi_p|e^{-\beta' H'(i,k)}|\phi_{\bar{p}}\rangle = \sum_{\substack{u,v,\bar{u},\\ \bar{v},w}} \sum_{q,\bar{q}} \langle\phi_p|u_i v_k\rangle\langle u_i w_j v_k|\psi_q\rangle\langle\psi_q|e^{-\beta H(i,j)-\beta H(j,k)}|\psi_{\bar{q}}\rangle\langle\psi_{\bar{q}}|\bar{u}_i w_j \bar{v}_k\rangle\langle\bar{u}_i\bar{v}_k|\phi_{\bar{p}}\rangle \,. \quad (3.8)$$

In the above equation, with the eigenstates shown in Tables 3.1 and 3.2, the largest block in $\langle\phi_p|e^{-\beta' H'(i,k)}|\phi_{\bar{p}}\rangle$ is 2×2 and the largest block in $\langle\psi_q|e^{-\beta H(i,j)-\beta H(j,k)}|\psi_{\bar{q}}\rangle$ is 4×4. (In previous work [7], some matrix elements in these blocks were incorrectly derived). Eq.(3.8) yields eleven independent elements for the matrix $\langle\phi_p|e^{-\beta' H'(i,k)}|\phi_{\bar{p}}\rangle$ of the renormalized system. These we label $\gamma_p \equiv \langle\phi_p|e^{-\beta' H'(i,k)}|\phi_p\rangle$, and express in terms of the matrix elements of the unrenormalized system, dictated by the right-hand side of Eq.(3.8). In the following equations, $\langle\psi_q||\psi_{\bar{q}}\rangle$ denotes $\langle\psi_q|e^{-\beta H(i,j)-\beta H(j,k)}|\psi_{\bar{q}}\rangle$:

$$\begin{aligned}
\gamma_1 &= \langle\psi_1||\psi_1\rangle + 2\langle\psi_2||\psi_2\rangle + \langle\psi_9||\psi_9\rangle,\\
\gamma_2 &= \langle\psi_3||\psi_3\rangle + \frac{1}{2}\langle\psi_8||\psi_8\rangle + \frac{3}{2}\langle\psi_{15}||\psi_{15}\rangle + \langle\psi_{24}||\psi_{24}\rangle,\\
\gamma_4 &= \langle\psi_6||\psi_6\rangle + \frac{1}{2}\langle\psi_{11}||\psi_{11}\rangle + \frac{3}{2}\langle\psi_{20}||\psi_{20}\rangle + \langle\psi_{32}||\psi_{32}\rangle,\\
\gamma_6 &= \langle\psi_{10}||\psi_{10}\rangle + 2\langle\psi_{26}||\psi_{26}\rangle + \langle\psi_{44}||\psi_{44}\rangle,\\
\gamma_7 &= \langle\psi_{13}||\psi_{13}\rangle + \langle\psi_{34}||\psi_{34}\rangle + \langle\psi_{38}||\psi_{38}\rangle + \langle\psi_{48}||\psi_{48}\rangle,\\
\gamma_8 &= \langle\psi_{12}||\psi_{12}\rangle + 2\langle\psi_{31}||\psi_{31}\rangle + \langle\psi_{47}||\psi_{47}\rangle,\\
\gamma_9 &= \langle\psi_{14}||\psi_{14}\rangle + \frac{2}{3}\langle\psi_{23}||\psi_{23}\rangle + \frac{4}{3}\langle\psi_{39}||\psi_{39}\rangle + \langle\psi_{49}||\psi_{49}\rangle,\\
\gamma_{12} &= \langle\psi_{25}||\psi_{25}\rangle + \frac{1}{2}\langle\psi_{45}||\psi_{45}\rangle + \frac{3}{2}\langle\psi_{50}||\psi_{50}\rangle + \langle\psi_{59}||\psi_{59}\rangle,\\
\gamma_{14} &= \langle\psi_{33}||\psi_{33}\rangle + \frac{1}{2}\langle\psi_{46}||\psi_{46}\rangle + \frac{3}{2}\langle\psi_{55}||\psi_{55}\rangle + \langle\psi_{62}||\psi_{62}\rangle,\\
\gamma_{16} &= \langle\psi_{43}||\psi_{43}\rangle + 2\langle\psi_{58}||\psi_{58}\rangle + \langle\psi_{64}||\psi_{64}\rangle,
\end{aligned} \quad (3.9)$$

$$\gamma_0 \equiv \langle\phi_6|e^{-\beta' H'(i,k)}|\phi_8\rangle$$
$$= \langle\psi_{10}||\psi_{12}\rangle + 2\langle\psi_{26}||\psi_{31}\rangle + \langle\psi_{44}||\psi_{47}\rangle. \tag{3.10}$$

3.2.3.3 Hamiltonian Closed Form under the Renormalization-Group Transformation

Since eleven interaction strengths can be independently fixed by the eleven γ_p, the Hamiltonian $-\beta' H'$ which is embodied in Eq.(3.9) has a more general form than that of the Hubbard Hamiltonian in Eq.(3.2). This generalized form of the pair Hamiltonian is

$$\begin{aligned}
-\beta H(i,j) = & \\
& - \sum_{\sigma} \left[t_0\, h_{i\,-\sigma} h_{j\,-\sigma} + t_1 (h_{i\,-\sigma} n_{j\,-\sigma} + n_{i\,-\sigma} h_{j\,-\sigma}) + t_2\, n_{i\,-\sigma} n_{j\,-\sigma} \right] \left(c^{\dagger}_{i\sigma} c_{j\sigma} + c^{\dagger}_{j\sigma} c_{i\sigma} \right) \\
& - t_x \left(c^{\dagger}_{i\uparrow} c_{j\uparrow} c^{\dagger}_{i\downarrow} c_{j\downarrow} + c^{\dagger}_{j\uparrow} c_{i\uparrow} c^{\dagger}_{j\downarrow} c_{i\downarrow} \right) - U \left(n_{i\uparrow} n_{i\downarrow} + n_{j\uparrow} n_{j\downarrow} \right) + \mu \left(n_i + n_j \right) + J\, \vec{S}_i \cdot \vec{S}_j \\
& + V_2 n_i n_j + V_3 \left(n_{i\uparrow} n_{i\downarrow} n_j + n_i n_{j\uparrow} n_{j\downarrow} \right) + V_4 n_{i\uparrow} n_{i\downarrow} n_{j\uparrow} n_{j\downarrow} \; + \; G \,,
\end{aligned} \tag{3.11}$$

where $h_{i\sigma} \equiv 1 - n_{i\sigma}$ is the hole (vacancy) operator and $\vec{S}_i = \frac{1}{2} \sum_{\sigma,\bar{\sigma}} c^{\dagger}_{i\sigma} \vec{s}_{\sigma\bar{\sigma}} c_{i\bar{\sigma}}$, with $\vec{s}_{\sigma\bar{\sigma}}$ the vector of Pauli spin matrices, is the spin operator at site i. In general, the Hubbard Hamiltonian, after one renormalization-group transformation, maps onto this generalized Hamiltonian, which has a form that stays closed under further renormalization-group transformations.

The kinetic energy part of the Hamiltonian in Eq.(3.11) distinguishes the four types of nearest-neighbor hopping events: **i) vacancy hopping** (the t_0 term): a vacancy (hole) hopping against a background of single-electron occupancy (half-filling); **ii) pair breaking or pair making** (the t_1 term): doubly occupied and completely unoccupied nearest-neighbor sites reverting to half-filling, or the reverse process; **iii) pair hopping** (the t_2 term): a pair hopping against a background of half-filling; **iv) vacancy - pair interchange** (the t_x term): doubly occupied and completely unoccupied nearest-neighbor sites exchanging positions.

The generalized Hamiltonian of Eq.(3.11) reduces to the Hubbard Hamiltonian of Eq.(3.2) for $t_0 = t_1 = t_2 = t$ and $t_x = J = V_2 = V_3 = V_4 = G = 0$. The renormalization-group flows occur in the 10-dimensional interaction space of the generalized Hamiltonian; the 3-dimensional interaction space of the Hubbard Hamiltonian contains the initial conditions of the renormalization-group flows.

The matrix elements of the renormalized pair Hamiltonian $-\beta' H'(i,k)$ are given in Table 3.3 in terms of the renormalized interaction constants. Table 3.3 allows us to solve for the renormalized interaction constants in terms of the γ_p given in Eq.(3.9):

$$t_0' = \frac{1}{2}\ln\frac{\gamma_4}{\gamma_2}, \quad t_1' = u\frac{\gamma_0}{\gamma_8-\gamma_6}, \quad t_2' = \frac{1}{2}\ln\frac{\gamma_{12}}{\gamma_{14}}, \quad t_x' = \frac{1}{2}\left(u - v + \ln\gamma_7\right),$$
$$U' = \frac{1}{2}\left(u - v + \ln\frac{\gamma_2^2\gamma_4^2}{\gamma_1^2\gamma_7}\right), \quad \mu' = \frac{1}{2}\ln\frac{\gamma_2\gamma_4}{\gamma_1^2}, \quad J' = -u - v + \ln\gamma_9,$$
$$V_2' = \frac{1}{4}\ln\frac{\gamma_1^4\gamma_9^3}{\gamma_2^4\gamma_4^4} + \frac{1}{4}(u+v), \quad V_3' = \frac{1}{2}\ln\frac{\gamma_2^3\gamma_4^3\gamma_{12}\gamma_{14}}{\gamma_1^2\gamma_7\gamma_9^3} - v, \quad V_4' = \ln\frac{\gamma_1\gamma_7\gamma_9^3\gamma_{16}}{\gamma_2^2\gamma_4^2\gamma_{12}^2\gamma_{14}^2} + 2v,$$
$$G' = \ln\gamma_1, \tag{3.12}$$

where

$$v = \frac{1}{2}\ln\left(\gamma_6\gamma_8 - \gamma_0^2\right),$$
$$u = \frac{\gamma_8-\gamma_6}{\sqrt{\left(\gamma_8-\gamma_6\right)^2 + 4\gamma_0^2}}\cosh^{-1}\left(\frac{\gamma_8+\gamma_6}{2e^v}\right).$$

This completes the determination of our renormalization-group transformation, whose flows in the ten-dimensional interaction space $(t_0, t_1, t_2, t_x,\ U, \mu, J, V_2, V_3, V_4)$ are to be analyzed. (G is an additive constant not influencing the flows of the 10 other interaction constants. However, for expectation value calculations, its derivatives must be included in Eq.(3.15).)

3.2.3.4 $d = 1$ Renormalization-Group Transformation

The transformation described above is the removal (decimation) of every other site in a linear array. This decimation produces the mapping of a Hamiltonian with

$-\beta' H'(i,k)$	ϕ_1	ϕ_2	ϕ_4	ϕ_7	ϕ_9	ϕ_{10}
ϕ_1	G'					
ϕ_2		$-t_0' + \mu' + G'$		0		
ϕ_4			$t_0' + \mu' + G'$			
ϕ_7				$t_x' - U' + 2\mu' + G'$		
ϕ_9			0		$2\mu' + \frac{1}{4}J' + V_2' + G'$	
ϕ_{10}						$2\mu' + \frac{1}{4}J' + V_2' + G'$

$-\beta' H'(i,k)$	ϕ_6	ϕ_8
ϕ_6	$-t_x' - U' + 2\mu' + G'$	$2t_1'$
ϕ_8	$2t_1'$	$2\mu' - \frac{3}{4}J' + V_2' + G'$

$-\beta' H'(i,k)$	ϕ_{12}	ϕ_{14}	ϕ_{16}
ϕ_{12}	$t_2' - U' + 3\mu' + 2V_2' + V_3' + G'$		
ϕ_{14}		$-t_2' - U' + 3\mu' + 2V_2' + V_3' + G'$	0
ϕ_{16}	0		$-2U' + 4\mu' + 4V_2' + 4V_3' + V_4' + G'$

Table 3.3: Block-diagonal matrix of the renormalized two-site Hamiltonian $-\beta' H'(i,k)$. The Hamiltonian being invariant under spin-reversal, the spin-flipped matrix elements are not shown.

interaction constants $\mathbf{K} = (t_0, t_1, t_2, t_x, U, \mu, J, V_2, V_3, V_4, G)$ onto another Hamiltonian with interaction constants

$$\mathbf{K}' = \mathbf{R}(\mathbf{K}). \tag{3.13}$$

The function $\mathbf{R}$ is calculated as follows:

(1) The matrix elements of $-\beta H(i,j) - \beta H(j,k)$ are determined in the three-site basis $\{\psi_q\}$ given in Table 3.2. In this basis, this matrix is block-diagonal as shown in Table 3.4, with the largest block being 4×4.

(2) The above block-diagonal matrix is exponentiated, yielding the matrix elements $\langle \psi_q | e^{-\beta H(i,j) - \beta H(j,k)} | \psi_{\bar{q}} \rangle$ which enter on the right-hand side of Eq.(3.8). This in turn yields the eleven γ_p, as given in Eq.(3.9).

(3) Using Eqs.(3.12), the interaction constants of the renormalized Hamiltonian $-\beta' H'(i,k)$, namely $(t_0', t_1', t_2',\ t_x', U', \mu', J', V_2', V_3',\ V_4', G')$ are found.

The initial conditions, for the iterated renormalization-group transformations that

	ψ_1
ψ_1	0

	ψ_2	ψ_3
ψ_2	2μ	$-\sqrt{2}t_0$
ψ_3	$-\sqrt{2}t_0$	μ

	ψ_6
ψ_6	μ

	ψ_9	ψ_{10}	ψ_{11}	ψ_{12}
ψ_9	$-2U+4\mu$	$-\sqrt{2}t_x$	$2t_1$	0
ψ_{10}	$-\sqrt{2}t_x$	$-U+2\mu$	$\sqrt{2}t_1$	0
ψ_{11}	$2t_1$	$\sqrt{2}t_1$	$3\mu-\frac{3}{4}J+V_2$	$-\sqrt{2}t_0$
ψ_{12}	0	0	$-\sqrt{2}t_0$	2μ

	ψ_8	ψ_{13}
ψ_8	$3\mu-\frac{3}{4}J+V_2$	$\sqrt{2}t_1$
ψ_{13}	$\sqrt{2}t_1$	$-U+2\mu$

	ψ_{14}	ψ_{15}
ψ_{14}	2μ	$-\sqrt{2}t_0$
ψ_{15}	$-\sqrt{2}t_0$	$3\mu+\frac{1}{4}J+V_2$

	ψ_{16}	ψ_{17}
ψ_{16}	$3\mu+\frac{1}{4}J+V_2$	$-\sqrt{2}t_0$
ψ_{17}	$-\sqrt{2}t_0$	2μ

	ψ_{20}
ψ_{20}	$3\mu+\frac{1}{4}J+V_2$

	ψ_{21}
ψ_{21}	$3\mu+\frac{1}{4}J+V_2$

	ψ_{24}	ψ_{25}	ψ_{26}	ψ_{31}
ψ_{24}	$-2U+5\mu+2V_2+V_3$	$-t_x$	t_2	t_1
ψ_{25}	$-t_x$	$-U+3\mu$	$-t_0$	t_1
ψ_{26}	t_2	$-t_0$	$-U+4\mu+2V_2+V_3$	0
ψ_{31}	t_1	t_1	0	$4\mu+2V_2$

	ψ_{23}	ψ_{32}	ψ_{33}	ψ_{34}
ψ_{23}	$4\mu-J+2V_2$	$-\sqrt{3}t_1$	$-\sqrt{3}t_1$	0
ψ_{32}	$-\sqrt{3}t_1$	$-2U+5\mu+2V_2+V_3$	$-t_x$	t_2
ψ_{33}	$-\sqrt{3}t_1$	$-t_x$	$-U+3\mu$	t_0
ψ_{34}	0	t_2	t_0	$-U+4\mu+2V_2+V_3$

	ψ_{39}
ψ_{39}	$4\mu+\frac{1}{2}J+2V_2$

	ψ_{40}
ψ_{40}	$4\mu+\frac{1}{2}J+2V_2$

	ψ_{43}	ψ_{44}	ψ_{46}	ψ_{47}
ψ_{43}	$-2U+4\mu$	$-\sqrt{2}t_x$	$-2t_1$	0
ψ_{44}	$-\sqrt{2}t_x$	$-3U+6\mu+4V_2+4V_3+V_4$	$-\sqrt{2}t_1$	0
ψ_{46}	$-2t_1$	$-\sqrt{2}t_1$	$-U+5\mu-\frac{3}{4}J+3V_2+V_3$	$-\sqrt{2}t_2$
ψ_{47}	0	0	$-\sqrt{2}t_2$	$-2U+6\mu+4V_2+2V_3$

	ψ_{45}	ψ_{48}
ψ_{45}	$-U+5\mu-\frac{3}{4}J+3V_2+V_3$	$-\sqrt{2}t_1$
ψ_{48}	$-\sqrt{2}t_1$	$-3U+6\mu+4V_2+4V_3+V_4$

	ψ_{49}	ψ_{50}
ψ_{49}	$-2U+6\mu+4V_2+2V_3$	$\sqrt{2}t_2$
ψ_{50}	$\sqrt{2}t_2$	$-U+5\mu+\frac{1}{4}J+3V_2+V_3$

	ψ_{51}	ψ_{52}
ψ_{51}	$-U+5\mu+\frac{1}{4}J+3V_2+V_3$	$\sqrt{2}t_2$
ψ_{52}	$\sqrt{2}t_2$	$-2U+6\mu+4V_2+2V_3$

	ψ_{55}
ψ_{55}	$-U+5\mu+\frac{1}{4}J+3V_2+V_3$

	ψ_{56}
ψ_{56}	$-U+5\mu+\frac{1}{4}J+3V_2+V_3$

	ψ_{58}	ψ_{59}
ψ_{58}	$-2U+6\mu+4V_2+2V_3$	$\sqrt{2}t_2$
ψ_{59}	$\sqrt{2}t_2$	$-3U+7\mu+6V_2+5V_3+V_4$

	ψ_{62}
ψ_{62}	$-3U+7\mu+6V_2+5V_3+V_4$

	ψ_{64}
ψ_{64}	$-4U+8\mu+8V_2+8V_3+2V_4$

Table 3.4: Diagonal matrix blocks of the unrenormalized three-site Hamiltonian $-\beta H(i,j) - \beta H(j,k)$. The Hamiltonian being invariant under spin-reversal, the spin-flipped matrix elements are not shown. The additive constant contribution $2G$, occurring at the diagonal terms, is also not shown.

constitute the renormalization-group flow, are the interaction constants of the Hubbard Hamiltonian, $\mathbf{K}_0 = (t_0 = t,\, t_1 = t,\, t_2 = t,\, t_x = 0,\, U,\, \mu,\, J = 0,\, V_2 = 0,\, V_3 = 0,\, V_4 = 0,\, G = 0)$.

3.2.3.5 $d > 1$ Renormalization-Group Transformation

The Migdal-Kadanoff approximation procedure [1, 2] (which has been remarkably effective in problems as diverse as lower-critical dimensions for different types of phase transitions; first- and second-order phase transitions in q-state Potts models; algebraic order in the $d = 2$ XY model; random-field, random-bond, spin-glass systems; quenched-disorder-induced criticality; etc.) is used to construct the renormalization-group transformation for $d > 1$. In the d-dimensional hypercubic lattice, a subset of the nearest-neighbor interactions are ignored, so that a hypercubic lattice (still d-dimensional) is left behind, in which each lattice point is connected by two consecutive nearest-neighbor segments of the original lattice. The decimation described above can then be applied to the site connecting these two segments of the original lattice, yielding the renormalized nearest-neighbor couplings between the lattice points of the new hypercubic lattice. To compensate for the nearest-neighbor interactions that are ignored, the couplings are multiplied by a factor of b^{d-1} after decimation, $b = 2$ being the length rescaling factor. Thus, the renormalization-group transformation of Eq.(3.13) in the previous section generalizes, for $d > 1$, to

$$\mathbf{K}' = b^{d-1}\mathbf{R}(\mathbf{K}). \tag{3.14}$$

The robust effectiveness of the Migdal-Kadanoff approximation is due to the fact that it is physically realizable on hierarchical lattices [3, 4, 5], where the connectivity of the Migdal-Kadanoff procedure is exactly reproduced and solved. These lattices (or equivalently the Migdal-Kadanoff procedure) provide solvable models, with which complex problems have been studied and understood. For example, frustrated [32], spin-glass [33], random-bond [34] and random-field [35], Schrödinger equation [36], lattice-vibration [37], dynamic scaling [38], aperiodic magnet [39], complex phase

diagram [40], and directed-path [41] systems, etc., have been solved on hierarchical lattices. Thus, the current work can also be considered a hierarchical lattice solution.

3.2.3.6 Supporting Results

New global phase diagrams obtained by approximate renormalization-group transformations are supported by the correct rendition of all of the special cases of the system solved. The Hamiltonian in Eq.(3.11), which is the system presently solved by approximate recursion relations, reduces in various limits to the Ising, quantum XY, and quantum Heisenberg spin systems. Our recursion relations correctly yield the lower critical-dimensions d_l of the Ising ($d_l = 1$), quantum XY ($d_l = 2$), and quantum Heisenberg ($d_l = 2$) spin systems. For the quantum XY spin system in $d = 2$, this approximation yields the algebraically ordered Kosterlitz-Thouless low-temperature phase.[30, 31] For the quantum Heisenberg spin system in $d = 3$, our recursion relations yield low-temperature antiferromagnetically (for $J < 0$) and ferromagnetically (for $J > 0$) ordered phases, each separated by a second-order transition from the high-temperature disordered phase. The antiferromagnetic transition temperature is thus found to be 1.22 times [18] the ferromagnetic transition temperature, a purely quantum mechanical effect, and to be compared with the value of 1.13 from series expansion [42, 43]. Furthermore, as purely off-diagonal quantum effects, the hopping-induced antiferromagnetism of the $d = 3$ Hubbard model is recovered and the scaling of the antiferromagnetic transition temperature is obtained with an excellent quantitative agreement, as discussed in Sec.3.2.5 at Eq.(3.18) and shown in Fig. 3-4. In fact, the scaling of the antiferromagnetic transition at strong-coupling (Fig. 3-4), as well as the results quoted above, and the disappearance of the transition at zero coupling (Fig. 3-5), indicate the validity of our approximation across the entire strong-to-weak coupling range. Finally, the Blume-Emery-Griffiths model is contained in the Hamiltonian of Eq.(3.11) and its global phase diagram [44] is obtained from our recursion relations. All of these results strongly support the validity of the global calculation here.

3.2.4 Renormalization-Group Analysis: Global Phase Diagram and Operator Expectation Values

From the recursion equations determined in the preceding section, flows are generated for initial values of t, U, and μ in the Hubbard Hamiltonian. The renormalization-group transformation, which constitutes each step of the flow, is effected numerically. Particular attention has to be given to the multiplication of small amplitudes with large exponentials, which can occur in the right-hand side of Eq.(3.8) when interaction constants become large, causing the computational difficulties encountered in previous work [7].

Each completely stable fixed point, namely sink of the renormalization-group flows, corresponds to a thermodynamic phase, and the global phase diagram is found by identifying the basin of attraction for every sink.[44] The expectation values for the operators occurring in the Hamiltonian are obtained from the conjugate recursion relations, [45]

$$n_\beta = b^{-d} n'_\alpha T_{\alpha\beta} \,, \tag{3.15}$$

with summation over the repeated index α implicit. The recursion matrix is

$$T_{\alpha\beta} = \frac{\partial K'_\alpha}{\partial K_\beta} \,, \tag{3.16}$$

where K_α is an interaction strength, namely a component in the interaction strength vector $\mathbf{K}$ defined before Eq.(3.13); n_α is the expectation value of the operator that occurs in the Hamiltonian with coefficient K_α. Eq.(3.15) is iterated along a trajectory until a phase sink limit. The left eigenvector of $T_{\alpha\beta}$ with eigenvalue b^d gives the expectation values at the phase sink, thereby completing the calculation of the expectation values of the initial point of the trajectory.

The observed phase sinks in the calculations for the $d = 3$ Hubbard model — the details of which are shown in Table 3.5 — have a property in common: at the sink limit, t_1 renormalizes toward zero. In the limit $t_1 \to 0$, analytic expressions are

derived to first order in t_1 for the matrix elements $\langle\psi_q|e^{-\beta H(i,j)-\beta H(j,k)}|\psi_{\bar{q}}\rangle$ on the right-hand side of Eq.(3.8). This yields, in the neighborhood of each phase sink, analytic renormalization-group equations. The analytic equations provide a useful check on the accuracy of the numerical calculations, and lead to closed-form expressions for limiting values of interaction strengths or ratios of limiting values of interaction strengths.

Flows that start at the boundaries between phases have their own fixed points, distinguished from phase sinks by having at least one unstable direction. After narrowing down onto the boundary and from there following a flow to the neighborhood of the unstable fixed point, a Newton-Raphson procedure is used to exactly locate this unstable fixed point. Analysis at these fixed points determines the phase transition properties. The expectation values calculated, as described above, at the phase boundaries allow us to redraw the phase diagram using expectation values n_α on the axes as well as t, U, and μ.

The Hamiltonian of Eq.(3.11) is covariant under particle-hole symmetry ($c_{i\sigma}^\dagger \rightarrow c_{i\sigma}$), which in Hamiltonian space takes the form of a mapping $\bar{\mathbf{K}} = \mathbf{S}(\mathbf{K})$. The function $\mathbf{S}$ is given by

$$\bar{t_0} = -t_2,\ \bar{t_1} = -t_1,\ \bar{t_2} = -t_0,\ \bar{t_x} = t_x,\ \bar{J} = J, \bar{U} = U - 2V_3 - V_4,$$
$$\bar{\mu} = -\mu + U - 2V_2 - 3V_3 - V_4,\ \bar{V_2} = V_2 + 2V_3 + V_4,\ \bar{V_3} = -V_3 - V_4,\ \bar{V_4} = V_4. \tag{3.17}$$

The subspace that is invariant under $\mathbf{S}$ corresponds to systems that are invariant under particle-hole exchange, and therefore are at half-filling: $\langle n_i\rangle = 1 = \langle h_i\rangle$. From Eq.(3.17), this subspace occurs at $t_0 = -t_2,\ t_1 = 0,\ 2\mu = U - 2V_2 - V_3,\ 2V_3 = -V_4$. For the original Hubbard Hamiltonian, all points with $\mu_0/U_0 = 1/2$ are mapped onto this subspace after the first renormalization-group step.

The Hubbard phase diagrams are plotted in the next section, for fixed U_0/t, in terms of $1/t$ (a temperature variable) versus μ_0/U_0 or $\langle n_i\rangle$. Since our renormalization-group transformation is also covariant under particle-hole symmetry, the phase diagrams are duly symmetric about $\mu_0/U_0 = 1/2$ or $\langle n_i\rangle = 1$.

3.2.5 Global Phase Diagram for $d = 3$

For $d = 3$ and a range of couplings $U_0/t = 5$ to 20, Figs. 3-2 show Hubbard phase diagrams in terms of temperature $(1/t)$ versus chemical potential (μ_0/U_0). The corresponding phase diagrams in temperature $(1/t)$ versus electron density $\langle n_i \rangle$ are in Fig. 3-3. The values of the interaction constants for each observed phase sink are listed in Table 3.5. The expectation values for each phase sink, also listed in Table 3.5, allow us to identify the phases as follows:

Hole-rich disordered (hD) phase: The electron density $\langle n_i \rangle$ is zero at the sink and, concomitantly, the electron densities $\langle n_i \rangle$ calculated inside this phase are low.

Near-half-filled disordered (nHD) phase: The basin of attraction of nHD occurs at $\mu_0/U_0 \neq 1/2$. The electron density $\langle n_i \rangle$ is 1 at the sink and, concomitantly, the electron densities $\langle n_i \rangle$ calculated inside this phase are closer to half-filling. **Half-filled disordered (HD) phase:** The sink is for the disordered phase at perfect half-filling, $\mu_0/U_0 = 1/2$ and $\langle n_i \rangle = 1$.

Electron-rich disordered (eD) phase: The electron density $\langle n_i \rangle$ is 2 at the sink and, concomitantly, the electron densities $\langle n_i \rangle$ calculated inside this phase are high.

Antiferromagnetic (AF) phase: The electron density $\langle n_i \rangle$ is 1 at the sink and, concomitantly, the electron densities $\langle n_i \rangle$ calculated inside this phase are closer to half-filling. The expectation value for the nearest-neighbor spin-spin correlation is $\langle \vec{S}_i \cdot \vec{S}_j \rangle = \frac{1}{4}$ at the sink. Note that the latter two spins are, on the original cubic lattice, distant spins on the same sublattice; from this, antiferromagnetism, $\langle \vec{S}_i \cdot \vec{S}_j \rangle < 0$ when the spins are on different sublattices of the original cubic lattice, is calculationally obtained throughout this phase. Since there is no explicit antiferromagnetic coupling in the initial Hubbard Hamiltonian, the antiferromagnetic phase is completely a quantum mechanical effect resulting from the kinetic energy term. In fact, at half-filling, second-order perturbation theory in t, valid for small t/U_0, must yield an effective antiferromagnetic coupling proportional to t^2/U_0. Thus, for small t/U_0, t^2/U_0 should equal the same constant at all antiferromagnetic phase transitions at

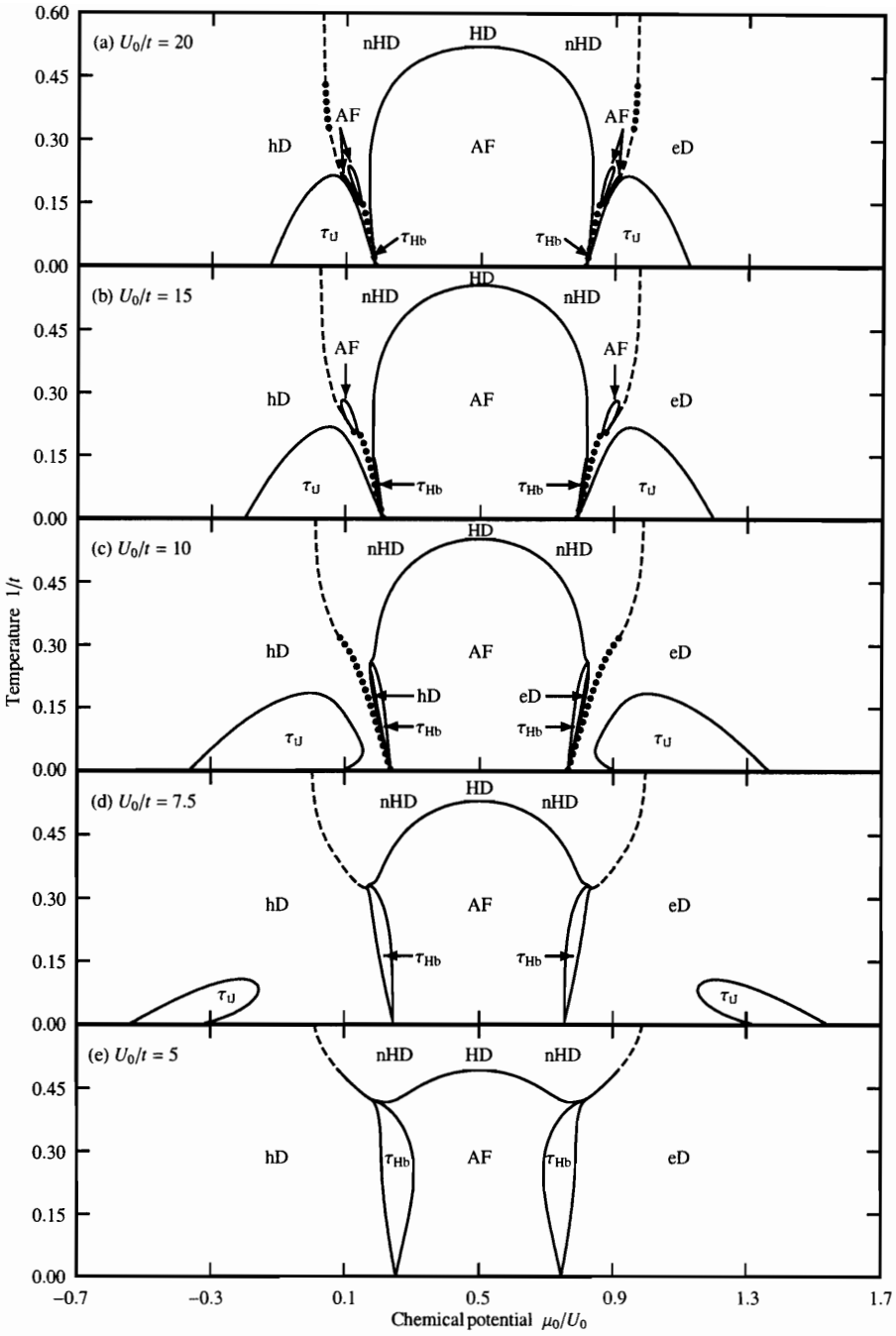

Figure 3-2: $d = 3$ Hubbard model phase diagrams in temperature versus chemical potential. The hole-rich disordered (hD), near-half-filled disordered (nHD), half-filled disordered (HD), electron-rich disordered (eD), antiferromagnetic (AF), τ_{Hb}, and τ_{tJ} phases are seen. The full curves are second-order phase boundaries, while the dotted curves are first-order boundaries. The dashed curves are not phase transitions, but disorder lines between the near-half-filled disordered and the hole-rich or electron-rich disordered phases. The progression (a) $U_0/t = 20$ through (e) $U_0/t = 5$ shows the changing phase diagram topology from strong to intermediate coupling. The τ_{tJ} phase, which is prominent at strong coupling, disappears entirely for $U_0/t \lesssim 6$, and the τ_{Hb} phase is prominent for intermediate couplings.

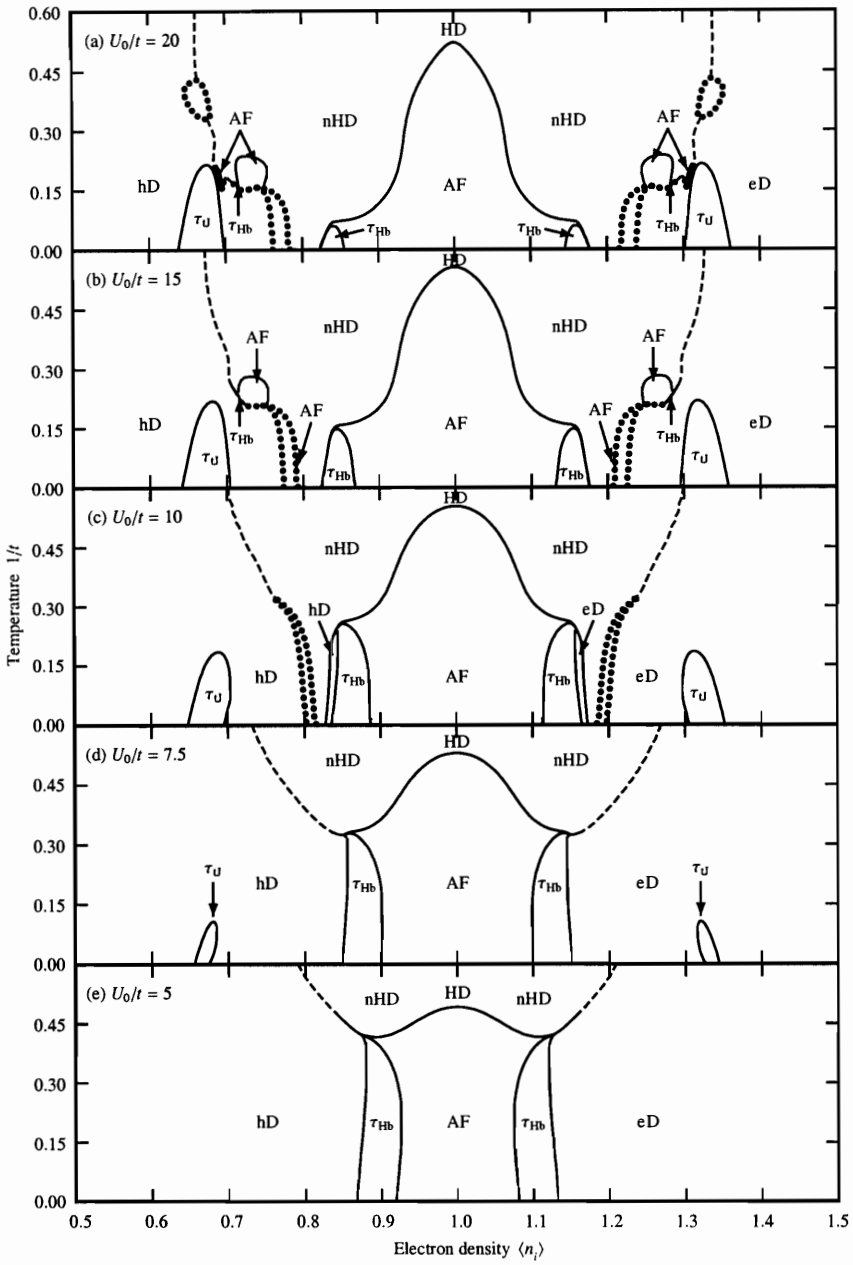

Figure 3-3: $d = 3$ Hubbard model phase diagrams in temperature versus electron density. The full curves are second-order phase boundaries. The coexistence boundaries of first-order transitions are drawn with dotted curves, with the unmarked areas inside corresponding to coexistence regions of the two phases at either side. The dashed curves are not phase transitions, but disorder lines between the near-half-filled disordered and the hole-rich or electron-rich disordered phases. Noteworthy is the narrowness of the first-order transitions, with jumps in the electron density of the order of a few percent (*i.e.*, the width of the coexistence region). The antiferromagnetic phase is unstable to about 8-15% hole (or electron) doping away from half-filling. In the intermediate U_0/t regime, the $\tau_{\rm Hb}$ phase appears for about 10-18% hole (or electron) doping. At larger U_0/t, the $\tau_{\rm tJ}$ phase dominates, and exists between 30-35% hole (or electron) doping.

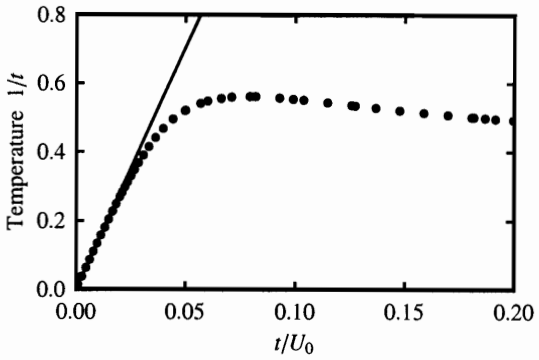

Figure 3-4: The data points are the calculated antiferromagnetic transition temperatures at half-filling. The linear relation that is expected for strong coupling at low temperatures (Sec.3.2.5) is obtained.

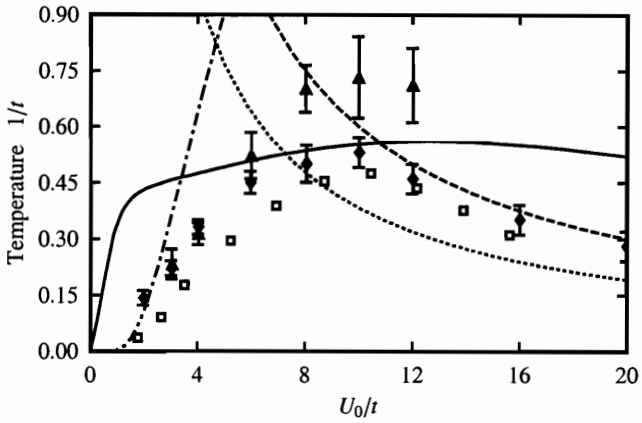

Figure 3-5: Comparison of the antiferromagnetic transition temperatures at half-filling for the $d = 3$ Hubbard model calculated from various approaches: the renormalization-group method of the present paper (solid line); QMC [46] (diamonds); QMC [47] (triangles); DMFT [48] (squares); RPA weak-coupling expansion [49] (dot-dashed line); and two approximations for the strong-coupling behavior—the high-temperature expansion of the Heisenberg model, $1/t = 3.83t/U_0$ [47] (dotted line) and Weiss mean-field theory, $1/t = 6t/U_0$ (dashed line).

half-filling (Recall that all of our coupling constants are dimensionless, incorporating the inverse temperature factor $1/kT$). Equivalently, t/U_0 should be linear in $1/t$ at all antiferromagnetic phase transitions at half-filling, for small t/U_0 and therefore for small $1/t$ (low temperature):

$$1/t \sim t/U_0 \,. \tag{3.18}$$

This is indeed rendered by our calculation, as seen in Fig. 3-4. For higher values of $1/t$, Eq.(3.18) is not applicable, since second-order perturbation theory does not

hold, and indeed our calculated curve in Fig. 3-4 deviates from linearity. On the other hand, the approximation in our recursion relation is even more justified, since the commutation relations that are ignored involve terms of order t^2.

The antiferromagnetic transition temperature as a function of coupling U_0/t is also shown in Fig. 3-5, together with calculated values from other approximation schemes for the $d = 3$ Hubbard model. We see that our results for intermediate coupling are comparable to those of quantum Monte Carlo studies [46, 47]. As expected, our transition temperature vanishes in the limit $U_0/t \to 0$, since there are no phase transitions for the non-interacting system. Thus, our approximation behaves correctly both at strong coupling (previous paragraph) and at weak coupling.

$\tau_{\mathbf{Hb}}$ and $\tau_{\mathbf{tJ}}$ phases: For large values of U_0/t, the novel phase found in the tJ model [18] (which we call τ_{tJ}) also occurs in the Hubbard model. In addition, we find a closely related phase (τ_{Hb}), unique to the Hubbard model, at smaller U_0/t. The two phases are characterized by very similar properties: the hopping strengths t_0, t_2, and t_x renormalize to $\pm\infty$, and the phase sinks have a non-zero vacancy hopping expectation value

$$\left\langle \sum_{\sigma} h_{i-\sigma} h_{j-\sigma} (c^{\dagger}_{i\sigma} c_{j\sigma} + c^{\dagger}_{j\sigma} c_{i\sigma}) \right\rangle = \begin{cases} -2/3 & (\tau_{\mathrm{tJ}}) \\ 0.663972 & (\tau_{\mathrm{Hb}}) \end{cases}, \tag{3.19}$$

for $\mu_0/U_0 < 1/2$, and a non-zero pair hopping expectation value

$$\left\langle \sum_{\sigma} n_{i-\sigma} n_{j-\sigma} (c^{\dagger}_{i\sigma} c_{j\sigma} + c^{\dagger}_{j\sigma} c_{i\sigma}) \right\rangle = \begin{cases} 2/3 & (\tau_{\mathrm{tJ}}) \\ -0.663972 & (\tau_{\mathrm{Hb}}) \end{cases}, \tag{3.20}$$

for $\mu_0/U_0 > 1/2$. In both cases, as expected for the occurrence of hopping, the electron densities at the sinks have values different from 0 (empty), 1 (half filled), or 2 (doubly occupied): $\langle n_i \rangle = 2/3$, $4/3$ and $\langle n_i n_j \rangle = 1/3$, $5/3$ for the τ_{tJ} phase, and $\langle n_i \rangle = 0.668014$, 1.331986 and $\langle n_i n_j \rangle = 0.336028$, 1.663972 for the τ_{Hb} phase. (At the sinks of non-τ phases, the electron density is, on the other hand, 0, 1, or 2.) There are also small spin correlations in the phase sink limits, $\langle \vec{S}_i \cdot \vec{S}_j \rangle = -1/4$ for

$\tau_{\rm tJ}$, and $\langle \vec{S}_i \cdot \vec{S}_j \rangle = 0.0840069$ for $\tau_{\rm Hb}$, which yield, throughout these phases, small antiferromagnetic correlations in the original system.

The boundaries in Fig. 3-2 are controlled by fourteen unstable fixed points, given in Table 3.6. For smaller values of U_0/t, the topology of the phase diagram is that of Fig. 3-2(e), where the AF/HD, AF/nHD, AF/$\tau_{\rm Hb}$, and hD/$\tau_{\rm Hb}$ boundaries are respectively controlled by the second-order fixed points C_1^*, C_2^*, C_3^*, and C_4^*. The latter three boundaries intersect at the multicritical point B_2, controlled by the fixed point B_2^*. A segment of the hD/nHD boundary just above this intersection is second-order, controlled by the fixed point C_5^*, ending at the multicritical point B_1, controlled by the fixed point B_1^*. The high-temperature section of the hD/nHD boundary is a disorder line, controlled by the null fixed point N*, *i.e.*, there is no phase transition above B_1.

As U_0/t is increased, the phase diagram topology becomes more complex. For $U_0/t \gtrsim 6$, the $\tau_{\rm tJ}$ phase appears, its boundary with hD controlled by the second-order fixed point C_6^*. Portions of the lower-temperature boundary between the hD and nHD phases become first-order (fixed point F_1^*), and islands of AF appear above the $\tau_{\rm tJ}$ phase; their boundaries with hD are also first-order (fixed point F_2^*). The intersections of these first-order boundaries with other phase boundaries are controlled by the additional multicritical points B_3^* and B_4^*, and by the critical endpoint L^* [44].

As the coupling U_0/t varies, a most interesting aspect of the changing phase diagram topology is the relative sizes of the $\tau_{\rm hB}$ and $\tau_{\rm tJ}$ phases. The $\tau_{\rm hB}$ phase is largest at intermediate values of U_0/t, and gradually decreases in size as we move into the strong-coupling regime, breaking up into narrow slivers until at large values of U_0/t only tiny remnants of it are left in the phase diagram. The $\tau_{\rm tJ}$ phase appears at intermediate values of U_0/t, grows in size as U_0/t is increased, and occupies a prominent place in the diagram next to the AF phase in the strong-coupling regime. As discussed in Sec.3.2.7, this is precisely what we expect, since the Hubbard phase diagram should approximately reproduce the tJ model results [18] in the large U_0/t limit.

Phase diagrams in terms of temperature versus electron density $\langle n_i \rangle$ are shown in

Phase sink	Interaction constants										Additional properties
	t_0	t_1	t_2	t_x	U	μ	J	V_2	V_3	V_4	
hole-rich disordered hD	0	0	0	0	∞	$-\infty$ $\mu/U=\text{const.}$	0	0	0	0	
near-half-filled disordered nHD	$2\ln 3$	0	$-2\ln 3$	∞ $\approx 0.24U$	∞	∞ $\approx 0.62U$	0	$-\infty$ $\approx -0.47U$	∞ $\approx 0.69U$	-∞ $\approx -1.38U$	$U-2\mu-2V_2-V_3=0$ $2V_3+V_4=0$
half-filled disordered HD	0	0	0	0	∞	∞ $=\frac{1}{2}U$	0	0	0	0	$U-2\mu=0$
electron-rich disordered eD	0	0	0	0	∞	∞ $\mu/U=\text{const.}$	0	0	0	0	
antiferro-magnetic AF ($\mu_0/U_0 \neq 1/2$)	$-\infty$ $\approx -0.29U$	0	∞ $\approx 0.29U$	∞ $\approx 0.14U$	∞	∞ $\approx 0.57U$	∞ $\approx 0.29U$	$-\infty$ $\approx -0.071U$	∞ $V_3/U \to 0$	$-\infty$ $V_4/U \to 0$	$U-2\mu-2V_2-V_3\to 0$ $2V_3+V_4\to 0$ $t_2-t_0\to 0$
antiferro-magnetic AF ($\mu_0/U_0 = 1/2$)	0	0	0	0	∞	∞ $\approx \frac{1}{2}U$	∞ $J/U \to 0$	$-\infty$ $\approx -\frac{1}{4}J$	∞ $\approx \frac{1}{2}J$	$-\infty$ $\approx -J$	$U-2\mu-2V_2-V_3=0$ $2V_3+V_4=0$ $t_2-t_0=0$
τ_{Hb} ($\mu_0/U_0 < 1/2$)	$-\infty$ $\approx -\frac{1}{4}U$	0	∞ $\approx \frac{1}{2}U$	$-\infty$ $\approx -\frac{1}{2}U$	∞	∞ $\approx \frac{1}{4}U$	∞ $\approx \frac{1}{2}U$	$-\infty$ $\approx -\frac{1}{8}U$	$-\infty$ $V_3/U \to 0$	∞ $V_4/U \to 0$	$t_0+\mu+\frac{1}{4}J+V_2$ ≈ -4.35
τ_{Hb} ($\mu_0/U_0 > 1/2$)	$-\infty$ $\approx -\frac{1}{2}U$	0	∞ $\approx \frac{1}{4}U$	$-\infty$ $\approx -\frac{1}{2}U$	∞	∞ $\approx U$	∞ $\approx \frac{1}{2}U$	$-\infty$ $\approx -\frac{1}{8}U$	∞ $V_3/U \to 0$	∞ $V_4/U \to 0$	$-t_2+U-\mu+\frac{1}{4}J$ $-V_2-V_3\approx -4.35$
τ_{tJ} ($\mu_0/U_0 < 1/2$)	∞ $\approx 0.13U$	0	$-\infty$ $\approx -1.46U$	∞ $\approx 0.52U$	∞	$-\infty$ $\approx -0.022U$	$-\infty$ $\approx -0.87U$	$-\infty$ $\approx -0.50U$	$-\infty$ $\approx -1.13U$	$-\infty$ $\approx -0.21U$	
τ_{tJ} ($\mu_0/U_0 > 1/2$)	∞ $\approx 0.42U$	0	$-\infty$ $\approx -0.038U$	∞ $\approx 0.15U$	∞	∞ $\approx 1.62U$	$-\infty$ $\approx -0.25U$	$-\infty$ $\approx -0.86U$	∞ $\approx 0.39U$	$-\infty$ $\approx -0.060U$	

Phase sink	Expectation values									
	$\langle T_0\rangle$	$\langle T_1\rangle$	$\langle T_2\rangle$	$\langle T_x\rangle$	$\langle n_{i\uparrow}n_{i\downarrow}\rangle$	$\langle n_i\rangle$	$\langle \vec{S}_i\cdot\vec{S}_j\rangle$	$\langle n_in_j\rangle$	$\langle n_{i\uparrow}n_{i\downarrow}n_j\rangle$	$\langle n_{i\uparrow}n_{i\downarrow}n_{j\uparrow}n_{j\downarrow}\rangle$
hD	0	0	0	0	0	0	0	0	0	0
nHD	0	0	0	0	0	1	0	1	0	0
HD	0	0	0	0	0	1	0	1	0	0
eD	0	0	0	0	1	2	0	4	2	1
AF	0	0	0	0	0	1	$\frac{1}{4}$	1	0	0
τ_{Hb}	$\left\{\begin{matrix}0.663\\ 972\\ 0\end{matrix}\right.$	0	$\left\{\begin{matrix}0\\ -0.66\\ 3972\end{matrix}\right.$	0	$\left\{\begin{matrix}0\\ 0.331\\ 986\end{matrix}\right.$	$\left\{\begin{matrix}0.668\\ 014\\ 1.331\\ 986\end{matrix}\right.$	0.0840 069	$\left\{\begin{matrix}0.336\\ 028\\ 1.663\\ 972\end{matrix}\right.$	$\left\{\begin{matrix}0\\ 0.331\\ 986\end{matrix}\right.$	0
τ_{tJ}	$\left\{\begin{matrix}-\frac{2}{3}\\ 0\end{matrix}\right.$	0	$\left\{\begin{matrix}0\\ \frac{2}{3}\end{matrix}\right.$	0	$\left\{\begin{matrix}0\\ \frac{1}{3}\end{matrix}\right.$	$\left\{\begin{matrix}\frac{2}{3}\\ \frac{4}{3}\end{matrix}\right.$	$-\frac{1}{4}$	$\left\{\begin{matrix}\frac{1}{3}\\ \frac{5}{3}\end{matrix}\right.$	$\left\{\begin{matrix}0\\ \frac{1}{3}\end{matrix}\right.$	0

Table 3.5: Interaction constants and expectation values at the phase sink fixed points. For τ_{Hb} and τ_{tJ}, the values for $\mu_0/U_0 \lessgtr \frac{1}{2}$ are given. The hopping expectation values $\langle T_\alpha\rangle$ are: $\langle T_0\rangle = \sum_\sigma \langle h_{i-\sigma}h_{j-\sigma}(c^\dagger_{i\sigma}c_{j\sigma} + c^\dagger_{j\sigma}c_{i\sigma})\rangle$, $\langle T_1\rangle = \sum_\sigma \langle (n_{i-\sigma}h_{j-\sigma} + h_{i-\sigma}n_{j-\sigma})(c^\dagger_{i\sigma}c_{j\sigma} + c^\dagger_{j\sigma}c_{i\sigma})\rangle$, $\langle T_2\rangle = \sum_\sigma \langle n_{i-\sigma}n_{j-\sigma}(c^\dagger_{i\sigma}c_{j\sigma} + c^\dagger_{j\sigma}c_{i\sigma})\rangle$, $\langle T_x\rangle = \langle c^\dagger_{i\uparrow}c_{j\uparrow}c^\dagger_{i\downarrow}c_{j\downarrow} + c^\dagger_{j\uparrow}c_{i\uparrow}c^\dagger_{j\downarrow}c_{i\downarrow}\rangle$.

	Basin	Type	Interaction constants										Additional properties	Relevant eigenvalue exponents (y)
			t_0	t_1	t_2	t_x	U	μ	J	V_2	V_3	V_4		
F_1^*	portion of hD/nHD boundary	1st order	$2\ln 3$	0	$-2\ln 3$	∞	∞	$-\infty$	0	∞	$-\infty$	$-\infty$	$2\mu+V_2\approx-0.396$ $U-2\mu-2V_2-V_3\to 0$	3
F_2^*	AF/hD boundary	1st order	$-\infty$	0	∞	∞	∞	$-\infty$	∞	∞	$-\infty$	∞	$U-2\mu-2V_2-V_3\to 0$ $8\mu+J+4V_2\approx-0.658$	3
C_1^*	AF/HD boundary	2nd order	0	0	0	0	∞	∞ $\approx\frac{1}{2}U$	1.376	-0.0650	0.130	-0.260	$U-2\mu-2V_2-V_3=0$ $2V_3+V_4=0$	0.715
C_2^*	AF/nHD boundary	2nd order	-0.554	0	0.554	∞	∞	∞	1.376	$-\infty$	∞	$-\infty$	$U-2\mu-2V_2-V_3\to 0$ $2V_3+V_4\to 0$	0.715
C_3^*	AF/τ_{Hb} boundary	2nd order	$-\infty$	0	∞	$-\infty$	∞	∞	∞	$-\infty$	∞	$-\infty$	$t_0+\mu+\frac{1}{4}J+V_2\approx-0.739$	1.68
C_4^*	hD/τ_{Hb} boundary	2nd order	$-\infty$	0	∞	$-\infty$	∞	$-\infty$	∞	∞	$-\infty$	∞	$t_0+\mu+\frac{1}{4}J+V_2\approx-5.178$ $8\mu+J+4V_2\approx 6.617$	1.42
C_5^*	portion of hD/nHD boundary	2nd order	-1.610	0	$-2\ln 3$	-1.594	∞	0.523	0	0.0108	-0.569	$-\infty$ $\approx -3U$		1.56
C_6^*	hD/τ_{tJ} boundary	2nd order	2.959	0	-29.585	9.629	∞	1.016	-13.692	-8.332	-18.259	$-\infty$		1.01
N^*	portion of hD/nHD boundary	null	0	0	$-2\ln 3$	0	∞	0	0	0	$4\ln\frac{\sqrt{3}}{2}$	$-\infty$ $\approx -3U$		2
L^*	F_1^*, F_2^*, C_2^* basins meet	critical endpoint	-0.554	0	0.554	∞	∞	$-\infty$	1.376	∞	$-\infty$	$-\infty$	$U-2\mu-2V_2-V_3\to 0$ $8\mu+J+4V_2\approx-0.798$	3 0.715155
B_1^*	C_5^*, N^* basins meet	multi-critical	-1.236	0	$-2\ln 3$	-1.005	∞	0.221	0	0.127	-0.652	$-\infty$ $\approx -3U$		1.73 0.22
B_2^*	C_2^*, C_3^*, C_4^*, C_5^* basins meet	multi-critical	-2.156	0	-1.555	-2.708	∞	1.559	0.321	-0.762	0.201	$-\infty$ $\approx -3U$		1.15 0.27
B_3^*	F_1^*, N^* basins meet	multi-critical	0	0	$-2\ln 3$	0	∞	-0.681	0	1.089	-0.438	$-\infty$ $\approx -3U$	$3U+V_4\approx 3.044$	2.56 0.96
B_4^*	F_2^*, C_3^*, C_4^* basins meet	multi-critical	$-\infty$	0	∞	$-\infty$	∞	$-\infty$	∞	∞	$-\infty$	$-\infty$	$t_0+\mu+\frac{1}{4}J+V_2\to 0$ $8\mu+J+4V_2\to 0$	2.68 1.90

Table 3.6: Unstable fixed points. The fixed points of the $\mu_0/U_0 \leq 1/2$ half space are given here.

Fig. 3-3. It is seen that the antiferromagnetic phase is unstable to at most 15% hole (or electron) doping at low temperatures. The τ_{Hb} and τ_{tJ} phases exist at different doping values, with τ_{Hb} appearing for approximately 10-18% doping, directly adjacent to the AF phase, and τ_{tJ} in the 30-35% doping range. The narrowness of the first-order transitions, with jumps in the electron density of the order of a few percent, is noteworthy.

3.2.6 Specific Heat Results

From the calculated expectation values of the operators occurring in the Hamiltonian [Eq.(3.2)], we have obtained the dimensionless internal energy per bond $\langle \beta H(i,j) \rangle$. Recall that dimensionless coupling constants are exhibited in the Hubbard Hamiltonian of Eq.(3.2), *e.g.*,

$$t = \frac{\tilde{t}}{k_B T}, \tag{3.21}$$

where $\tilde{t}$ is a constant that does not depend on temperature. The specific heat is calculated with

$$C = \frac{\partial \langle H(i,j) \rangle}{\partial T} = k_B \left\{ \frac{\partial}{\partial t^{-1}} \langle c^{\dagger}_{i\sigma} c_{j\sigma} + c^{\dagger}_{j\sigma} c_{i\sigma} \rangle + \frac{U}{t} \frac{\partial}{\partial t^{-1}} \langle n_{i\uparrow} n_{i\downarrow} + n_{j\uparrow} n_{j\downarrow} \rangle \right\}. \tag{3.22}$$

The partial derivatives are taken at fixed U_0/t and at fixed density $\langle n_i \rangle$.

In Fig. 3-6 we plot $\gamma = C/T$ for $U_0/t = 15$ at several different electron densities. (The corresponding phase diagram is shown in Fig. 3-3(b)). At half-filling, $\langle n_i \rangle = 1.00$, we observe a broad peak near the HD/AF transition temperature, which we can attribute to the onset of spin order. As we dope the system with holes, this peak gets sharper, becoming most pronounced near $\langle n_i \rangle = 0.68$, directly above the transition temperature between the hD and τ_{tJ} phases. In fact, the C/T curve shows a multipeak structure near the transition, a general characteristic of the phase diagram region just above the τ_{tJ} phase. At electron density $\langle n_i \rangle = 0.60$, no longer in the τ_{tJ} range, the peak decreases in size and broadens out again.

The distinct nature of the τ_{tJ} and τ_{Hb} phases becomes clear when we look at the

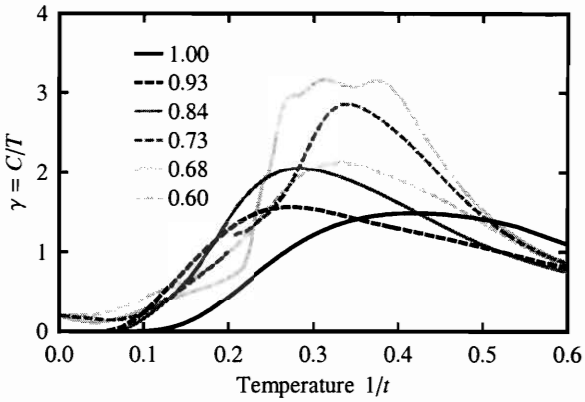

Figure 3-6: The specific heat coefficient $\gamma = C/T$ as a function of temperature for $U_0/t = 15$, at several different electron densities $\langle n_i \rangle$ indicated in the legend. For this temperature range the densities $\langle n_i \rangle = 1.00$ and 0.93 lie inside the antiferromagnetic (AF) phase, 0.84 inside the $\tau_{\rm Hb}$ phase, 0.73 and 0.60 inside the hole-rich disordered (hD) phase, and 0.68 inside the $\tau_{\rm tJ}$ phase. Here and in the following figures, γ is shown in units of $k_B^2/\tilde{t}$, where $\tilde{t}$ is the temperature-independent constant in Eq. (3.21).

low temperature specific heat. In Fig. 3-7 we plot the coefficient $\gamma = C/T$ as a function of electron density for $U_0/t = 15$ and at low temperature $1/t = 0.085$. In the limit as $T \to 0$, γ is a measure of the linear contribution to the specific heat due to quasiparticle excitations. Near half-filling, γ is close to zero, increases to a small level with sufficient hole doping, falls to near zero again in the $\tau_{\rm Hb}$ phase, and dramatically increases only after the system makes a narrow first-order transition to the hole-rich disordered phase. The steady rise of γ in the hD phase with further hole doping is consistent with a Fermi liquid interpretation of this phase. The increase in γ is interrupted by the $\tau_{\rm tJ}$ interval, where the curve makes a sharp oscillation, but continues in the hD region on the other side.

We see that the $\tau_{\rm tJ}$ phase has non-zero γ at low temperatures, while the $\tau_{\rm Hb}$ phase does not. In Figs. 3-8(a) and 3-8(b) we contrast the two τ phases directly, comparing representative C/T curves for $\tau_{\rm tJ}$ and $\tau_{\rm Hb}$ transitions. We observe that in the $\tau_{\rm Hb}$ phase the low-temperature specific heat exhibits an exponential form characteristic of a gap in the quasiparticle spectrum. Specific heat data points for temperatures $1/t < 0.2$, shown in the top right inset of Fig. 3-8(b), were found to fit a theoretical curve of the

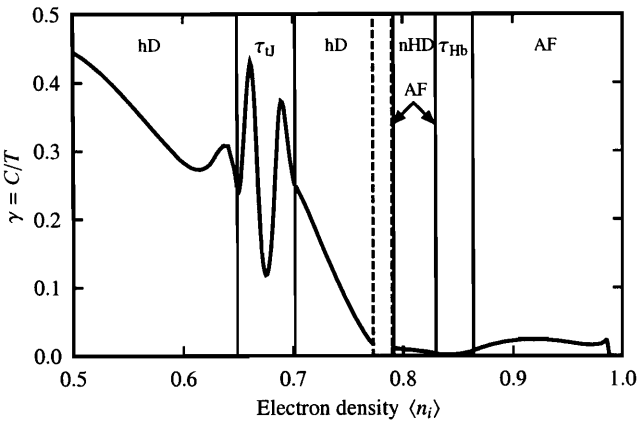

Figure 3-7: The specific heat coefficient $\gamma = C/T$ for $U_0/t = 15$ at the low temperature of $1/t = 0.085$, as a function of electron density $\langle n_i \rangle$. The corresponding phases are indicated near the top of the figure, with second-order phase boundaries marked by thin vertical lines. The interval between the vertical dashed lines corresponds to the first-order phase transition.

same form as in the $T \to 0$ limit of a weakly-coupled, BCS-type superconductor,

$$\frac{C}{k_B} = \frac{A}{T^{3/2}} \exp\left(-\frac{\Delta}{T}\right) , \tag{3.23}$$

with a best-fit coefficient $A = 1.02 \pm 0.06$ and a zero-temperature gap $\Delta = 1.01 \pm 0.01$, where t^{-1} is used as the temperature variable. In contrast, the τ_{tJ} phase clearly has a gapless spectrum, as we see in the C/T curve of Fig. 3-8(a). As mentioned earlier, we also clearly see multiple peaks in the specific heat just above the hD/τ_{tJ} transition temperature.

The τ_{tJ} and τ_{Hb} phases have similar properties at the phase sink, most notably a non-zero hopping amplitude, and thus are both good candidates for superconductivity. Since the two phases are dominant in different U_0/t regimes, their contrasting specific heat characteristics can potentially be understood as the difference between strongly-coupled and weakly-coupled superconducting phases. For the strongly-coupled, BEC-like case, pairing occurs above T_c, and these tightly bound bosonic pairs condense at the transition temperature. The double-peak structure in the specific heat above the τ_{tJ} phase is a possible indicator of such pair formation. Additionally, we expect that a BEC-like superconducting transition in three dimensions should have a specific heat

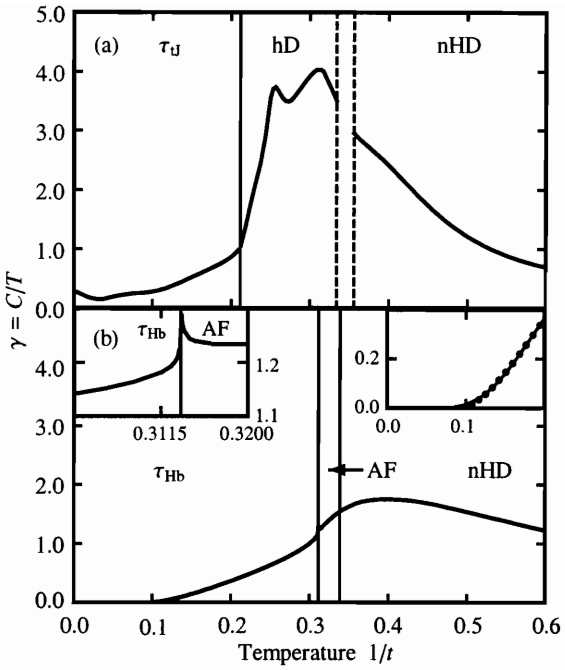

Figure 3-8: The specific heat coefficient $\gamma = C/T$ as a function of temperature for two different electron densities and values of U_0/t: (a) $\langle n_i \rangle = 0.68$, $U_0/t = 20$; (b) $\langle n_i \rangle = 0.875$, $U_0/t = 7.5$. Phases are indicated near the top of the figures, with second-order phase boundaries marked by thin vertical lines. The interval between the vertical dashed lines corresponds to a first-order phase transition. In diagram (b) the top left inset shows a close-up of the cusp in γ at the AF/τ_{Hb} transition temperature. The data points in the top right inset are calculated γ values for temperatures $1/t < 0.2$, fitted to a BCS-like exponential curve of the form $C/k_BT = \frac{A}{T^{5/2}} \exp\left(-\frac{\Delta}{T}\right)$, with best-fit parameters $A = 1.02 \pm 0.06$ and $\Delta = 1.01 \pm 0.01$, where t^{-1} is used as the temperature variable.

critical exponent $\alpha = -1$ [29]. Analysis of the C_6^* fixed point, governing the hD/τ_{tJ} boundary, yields the result $\alpha = -0.97$. The presence of low-lying excitations in a Bose gas is also consistent with the fact that we do not see a gap in the low-temperature specific heat of the τ_{tJ} phase.

Turning now to the τ_{Hb} phase, we already noted that its specific heat can be closely fitted at low temperatures to a BCS-like exponential curve, which is exactly what we would expect for a weakly-coupled superconducting phase. Analysis of the C_3^* fixed point, controlling the AF/τ_{Hb} boundary, yields a specific heat coefficient $\alpha = -0.27$. This translates into a finite cusp at the transition temperature, as shown in the top left inset of Fig. 3-8(b). For weak and intermediate couplings the superconducting

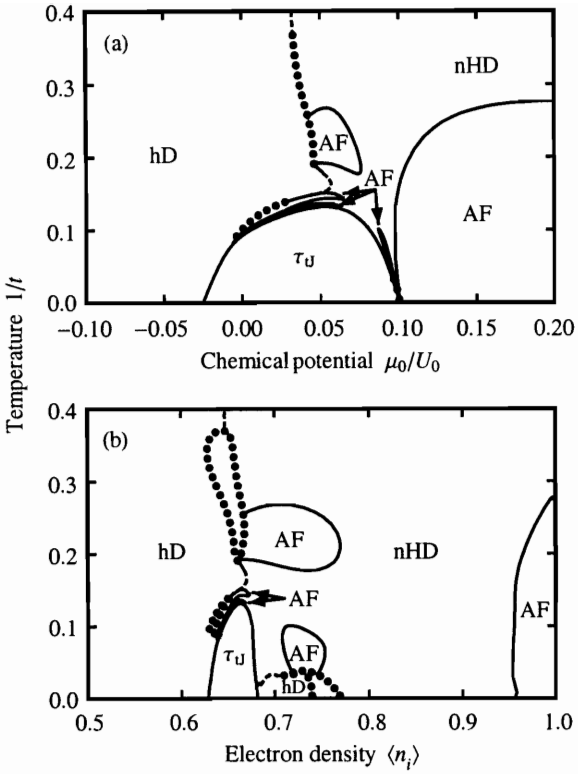

Figure 3-9: $d = 3$ Hubbard model phase diagram for large Coulomb repulsion $U_0/t = 50$ in temperature versus (a) chemical potential, (b) electron density $\langle n_i \rangle$. The full curves are second-order phase boundaries, while the dotted curves indicate first-order boundaries. The dashed lines are not phase transitions, but disorder lines between the near-half-filled disordered and hole-rich disordered phases.

transition is expected to belong to the universality class of the $d = 3$ XY model, with $\alpha = -0.013$ [50] (examples of transitions in this class include the superfluid transition of ^{4}He, the superconducting transition in certain high-T_c materials like Y-123, and also in conventional superconductors, though for the latter the critical region is too narrow to be observed experimentally) [29]. Our calculated α is closer to the $d = 3$ XY than to the BEC value, supporting the weak-coupling interpretation of the τ_{Hb} phase.

3.2.7 The tJ Limit of the Hubbard Model

In the strong-coupling limit $U_0 \gg t$, second-order perturbation theory in t/U_0 applied to the Hubbard model leads to the following Hamiltonian (known as the tJ model) [16,

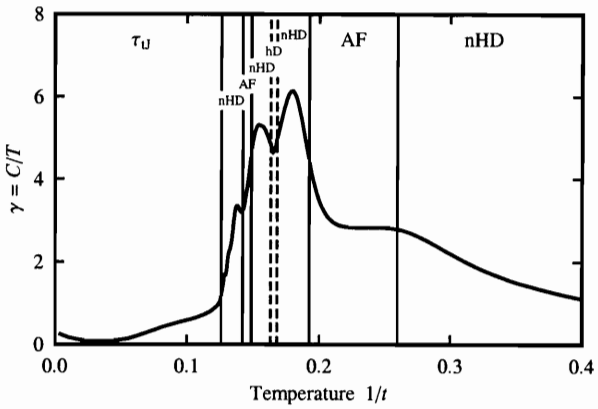

Figure 3-10: The specific heat coefficient $\gamma = C/T$ as a function of temperature for $U_0/t = 50$ and $\langle n_i \rangle = 0.67$. Phases are indicated near the top of the figure, with second-order phase boundaries marked by thin vertical lines. The dashed lines are not phase transitions, but disorder lines between the near-half-filled disordered and hole-rich disordered phases.

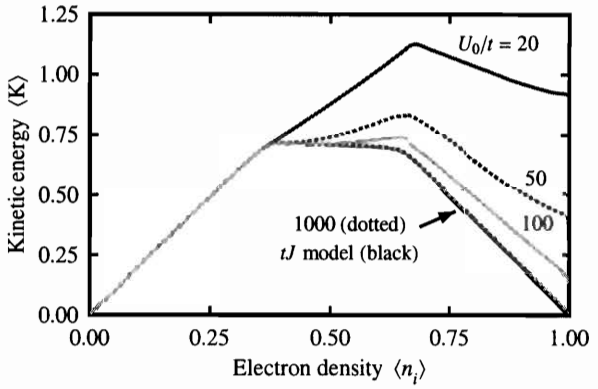

Figure 3-11: The kinetic energy per bond $\langle K \rangle = -\sum_\sigma \langle c^\dagger_{i\sigma} c_{j\sigma} + c^\dagger_{j\sigma} c_{i\sigma} \rangle$ as a function of electron density $\langle n_i \rangle$ at temperature $1/t = 0.2$ for Coulomb repulsions $U_0/t = 20$, 50, 100, and 1000 (indicated by numbers next to each curve). The solid curve at the bottom is the result calculated using the tJ model renormalization-group equations [18, 19] at the same temperature, with the corresponding $J/t = 0.004$.

17, 18, 19, 51, 52, 53, 54, 55],

$$H_{tJ} = -t \sum_{\langle ij \rangle, \sigma} P \left(c^\dagger_{i\sigma} c_{j\sigma} + c^\dagger_{j\sigma} c_{i\sigma} \right) P + J \sum_{\langle ij \rangle} (\vec{S}_i \cdot \vec{S}_j - \frac{1}{4} n_i n_j) \,, \tag{3.24}$$

where $J = 4t^2/U$ and P is a projection operator prohibiting double occupation of a lattice site. In addition to the terms shown above, the perturbation theory generates a three-site term of the form $\sum_{\langle ikj \rangle} c^\dagger_{i\sigma} (S_k)_{\sigma\sigma'} c_{j\sigma'}$, but this term is usually ignored,

from the assumption that it does not radically alter the physics of the tJ model. (Our current results, directly from the strong-coupling limit of the actual Hubbard model, confirm this assumption.) We thus expect that our Hubbard model approach in the limit of large U_0/t should give results qualitatively similar to those found for the tJ model in earlier renormalization-group studies [18, 19]. The phases of the tJ model found in these studies are identical to those of the Hubbard model, except that there is no τ_{Hb} phase.

Fig. 3-9 shows the Hubbard model phase diagram in terms of temperature versus chemical potential and temperature versus electron density for $U_0/t = 50$. At this large coupling, we do indeed observe a phase diagram very similar to that found in the earlier study of the tJ model [18, 19]. In particular, the τ_{tJ} phase is surrounded by AF islands, and directly above τ_{tJ} we get a lamellar structure of alternating AF, nHD, and hD phases. The AF phase near half-filling is unstable to only about 5% hole doping. This phase diagram can be seen as an evolution from the $U_0/t = 20$ result of Figs. 3-2(a) and 3-3(a), with the τ_{hB} entirely disappearing at $U_0/t = 50$ except for infinitesimal slivers. The multiple peaks in the specific heat above the τ_{tJ} transition persist in the strong-coupling limit, as seen in Fig. 3-10, which plots the specific heat coefficient γ for $U/t_0 = 50$ at $\langle n_i \rangle = 0.67$. The peak structure here is more complex than in Fig. 3-8(a), due to the above-mentioned lamellar phases.

We can also observe the evolution from the Hubbard to the tJ limits through the expectation value of the kinetic energy per bond, $\langle K \rangle = -\sum_\sigma \langle c^\dagger_{i\sigma} c_{j\sigma} + c^\dagger_{j\sigma} c_{i\sigma} \rangle$, which is proportional to the density of free carriers in the system. Fig. 3-11 shows $\langle K \rangle$ as a function of electron density for the temperature $1/t = 0.2$, calculated at several different couplings U_0/t. As U_0/t is increased, the value of $\langle K \rangle$ at half-filling is reduced, and when $U_0/t = 1000$ we are close to the tJ limit, with the kinetic energy at half-filling almost zero, indicating no available free carriers due to the prohibitively high energy of double occupation. The $U_0/t = 1000$ curve almost exactly overlaps the result calculated from the tJ model renormalization-group equations at the same temperature using the corresponding coupling $J/t = 4t/U_0 = 0.004$.

References

[1] A.A. Migdal, Zh. Eksp. Teor. Fiz. **69**, 1457 (1975) [Sov. Phys. JETP **42**, 743 (1976)].

[2] L.P. Kadanoff, Ann. Phys. (N.Y.) **100**, 359 (1976).

[3] A.N. Berker and S. Ostlund, J. Phys. C **12**, 4961 (1979).

[4] M. Kaufman and R.B. Griffiths, Phys. Rev. B **24**, 496 (1981).

[5] M. Kaufman and R.B. Griffiths, Phys. Rev. B **30**, 244 (1984).

[6] J. Hubbard, Proc. R. Soc. A **276**, 238 (1963); **277**, 237 (1964); **281**, 401 (1964).

[7] G. Migliorini and A.N. Berker, Eur. Phys. J. B **17**, 3 (2000).

[8] K.G. Wilson, Phys. Rev. B **4**, 3174, 3184 (1971).

[9] J.E. Hirsch, Phys. Rev. B **22**, 5259 (1980).

[10] B. Fourcade and G. Spronken, Phys. Rev. B **29**, 5012, 5089, 5096 (1984).

[11] C. Vanderzande and A.L. Stella, J. Phys. C **17**, 2075 (1984).

[12] C. Vanderzande, J. Phys. A **18**, 889 (1985).

[13] S.A. Cannas, F.A. Tamarit, and C. Tsallis, Solid State Commun. **78**, 685 (1991).

[14] S.A. Cannas and C. Tsallis, Z. Phys. **89**, 195 (1992).

[15] A.C. Cosentini, M. Capone, L. Guidoni, and G. Bachelet, Phys. Rev. B **58**, 18235 (1998).

[16] P.W. Anderson, Science **235**, 1196 (1987).

[17] G. Baskaran, Z. Zhou, and P.W. Anderson, Solid State Commun. **63**, 973 (1987).

[18] A. Falicov and A.N. Berker, Phys. Rev. B **51**, 12458 (1995).

[19] A. Falicov and A.N. Berker, Turk. J. Phys. **19**, 127 (1995).

[20] F.C. Chou and D.C. Johnston, Phys. Rev. B **54**, 572 (1996).

[21] J. Solyom, Adv. Phys. **28**, 201 (1979).

[22] J. Voit, Rep. Prog. Phys. **57**, 977 (1994).

[23] D. Zanchi and H.J. Schulz, Europhys. Lett. **44**, 235 (1997).

[24] D. Zanchi and H.J. Schulz, Phys. Rev. B **61**, 13609 (2000).

[25] C.J. Halboth and W. Metzner, Phys. Rev. B **61**, 7364 (2000).

[26] C.J. Halboth and W. Metzner, Phys. Rev. Lett. **85**, 5162 (2000).

[27] C. Honerkamp, M. Salmhofer, N. Furukawa, and T.M. Rice, Phys. Rev. B **63**, 035109 (2001).

[28] C. Honerkamp, M. Salmhofer, and T.M. Rice, Eur. Phys. J. B **27**, 127 (2002).

[29] A. Junod, A. Erb, and C. Renner, Physica C **317-318**, 333 (1999).

[30] M. Suzuki and H. Takano, Phys. Lett. A **69**, 426 (1979).

[31] H. Takano and M. Suzuki, J. Stat. Phys. **26**, 635 (1981).

[32] S.R. McKay, A.N. Berker, and S. Kirkpatrick, Phys. Rev. Lett. **48**, 767 (1982).

[33] G. Migliorini and A.N. Berker, Phys. Rev. B **57**, 426 (1998).

[34] D. Andelman and A.N. Berker, Phys. Rev. B **29**, 2630 (1984).

[35] A. Falicov, A.N. Berker, and S.R. McKay, Phys. Rev. B **51**, 8266 (1995).

[36] E. Domany, S. Alexander, D. Bensimon, and L.P. Kadanoff, Phys. Rev. B **28**, 3110 (1983).

[37] J.-M. Langlois, A.-M.S. Tremblay, and B.W. Southern, Phys. Rev. B **28**, 218 (1983).

[38] R.B. Stinchcombe and A.C. Maggs, J. Phys. A **19**, 1949 (1986).

[39] T.A.S. Haddad, S.T.R. Pinho, and S.R. Salinas, Phys. Rev. E **61**, 3330 (2000).

[40] J.-X. Le and Z.R. Yang, Phys. Rev. E **69**, 066107 (2004).

[41] R.A. da Silveira and J.-P. Bouchaud, Phys. Rev. Lett. **93**, 015901 (2004).

[42] G.S. Rushwood and P.J. Wood, Mol. Phys. **6**, 409 (1963).

[43] J. Oitmaa and W. Zheng, J. Phys.: Condens. Matter **16**, 8653 (2004).

[44] A.N. Berker and M. Wortis, Phys. Rev. B **14**, 4946 (1976).

[45] A.N. Berker, S. Ostlund, and F.A. Putnam, Phys. Rev. B **17**, 3650 (1978).

[46] R.T. Scalettar, D.J. Scalapino, R.L. Sugar, and D. Toussaint, Phys. Rev. B **39**, 4711 (1989).

[47] J.E. Hirsch, Phys. Rev. B **35**, 1851 (1987).

[48] M. Jarrell, Phys. Rev. Lett. **69**, 168 (1992).

[49] A.-M. Daré and G. Albinet, Phys. Rev. B **61**, 4567 (2000).

[50] J.A. Lipa, D.R. Swanson, J.A. Nissen, T.C.P. Chui, and U.E. Israelsson, Phys. Rev. Lett. **76**, 944 (1996).

[51] K.A. Chao, J. Spalek, and A.M. Oles, J. Phys. C **10**, L271 (1977).

[52] J.E. Hirsch, Phys. Rev. Lett. **54**, 1317 (1985).

[53] J.K. Freericks and L.M. Falicov, Phys. Rev. B **42**, 4960 (1990).

[54] K.M. Rabe and R.N. Bhatt, J. Appl. Phys. **69**, 4508, (1991).

[55] P.M. Bares, G. Blatter, and M. Ogata, Phys. Rev. B **44**, 130 (1991).

Chapter 4

The tJ Model in $d = 3$

4.1 Introduction

The renormalization-group transformation described in the last two chapters allows us to calculate the expectation values of operators appearing in the renormalized Hamiltonian, and thus any quantities—specific heat, susceptibilities—that can be derived from them. To go beyond this and examine additional properties of the system typically involves adding terms to the original Hamiltonian. The more complex and general a system we start with, the larger the parameter space onto which it is mapped by renormalization, making a wider variety of thermodynamic averages available for study. For example, by coupling the Hamiltonian to a vector potential, adding phase factors to the electron hopping terms, we will see below that we can calculate conjugate current densities and the superfluid weight.

With every addition to the system, however, numerically implementing the renormalization-group transformation becomes more complicated. The problem is not with generating a larger number of interaction terms in the generalized Hamiltonian—we saw in Chapter 1 that following the flows of even 17 interaction constants is possible—but the fact that for $d > 1$ the phase sinks of the renormalization-group flows usually involve a subset of the interaction constants going to $\pm\infty$ (as seen in Table 3.5 for the case of the $d = 3$ Hubbard model). Calculating the recursion relations as we approach these sinks involves exponentiating, combining, and taking logarithms of ma-

trices containing extremely large elements. The most delicate step in the procedure is taking the logarithm of the block-diagonal matrix representing the exponentiated renormalized two-site Hamiltonian. The elements in this matrix are linear combinations of the form $\sum_i c_i e^{x_i}$, where the exponents x_i tend to blow up at the phase sink, and thus the $c_i e^{x_i}$ terms may vary over many orders of magnitude. It is crucial when taking the matrix logarithm that important numerical information is not lost because of computer precision constraints. We have developed specialized routines to handle such cases, details of which can be found in Appendix A. Even with these routines there are limitations. Calculating matrix logarithms at arbitrary precision may be relatively easy for the 2×2 blocks we have encountered thus far in the renormalized two-site Hamiltonian matrix, and is still tractable for the 3×3 blocks we will see in another context later in this chapter. But with larger matrices the arithmetic operations needed to calculate the logarithm increase dramatically, and it becomes harder to prevent significant numerical error as we approach a phase sink.

With these considerations in mind, for the remainder of the thesis we will focus primarily on the tJ model. Since it represents the strong-coupling limit of the Hubbard model, with double occupation prohibited, there are only 3 possible states per site—empty, spin up, and spin down. As a result, we end up dealing with smaller matrices while calculating the recursion relations, and this makes the tJ model a simpler starting point for the various extensions we plan to make—coupling to a vector potential in the following section, incorporating anisotropy in Chapter 5 and disorder in Chapter 7. Since the τ phase is present in the isotropic $d = 3$ tJ model [1, 2], this is where we turn first, to investigate the doping dependence of the superfluid weight, free carrier density, and specific heat.

4.2 Superfluid Weight, Free Carrier Density, and Specific Heat of the $d = 3$ tJ Model at Finite Temperatures

Michael Hinczewski and A. Nihat Berker
Department of Physics, Istanbul Technical University,
Maslak 34469, Istanbul, Turkey,
Department of Physics, Massachusetts Institute of Technology,
Cambridge, Massachusetts 02139, U.S.A.,
Feza Gürsey Research Institute, TÜBITAK - Bosphorus University,
Çengelköy 81220, Istanbul, Turkey

Abstract

The superfluid weight, free carrier density, and specific heat of the three-dimensional tJ model are calculated by renormalization-group theory. We find that optimal hole doping for superfluidity occurs in the electron density range of $\langle n_i \rangle \approx 0.63$–$0.68$, where the superfluid weight n_s/m^* reaches a local maximum. This density range is within the novel τ phase, where the electron hopping strength renormalizes to infinity, the system remains partially filled at all length scales, and the electron-hopping expectation value remains distinctively non-zero at all length scales. The calculated superfluid weight drops off sharply in the overdoped region. Under hole doping, the calculated density of free carriers increases until optimal doping and remains approximately constant in the overdoped region, as seen experimentally in high-T_c materials. Furthermore, from calculation of the specific heat coefficient γ, we see clear evidence of a gap in the excitation spectrum for the τ phase.

PACS numbers: 74.72.-h, 71.10.Fd, 05.30.Fk, 74.25.Dw

arXiv: cond-mat/0503631

4.2.1 Introduction

The variation of the superfluid number density n_s with temperature and carrier doping is of fundamental importance in describing the unique properties of the superconducting state in high-T_c cuprates. Experimentally, muon-spin-rotation techniques are used to determine the closely related quantity n_s/m^* (also known as the superfluid weight), where m^* is the effective mass of the carriers in the superfluid. In the underdoped region of high-T_c materials, n_s/m^* increases with doping, and the low-temperature superfluid weight is correlated with T_c.[3, 4] As the materials are doped past the optimal value (where T_c is the highest), n_s/m^* peaks and rapidly decreases.[5, 6, 7] The decrease in n_s/m^* is surprising since the total density of free carriers saturates at optimal doping and remains almost constant in the overdoped region.[8] By contrast, in a conventional superconductor, described by BCS theory, these two quantities have the same doping dependence.

The tJ model is a promising starting point in understanding these properties of cuprate superconductors. Mean-field $U(1)$ and $SU(2)$ slave-boson theories of the tJ Hamiltonian have reproduced some aspects of the doping and temperature dependences of n_s/m^*.[9, 10] More direct, unbiased numerical techniques applied to a 4×4 tJ cluster have observed a large peak in n_s/m^* in the same region where pairing correlations indicate a superconducting ground state.[11] A general limitation of these types of studies is that no finite-cluster approach can unambiguously identify phase transitions in the system, or exhibit the non-analytic behavior of thermodynamic quantities at these transitions.

Alternatively, the physics of the bulk model can be studied through the position-space renormalization-group method, which has been used to determine the phase structure and thermodynamic properties of the tJ and Hubbard models at finite temperatures.[2, 1, 12, 13] In particular, Falicov and Berker's calculation for the tJ model in $d = 3$ with the realistic coupling $J/t = 0.444$ produced a rich, multicritical phase diagram [2, 1], with a novel low-temperature phase (called "τ") for $30 - 40\%$ hole doping where the electron hopping strength in the Hamiltonian renormalizes to

infinity under repeated scale changes, while the system remains partially filled. This is the possible signature of a superconducting phase, and it is notable that a similar phase was also observed in the $d = 3$ Hubbard model.[12, 13]

Our present study further develops this renormalization-group method, to yield the superfluid weight of the tJ model as a function of temperature and hole doping. Our approach reproduces phenomenological features of high-T_c materials. In particular we find that optimal doping is located in the vicinity of the τ phase, where n_s/m^* peaks and then is sharply reduced with overdoping. Moreover, we also find that the density of free carriers increases until optimal doping, and saturates in overdoped region. These results suggest that the τ phase might indeed correspond to the superconducting phase in cuprates. Further supporting this idea, we present specific heat calculations that show clear evidence of a gap in the quasiparticle spectrum for the τ phase.

4.2.2 The tJ Hamiltonian

We consider a d-dimensional hypercubic lattice where the tJ model for electron conduction is defined by the Hamiltonian

$$H = P\left[\tilde{t}\sum_{\langle ij\rangle,\sigma}\left(c^{\dagger}_{i\sigma}c_{j\sigma}+c^{\dagger}_{j\sigma}c_{i\sigma}\right)+\tilde{J}\sum_{\langle ij\rangle}\mathbf{S}_i\cdot\mathbf{S}_j-\tilde{V}\sum_{\langle ij\rangle}n_in_j-\tilde{\mu}\sum_i n_i\right]P\,, \quad (4.1)$$

where $c^{\dagger}_{i\sigma}$ and $c_{i\sigma}$ are creation and annihilation operators, obeying anticommutation rules, for an electron with spin $\sigma = \uparrow$ or $\downarrow$ at lattice site i, $n_{i\sigma} = c^{\dagger}_{i\sigma}c_{i\sigma}$, $n_i = n_{i\uparrow} + n_{i\downarrow}$ are the number operators, and $\mathbf{S}_i = \frac{1}{2}\sum_{\sigma\sigma'} c^{\dagger}_{i\sigma}\mathbf{s}_{\sigma\sigma'}c_{i\sigma'}$ is the single-site spin operator, with $\mathbf{s}$ the vector of Pauli spin matrices. The entire Hamiltonian is sandwiched between projection operators $P = \prod_i(1 - n_{i\downarrow}n_{i\uparrow})$, which project out states with doubly-occupied sites. The interaction constants $\tilde{t}$, $\tilde{J}$, $\tilde{V}$ describe the following physical features: electron hopping ($\tilde{t}$), a nearest-neighbor antiferromagnetic coupling ($\tilde{J} > 0$), and a nearest-neighbor interaction ($\tilde{V}$). The standard tJ Hamiltonian is a special case of Eq. (4.1) with $\tilde{V}/\tilde{J} = 1/4$. For convenience, we introduce dimension-

less interaction constants t, J, V, μ, and rearrange the $\tilde{\mu}$ chemical potential term to group the Hamiltonian into a single lattice summation:

$$\begin{aligned} -\beta H &= \sum_{\langle ij \rangle} P\left[-t \sum_{\sigma} \left(c_{i\sigma}^{\dagger} c_{j\sigma} + c_{j\sigma}^{\dagger} c_{i\sigma}\right) - J\mathbf{S}_i \cdot \mathbf{S}_j + V n_i n_j + \mu(n_i + n_j)\right] P \\ &\equiv \sum_{\langle ij \rangle} \{-\beta H(i,j)\} \,. \end{aligned} \tag{4.2}$$

Here $\beta = 1/k_B T$, so that the interaction constants are related by $t = \beta\tilde{t}$, $J = \beta\tilde{J}$, $V = \beta\tilde{V}$, $\mu = \beta\tilde{\mu}/2d$. The total Hamiltonian is now written as a sum of pair Hamiltonians $-\beta H(i,j)$. The sum over nearest-neighbor sites (i,j) is taken so that the position of site j is $\mathbf{r}_j = \mathbf{r}_i + \mathbf{a}_k$, where $\mathbf{a}_k$ is one of the d lattice vectors. Since changing the sign of t is equivalent to redefining the phase at every other site in the system, we shall choose $t > 0$ with no loss of generality. The effective temperature variable will be $1/t = k_B T$, where we have taken $\tilde{t} = 1$ as the unit of energy.

In order to study the superfluid weight, we introduce periodic boundary conditions, by considering the system as a ring in each axis direction threaded by a magnetic flux. We choose the vector potential $\mathbf{A}$ associated with the flux to have components $A/\sqrt{d}$ along each axis, so that the pair Hamiltonian becomes

$$-\beta H(i,j) = P\left[-t \sum_{\sigma} \left(e^{i\phi} c_{i\sigma}^{\dagger} c_{j\sigma} + e^{-i\phi} c_{j\sigma}^{\dagger} c_{i\sigma}\right) - J\mathbf{S}_i \cdot \mathbf{S}_j + V n_i n_j + \mu(n_i + n_j)\right] P \,, \tag{4.3}$$

where $\phi = aA/\sqrt{d}$ and a is the lattice spacing. For simplicity, we have adopted units so that $\hbar = c = e = 1$. In the presence of the applied phase twist ϕ, the superfluid weight n_s/m^* is related to the curvature of the total free energy F near $\phi = 0$,[14, 15]

$$\frac{n_s}{m^*} = \frac{1}{Na^2} \lim_{A \to 0} \frac{\partial^2 F}{\partial A^2} = \frac{1}{Nd} \lim_{\phi \to 0} \frac{\partial^2 F}{\partial \phi^2} \,, \tag{4.4}$$

where $N \to \infty$ is the total number of lattice sites. Later we shall show how this quantity can be calculated from the renormalization-group transformation developed

in the next section.

4.2.3 Renormalization-Group Transformation

4.2.3.1 Recursion Relations

The position-space renormalization-group method used here starts with an approximate decimation in $d = 1$, which is then generalized to higher dimensions by the Migdal-Kadanoff procedure [2, 1]. In $d = 1$, the Hamiltonian of Eq. (4.2) takes the form:

$$-\beta H = \sum_i \{-\beta H(i, i+1)\} , \tag{4.5}$$

where $i = 1, 2, 3, \ldots$. The decimation consists of finding a thermodynamically equivalent system, described by the Hamiltonian $-\beta' H'$, which depends only on the states of the odd-numbered sites. Since the quantum operators in the Hamiltonian do not commute, an exact decimation even in one dimension is not possible. We can carry out an approximate decimation as follows [16, 17]:

$$\begin{aligned}
\mathrm{Tr}_{\mathrm{even}} e^{-\beta H} =& \mathrm{Tr}_{\mathrm{even}} e^{\sum_i \{-\beta H(i,i+1)\}} \\
=& \mathrm{Tr}_{\mathrm{even}} e^{\sum_i^{\mathrm{even}} \{-\beta H(i-1,i) - \beta H(i,i+1)\}} \\
\simeq& \prod_i^{\mathrm{even}} \mathrm{Tr}_i e^{\{-\beta H(i-1,i) - \beta H(i,i+1)\}} \\
=& \prod_i^{\mathrm{even}} e^{-\beta' H'(i-1,i+1)} \\
\simeq& e^{\sum_i^{\mathrm{even}} \{-\beta' H'(i-1,i+1)\}} = e^{-\beta' H'} .
\end{aligned} \tag{4.6}$$

Here $-\beta' H'$ is the Hamiltonian for the renormalized system, and $\mathrm{Tr}_{\mathrm{even}}$ is a trace over the degrees of freedom at all even-numbered sites. In the two approximate steps, marked by $\simeq$ in Eq. (4.6), we ignore the non-commutation of operators separated beyond three consecutive sites of the unrenormalized system (conversely, this means that anticommutation rules are taken into account within three consecutive sites at all successive length scales, as the renormalization-group procedure is repeated). These

two steps involve the same approximation but in opposite directions, which gives some mutual compensation. Earlier studies of quantum spin systems have shown the success of this approximation at predicting finite-temperature behavior.[16, 17]

The renormalization-group mapping can be extracted from the third and fourth lines of Eq.(4.6):

$$e^{-\beta' H'(i,k)} = \mathrm{Tr}_j e^{-\beta H(i,j) - \beta H(j,k)}, \tag{4.7}$$

where i, j, k are three consecutive sites of the unrenormalized system. The operators $-\beta' H'(i,k)$ and $-\beta H(i,j) - \beta H(j,k)$ act on the space of two-site and three-site states respectively, so that, in terms of matrix elements,

$$\langle u_i v_k | e^{-\beta' H'(i,k)} | \bar{u}_i \bar{v}_k \rangle = \sum_{w_j} \langle u_i \, w_j \, v_k | e^{-\beta H(i,j) - \beta H(j,k)} | \bar{u}_i \, w_j \, \bar{v}_k \rangle \, , \tag{4.8}$$

where $u_i, w_j, v_k, \bar{u}_i, \bar{v}_k$ are single-site state variables. Eq.(4.8) is the contraction of a 27×27 matrix on the right into a 9×9 matrix on the left. We block-diagonalize the left and right sides of Eq.(4.8) by choosing basis states which are the eigenstates of total particle number, total spin magnitude, total spin z-component, and parity. We denote the set of 9 two-site eigenstates by $\{|\phi_p\rangle\}$ and the set of 27 three-site eigenstates by $\{|\psi_q\rangle\}$, and list them in Tables 4.1 and 4.2. Eq.(4.8) is rewritten as

$$\begin{aligned} &\langle \phi_p | e^{-\beta' H'(i,k)} | \phi_{\bar{p}} \rangle = \\ &\quad \sum_{\substack{u,v,\bar{u}, \\ \bar{v},w}} \sum_{q,\bar{q}} \langle \phi_p | u_i v_k \rangle \langle u_i w_j v_k | \psi_q \rangle \langle \psi_q | e^{-\beta H(i,j) - \beta H(j,k)} | \psi_{\bar{q}} \rangle \langle \psi_{\bar{q}} | \bar{u}_i w_j \bar{v}_k \rangle \langle \bar{u}_i \bar{v}_k | \phi_{\bar{p}} \rangle \, . \end{aligned} \tag{4.9}$$

Eq. (4.9) yields six independent elements for the matrix $\langle \phi_p | e^{-\beta' H'(i,k)} | \phi_{\bar{p}} \rangle$, which we label γ_p as follows:

$$\begin{aligned} \gamma_p &\equiv \langle \phi_p | e^{-\beta' H'(i,k)} | \phi_p \rangle \quad \text{for } p = 1, 2, 4, 6, 7, \\ \gamma_0 &\equiv \langle \phi_2 | e^{-\beta' H'(i,k)} | \phi_4 \rangle \, . \end{aligned} \tag{4.10}$$

To calculate the γ_p, we determine the matrix elements of $-\beta H(i,j) - \beta H(j,k)$ in the three-site basis $\{\psi_q\}$, as listed in Table 4.3, and exponentiate the matrix blocks to find

n	p	s	m_s	Two-site basis states
0	+	0	0	$\|\phi_1\rangle = \|\circ\circ\rangle$
1	+	1/2	1/2	$\|\phi_2\rangle = \frac{1}{\sqrt{2}}\{\|\uparrow\circ\rangle + \|\circ\uparrow\rangle\}$
1	−	1/2	1/2	$\|\phi_4\rangle = \frac{1}{\sqrt{2}}\{\|\uparrow\circ\rangle - \|\circ\uparrow\rangle\}$
2	−	0	0	$\|\phi_6\rangle = \frac{1}{\sqrt{2}}\{\|\uparrow\downarrow\rangle - \|\downarrow\uparrow\rangle\}$
2	+	1	1	$\|\phi_7\rangle = \|\uparrow\uparrow\rangle$
2	+	1	0	$\|\phi_9\rangle = \frac{1}{\sqrt{2}}\{\|\uparrow\downarrow\rangle + \|\downarrow\uparrow\rangle\}$

Table 4.1: The two-site basis states, with the corresponding particle number (n), parity (p), total spin (s), and total spin z-component (m_s) quantum numbers. The states $|\phi_3\rangle$, $|\phi_5\rangle$, and $|\phi_8\rangle$, are obtained by spin reversal from $|\phi_2\rangle$, $|\phi_4\rangle$, and $|\phi_7\rangle$, respectively.

n	p	s	m_s	Three-site basis states
0	+	0	0	$\|\psi_1\rangle = \|\circ\circ\circ\rangle$
1	+	1/2	1/2	$\|\psi_2\rangle = \|\circ\uparrow\circ\rangle$, $\|\psi_3\rangle = \frac{1}{\sqrt{2}}\{\|\uparrow\circ\circ\rangle + \|\circ\circ\uparrow\rangle\}$
1	−	1/2	1/2	$\|\psi_6\rangle = \frac{1}{\sqrt{2}}\{\|\uparrow\circ\circ\rangle - \|\circ\circ\uparrow\rangle\}$
2	+	0	0	$\|\psi_8\rangle = \frac{1}{2}\{\|\uparrow\downarrow\circ\rangle - \|\downarrow\uparrow\circ\rangle - \|\circ\uparrow\downarrow\rangle + \|\circ\downarrow\uparrow\rangle\}$
2	−	0	0	$\|\psi_9\rangle = \frac{1}{2}\{\|\uparrow\downarrow\circ\rangle - \|\downarrow\uparrow\circ\rangle + \|\circ\uparrow\downarrow\rangle - \|\circ\downarrow\uparrow\rangle\}$, $\|\psi_{10}\rangle = \frac{1}{\sqrt{2}}\{\|\uparrow\circ\downarrow\rangle - \|\downarrow\circ\uparrow\rangle\}$
2	+	1	1	$\|\psi_{11}\rangle = \|\uparrow\circ\uparrow\rangle$, $\|\psi_{12}\rangle = \frac{1}{\sqrt{2}}\{\|\uparrow\uparrow\circ\rangle + \|\circ\uparrow\uparrow\rangle\}$
2	+	1	0	$\|\psi_{13}\rangle = \frac{1}{2}\{\|\uparrow\downarrow\circ\rangle + \|\downarrow\uparrow\circ\rangle + \|\circ\uparrow\downarrow\rangle + \|\circ\downarrow\uparrow\rangle\}$, $\|\psi_{14}\rangle = \frac{1}{\sqrt{2}}\{\|\uparrow\circ\downarrow\rangle + \|\downarrow\circ\uparrow\rangle\}$
2	−	1	1	$\|\psi_{17}\rangle = \frac{1}{\sqrt{2}}\{\|\uparrow\uparrow\circ\rangle - \|\circ\uparrow\uparrow\rangle\}$
2	−	1	0	$\|\psi_{18}\rangle = \frac{1}{2}\{\|\uparrow\downarrow\circ\rangle + \|\downarrow\uparrow\circ\rangle - \|\circ\uparrow\downarrow\rangle - \|\circ\downarrow\uparrow\rangle\}$
3	+	1/2	1/2	$\|\psi_{20}\rangle = \frac{1}{\sqrt{6}}\{2\|\uparrow\downarrow\uparrow\rangle - \|\uparrow\uparrow\downarrow\rangle - \|\downarrow\uparrow\uparrow\rangle\}$
3	−	1/2	1/2	$\|\psi_{22}\rangle = \frac{1}{\sqrt{2}}\{\|\uparrow\uparrow\downarrow\rangle - \|\downarrow\uparrow\uparrow\rangle\}$
3	+	3/2	3/2	$\|\psi_{24}\rangle = \|\uparrow\uparrow\uparrow\rangle$
3	+	3/2	1/2	$\|\psi_{25}\rangle = \frac{1}{\sqrt{3}}\{\|\uparrow\downarrow\uparrow\rangle + \|\uparrow\uparrow\downarrow\rangle + \|\downarrow\uparrow\uparrow\rangle\}$

Table 4.2: The three-site basis states, with the corresponding particle number (n), parity (p), total spin (s), and total spin z-component (m_s) quantum numbers. The states $|\psi_{4-5}\rangle$, $|\psi_7\rangle$, $|\psi_{15-16}\rangle$, $|\psi_{19}\rangle$, $|\psi_{21}\rangle$, $|\psi_{23}\rangle$, $|\psi_{26-27}\rangle$, are obtained by spin reversal from $|\psi_{2-3}\rangle$, $|\psi_6\rangle$, $|\psi_{11-12}\rangle$, $|\psi_{17}\rangle$, $|\psi_{20}\rangle$, $|\psi_{22}\rangle$, $|\psi_{24-25}\rangle$, respectively.

the elements $\langle\psi_q|e^{-\beta H(i,j)-\beta H(j,k)}|\psi_{\bar{q}}\rangle$ which enter on the right-hand side of Eq. (4.9). In this way the γ_p are functions of the interaction constants in the unrenormalized Hamiltonian, $\gamma_p = \gamma_p(t, \phi, J, V, \mu)$.

Since the matrix $\langle\phi_p|e^{-\beta' H'(i,k)}|\phi_{\bar{p}}\rangle$ is determined by six independent elements γ_p, the renormalized pair Hamiltonian $-\beta' H'(i,k)$ involves six interaction constants,

	ψ_1
ψ_1	0

	ψ_2	ψ_3	ψ_6
ψ_2	2μ	$-\sqrt{2}t\cos\phi$	$i\sqrt{2}t\sin\phi$
ψ_3	$-\sqrt{2}t\cos\phi$	μ	$i\Delta_1$
ψ_6	$-i\sqrt{2}t\sin\phi$	$-i\Delta_1$	μ

	ψ_8	ψ_9	ψ_{10}
ψ_8	$\frac{3}{4}J+V+3\mu$	$-i\Delta_3$	$-i\sqrt{2}t\sin\phi$
ψ_9	$i\Delta_3$	$\frac{3}{4}J+V+3\mu$	$-\sqrt{2}t\cos\phi$
ψ_{10}	$i\sqrt{2}t\sin\phi$	$-\sqrt{2}t\cos\phi$	2μ

	ψ_{11}	ψ_{12}	ψ_{17}
ψ_{11}	2μ	$-\sqrt{2}t\cos\phi$	$i\sqrt{2}t\sin\phi$
ψ_{12}	$-\sqrt{2}t\cos\phi$	$-\frac{1}{4}J+V+3\mu$	$i\Delta_2$
ψ_{17}	$-i\sqrt{2}t\sin\phi$	$-i\Delta_2$	$-\frac{1}{4}J+V+3\mu$

	ψ_{13}	ψ_{14}	ψ_{18}
ψ_{13}	$-\frac{1}{4}J+V+3\mu$	$-\sqrt{2}t\cos\phi$	$i\Delta_4$
ψ_{14}	$-\sqrt{2}t\cos\phi$	2μ	$i\sqrt{2}t\sin\phi$
ψ_{18}	$-i\Delta_4$	$-i\sqrt{2}t\sin\phi$	$-\frac{1}{4}J+V+3\mu$

	ψ_{20}
ψ_{20}	$J+2V+4\mu$

	ψ_{22}
ψ_{22}	$2V+4\mu$

	ψ_{24}
ψ_{24}	$-\frac{1}{2}J+2V+4\mu$

	ψ_{25}
ψ_{25}	$-\frac{1}{2}J+2V+4\mu$

Table 4.3: Diagonal matrix blocks of the unrenormalized three-site Hamiltonian $-\beta H(i,j)-\beta H(j,k)$. The Hamiltonian being invariant under spin-reversal, the spin-flipped matrix elements are not shown. The additive constant contribution $2G$, occurring at the diagonal terms, is also not shown. The additional Δ_i terms, which are not part of the original three-site Hamiltonian, are explained in Sec.4.2.3.

namely those of the original types of interactions and an additive constant:

$$-\beta' H'(i,k) = P\Big[-t'\sum_{\sigma}\left(e^{i\phi'}c^{\dagger}_{i\sigma}c_{j\sigma}+e^{-i\phi'}c^{\dagger}_{j\sigma}c_{i\sigma}\right) - J'\mathbf{S}_i\cdot\mathbf{S}_j+V'n_in_j+\mu'(n_i+n_j)+G'\Big]P\,, \quad (4.11)$$

The matrix elements of $-\beta' H'(i,k)$ in the $\{\phi_p\}$ basis are shown in Table 4.4. Exponentiating this matrix, we can solve for the renormalized interaction constants

	ϕ_1	ϕ_2	ϕ_4	ϕ_6	ϕ_7	ϕ_9
ϕ_1	G'					
ϕ_2		$-t'\cos\phi'+\mu'+G'$	$it'\sin\phi'$		0	
ϕ_4		$-it'\sin\phi'$	$t'\cos\phi'+\mu'+G'$			
ϕ_6				$\frac{3}{4}J'+V_2'+2\mu'+G'$		
ϕ_7			0		$-\frac{1}{4}J'+V_2'+2\mu'+G'$	
ϕ_9						$-\frac{1}{4}J'+V_2'+2\mu'+G'$

Table 4.4: Block-diagonal matrix of the renormalized two-site Hamiltonian $-\beta' H'(i,k)$. The Hamiltonian being invariant under spin-reversal, the spin-flipped matrix elements are not shown.

$(t', \phi', J', V', \mu', G')$ in terms of the γ_p:

$$
\begin{aligned}
t' &= \operatorname{sign}(\gamma_4 - \gamma_2)\cosh^{-1}\left(\frac{\gamma_2+\gamma_4}{2e^v}\right), \\
\phi' &= \tan^{-1}\left(\frac{2\,\mathrm{Im}\,\gamma_0}{\gamma_4-\gamma_2}\right), \qquad J' = \ln\frac{\gamma_6}{\gamma_7}, \\
V' &= \frac{1}{4}\left\{\ln(\gamma_1^4\gamma_6\gamma_7^3) - 8v\right\}, \qquad \mu' = v - \ln\gamma_1, \\
G' &= \ln\gamma_1,
\end{aligned}
\tag{4.12}
$$

where

$$
v = \frac{1}{2}\ln\left(\gamma_2\gamma_4 - \gamma_0^*\gamma_0\right).
$$

The approximate $d = 1$ decimation contained in Eqs. (4.9)-(4.12) can be expressed as a mapping of a Hamiltonian with interaction constants $\mathbf{K} = \{G, t, J, V, \mu, \phi\}$ onto another Hamiltonian with interactions constants

$$
\mathbf{K}' = \mathbf{R}(\mathbf{K}). \tag{4.13}
$$

The Migdal-Kadanoff procedure [18, 19] is used to construct the renormalization-group transformation for $d > 1$. We ignore a subset of the nearest-neighbor inter-

actions in the d-dimensional hypercubic lattice, leaving behind a new d-dimensional hypercubic lattice where each point is connected to its neighbor by two consecutive nearest-neighbor segments of the original lattice. We apply the decimation described above to the middle site between the two consecutive segments, giving the renormalized nearest-neighbor couplings for the points in the new lattice. We compensate for the interactions that are ignored in the original lattice by multiplying by a factor of b^{d-1} the interactions after the decimation, $b = 2$ being the length rescaling factor. Thus, the renormalization-group transformation of Eq. (4.13) generalizes, for $d > 1$, to

$$\mathbf{K}' = b^{d-1}\mathbf{R}(\mathbf{K}). \tag{4.14}$$

4.2.3.2 Renormalization-Group Transformation in the Presence of Magnetic Flux

In order to correctly model the response of the system to an applied magnetic flux, the renormalization-group approximation described in the last two sections needs to be extended. To see this, we first review the formalism for calculating thermodynamic densities from the renormalization-group flows.[20] Conjugate to each interaction K_α of $\mathbf{K} = \{K_\alpha\}$, there is a density M_α (e.g., kinetic energy, electron density),

$$M_\alpha = \frac{1}{Nd}\frac{\partial \ln Z}{\partial K_\alpha}, \tag{4.15}$$

where $Z(\mathbf{K})$ is the partition function. We can relate the densities at the two consecutive points along a renormalization-group trajectory by

$$M_\alpha = b^{-d} M'_\beta T_{\beta\alpha}, \quad \text{where} \qquad T_{\beta\alpha} \equiv \frac{\partial K'_\beta}{\partial K_\alpha}, \tag{4.16}$$

with summation over repeated indices implied. At a fixed point of the renormalization-group transformation, corresponding to a phase transition or a phase sink, the densities $M_\alpha = M'_\alpha \equiv M^*_\alpha$ are the left eigenvector with eigenvalue b^d of the recursion matrix $\mathbf{T}$ evaluated at the fixed point. The densities at the starting point of the trajectory

(the actual physical system) are computed by iterating Eq. (4.16) until a fixed point is effectively reached. If $\mathbf{T}^{(k)}$ is the recursion matrix of the (k)th renormalization-group iteration, then for large k, we can express the densities of the actual system $\mathbf{M}$ as

$$\mathbf{M} \simeq b^{-kd}\mathbf{M}^* \cdot [\mathbf{T}^{(k)}] \cdot [\mathbf{T}^{(k-1)}] \cdot \cdots \cdot [\mathbf{T}^{(1)}]. \tag{4.17}$$

The renormalization-group transformation incorporated in Eqs. (4.9)-(4.14) gives

$$\begin{gathered} \frac{\partial t'}{\partial \phi} = \frac{\partial J'}{\partial \phi} = \frac{\partial V'}{\partial \phi} = \frac{\partial G'}{\partial \phi} = 0\,, \\ \frac{\partial \phi'}{\partial t} = \frac{\partial \phi'}{\partial J} = \frac{\partial \phi'}{\partial V} = \frac{\partial \phi'}{\partial \mu} = 0\,, \quad \frac{\partial \phi'}{\partial \phi} = 2\,, \end{gathered} \tag{4.18}$$

for all ϕ. The 6×6 recursion matrix $\mathbf{T}$ will then have the form

$$\mathbf{T} = \left(\begin{array}{cccc|c} b^d & \frac{\partial G'}{\partial t} & \cdots & \frac{\partial G'}{\partial \mu} & \\ 0 & \frac{\partial t'}{\partial t} & \cdots & \frac{\partial t'}{\partial \mu} & 0 \\ \vdots & \vdots & \ddots & \vdots & \\ 0 & \frac{\partial \mu'}{\partial t} & \cdots & \frac{\partial \mu'}{\partial \mu} & \\ \hline & 0 & & & 2 \end{array}\right) \tag{4.19}$$

at every step in the flow. This leads to

$$M_6^* = 0 \quad \text{and} \quad \frac{\partial}{\partial \phi} \ln Z = M_6 = 0\,, \tag{4.20}$$

for all points of the phase diagram. This superfluid weight of zero for all temperatures and electronic densities is clearly due to the oversimplification in our initial approximation.

The source of the problem is the three-site cluster approximation used in deriving the recursion relations. In modifying the original approximation scheme, we seek to incorporate the effect of the non-commutations extending beyond the three-site cluster. Turning to the matrix elements of $-\beta H(i,j) - \beta H(j,k)$ listed in Table 4.3, we note the terms Δ_i, $i = 1, \ldots, 4$. Using the original Hamiltonian of Eq. (4.3)

restricted to the three-cluster, the matrix elements involving these terms are all zero. However, non-commutativity extending beyond the three-cluster makes, as we see below, these matrix elements non-zero.

We can estimate the magnitude of the matrix elements Δ_i by considering a five-site cluster, described by Hamiltonian $-\beta H(h,i) - \beta H(i,j) - \beta H(j,k) - \beta H(k,l)$, where (h,i,j,k,l) are consecutive sites. In the spirit of Eq. (4.8), we generate effective couplings for the three-cluster by tracing over the degrees of freedom at the outside sites in the five-cluster,

$$\langle u_i\, v_j\, w_k | e^{-\tilde{\beta}\tilde{H}(i,j,k)} | \bar{u}_i\, \bar{v}_j\, \bar{w}_k \rangle = \sum_{t_h, x_l} \langle t_h\, u_i\, v_j\, w_k\, x_l | e^{-\beta H(h,i) - \beta H(i,j) - \beta H(j,k) - \beta H(k,l)} | t_h\, \bar{u}_i\, \bar{v}_j\, \bar{w}_k\, x_l \rangle \ , \quad (4.21)$$

where the subscripted variables refer to single-site states. From the above equation, we can extract the matrix elements of an effective three-cluster Hamiltonian $-\tilde{\beta}\tilde{H}(i,j,k)$. Eq. (4.21) is the contraction of a 243×243 matrix on the right-hand side into a 27×27 matrix on the left. We simplify our task by using the $\{\psi_p\}$ basis on the left, and choosing an appropriate five-site basis to block-diagonalize the 243×243 right-hand matrix.

Since $-\tilde{\beta}\tilde{H}(i,j,k)$ is derived from the decimation of a five-cluster, it will have a more general form than $-\beta H(i,j) - \beta H(j,k)$, and approximately reflect the effect of the three-cluster non-commutations with the external sites. However our approximation scheme must also satisfy an important constraint: the $\phi \to 0$ limit should yield the same renormalization-group transformation used in earlier studies of the tJ model [2, 1]. To achieve this, we modify only a subset of the matrix elements of $-\beta H(i,j) - \beta H(j,k)$, namely those which are zero in the original scheme when $\phi \neq 0$,

but whose corresponding elements in $-\tilde{\beta}\tilde{H}(i,j,k)$ are non-zero:

$$\begin{aligned}
\Delta_1 &= \text{sign}(\phi t)|\langle\psi_3|\tilde{\beta}\tilde{H}(i,j,k)|\psi_6\rangle|, \\
\Delta_2 &= \text{sign}(\phi t)|\langle\psi_{12}|\tilde{\beta}\tilde{H}(i,j,k)|\psi_{17}\rangle|, \\
\Delta_3 &= \text{sign}(\phi t)|\langle\psi_8|\tilde{\beta}\tilde{H}(i,j,k)|\psi_9\rangle|, \\
\Delta_4 &= \text{sign}(\phi t)|\langle\psi_{13}|\tilde{\beta}\tilde{H}(i,j,k)|\psi_{18}\rangle|.
\end{aligned} \tag{4.22}$$

The $\text{sign}(\phi t)$ prefactors guarantee that couplings between the same types of three-cluster states have the same sign. For example, $|\psi_2\rangle$ and $|\psi_3\rangle$ share the same n, p, s, and m_s quantum numbers, as can be seen from Table 4.2. A nonzero ϕ couples $|\psi_2\rangle$ to $|\psi_6\rangle$, a state with the same n, s, and m_s, but opposite parity. From the second block in Table 4.3, the associated matrix element is $\langle\psi_2|\cdots|\psi_6\rangle = i\sqrt{2}t\sin(\phi)$. The Δ_1 elements in that block have an analogous role, coupling $|\psi_3\rangle$ to $|\psi_6\rangle$. The prefactor in the Δ_1 expression of Eq. (4.22) sets the sign of the element $\langle\psi_3|\cdots|\psi_6\rangle = i\Delta_1$ to equal that of $\langle\psi_2|\cdots|\psi_6\rangle$. Since our calculations are all done for small ϕ, $\text{sign}(\sin\phi) = \text{sign}(\phi)$. Similar reasoning applies to the prefactors of the other Δ_i elements.

Through Eq. (4.21), the Δ_i are functions of the interactions strengths in the unrenormalized Hamiltonian, $\Delta_i = \Delta_i(t, J, V, \mu, \phi)$. They scale like ϕ for small ϕ, and duly vanish in the limit $\phi \to 0$. As will be explained below, finding the superfluid weight involves calculating a thermodynamic density in the $\phi \to 0$ limit, so we shall be working in the regime where the Δ_i are vanishingly small. The result of the extended calculation, taking into account the quantum mechanical backflow into the three-cluster, is that Eqs. (4.18) no longer hold, $\partial \ln Z/\partial\phi \neq 0$ in general, and we obtain interesting nontrivial results for n_s/m^*.

4.2.3.3 Calculation of the Superfluid Weight

The superfluid weight of Eq. (4.4) is expressed as a derivative of the total free energy $F = F(n, T, \phi)$, where $n = \langle n_i\rangle$ is the electron density. In terms of the conjugate current

$$j(n, T, \phi) = \frac{1}{Nd}\left.\frac{\partial F}{\partial\phi}\right|_{n,T}, \tag{4.23}$$

Eq. (4.4) becomes

$$\frac{n_s}{m^*}(n,T) = \lim_{\phi\to 0} \left.\frac{\partial j}{\partial \phi}\right|_{n,T} . \tag{4.24}$$

In terms of the grand potential $\Omega(\mu,T,\phi) = -(1/\beta)\ln Z$,

$$j(\mu,T,\phi) = \frac{1}{Nd} \left.\frac{\partial \Omega}{\partial \phi}\right|_{\mu,T} , \tag{4.25}$$

and

$$n(\mu,T,\phi) = -\frac{\beta}{2Nd} \left.\frac{\partial \Omega}{\partial \mu}\right|_{T,\phi} . \tag{4.26}$$

Relating the partial derivatives of j with respect to ϕ through

$$\left.\frac{\partial j}{\partial \phi}\right|_{\mu,T} = \left.\frac{\partial j}{\partial n}\right|_{\phi,T} \left.\frac{\partial n}{\partial \phi}\right|_{\mu,T} + \left.\frac{\partial j}{\partial \phi}\right|_{n,T} , \tag{4.27}$$

and using the Maxwell relation $\left.\frac{\partial n}{\partial \phi}\right|_{\mu,T} = -\frac{\beta}{2}\left.\frac{\partial j}{\partial \mu}\right|_{\phi,T}$,

$$\left.\frac{\partial j}{\partial \phi}\right|_{\mu,T} = -\frac{\beta}{2}\left.\frac{\partial j}{\partial n}\right|_{\phi,T} \left.\frac{\partial j}{\partial \mu}\right|_{\phi,T} + \left.\frac{\partial j}{\partial \phi}\right|_{n,T} . \tag{4.28}$$

The current j is zero when $\phi = 0$, so that the first term on the right-hand side above is also zero in the limit $\phi \to 0$, and we find that $\lim_{\phi\to 0}\left.\frac{\partial j}{\partial \phi}\right|_{\mu,T} = \lim_{\phi\to 0}\left.\frac{\partial j}{\partial \phi}\right|_{n,T}$. Thus Eq. (4.24) can be equivalently written as

$$\frac{n_s}{m^*}(\mu,T) = \lim_{\phi\to 0}\left.\frac{\partial j}{\partial \phi}\right|_{\mu,T} = \frac{1}{Nd}\lim_{\phi\to 0}\left.\frac{\partial^2 \Omega}{\partial \phi^2}\right|_{\mu,T} = -\frac{1}{\beta Nd}\lim_{\phi\to 0}\left.\frac{\partial^2 \ln Z}{\partial \phi^2}\right|_{\mu,T} . \tag{4.29}$$

This is the form we shall use when calculating the superfluid weights.

4.2.4 Results

4.2.4.1 Global Phase Diagram for $d = 3$

Each sink, or completely stable fixed point of the renormalization-group flows, corresponds to a thermodynamic phase, and we find the global phase diagram by determining the basin of attraction for every sink [21]. Flows that start at the boundaries

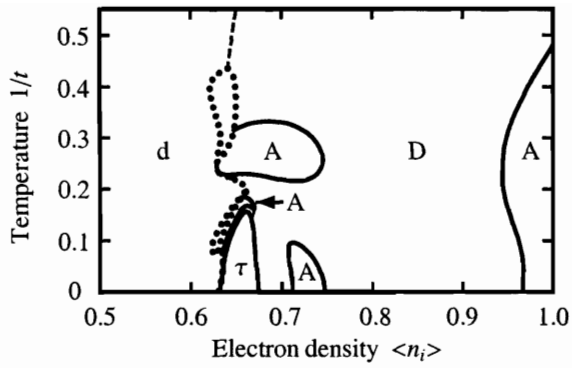

Phase sink	Expectation values			
	$\sum_\sigma \langle c^\dagger_{i\sigma} c_{j\sigma} + c^\dagger_{j\sigma} c_{i\sigma} \rangle$	$\langle n_i \rangle$	$\langle \mathbf{S}_i \cdot \mathbf{S}_j \rangle$	$\langle n_i n_j \rangle$
d	0	0	0	0
D	0	1	0	1
A	0	1	$\frac{1}{4}$	1
τ	$-\frac{2}{3}$	$\frac{2}{3}$	$-\frac{1}{4}$	$\frac{1}{3}$

Table 4.5: Expectation values at the phase-sink fixed points.

between phases have their own fixed points, distinguished from phase sinks by having at least one unstable direction. Analysis of these fixed points determines whether the phase transition is first- or second-order. As explained above, the thermodynamic densities, which are the expectation values of operators occurring in the Hamiltonian, can also be calculated from the renormalization-group flows. In particular, we determine the single-site electron density $\langle n_i \rangle$. For the coupling $J/t = 0.444$ and $\phi = 0$, the phase diagram in terms of $\langle n_i \rangle$ and temperature $1/t$ is shown in Fig. 4-1 [2, 1].

The nature of the various phases is epitomized by the thermodynamic densities $\mathbf{M}^*$ calculated at each phase sink (Table 4.5), which underpin the calculation of densities throughout their respective phases (Eq. (4.17)). We summarize the phase properties below (for a more detailed discussion, see [2, 1]):

Dilute disordered phase (d): The electron density $\langle n_i \rangle = 0$ at the sink and, as a result, the $\langle n_i \rangle$ calculated inside this phase are low.

Dense disordered phase (D): The electron density $\langle n_i \rangle = 1$ at the sink and, as a result, the $\langle n_i \rangle$ calculated inside this phase are close to 1.

Antiferromagnetic phase (A): The electron density $\langle n_i \rangle = 1$ at the sink, so that this phase is also densely filled. The nearest-neighbor spin-spin correlation $\langle \mathbf{S}_i \cdot \mathbf{S}_j \rangle = 1/4$ at the sink. Two spins that are nearest neighbors at the sink are distant members of the same sublattice in the original cubic lattice. The non-zero value of the correlation function at the sink leads to $\langle \mathbf{S}_i \cdot \mathbf{S}_j \rangle < 0$ for nearest-neighbor sites of the original, unrenormalized system.

τ phase: This is a novel phase, characterized by partial-filling at the phase sink, $\langle n_i \rangle = 2/3$. It is the only phase where the electron hopping strength t does not renormalize to zero after repeated rescalings; instead, $t \to \infty$ at the sink. As a result, the expectation value of the electron hopping operator at the sink is non-zero, $\sum_\sigma \langle c^\dagger_{i\sigma} c_{j\sigma} + c^\dagger_{j\sigma} c_{i\sigma} \rangle = -2/3$. This property makes it a possible tJ model analogue to the superconducting phase in high-T_c materials. The superfluid weight and thermodynamic results discussed below certainly support this idea.

In the limit $\langle n_i \rangle = 1$, the system exhibits antiferromagnetic order at low temperatures, as expected from the spin-spin coupling in the Hamiltonian. Upon hole doping, there is a competition between the A and D phases, which respectively minimize antiferromagnetic potential energy and hole kinetic energy. Note the extent of the A phase near $\langle n_i \rangle = 1$, which persists only up to a small amount of hole doping $\delta = 1 - \langle n_i \rangle \lesssim 0.05$. This feature is directly reminiscent of the antiferromagnetic phase in certain high-T_c materials, for example $La_{2-x}Sr_xCuO_4$ [22]. At intermediate dopings $\delta \approx 0.32 - 0.37$, we have a low-temperature τ phase, surrounded by islands of antiferromagnetism. (When the hopping strength t increases under rescaling, this also lowers the free energy of antiferromagnetically long-range ordered states, which leads to these islands of A in the vicinity of the τ phase.[1]) At hole dopings $\delta \gtrsim 0.37$, there is a transition to a dilute disordered phase, with a narrow region of first-order coexistence at lower temperatures.

4.2.4.2 Superfluid Weight and Kinetic Energy

Using the method of calculating thermodynamic densities described above, we determine $(1/Nd)\partial \ln Z/\partial\phi$ at small ϕ. Taking the numerical derivative of this quantity at $\phi = 0$, we find n_s/m^* through Eq. (4.29). The superfluid weight is plotted as a function of electron density in Fig. 4-2, along four different constant temperature cross-sections of the phase diagram. For comparison, we also show in the same figure the calculated average kinetic energy per bond $\langle K \rangle$, where $K = -\sum_\sigma \left(c^\dagger_{i\sigma} c_{j\sigma} + c^\dagger_{j\sigma} c_{i\sigma} \right)$. $\langle K \rangle$ and the total weight of $\sigma_1(\omega, T)$, the real part of the optical conductivity, are related by the sum rule [23],

$$\int_0^\infty d\omega\, \sigma_1(\omega, T) = \frac{\pi e^2}{2} \langle K \rangle \,. \tag{4.30}$$

In comparing the properties of the tJ model to those of high-T_c materials, we keep in mind that the tJ Hamiltonian describes a one-band model, so cannot account for interband transitions. For real materials, the full conductivity sum rule has the form

$$\int_0^\infty d\omega\, \sigma_1(\omega, T) = \frac{\pi e^2 n}{2m} \,, \tag{4.31}$$

where n is the total density of electrons and m is the free electron mass. The right-hand side of Eq. (4.31) is independent of electron-electron interactions, in contrast to the right-hand side of Eq. (4.30), where $\langle K \rangle$ will vary with the interaction strengths in the Hamiltonian. The optical conductivity of actual materials incorporates both transitions within the conduction band and those to higher bands, while the tJ model contains only the conduction band. We can look at Eq. (4.30) as a partial sum rule [24, 23], which reflects the spectral weight of the free carriers in the conduction band.

The experimental quantity we are interested in modeling is the effective density of free carriers, which in actual materials is calculated from the low-frequency spectral weight [25],

$$n_{\text{free}}(T) = \frac{2m}{\pi e^2} \int_0^{\omega_0} d\omega\, \sigma_1(\omega, T) \,. \tag{4.32}$$

For high T_c materials, the cutoff frequency is typically chosen around $\hbar\omega_0 \approx 1$ eV so as to include only intraband transitions. For comparison with the tJ model, we identify the right-hand side of Eq. (4.30) with

$$\frac{\pi e^2}{2}\langle K\rangle = \frac{\pi e^2 n_{\text{free}}(T)}{2m}\,. \tag{4.33}$$

The superfluid weight satisfies the inequality [26]

$$\frac{n_s}{m^*} \leq \langle K\rangle = \frac{n_{\text{free}}}{m}\,, \tag{4.34}$$

which is obeyed in our results in Fig. 4-2.

The superfluid weight graphs at the sampled temperatures show a clear bipartite structure, with a peak at low $\langle n_i\rangle$, and another peak at high $\langle n_i\rangle$ (which develops into two closely spaced peaks at lower temperatures). In between these is a region of low superfluid weight, with a minimum near $\langle n_i\rangle \simeq 0.385$, approximately independent of temperature. Looking at the nearest-neighbor density-density correlation $\langle n_i n_j\rangle$ as shown in Fig. 4-3, we see that $\langle n_i\rangle \simeq 0.385$ is also the electron density separating two different regimes of the system: an extremely dilute regime, where $\langle n_i n_j\rangle \simeq 0$, and a partially-to-densely filled regime, where $\langle n_i n_j\rangle > 0$. It is therefore useful to discuss the superfluid weight and kinetic energy results in terms of these two regimes.

Extremely dilute regime, $\langle n_i\rangle \lesssim 0.385$

The system in this regime is a dilute gas of electrons. For low $\langle n_i\rangle$, the kinetic energy per bond $\langle K\rangle \simeq 2\langle n_i\rangle$, which follows if the density of free carriers is just the density of electrons, $n_{\text{free}} = \langle n_i\rangle$, and the mass of the carriers $m = 1/2$. The interaction terms in the tJ Hamiltonian create an attractive potential of strength $-\tilde{J}$ between electrons in singlet-states on neighboring sites. For a coupling $J/t = 0.444$, this attraction is too weak to form two-body bound states, but since we are in three dimensions, even a weak attractive potential is sufficient for the formation of an electron superfluid at low temperatures [27, 28]. In fact, we see a peak in n_s/m^*

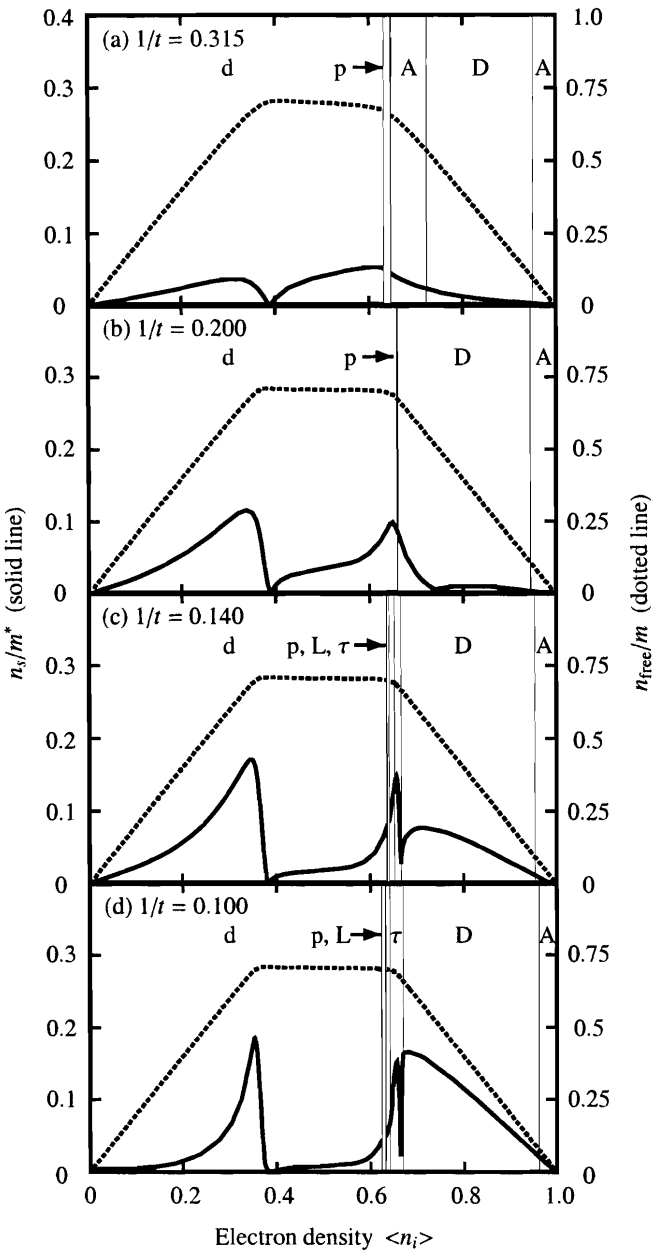

Figure 4-2: The superfluid weight n_s/m^* (solid line) and free carrier density n_{free}/m (dotted line) as a function of electron density at four different values of temperature $1/t$. The corresponding phases are indicated above the plots, and the location of phase boundaries marked by thin vertical lines. The symbol p refers to a region of forbidden densities due to the discontinuity at a first-order transition. The symbol L refers to a "lamellar" region where narrow slivers of the A and D phases alternate.

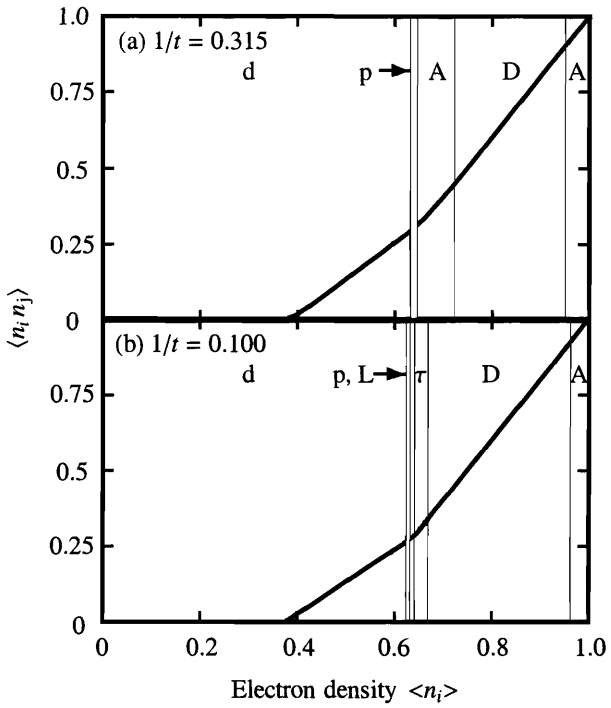

Figure 4-3: The nearest-neighbor density-density correlation $\langle n_i n_j \rangle$ as a function of electron density at two different values of temperature $1/t$. The corresponding phases are indicated above the plots, and the location of phase boundaries marked by thin vertical lines. The symbol p refers to a region of forbidden densities due to the discontinuity at a first-order transition. The symbol L refers to a "lamellar" region where narrow slivers of the A and D phases alternate.

develop around $\langle n_i \rangle \approx 0.3$–$0.35$, and this peak grows as the temperature is lowered from $1/t = 0.315$ to 0.1. For low $\langle n_i \rangle$, the superfluid weight increases with electron density and $\langle K \rangle$. The location of the peak in n_s/m^* is just before $\langle K \rangle$ comes to its maximum and levels off. As the density of free carriers saturates near $\langle n_i \rangle \simeq 0.385$, there is a sharp drop in n_s/m^*, and $\langle n_i n_j \rangle$ begins to increase from zero. At this density the physical characteristics of the system abruptly change, without however inducing a phase transition.

Partially-to-densely filled regime, $\langle n_i \rangle \gtrsim 0.385$

For intermediate densities $\langle n_i \rangle \approx 0.385$–$0.63$, the kinetic energy $\langle K \rangle$ remains approximately constant. Near $\langle n_i \rangle \simeq 0.63$, there is a phase transition to a densely filled phase (either D or A). We go from a physical picture where the carriers are electrons

in a mostly empty background to one where the carriers are holes moving in a mostly filled background. These holes condense into a superfluid at lower temperatures, and the peak in n_s/m^* occurs in the vicinity of the dilute-dense narrow first-order phase transition. For $1/t \lesssim 0.16$, the maximum superfluid weight is reached inside the τ phase. In the densely filled regime, $\langle n_i \rangle \gtrsim 0.63$, the kinetic energy goes linearly as $\langle K \rangle \simeq 2(1 - \langle n_i \rangle) = 2\delta$, as expected if the free carriers are holes.

For hole-doped high-T_c materials, the density of free carriers increases with δ until the doping level optimal for superconductivity is reached, and remains approximately constant in the overdoped regime.[8] The superfluid weight, in contrast, peaks near optimal doping and sharply decreases with overdoping. These trends are reproduced in our numerical results, identifying, from our calculated n_s/m^* maxima, the optimal doping for the tJ model as $\delta \approx 0.32$–0.37, the range of densities where the τ phase occurs. Note that optimal doping for high-T_c materials is lower than this, typically around $\delta = 0.15$, and the closely spaced double-peak structure of n_s/m^* at low temperatures near optimal doping is not observed. On the other hand, our approximation for the $d = 3$ tJ model is closer to experiment in this respect than earlier numerical studies of the tJ model, which focused mostly on finite-cluster techniques applied to the $d = 2$ system [29]. In these earlier studies optimal doping is identified near $\langle n_i \rangle = 0.5$ on the basis of d-wave pairing correlations and the peak in the superfluid weight [11]. Also in these earlier studies, the kinetic energy has a maximum at $\langle n_i \rangle = 0.5$, but, unlike experiments, does not saturate with overdoping [30].

To complete the description of the superfluid weight in this regime, in Fig. 4-4 we show n_s/m^* as a function of temperature $1/t$ at various electron densities $\langle n_i \rangle$. For systems with small to optimal hole dopings, shown in Fig. 4-4(a), there is a clear onset temperature near $1/t \simeq 0.2$ below which the superfluid weight rises rapidly, until it levels off near zero temperature. This behavior is in good comparison with experimental results with $YBa_2Cu_3O_{6+x}$ [31]. As we move past optimal doping to the overdoped systems of Fig. 4-4(b), we see a marked change in behavior, with the low temperature n_s/m^* suppressed.

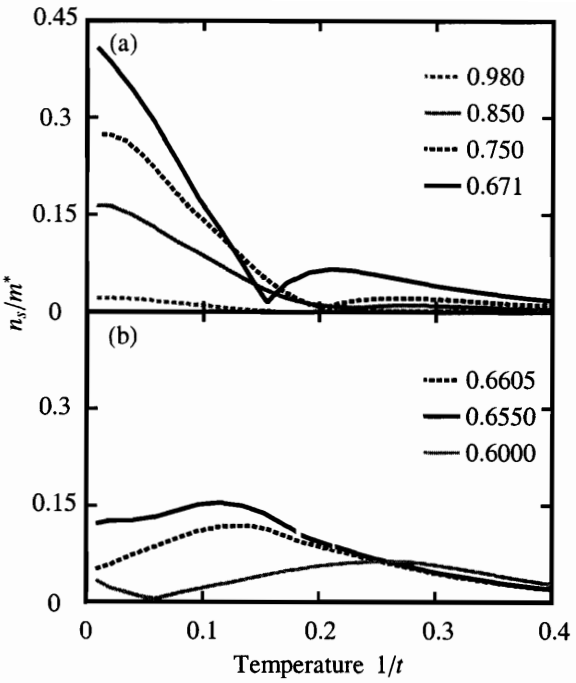

Figure 4-4: The superfluid weight n_s/m^* as a function of temperature $1/t$ for various electron densities $\langle n_i \rangle$ indicated in the legends. Fig. 4-4(a) shows results in the range of small to optimal hole doping, while Fig. 4-4(b) shows results for hole overdoped systems.

4.2.4.3 Specific Heat

Since the superfluid weight peaks inside the τ phase at low temperatures, it is interesting to check whether the τ region has any other general characteristics of a superconducting phase. We have added a magnetic field spin coupling term to the tJ Hamiltonian and have shown that the τ phase continues to exist when $H \neq 0$, up to a critical field $H_c(T)$, which decreases with increasing temperature and goes to zero at the temperature of the τ phase boundary. In our present study, we look at the spectrum of excitations of the system through the specific heat per bond

$$C(n,T) = \left. \frac{\partial \langle H(i,j) \rangle}{\partial T} \right|_n , \tag{4.35}$$

calculated for $\phi = 0$. If the τ phase corresponds to the superconducting phase in real materials, we should see evidence of a gap in the excitation spectrum.

The results for C as a function of temperature $1/t$ are plotted in Fig. 4-5 for a

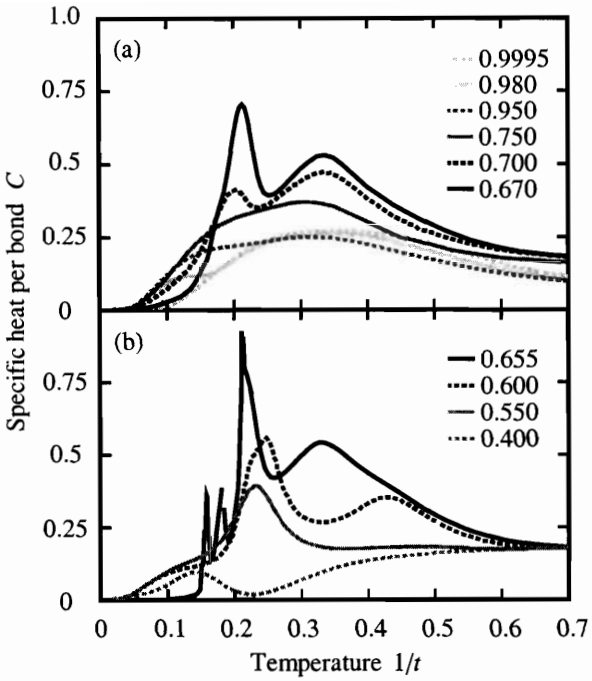

Figure 4-5: The specific heat per bond C, in units of k_B, as a function of temperature $1/t$ for various electron densities $\langle n_i \rangle$ (indicated in the legends). Fig. 4-5(a) shows results in the range of small to optimal hole doping, while Fig. 4-5(b) shows results for hole overdoped systems. The small discontinuities in the plot for $\langle n_i \rangle = 0.655$ reflect temperature ranges where that particular density does not appear because of the narrow first-order phase transition.

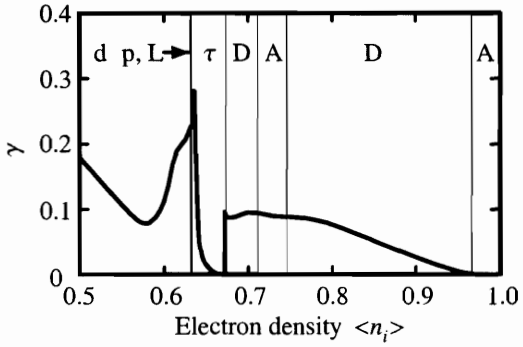

Figure 4-6: The specific heat coefficient $\gamma = C/T$, in units of k_B^2, as a function of electron density $\langle n_i \rangle$ at temperature $1/t = 0.015$. The corresponding phases are indicated above the plot, and the location of phase boundaries marked by thin vertical lines. The symbol p refers to a region of forbidden densities due to the narrow discontinuity at a first-order transition. The symbol L refers to a "lamellar" region where narrow slivers of the A and D phases alternate.

series of different electronic densities $\langle n_i \rangle$. Starting at $\langle n_i \rangle = 0.9995$, the smallest hole doping shown in Fig. 4-5(a), we observe a broad peak around $1/t \simeq 0.33$, corresponding to $k_B T \simeq 0.75\tilde{J}$. We can identify this peak with the thermal excitation of the spin degrees of freedom. As we dope the system with holes, the weight under the curve at lower temperatures increases due to excitation of charge degrees of freedom. As we approach optimal doping, a second peak develops around $1/t \simeq 0.2$. Note that this approximately coincides with the onset temperature below which we see a dramatic increase in n_s/m^* in Fig. 4-4. The spin-excitation peak is also enhanced for $\langle n_i \rangle \approx 0.65$–$0.75$, which is related to the appearance of an antiferromagnetic island around $1/t \simeq 0.3$ in that density range.

The peak at $1/t \simeq 0.2$ grows rapidly near optimal doping, reminiscent of the specific heat anomaly of high-T_c materials [32, 33]. For $\langle n_i \rangle = 0.655$ we see the appearance of two subsidiary peaks below the main one at $1/t \simeq 0.2$. These smaller peaks may be related to the complicated lamellar structure of A and D regions above the τ phase boundary. For temperatures $1/t \lesssim 0.16$, inside the τ phase, the specific heat is strongly suppressed, reflecting the opening up of a gap in the excitation spectrum. We can see this gap more directly by looking at the low-temperature limit of the specific heat. Quasiparticle excitations contribute a linear term to the specific heat $C \simeq \gamma T$ for small T. In Fig. 4-6, we plot $\gamma = C/T$ as a function of electron density at a low temperature, $1/t = 0.015$. The specific heat coefficient $\gamma \simeq 0$ in the A phase near half-filling, but then grows with increasing hole doping. At the onset of the τ phase a gap opens in the quasiparticle spectrum, γ falls sharply, and stays small until it rises again near the phase boundary. Qualitatively, this doping-dependence of the low-temperature specific heat coefficient agrees well with the experimental results for high-T_c superconducting materials [32].

4.2.5 Conclusions

We have developed a position-space renormalization-group approximation to study the superfluid weight of the three-dimensional tJ model. Our results indicate that

optimal hole doping for this system occurs in the density range of the τ phase, $\langle n_i \rangle \approx$ 0.63–0.68, where n_s/m^* reaches a local maximum. While the superfluid weight drops off sharply in the overdoped region, the density of free carriers, proportional to the kinetic energy, remains approximately constant, as seen experimentally in high-T_c materials. From calculations of the specific heat coefficient γ, we see clear evidence of a gap in the excitation spectrum for the τ phase. Earlier renormalization group studies [2, 1] had suspected that the τ phase corresponds to the superconducting phase of high-T_c materials, and this idea was reinforced when an analogous phase was discovered in the Hubbard model [12, 13]. Our present results justify this suspicion.

References

[1] A. Falicov and A.N. Berker, Phys. Rev. B **51**, 12458 (1995).

[2] A. Falicov and A.N. Berker, Turk. J. Phys. **19**, 127 (1995).

[3] Y.J. Uemura, G.M. Luke, B.J. Sternlieb, J.H. Brewer, J.F. Carolan, W.N. Hardy, R. Kadono, J.R. Kempton, R.F. Kiefl, S.R. Kreitzman, P. Mulhern, T.M. Riseman, D.L. Williams, B.X. Yang, S. Uchida, H. Takagi, J. Gopalakrishnan, A.W. Sleight, M.A. Subramanian, C.L. Chien, M.Z. Cieplak, G. Xiao, V.Y. Lee, B.W. Statt, C.E. Stronach, W. J. Kossler, and X.H. Yu, Phys. Rev. Lett. **62**, 2317 (1989).

[4] C. Bernhard, C. Niedermayer, U. Binninger, A. Hofer, C. Wenger, J.L. Tallon, G.V.M. Williams, E.J. Ansaldo, J.I. Budnick, C.E. Stronach, D.R. Noakes, and M.A. Blankson-Mills, Phys. Rev. B **52**, 10488 (1995).

[5] C. Niedermayer, C. Bernhard, U. Binninger, H. Glückler, J.L. Tallon, E.J. Ansaldo, and J.I. Budnick, Phys. Rev. Lett. **71**, 1764 (1993).

[6] J.P. Locquet, Y. Jaccard, A. Cretton, E.J. Williams, F. Arrouy, E. Mächler, T. Schneider, Ø. Fischer, and P. Martinoli, Phys. Rev. B **54**, 7481 (1996).

[7] C. Bernhard, J.L. Tallon, T. Blasius, A. Golnik, and C. Niedermayer, Phys. Rev. Lett. **86**, 1614 (2001).

[8] A.V. Puchkov, P. Fournier, T. Timusk, and N.N. Kolesnikov, Phys. Rev. Lett. **77**, 1853 (1996).

[9] S.-S. Lee and S.-H.S. Salk, Phys. Rev. B **64**, 052501 (2001).

[10] S.-S. Lee and S.-H.S. Salk, cond-mat/0212582.

[11] E. Dagotto and J. Riera, Phys. Rev. Lett. **70**, 682 (1993).

[12] G. Migliorini and A.N. Berker, Eur. Phys. J. B **17**, 3 (2000).

[13] M. Hinczewski and A.N. Berker, cond-mat/0503226.

[14] M.E. Fisher, M.N. Barber, and D. Jasnow, Phys. Rev. A **8**, 1111 (1973).

[15] D.J. Scalapino, S.R. White, and S. Zhang, Phys. Rev. B **47**, 7995 (1993).

[16] M. Suzuki and H. Takano, Phys. Lett. A **69**, 426 (1979).

[17] H. Takano and M. Suzuki, J. Stat. Phys. **26**, 635 (1981).

[18] A.A. Migdal, Zh. Eksp. Teor. Fiz. **69**, 1457 (1975) [Sov. Phys. JETP **42**, 743 (1976)].

[19] L.P. Kadanoff, Ann. Phys. (N.Y.) **100**, 359 (1976).

[20] A.N. Berker, S. Ostlund, and F.A. Putnam, Phys. Rev. B **17**, 3650 (1978).

[21] A.N. Berker and M. Wortis, Phys. Rev. B **14**, 4946 (1976).

[22] M. Imada, A. Fujimori, and Y. Tokura, Rev. Mod. Phys. **70**, 1039 (1998).

[23] L. Tan and J. Callaway, Phys. Rev. B **46**, 5499 (1992).

[24] D. Baeriswyl, C. Gros, and T.M. Rice, Phys. Rev. B **35**, 8391 (1987).

[25] J. Orenstein, G.A. Thomas, A.J. Millis, S.L. Cooper, D.H. Rapkine, T. Timusk, L.F. Schneemeyer, and J.V. Waszczak, Phys. Rev. B **42**, 6342 (1990).

[26] A. Paramekanti, N. Trivedi, and M. Randeria, Phys. Rev. B **57**, 11639 (1998).

[27] V.J. Emery, S.A. Kivelson, and H.Q. Lin, Phys. Rev. Lett. **64**, 475 (1990).

[28] M. Randeria, J.-M. Duan, and L.-Y. Shieh, Phys. Rev. Lett. **62**, 981 (1989).

[29] E. Dagotto, Rev. Mod. Phys. **66**, 763 (1994).

[30] E. Dagotto, A. Moreo, F. Ortolani, D. Poilblanc, and J. Riera, Phys. Rev. B **45**, 10741 (1992).

[31] Y. Zuev, M.S. Kim, and T.R. Lemberger, cond-mat/0410135.

[32] J.W. Loram, K.A. Mirza, J.R. Cooper, and W.Y. Liang, Phys. Rev. Lett. **71**, 1740 (1993).

[33] J.W. Loram, K.A. Mirza, J.M. Wade, J.R. Cooper, and W.Y. Liang, Physica C **235-240**, 134 (1994).

Chapter 5

The Anisotropic tJ Model

5.1 Introduction

A natural question arises from the studies of the $d = 3$ Hubbard and tJ models in the previous chapters: how relevant are these phase diagrams to high-T_c materials, where the interlayer couplings between the CuO_2 planes are weak, and the physics is believed to have a largely two-dimensional character? At first glance, the situation does not look promising, because the isotropic $d = 2$ Migdal-Kadanoff approximation does not yield any interesting phase structure in the tJ or Hubbard models: neither the τ nor the antiferromagnetic phases appear. For the latter this is the expected result, since a finite Néel temperature requires a nonzero interlayer coupling. As for the τ phase, does its absence in $d = 2$ mean it is a strictly three-dimensional phenomenon?

We seek out answers to these questions in the anisotropic $d = 3$ tJ model, which has distinct in-plane and out-of-plane interaction constants. By observing this system as the interlayer coupling is weakened, we can see if the τ phase persists down to the quasi-two-dimensional regime. Since we cannot directly use the isotropic Migdal-Kadanoff procedure for the anisotropic model, we have to develop a new renormalization-group transformation. At the same time we know that the anisotropic model reduces to an isotropic $d = 3$ system when all the couplings are the same, or to a collection of independent $d = 2$ systems when the out-of-plane coupling is zero, or independent $d = 1$ systems when the in-plane coupling is zero. In all these limiting

cases, our renormalization-group transformation ought to reproduce the result of the isotropic Migdal-Kadanoff method.

We can look at this problem in another way, by exploiting the one-to-one relationship between Migdal-Kadanoff renormalization-group transformations and hierarchical lattices. We know that the Migdal-Kadanoff recursion relations for $d = 1$, 2, and 3 can each be implemented exactly on a different hierarchical lattice. Extending this logic, the recursion relations for the anisotropic model correspond to a nonuniform hierarchical lattice—one with two different types of bonds, representing the in-plane and out-of-plane couplings. This nonuniform lattice must reduce to one of the Migdal-Kadanoff hierarchical lattices in the case where one of the bond types is zero, or both are equal. In the following section we show how to construct a nonuniform hierarchical lattice satisfying this constraint, and thus derive an approximate renormalization-group transformation for the anisotropic tJ model.

5.2 $d = 3$ Anisotropic and $d = 2$ tJ Models: Phase Diagrams, Thermodynamic Properties, and Chemical Potential Shift

Michael Hinczewski and A. Nihat Berker
Department of Physics, Istanbul Technical University, Maslak 34469, Istanbul, Turkey,
Department of Physics, Massachusetts Institute of Technology, Cambridge, Massachusetts 02139, U.S.A.,
Feza Gürsey Research Institute, TÜBITAK - Bosphorus University, Çengelköy 81220, Istanbul, Turkey

Abstract

The anisotropic $d = 3$ tJ model is studied by renormalization-group theory, yielding the evolution of the system as interplane coupling is varied from the isotropic three-dimensional to quasi-two-dimensional regimes. Finite-temperature phase diagrams, chemical potential shifts, and in-plane and interplane kinetic energies and antiferromagnetic correlations are calculated for the entire range of electron densities. We find that the novel τ phase, seen in earlier studies of the isotropic $d = 3$ tJ model, and potentially corresponding to the superconducting phase in high-T_c materials, persists even for strong anisotropy. While the τ phase appears at low temperatures at $30 - 35\%$ hole doping away from $\langle n_i \rangle = 1$, at smaller hole dopings we see a complex lamellar structure of antiferromagnetic and disordered regions, with a suppressed chemical potential shift, a possible marker of incommensurate ordering in the form of microscopic stripes. An investigation of the renormalization-group flows for the isotropic two-dimensional tJ model also shows a pre-signature of the τ phase, which appears with finite transition temperatures upon addition of the smallest interplane coupling.

PACS numbers: 74.72.-h, 71.10.Fd, 05.30.Fk, 74.25.Dw

arXiv: cond-mat/0504741

5.2.1 Introduction

The anisotropic nature of high-T_c materials, where groups of one or more CuO_2 planes are weakly coupled through block layers that act as charge reservoirs, has led to intense theoretical focus on two-dimensional models of electron conduction.[1] However, a full understanding of the cuprates will require taking into account physics along the third dimension. Crucial aspects of the phase diagram, like the finite value of the Néel temperature, depend on interplanar coupling [2], and going beyond two dimensions is also necessary to explain the behavior of T_c as the number of CuO_2 layers per unit cell is increased [3].

As a simplified description of strongly correlated electrons in an anisotropic system, we look at the tJ model on a cubic lattice with uniform interaction strengths in the xy planes, and a weaker interaction in the z direction. To obtain a finite-temperature phase diagram for the entire range of electron densities, we extend to anisotropic systems the renormalization-group approach that has been applied successfully in earlier studies of both tJ and Hubbard models as isotropic $d = 3$ systems.[5, 4, 6, 7] For the $d = 3$ isotropic tJ model, this approach has yielded an interesting phase diagram with antiferromagnetism near $\langle n_i \rangle = 1$ and a new low-temperature "τ" phase for 30-35% hole doping. Within this τ phase, the magnitude of the electron hopping strength in the Hamiltonian tends to infinity as the system is repeatedly rescaled, making it a possible analog of the superconducting phase in high-T_c materials.[4, 5] In fact, the calculated superfluid weight shows a marked peak in the τ phase, and both the temperature profile of the superfluid weight and the density of free carriers with hole doping is reminiscent of experimental results in cuprates.[7] Given these potential links with cuprate physics, the next logical step is to ask whether the τ phase is present in the strongly anisotropic regime, which is the one directly relevant to high-temperature superconductivity.

The extension of the position-space renormalization-group method to spatial anisotropy has recently been demonstrated with $d = 3$ Ising, XY magnetic and percolation systems.[8] We apply a similar anisotropic generalization to the electronic conduction

model and find the evolution of the phase diagram from the isotropic $d = 3$ to the quasi $d = 2$ cases. While transition temperatures become lower, the τ phase does continue to exist even for very weak interplanar coupling. The density range of the τ phase remains stable as anisotropy is increased, while for 5-30% hole doping an intricate structure of antiferromagnetic and disordered phases develops, a possible indicator of underlying incommensurate order, manifested through the formation of microscopic stripes. Consistent with this interpretation, our system in this density range shows a characteristic "pinning" of the chemical potential with hole doping.

Lastly, we turn from the $d = 3$ anisotropic case to the $d = 2$ tJ model, where earlier studies [5, 4] have found no τ phase (but have elucidated the occurrence/non-occurrence of phase separation). Nevertheless, by looking at the low-temperature behavior of the renormalization-group flows, we find a compelling pre-signature of the τ phase even in $d = 2$, at exactly the density range where the τ phase appears when the slightest interplanar coupling is added to the system.

5.2.2 Anisotropic tJ Hamiltonian

We consider the tJ Hamiltonian on a cubic lattice with different interaction strenghts for nearest neighbors lying in the xy plane or along the z direction (respectively denoted by $\langle ij\rangle_{xy}$ and $\langle ij\rangle_z$):

$$H = P\left[\tilde{t}_{xy}\sum_{\langle ij\rangle_{xy},\sigma}\left(c^\dagger_{i\sigma}c_{j\sigma}+c^\dagger_{j\sigma}c_{i\sigma}\right)+\tilde{t}_z\sum_{\langle ij\rangle_z,\sigma}\left(c^\dagger_{i\sigma}c_{j\sigma}+c^\dagger_{j\sigma}c_{i\sigma}\right)\right.$$
$$\left.+\tilde{J}_{xy}\sum_{\langle ij\rangle_{xy}}\mathbf{S}_i\cdot\mathbf{S}_j+\tilde{J}_z\sum_{\langle ij\rangle_z}\mathbf{S}_i\cdot\mathbf{S}_j-\tilde{V}_{xy}\sum_{\langle ij\rangle_{xy}}n_in_j-\tilde{V}_z\sum_{\langle ij\rangle_z}n_in_j-\tilde{\mu}\sum_i n_i\right]P. \tag{5.1}$$

Here $c^\dagger_{i\sigma}$ and $c_{i\sigma}$ are creation and annihilation operators, obeying anticommutation rules, for an electron with spin $\sigma = \uparrow$ or $\downarrow$ at lattice site i, $n_{i\sigma} = c^\dagger_{i\sigma}c_{i\sigma}$, $n_i = n_{i\uparrow} + n_{i\downarrow}$ are the number operators, and $\mathbf{S}_i = \frac{1}{2}\sum_{\sigma\sigma'} c^\dagger_{i\sigma}\mathbf{s}_{\sigma\sigma'}c_{i\sigma'}$ is the single-site spin operator, with $\mathbf{s}$ the vector of Pauli spin matrices. The entire Hamiltonian is sandwiched

between projection operators $P = \prod_i (1 - n_{i\downarrow} n_{i\uparrow})$, which project out states with doubly-occupied sites. The standard, isotropic tJ Hamiltonian obtains when $\tilde{t}_{xy} = \tilde{t}_z$, $\tilde{J}_{xy} = \tilde{J}_z$, $\tilde{V}_{xy} = \tilde{V}_z$, and $\tilde{V}_{xy}/\tilde{J}_{xy} = \tilde{V}_z/\tilde{J}_z = 1/4$.

For simplicity, we rewrite Eq. (5.1) using dimensionless interaction constants, and rearrange the $\tilde{\mu}$ chemical potential term to group the Hamiltonian into summations over the xy and z bonds:

$$\begin{aligned} -\beta H = & \sum_{\langle ij \rangle_{xy}} P \Big[-t_{xy} \sum_{\sigma} \left(c^{\dagger}_{i\sigma} c_{j\sigma} + c^{\dagger}_{j\sigma} c_{i\sigma} \right) - J_{xy} \mathbf{S}_i \cdot \mathbf{S}_j + V_{xy} n_i n_j + \mu (n_i + n_j) \Big] P \\ & + \sum_{\langle ij \rangle_z} P \Big[-t_z \sum_{\sigma} \left(c^{\dagger}_{i\sigma} c_{j\sigma} + c^{\dagger}_{j\sigma} c_{i\sigma} \right) - J_z \mathbf{S}_i \cdot \mathbf{S}_j + V_z n_i n_j + \mu (n_i + n_j) \Big] P \\ & \equiv \sum_{\langle ij \rangle_{xy}} \{ -\beta H_{xy}(i,j) \} + \sum_{\langle ij \rangle_z} \{ -\beta H_z(i,j) \} \, . \end{aligned} \tag{5.2}$$

Here $\beta = 1/k_B T$, so that the interaction constants are related by $t_{xy} = \beta \tilde{t}_{xy}$, $t_z = \beta \tilde{t}_z$, $J_{xy} = \beta \tilde{J}_{xy}$, $J_z = \beta \tilde{J}_z$, $V_{xy} = \beta \tilde{V}_{xy}$, $V_z = \beta \tilde{V}_z$, and $\mu = \beta \tilde{\mu}/6$.

5.2.3 Renormalization-Group Theory

5.2.3.1 Isotropic Transformation and Anisotropic Expectations

Since the isotropic model is a special case of Eq. (5.1), let us briefly outline the main steps in effecting the renormalization equations of earlier, isotropic studies [4, 5, 7]. We begin by setting up a decimation transformation for a one-dimensional tJ chain, finding a thermodynamically equivalent Hamiltonian by tracing over the degrees of freedom at every other lattice site. With the vector $\mathbf{K}$ whose elements are the interaction constants in the Hamiltonian, the decimation can be expressed as a mapping of the original $d = 1$ system onto a new system with interaction constants

$$\mathbf{K}' = \mathbf{R}(\mathbf{K}) \, . \tag{5.3}$$

The Migdal-Kadanoff [9, 10] procedure has been remarkably successful, for systems both classical and quantum, in extending this transformation to $d > 1$ (for an overview, see [6]). In this procedure, a subset of the nearest-neighbor interactions in the lattice are ignored, leaving behind a new d-dimensional hypercubic lattice where each point is connected to its neighbor by two consecutive nearest-neighbor segments of the original lattice. The decimation described above is applied to the middle site between the two consecutive segments, giving the renormalized nearest-neighbor couplings for the points forming the new lattice. We compensate for the interactions that are ignored in the original lattice by multiplying the interactions after the decimation by b^{d-1}, where $b = 2$ is the length rescaling factor. Thus for $d > 1$ the renormalization-group transformation of Eq. (5.3) generalizes to

$$\mathbf{K}' = b^{d-1}\mathbf{R}(\mathbf{K}), \tag{5.4}$$

which, through flows in a four-dimensional Hamiltonian space (for the Hubbard model, 10-dimensional Hamiltonian space [6]), yields a rich array of physical phenomena.

With the anisotropic tJ Hamiltonian on a cubic lattice (Eq. (5.1)), there are two intercoupled sets of interaction constants, $\mathbf{K}_{xy}$ and $\mathbf{K}_z$, and further development of the transformation is needed. However, there are three particular instances where the transformation in Eq. (5.4) is directly applicable. When $\mathbf{K}_{xy} = \mathbf{K}_z$, we have the $d = 3$ isotropic case, so the appropriate renormalization-group equations are

$$\mathbf{K}'_{xy} = 4\,\mathbf{R}(\mathbf{K}_{xy})\,, \qquad \mathbf{K}'_z = 4\,\mathbf{R}(\mathbf{K}_z)\,. \tag{5.5}$$

When $\mathbf{K}_{xy} \neq 0$ and $\mathbf{K}_z = 0$, we have a system of decoupled isotropic $d = 2$ planes, and the transformation is given by

$$\mathbf{K}'_{xy} = 2\,\mathbf{R}(\mathbf{K}_{xy})\,, \qquad \mathbf{K}'_z = 0\,. \tag{5.6}$$

Similarly, when $\mathbf{K}_{xy} = 0$ and $\mathbf{K}_z \neq 0$, we have decoupled $d = 1$ chains, and

$$\mathbf{K}'_{xy} = 0\,, \qquad \mathbf{K}'_z = \mathbf{R}(\mathbf{K}_z)\,. \tag{5.7}$$

The renormalization-group transformation for the anisotropic model described in the following sections recovers the correct results, Eqs.(5.5)-(5.7), for these three cases.

5.2.3.2 Hierarchical Lattice Model for Anisotropy

A one-to-one correspondance exists between Migdal-Kadanoff and other approximate renormalization-group transformations on the one hand, and exact renormalization-group transformations of corresponding hierarchical lattices on the other hand, through the sharing of identical recursion relations.[11, 12] The correspondance guarantees the fulfilment of general physical preconditions on the results of approximate renormalization-group transformations, since the latter are thus "physically realizable". This correspondance has recently been exploited to develop renormalization-group transformations for spatially anisotropic Ising, XY magnetic and percolation systems.[8] Similarly, to derive an approximate renormalization-group transformation for the anisotropic tJ Hamiltonian, consider the nonuniform hierarchical model depicted in Fig. 5-1. The two types of bonds in the lattice, corresponding to xy and z bonds, are drawn with solid and dashed lines respectively. The hierarchical model is constructed by replacing each single bond of a given type with the connected cluster of bonds shown in Fig. 5-1(b), and repeating this step an arbitrary number of times. Fig. 5-1(c) shows the next stage in the construction for the two graphs in column (b). The renormalization-group transformation on this hierarchical lattice consists of decimating over the four inner sites in each cluster, to generate a renormalized interaction between the two outer sites, thus reversing the construction process, going from the graphs in column (b) of Fig. 5-1 to those in column (a). This renormalization-group transformation has the desired feature that in all three of the cases described above, it reproduces the various isotropic recursion relations of Eqs. (5.5)-(5.7).

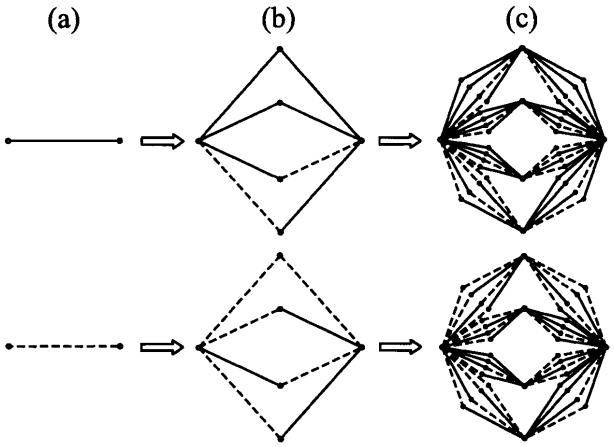

Figure 5-1: Construction of the hierarchical model. Solid lines correspond to xy bonds, while dashed lines correspond to z bonds.

5.2.3.3 Renormalization-Group Equations for Anisotropic System

The hierarchical lattice can be subdivided into individual clusters of bonds shown in Fig. 5-1(b). We label these two types of clusters the "xy cluster" (Fig. 5-1(b) top) and the "z cluster" (Fig. 5-1(b) bottom). The sum over $\langle ij \rangle_{xy\ \mathrm{clus}}$ denotes a sum over the outer sites of all the xy clusters, and analogously $\langle ij \rangle_{z\ \mathrm{clus}}$ denotes a sum over the outer sites of all z clusters. For a given cluster with outer sites ij, the associated inner sites are labeled $k_1^{(ij)}, \ldots, k_4^{(ij)}$. Then the tJ Hamiltonian on the anisotropic lattice has the form

$$\begin{aligned}
-\beta H = \sum_{\langle ij \rangle_{xy\ \mathrm{clus}}} \Big[& -\beta H_{xy}(i, k_1^{(ij)}) - \beta H_{xy}(k_1^{(ij)}, j) - \beta H_{xy}(i, k_2^{(ij)}) - \beta H_{xy}(k_2^{(ij)}, j) \\
& - \beta H_{xy}(i, k_3^{(ij)}) - \beta H_z(k_3^{(ij)}, j) - \beta H_z(i, k_4^{(ij)}) - \beta H_{xy}(k_4^{(ij)}, j) \Big] \\
+ \sum_{\langle ij \rangle_{z\ \mathrm{clus}}} \Big[& -\beta H_z(i, k_1^{(ij)}) - \beta H_z(k_1^{(ij)}, j) - \beta H_z(i, k_2^{(ij)}) - \beta H_{xy}(k_2^{(ij)}, j) \\
& - \beta H_{xy}(i, k_3^{(ij)}) - \beta H_z(k_3^{(ij)}, j) - \beta H_z(i, k_4^{(ij)}) - \beta H_{xy}(k_4^{(ij)}, j) \Big] .
\end{aligned} \tag{5.8}$$

The renormalization-group transformation consists of finding a thermodynamically equivalent Hamiltonian $-\beta' H'$ that involves only the outer sites of each cluster.

Since we are dealing with a quantum system, the non-commutation of the operators in the Hamiltonian means that this decimation, tracing over the degrees of freedom at the k sites, can only be carried out approximately [13, 14]:

$$
\begin{aligned}
\mathrm{Tr}_{k \text{ sites}}\, e^{-\beta H} \simeq & \prod_{\langle ij\rangle_{xy} \text{ clus}} \Big[\mathrm{Tr}_{k_1^{(ij)}}\, e^{-\beta H_{xy}(i,k_1^{(ij)}) - \beta H_{xy}(k_1^{(ij)},j)}\, \mathrm{Tr}_{k_2^{(ij)}}\, e^{-\beta H_{xy}(i,k_2^{(ij)}) - \beta H_{xy}(k_2^{(ij)},j)} \\
& \qquad \mathrm{Tr}_{k_3^{(ij)}}\, e^{-\beta H_{xy}(i,k_3^{(ij)}) - \beta H_z(k_3^{(ij)},j)}\, \mathrm{Tr}_{k_4^{(ij)}}\, e^{-\beta H_z(i,k_4^{(ij)}) - \beta H_{xy}(k_4^{(ij)},j)} \Big] \\
& \cdot \prod_{\langle ij\rangle_{z} \text{ clus}} \Big[\mathrm{Tr}_{k_1^{(ij)}}\, e^{-\beta H_z(i,k_1^{(ij)}) - \beta H_z(k_1^{(ij)},j)}\, \mathrm{Tr}_{k_2^{(ij)}}\, e^{-\beta H_z(i,k_2^{(ij)}) - \beta H_{xy}(k_2^{(ij)},j)} \\
& \qquad \mathrm{Tr}_{k_3^{(ij)}}\, e^{-\beta H_{xy}(i,k_3^{(ij)}) - \beta H_z(k_3^{(ij)},j)}\, \mathrm{Tr}_{k_4^{(ij)}}\, e^{-\beta H_z(i,k_4^{(ij)}) - \beta H_{xy}(k_4^{(ij)},j)} \Big] \\
= & \prod_{\langle ij\rangle_{xy} \text{ clus}} \Big[e^{-\beta' H'_{xy,xy}(i,j)} e^{-\beta' H'_{xy,xy}(i,j)} e^{-\beta' H'_{xy,z}(i,j)} e^{-\beta' H'_{z,xy}(i,j)} \Big] \\
& \cdot \prod_{\langle ij\rangle_{z} \text{ clus}} \Big[e^{-\beta' H'_{z,z}(i,j)} e^{-\beta' H'_{xy,z}(i,j)} e^{-\beta' H'_{z,xy}(i,j)} e^{-\beta' H'_{z,xy}(i,j)} \Big] \\
\simeq & \exp\Bigg\{ \sum_{\langle ij\rangle_{xy} \text{ clus}} \left[-2\beta' H'_{xy,xy}(i,j) - \beta' H'_{xy,z}(i,j) - \beta' H'_{z,xy}(i,j) \right] \\
& \qquad + \sum_{\langle ij\rangle_{z} \text{ clus}} \left[-\beta' H'_{z,z}(i,j) - \beta' H'_{xy,z}(i,j) - 2\beta' H'_{z,xy}(i,j) \right] \Bigg\} \\
= & \, e^{\sum_{\langle ij\rangle_{xy} \text{ clus}} \left[-\beta' H'_{xy}(i,j) \right] + \sum_{\langle ij\rangle_{z} \text{ clus}} \left[-\beta' H'_{z}(i,j) \right]} = e^{-\beta' H'} \, .
\end{aligned}
\tag{5.9}
$$

Here $-\beta' H'_{A,B}(i,j)$, where A, B can each be either xy or z, is

$$
e^{-\beta' H'_{A,B}(i,j)} = \mathrm{Tr}_k\, e^{-\beta H_A(i,k) - \beta H_B(k,j)} \, . \tag{5.10}
$$

In the two approximate steps, marked by $\simeq$ in Eq. (5.9), we ignore the non-commutation of operators outside three-site segments of the unrenormalized system. (On the other hand, anticommutation rules are correctly accounted for within the three-site segments, at all successive length scales in the iterations of the renormalization-group transformation.) These two steps involve the same approximation but in opposite directions, which gives some mutual compensation. This approach has been shown to successfully predict finite-temperature behavior in earlier studies [13, 14].

Derivation of the renormalization-group equations involves extracting the algebraic form of the operators $-\beta' H'_{A,B}(i,j)$ from Eq. (5.10). Since $e^{-\beta' H'_{A,B}(i,j)}$ and $e^{-\beta H_A(i,k)-\beta H_B(k,j)}$ act on the space of two-site and three-site states respectively, Eq. (5.10) can be rewritten in terms of matrix elements as

$$\langle u_i v_j | e^{-\beta' H'_{A,B}(i,j)} | \bar{u}_i \bar{v}_j \rangle = \sum_{w_k} \langle u_i w_k v_j | e^{-\beta H_A(i,k)-\beta H_B(k,j)} | \bar{u}_i w_k \bar{v}_j \rangle \,, \tag{5.11}$$

where $u_i, w_k, v_j, \bar{u}_i, \bar{v}_j$ are single-site state variables. Eq.(5.11) is the contraction of a 27×27 matrix on the right into a 9×9 matrix on the left. We block-diagonalize the left and right sides of Eq.(5.11) by choosing basis states which are the eigenstates of total particle number, total spin magnitude, total spin z-component, and parity. We denote the set of 9 two-site eigenstates by $\{|\phi_p\rangle\}$ and the set of 27 three-site eigenstates by $\{|\psi_q\rangle\}$, and list them in Tables 5.1 and 5.2. Eq.(5.11) is rewritten as

$$\begin{aligned}
&\langle \phi_p | e^{-\beta' H'_{A,B}(i,j)} | \phi_{\bar{p}} \rangle = \\
&\sum_{\substack{u,v,\bar{u},\\ \bar{v},w}} \sum_{q,\bar{q}} \langle \phi_p | u_i v_j \rangle \langle u_i w_k v_j | \psi_q \rangle \langle \psi_q | e^{-\beta H_A(i,k)-\beta H_B(k,j)} | \psi_{\bar{q}} \rangle \langle \psi_{\bar{q}} | \bar{u}_i w_k \bar{v}_j \rangle \langle \bar{u}_i \bar{v}_j | \phi_{\bar{p}} \rangle \,.
\end{aligned} \tag{5.12}$$

Eq. (5.12) yields six independent elements for the matrix $\langle \phi_p | e^{-\beta' H'_{A,B}(i,j)} | \phi_{\bar{p}} \rangle$, labeled γ_p as follows:

$$\begin{aligned}
\gamma_p &\equiv \langle \phi_p | e^{-\beta' H'_{A,B}(i,j)} | \phi_p \rangle \quad \text{for } p = 1, 2, 4, 6, 7, \\
\gamma_0 &\equiv \langle \phi_2 | e^{-\beta' H'_{A,B}(i,j)} | \phi_4 \rangle \,.
\end{aligned} \tag{5.13}$$

The number of γ_p is also the number of interaction strengths that are independently fixed in the Hamiltonian $-\beta' H'_{A,B}(i,j)$, which consequently must have a more general form than the two-site Hamiltonians in Eq. (5.2). The generalized form of the pair

n	p	s	m_s	Two-site basis states
0	+	0	0	$\|\phi_1\rangle = \|\circ\circ\rangle$
1	+	1/2	1/2	$\|\phi_2\rangle = \frac{1}{\sqrt{2}}\{\|\uparrow\circ\rangle + \|\circ\uparrow\rangle\}$
1	−	1/2	1/2	$\|\phi_4\rangle = \frac{1}{\sqrt{2}}\{\|\uparrow\circ\rangle - \|\circ\uparrow\rangle\}$
2	−	0	0	$\|\phi_6\rangle = \frac{1}{\sqrt{2}}\{\|\uparrow\downarrow\rangle - \|\downarrow\uparrow\rangle\}$
2	+	1	1	$\|\phi_7\rangle = \|\uparrow\uparrow\rangle$
2	+	1	0	$\|\phi_9\rangle = \frac{1}{\sqrt{2}}\{\|\uparrow\downarrow\rangle + \|\downarrow\uparrow\rangle\}$

Table 5.1: The two-site basis states, with the corresponding particle number (n), parity (p), total spin (s), and total spin z-component (m_s) quantum numbers. The states $|\phi_3\rangle$, $|\phi_5\rangle$, and $|\phi_8\rangle$ are obtained by spin reversal from $|\phi_2\rangle$, $|\phi_4\rangle$, and $|\phi_7\rangle$, respectively.

Hamiltonian is

$$-\beta H(i,j) = P\Big[-t\sum_{\sigma}\left(c^{\dagger}_{i\sigma}c_{j\sigma} + c^{\dagger}_{j\sigma}c_{i\sigma}\right) - J\mathbf{S}_i\cdot\mathbf{S}_j + Vn_in_j + \mu(n_i+n_j) + \nu(n_i-n_j) + G\Big]P \tag{5.14}$$

The new terms here are: G, the additive constant that appears in all renormalization-group calculations, does not affect the flows, but enters the determination of expectation values; and $\nu(n_i - n_j)$, a staggered term arising from decimation across two consecutive bonds of different strengths. Provisions for handling the ν term will be described later in this section.

To calculate the γ_p, we determine the matrix elements of $-\beta H_A(i,k) - \beta H_B(k,j)$ in the three-site basis $\{\psi_q\}$. $-\beta H_A$ and $-\beta H_B$ have the form of Eq. (5.14), with interaction constants $\{t_A, J_A, V_A, \mu_A, \nu_A, G_A\}$ and $\{t_B, J_B, V_B, \mu_B, \nu_B, G_B\}$ respectively. The resulting matrix elements are listed in Table 5.3. We exponentiate the matrix blocks to find the elements $\langle\psi_q|e^{-\beta H_A(i,k)-\beta H_B(k,j)}|\psi_{\bar{q}}\rangle$ which enter on the right-hand side of Eq. (5.12). In this way the γ_p are obtained as functions of the interaction constants in the unrenormalized two-site Hamiltonians, $\gamma_p = \gamma_p(\{t_A, J_A, \ldots\}, \{t_B, J_B, \ldots\})$.

The matrix elements of $-\beta' H'_{A,B}(i,j)$ in the $\{\phi_p\}$ basis are shown in Table 5.4. Exponentiating this matrix, we solve for the renormalized interaction constants (t',

n	p	s	m_s	Three-site basis states
0	+	0	0	$\vert\psi_1\rangle = \vert \circ\,\circ\,\circ\rangle$
1	+	1/2	1/2	$\vert\psi_2\rangle = \vert\circ\uparrow\circ\rangle$, $\vert\psi_3\rangle = \frac{1}{\sqrt{2}}\{\vert\uparrow\circ\circ\rangle + \vert\circ\circ\uparrow\rangle\}$
1	−	1/2	1/2	$\vert\psi_6\rangle = \frac{1}{\sqrt{2}}\{\vert\uparrow\circ\circ\rangle - \vert\circ\circ\uparrow\rangle\}$
2	+	0	0	$\vert\psi_8\rangle = \frac{1}{2}\{\vert\uparrow\downarrow\circ\rangle - \vert\downarrow\uparrow\circ\rangle - \vert\circ\uparrow\downarrow\rangle + \vert\circ\downarrow\uparrow\rangle\}$
2	−	0	0	$\vert\psi_9\rangle = \frac{1}{2}\{\vert\uparrow\downarrow\circ\rangle - \vert\downarrow\uparrow\circ\rangle + \vert\circ\uparrow\downarrow\rangle - \vert\circ\downarrow\uparrow\rangle\}$, $\vert\psi_{10}\rangle = \frac{1}{\sqrt{2}}\{\vert\uparrow\circ\downarrow\rangle - \vert\downarrow\circ\uparrow\rangle\}$
2	+	1	1	$\vert\psi_{11}\rangle = \vert\uparrow\circ\uparrow\rangle$, $\vert\psi_{12}\rangle = \frac{1}{\sqrt{2}}\{\vert\uparrow\uparrow\circ\rangle + \vert\circ\uparrow\uparrow\rangle\}$
2	+	1	0	$\vert\psi_{13}\rangle = \frac{1}{2}\{\vert\uparrow\downarrow\circ\rangle + \vert\downarrow\uparrow\circ\rangle + \vert\circ\uparrow\downarrow\rangle + \vert\circ\downarrow\uparrow\rangle\}$, $\vert\psi_{14}\rangle = \frac{1}{\sqrt{2}}\{\vert\uparrow\circ\downarrow\rangle + \vert\downarrow\circ\uparrow\rangle\}$
2	−	1	1	$\vert\psi_{17}\rangle = \frac{1}{\sqrt{2}}\{\vert\uparrow\uparrow\circ\rangle - \vert\circ\uparrow\uparrow\rangle\}$
2	−	1	0	$\vert\psi_{18}\rangle = \frac{1}{2}\{\vert\uparrow\downarrow\circ\rangle + \vert\downarrow\uparrow\circ\rangle - \vert\circ\uparrow\downarrow\rangle - \vert\circ\downarrow\uparrow\rangle\}$
3	+	1/2	1/2	$\vert\psi_{20}\rangle = \frac{1}{\sqrt{6}}\{2\vert\uparrow\downarrow\uparrow\rangle - \vert\uparrow\uparrow\downarrow\rangle - \vert\downarrow\uparrow\uparrow\rangle\}$
3	−	1/2	1/2	$\vert\psi_{22}\rangle = \frac{1}{\sqrt{2}}\{\vert\uparrow\uparrow\downarrow\rangle - \vert\downarrow\uparrow\uparrow\rangle\}$
3	+	3/2	3/2	$\vert\psi_{24}\rangle = \vert\uparrow\uparrow\uparrow\rangle$
3	+	3/2	1/2	$\vert\psi_{25}\rangle = \frac{1}{\sqrt{3}}\{\vert\uparrow\downarrow\uparrow\rangle + \vert\uparrow\uparrow\downarrow\rangle + \vert\downarrow\uparrow\uparrow\rangle\}$

Table 5.2: The three-site basis states, with the corresponding particle number (n), parity (p), total spin (s), and total spin z-component (m_s) quantum numbers. The states $|\psi_{4-5}\rangle$, $|\psi_7\rangle$, $|\psi_{15-16}\rangle$, $|\psi_{19}\rangle$, $|\psi_{21}\rangle$, $|\psi_{23}\rangle$, $|\psi_{26-27}\rangle$ are obtained by spin reversal from $|\psi_{2-3}\rangle$, $|\psi_6\rangle$, $|\psi_{11-12}\rangle$, $|\psi_{17}\rangle$, $|\psi_{20}\rangle$, $|\psi_{22}\rangle$, $|\psi_{24-25}\rangle$, respectively.

J', V', μ', ν', G') in terms of the γ_p:

$$t' = u, \qquad J' = \ln\frac{\gamma_6}{\gamma_7}, \qquad V' = \frac{1}{4}\left\{\ln(\gamma_1^4\gamma_6\gamma_7^3) - 8v\right\}, \qquad \mu' = v - \ln\gamma_1,$$
$$\nu' = \frac{2u\gamma_0}{\gamma_4 - \gamma_2}, \qquad G' = \ln\gamma_1, \tag{5.15}$$

where

$$v = \frac{1}{2}\ln\left(\gamma_2\gamma_4 - \gamma_0^2\right),$$
$$u = \frac{\gamma_4 - \gamma_2}{\sqrt{(\gamma_4 - \gamma_2)^2 + 4\gamma_0^2}}\cosh^{-1}\left(\frac{\gamma_4 + \gamma_2}{2e^v}\right).$$

The renormalization-group transformation described by Eqs. (5.12)-(5.15) can be expressed as a mapping of a three-site Hamiltonian with bonds having interaction constants $\mathbf{K}_A = \{t_A, J_A, V_A, \mu_A, \nu_A, G_A\}$ and $\mathbf{K}_B = \{t_B, J_B, V_B, \mu_B, \nu_B, G_B\}$ onto a two-site Hamiltonian with interaction constants

$$\mathbf{K}' = \mathbf{R}(\mathbf{K}_A, \mathbf{K}_B). \tag{5.16}$$

	ψ_1
ψ_1	0

	ψ_2	ψ_3	ψ_6
ψ_2	$\mu_A+\mu_B-\nu_A+\nu_B$	$-\frac{1}{\sqrt{2}}(t_A+t_B)$	$\frac{1}{\sqrt{2}}(t_B-t_A)$
ψ_3	$-\frac{1}{\sqrt{2}}(t_A+t_B)$	$\frac{1}{2}(\mu_A+\mu_B+\nu_A-\nu_B)$	$\frac{1}{2}(\mu_A-\mu_B+\nu_A+\nu_B)$
ψ_6	$\frac{1}{\sqrt{2}}(t_B-t_A)$	$\frac{1}{2}(\mu_A-\mu_B+\nu_A+\nu_B)$	$\frac{1}{2}(\mu_A+\mu_B+\nu_A-\nu_B)$

	ψ_8	ψ_9	ψ_{10}
ψ_8	$\frac{1}{2}(\frac{3}{4}J_A+\frac{3}{4}J_B+V_A+V_B+3\mu_A+3\mu_B-\nu_A+\nu_B)$	$\frac{1}{2}(\frac{3}{4}J_A-\frac{3}{4}J_B+V_A-V_B+\mu_A-\mu_B+\nu_A+\nu_B)$	$\frac{1}{\sqrt{2}}(t_A-t_B)$
ψ_9	$\frac{1}{2}(\frac{3}{4}J_A-\frac{3}{4}J_B+V_A-V_B+\mu_A-\mu_B+\nu_A+\nu_B)$	$\frac{1}{2}(\frac{3}{4}J_A+\frac{3}{4}J_B+V_A+V_B+3\mu_A+3\mu_B-\nu_A+\nu_B)$	$-\frac{1}{\sqrt{2}}(t_A+t_B)$
ψ_{10}	$\frac{1}{\sqrt{2}}(t_A-t_B)$	$-\frac{1}{\sqrt{2}}(t_A+t_B)$	$\mu_A+\mu_B+\nu_A-\nu_B$

	ψ_{11}	ψ_{12}	ψ_{17}
ψ_{11}	$\mu_A+\mu_B+\nu_A-\nu_B$	$-\frac{1}{\sqrt{2}}(t_A+t_B)$	$\frac{1}{\sqrt{2}}(t_A-t_B)$
ψ_{12}	$-\frac{1}{\sqrt{2}}(t_A+t_B)$	$\frac{1}{2}(-\frac{1}{4}J_A-\frac{1}{4}J_B+V_A+V_B+3\mu_A+3\mu_B-\nu_A+\nu_B)$	$\frac{1}{2}(-\frac{1}{4}J_A+\frac{1}{4}J_B+V_A-V_B+\mu_A-\mu_B+\nu_A+\nu_B)$
ψ_{17}	$\frac{1}{\sqrt{2}}(t_A-t_B)$	$\frac{1}{2}(-\frac{1}{4}J_A+\frac{1}{4}J_B+V_A-V_B+\mu_A-\mu_B+\nu_A+\nu_B)$	$\frac{1}{2}(-\frac{1}{4}J_A-\frac{1}{4}J_B+V_A+V_B+3\mu_A+3\mu_B-\nu_A+\nu_B)$

	ψ_{13}	ψ_{14}	ψ_{18}
ψ_{13}	$\frac{1}{2}(-\frac{1}{4}J_A-\frac{1}{4}J_B+V_A+V_B+3\mu_A+3\mu_B-\nu_A+\nu_B)$	$-\frac{1}{\sqrt{2}}(t_A+t_B)$	$\frac{1}{2}(-\frac{1}{4}J_A+\frac{1}{4}J_B+V_A-V_B+\mu_A-\mu_B+\nu_A+\nu_B)$
ψ_{14}	$-\frac{1}{\sqrt{2}}(t_A+t_B)$	$\mu_A+\mu_B+\nu_A-\nu_B$	$\frac{1}{\sqrt{2}}(t_A-t_B)$
ψ_{18}	$\frac{1}{2}(-\frac{1}{4}J_A+\frac{1}{4}J_B+V_A-V_B+\mu_A-\mu_B+\nu_A+\nu_B)$	$\frac{1}{\sqrt{2}}(t_A-t_B)$	$\frac{1}{2}(-\frac{1}{4}J_A-\frac{1}{4}J_B+V_A+V_B+3\mu_A+3\mu_B-\nu_A+\nu_B)$

	ψ_{20}	ψ_{22}
ψ_{20}	$\frac{1}{2}J_A+\frac{1}{2}J_B+V_A+V_B+2\mu_A+2\mu_B$	$\frac{\sqrt{3}}{4}(J_B-J_A)$
ψ_{22}	$\frac{\sqrt{3}}{4}(J_B-J_A)$	$V_A+V_B+2\mu_A+2\mu_B$

	ψ_{24}
ψ_{24}	$-\frac{1}{4}J_A-\frac{1}{4}J_B+V_A+V_B+2\mu_A+2\mu_B$

	ψ_{25}
ψ_{25}	$-\frac{1}{4}J_A-\frac{1}{4}J_B+V_A+V_B+2\mu_A+2\mu_B$

Table 5.3: Diagonal matrix blocks of the unrenormalized three-site Hamiltonian $-\beta H_A(i,k)-\beta H_B(k,j)$. The Hamiltonian being invariant under spin-reversal, the spin-flipped matrix elements are not shown. The additive constant contribution G_A+G_B, occurring at the diagonal terms, is also not shown.

	ϕ_1	ϕ_2	ϕ_4	ϕ_6	ϕ_7	ϕ_9
ϕ_1	G'					
ϕ_2		$-t'+\mu'+G'$	ν'		0	
ϕ_4		ν'	$t'+\mu'+G'$			
ϕ_6				$\frac{3}{4}J'+V'+2\mu'+G'$		
ϕ_7			0		$-\frac{1}{4}J'+V'+2\mu'+G'$	
ϕ_9						$-\frac{1}{4}J'+V'+2\mu'+G'$

Table 5.4: Block-diagonal matrix of the renormalized two-site Hamiltonian $-\beta' H'(i,j)$. The Hamiltonian being invariant under spin-reversal, the spin-flipped matrix elements are not shown.

When $\nu_A = \nu_B = 0$, this mapping has the property that if $\mathbf{R}(\mathbf{K}_A, \mathbf{K}_B) = \{t', J', V', \mu', \nu', G'\}$, then $\mathbf{R}(\mathbf{K}_B, \mathbf{K}_A)$ gives the same result, except that the sign of ν' is switched. So $\mathbf{R}(\mathbf{K}_A, \mathbf{K}_A)$ has a zero ν' component.

From Eq. (5.9), the renormalized xy- and z-bond interaction constants are

$$\begin{aligned} \mathbf{K}'_{xy} &= 2\mathbf{R}(\mathbf{K}_{xy}, \mathbf{K}_{xy}) + \mathbf{R}(\mathbf{K}_{xy}, \mathbf{K}_z) + \mathbf{R}(\mathbf{K}_z, \mathbf{K}_{xy})\,, \\ \mathbf{K}'_z &= \mathbf{R}(\mathbf{K}_z, \mathbf{K}_z) + \mathbf{R}(\mathbf{K}_{xy}, \mathbf{K}_z) + 2\mathbf{R}(\mathbf{K}_z, \mathbf{K}_{xy})\,. \end{aligned} \tag{5.17}$$

The staggered ν' term cancels out in $\mathbf{K}'_{xy}$. In constructing the anisotropic hierarchical lattice, we could have used a graph in which the lowest two bonds in Fig. 5-1(b) are interchanged. Averaging over these two realizations,

$$\mathbf{K}'_z = \mathbf{R}(\mathbf{K}_z, \mathbf{K}_z) + \frac{3}{2}\mathbf{R}(\mathbf{K}_{xy}, \mathbf{K}_z) + \frac{3}{2}\mathbf{R}(\mathbf{K}_z, \mathbf{K}_{xy})\,, \tag{5.18}$$

the ν' term cancels out in $\mathbf{K}'_z$ as well.

5.2.4 Phase Diagrams and Expectation Values as a Function of Anisotropy

Thermodynamic properties of the system, including the global phase diagram and expectation values of operators occurring in the Hamiltonian, are obtained from the

analysis of the renormalization-group flows [15]. The initial conditions for the flows are the interaction constants in the original anisotropic tJ Hamiltonian. For the numerical results presented below, we use the following initial form: $t_{xy} = t$, $t_z = \alpha_t t$, $J_{xy} = J$, $J_z = \alpha_J J$, $V_{xy} = J_{xy}/4$, $V_z = J_z/4$, where $0 \leq \alpha_t, \alpha_J \leq 1$. For the anisotropy parameters α_t and α_J, we use $\alpha_J = \alpha_t^2$, as dictated from the derivation of the tJ Hamiltonian from the large-U limit of the Hubbard model [16].

Phase diagrams for the coupling $J/t = 0.444$ and various values of $\alpha_t = t_z/t_{xy}$ are shown in Figs. 5-2 and 5-3. The temperature variable is $1/t$, and the diagrams are plotted both in terms of chemical potential μ/J and electron density $\langle n_i \rangle$. The phases in the diagrams are those found in earlier studies of the isotropic $d = 3$ tJ model [5, 4], which can be consulted for a more detailed description. Here we summarize the salient features of the phases.

Each phase is associated with a completely stable fixed point (sink) of the renormalization-group flows, and thermodynamic densities calculated at the fixed point epitomize (and determine [7], e.g. as seen in the results displayed in Fig. 5-4) characteristics of the entire phase. The results are shown in Table 5.5. The **dilute disordered (d)** and **dense disordered (D)** phases have $\langle n_i \rangle = 0$ and 1 at their respective phase sinks, so the electron densities in these phases are accordingly small in the one case and close to 1 in the other. Both phases lack long-range spin order, since $\langle \mathbf{S}_i \cdot \mathbf{S}_j \rangle = 0$ at the sinks. On the other hand, the **antiferromagnetic (A)** phase has $\langle n_i \rangle = 1$ and a nonzero nearest-neighbor spin-spin correlation $\langle \mathbf{S}_i \cdot \mathbf{S}_j \rangle = 1/4$ at the phase sink. Since nearest-neighbor spins at the sink are distant members of the same sublattice in the unrenormalized system, this positive value for $\langle \mathbf{S}_i \cdot \mathbf{S}_j \rangle$ is expected, and leads to $\langle \mathbf{S}_i \cdot \mathbf{S}_j \rangle < 0$ for nearest neighbors of the original system, as seen in the last row of Fig. 5-4.

In the antiferromagnetic and the two disordered phases, the electron hopping strengths t_{xy} and t_z tend to zero after repeated rescalings. The system is either completely empty or filled in this limit, and the expectation value of the kinetic energy operator $\langle K \rangle \equiv -\sum_\sigma \langle c_{i\sigma}^\dagger c_{j\sigma} + c_{j\sigma}^\dagger c_{i\sigma} \rangle$ is zero at the sink. The **τ phase** is interesting in contrast because the magnitudes of t_{xy} and t_z both tend to ∞, and we

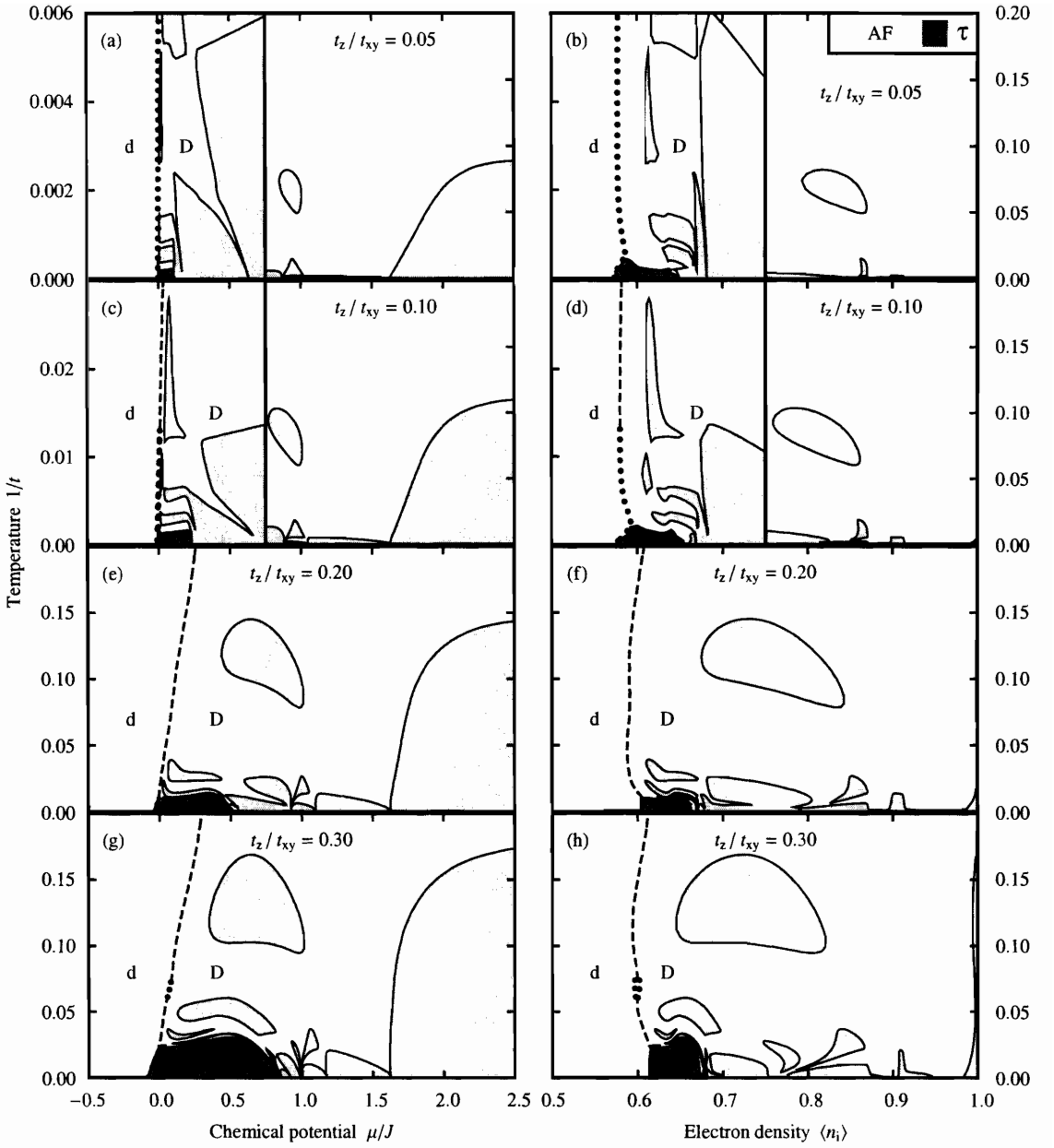

Figure 5-2: Phase diagrams of the anisotropic tJ model with $J/t = 0.444$ in temperature vs. chemical potential (first column) and temperature vs. electron density (second column). The degree of anisotropy varies from $t_z/t_{xy} = 0.05$ in Fig. 5-2(a)-(b) to $t_z/t_{xy} = 0.30$ in Fig. 5-2(g)-(h). Note the expanded temperature scales on the left panels of Fig. 5-2(a)-(d). The dense disordered (D), dilute disordered (d), antiferromagnetic (A), and τ phases are shown. The A and τ regions are colored light and dark gray respectively. Second-order phase transitions are drawn with full curves, first-order transitions with dotted curves. The unmarked areas within the dotted curves in the temperature vs. electron density figures are narrow coexistence regions between the two phases at either side. Dashed curves are not phase transitions, but disorder lines between the dense disordered and dilute disordered phases.

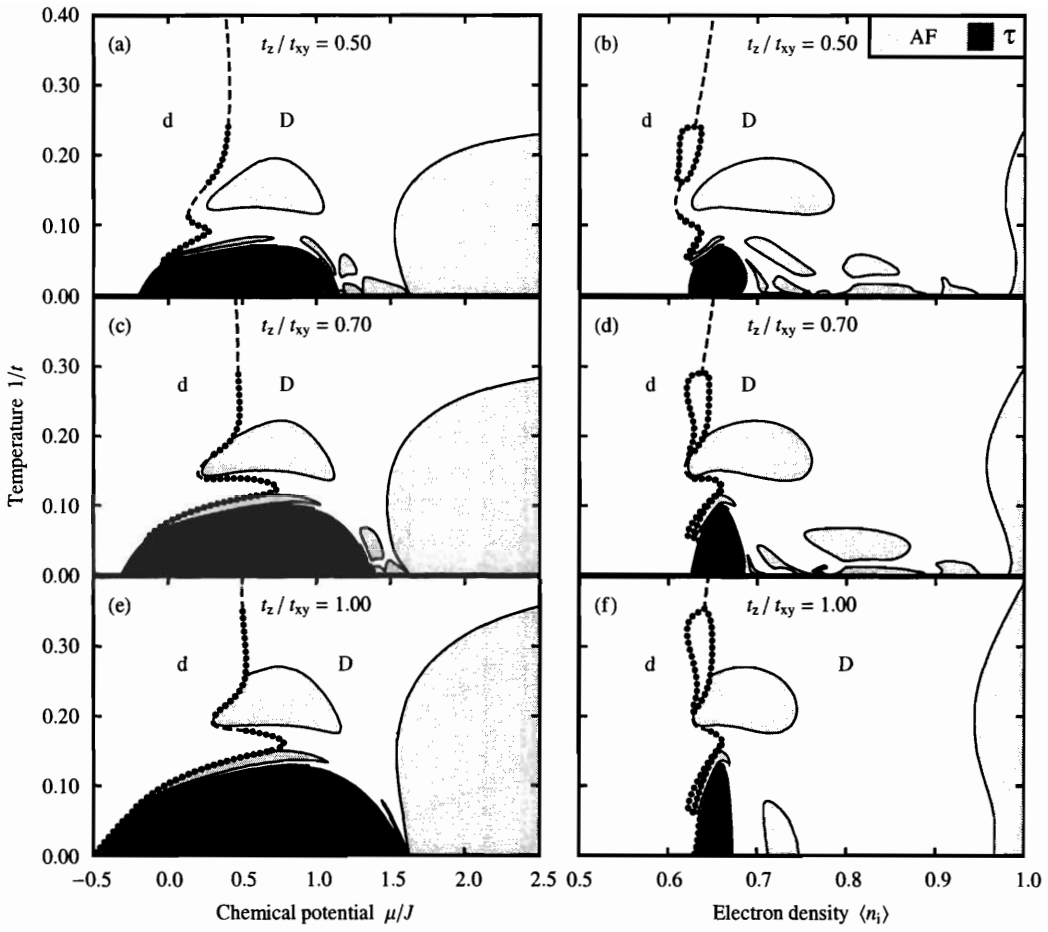

Figure 5-3: The continuation of the phase diagrams in Fig. 5-2 for t_z/t_{xy} between 0.5 and 1.

Phase sink	Expectation values			
	$-\sum_\sigma \langle c^\dagger_{i\sigma} c_{j\sigma} + c^\dagger_{j\sigma} c_{i\sigma} \rangle$	$\langle n_i \rangle$	$\langle \mathbf{S}_i \cdot \mathbf{S}_j \rangle$	$\langle n_i n_j \rangle$
d	0	0	0	0
D	0	1	0	1
A	0	1	$\frac{1}{4}$	1
τ	$\frac{2}{3}$	$\frac{2}{3}$	$-\frac{1}{4}$	$\frac{1}{3}$

Table 5.5: Expectation values at the phase-sink fixed points.

find partial filling, $\langle n_i \rangle = 2/3$, and a nonzero kinetic energy $\langle K \rangle = 2/3$ at the phase sink. This makes the τ phase a candidate for superconductivity. In fact, we have shown in a previous work [7] that the superfluid weight has a pronounced peak in the τ phase, there is evidence of a gap in the quasiparticle spectrum, and the free carrier density in the vicinity of the τ phase has properties seen experimentally in high-T_c materials [17, 18].

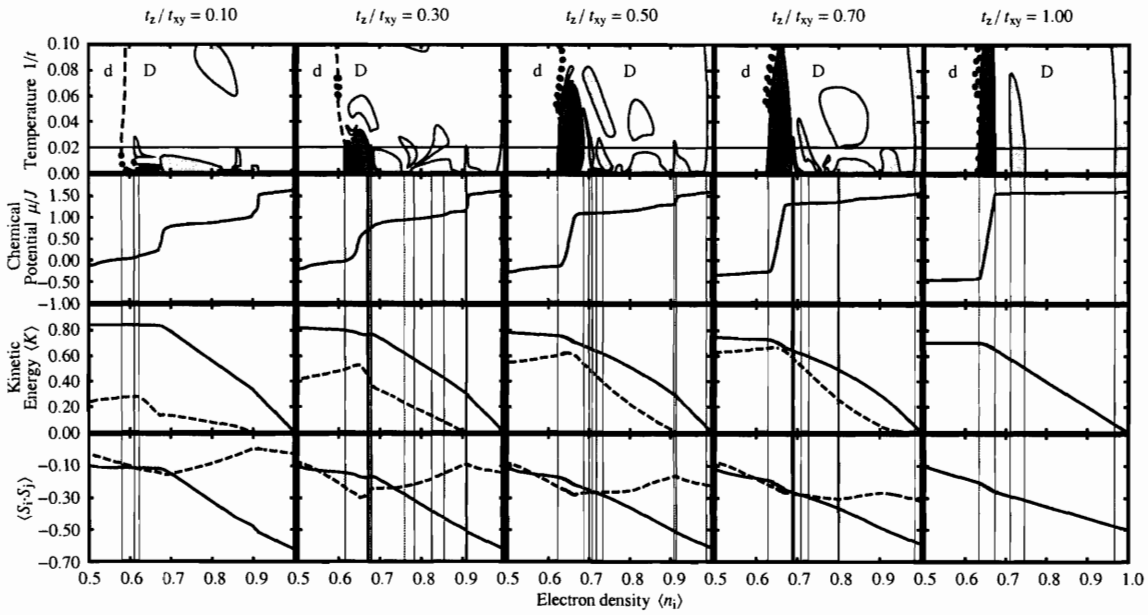

Figure 5-4: Thermodynamic properties along slices of the phase diagrams at the constant temperature $1/t = 0.02$. The degree of anisotropy varies from $t_z/t_{xy} = 0.10$ in the first column to $t_z/t_{xy} = 1.00$ in the last column. The top row contains the temperature vs. electron density phase diagrams and a thin horizontal line marking the slice. The antiferromagnetic and τ phases are colored light and dark gray respectively. The rows below this show the chemical potential μ/J, kinetic energy $\langle K \rangle = -\sum_\sigma \langle c^\dagger_{i\sigma} c_{j\sigma} + c^\dagger_{j\sigma} c_{i\sigma} \rangle$, and nearest-neighbor spin-spin correlation $\langle \mathbf{S}_i \cdot \mathbf{S}_j \rangle$. For the $\langle K \rangle$ and $\langle \mathbf{S}_i \cdot \mathbf{S}_j \rangle$ graphs, full curves denote results for nearest neighbors along the xy plane, while dashed curves denote those for nearest neighbors along the z direction. (In the $t_z/t_{xy} = 1$ column, these two curves overlap.) Thin vertical lines mark the location of phase transitions.

Figs. 5-2 and 5-3 clearly demonstrate that the τ phase is not unique to the isotropic $d = 3$ case, but exists at all values of t_z/t_{xy}, even persisting in the weak interplane coupling limit. Fig. 5-2 shows the evolution of the phase diagram in the strongly anisotropic regime, for t_z/t_{xy} between 0.05 and 0.30, while Fig. 5-3 completes the evolution from $t_z/t_{xy} = 0.5$ to the fully isotropic case where $t_z/t_{xy} = 1$. The τ phase is present even for $t_z/t_{xy} = 0.05$ and 0.10, but only at very low temperatures close to the d/D first-order phase transition that itself is distinct by its very narrow coexistence region. As the interplane coupling is increased, the τ phase transition temperatures also get larger, but the density range in which the phase occurs, namely $\langle n_i \rangle$ around 0.65, remains unchanged.

As expected, the antiferromagnetic transition temperatures also increase with the

interplane coupling. The phase diagrams all share an antiferromagnetic region near $\langle n_i \rangle = 1$, which is confined to $\langle n_i \rangle$ very close to 1 in the strongly anisotropic limit, but becomes more stable to hole doping as t_z/t_{xy} gets larger. Away from $\langle n_i \rangle = 1$, in the range of 5-35% hole doping, there are thin slivers and islands of antiferromagnetism separated by regions of the dense disordered phase. For $t_z/t_{xy} = 1$, we see these mostly around the τ phase, but as anisotropy is introduced into the system, the structure of the antiferromagnetic regions becomes more complex, and spread out over a wider range of densities. The lamellar structure of A and D phases hereB potentially indicates an underlying incommensurate order [5]. The physical significance of this possibility will be discussed below.

Further insight into the nature of the τ phase can be gained by looking at thermodynamic densities on a constant-temperature slice of the phase diagram. Fig. 5-4 plots the chemical potential μ/J, kinetic energy $\langle K \rangle$, and nearest-neighbor spin-spin correlation $\langle \mathbf{S}_i \cdot \mathbf{S}_j \rangle$ at the temperature $1/t = 0.02$ for several values of t_z/t_{xy}. Averages over the xy bonds, $\langle\ \rangle_{xy}$ are drawn with full curves in the figure, and averages taken over the z bonds, $\langle\ \rangle_z$ are drawn with dashed curves.

Consider first the kinetic energy expectation value $\langle K \rangle = -\sum_\sigma \langle c^\dagger_{i\sigma} c_{j\sigma} + c^\dagger_{j\sigma} c_{i\sigma} \rangle$. The xy bond kinetic energy $\langle K \rangle_{xy}$ grows with hole doping until the density range where the τ phase occurs, and then levels off. This behavior is seen for the whole range of t_z/t_{xy}. In our earlier study [7] we related $\langle K \rangle$ to the density of free carriers, and showed that the saturation of this quantity in the overdoped regime resembles experimental results in high-T_c materials. As for $\langle K \rangle_z$, it is significantly reduced with increasing anisotropy, since interplane hopping is suppressed. $\langle K \rangle_z$ peaks in the τ phase, and decreases for larger dopings.

This small peak in $\langle K \rangle_z$, which is most pronounced in the strongly anisotropic regime, is accompanied by an enhancement in the τ phase of the z-bond antiferromagnetic nearest-neighbor spin-spin correlation, $\langle \mathbf{S}_i \cdot \mathbf{S}_j \rangle_z$. For the xy planes, $\langle \mathbf{S}_i \cdot \mathbf{S}_j \rangle_{xy}$ generally increases (i.e., becomes less negative) with hole doping from a large negative value near $\langle n_i \rangle = 1$, as additional holes weaken the antiferromagnetic order. This increase becomes much less pronounced when the τ phase is reached, and $\langle \mathbf{S}_i \cdot \mathbf{S}_j \rangle_{xy}$ be-

comes nearly constant for large hole dopings in the strongly anisotropic limit. Rather than increasing with hole doping, $\langle \mathbf{S}_i \cdot \mathbf{S}_j \rangle_z$ shows the opposite behavior in the 10-35% doping range, decreasing and reaching a minimum within the τ phase.

The final aspect of the τ phase worth noting is the large change in chemical potential μ/J over the narrow density range where this phase occurs. This is in contrast to broad regions at smaller hole dopings where the chemical potential change is much shallower, and which correspond to those parts of the phase diagram where A and D alternate. We can see this directly in the phase diagram topology in Figs. 5-2 and 5-3, particularly for larger t_z/t_{xy}. The τ phase has a very wide extent in terms of chemical potential, but becomes very narrow in the corresponding electron density diagram. The converse is true for the complex lamellar structure of A and D phases sandwiched between the τ phase and the main antiferromagnetic region near $\langle n_i \rangle = 1$. We shall return to this point in our discussion of the purely two-dimensional results.

5.2.5 The Two-Dimensional Isotropic tJ Model and Chemical Potential Shift

The above analysis leads to a basic question: how do results for a strongly anisotropic $d = 3$ tJ model compare to results obtained directly for the isotropic $d = 2$ system? The latter was studied in Refs. [4, 5], which yielded a phase diagram with only dense and dilute disordered phases, separated by a first-order transition at low temperatures, ending in a critical point, but only for low values of t/J. The absence of any antiferromagnetic order is consistent with the Mermin-Wagner theorem [19]. As seen above, at least a weak coupling in the z direction is required for a finite Néel temperature. What about the absence in $d = 2$ of the τ phase? It turns out that there is a pre-signature of the τ phase in $d = 2$, and it appears exactly where we find the actual phase upon adding the slightest interplane coupling.

The τ phase fixed point is not an a true fixed point of the $d = 2$ recursion relations, but it is a "quasifixed" point in the sense that renormalization-group flows come close, stay in its vicinity for many iterations, before crossing over along the disorder line

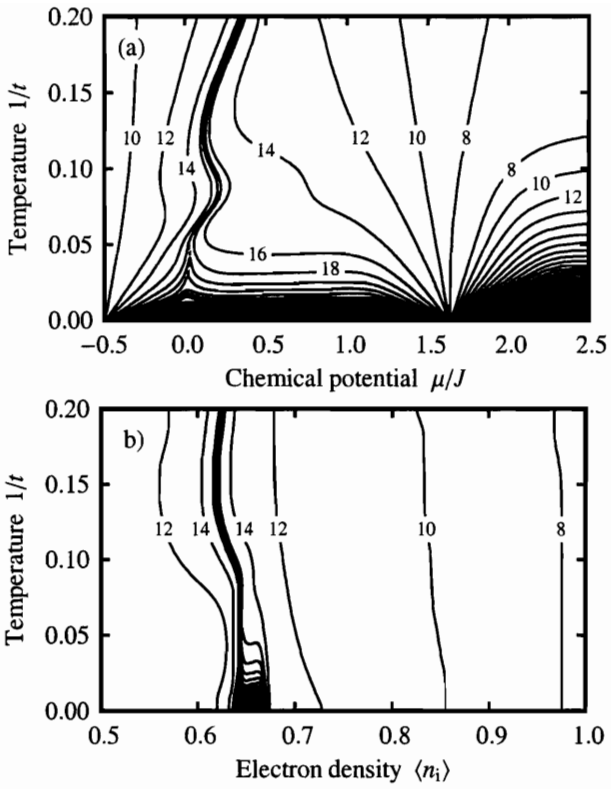

Figure 5-5: Contour diagrams showing the number of iterations required to reach a disordered phase sink in the $d = 2$ isotropic tJ model with $J/t = 0.444$. Fig. 5-5(a) is plotted in terms of temperature vs. chemical potential, while Fig. 5-5(b) is in terms of temperature vs. electron density.

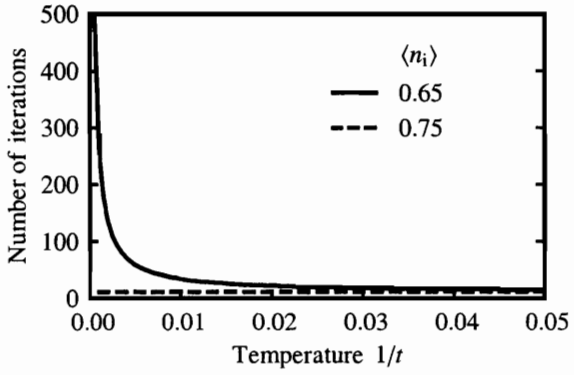

Figure 5-6: Number of iterations required to reach a disordered phase sink in the $d = 2$ isotropic tJ model, plotted as a function of temperature for two different values of $\langle n_i \rangle$.

to one of the disordered sinks. This is particularly true for low temperatures, where the quasifixed point is essentially indistinguishable numerically from a real one. This may be an artifact of the Migdal-Kadanoff approximation, as it is also seen when the approximation is applied to the $d = 2$ XY model, giving a quasifixed-line behavior where one expects an actual fixed line [20, 21]. Nevertheless, since regions of the phase diagram which are approximately basins of attraction of the quasifixed point are characterized by a sharp rise in the number of iterations required to reach the disordered sinks, we can extract useful information by counting these iterations.

We choose a numerical cutoff for when the interaction constants in the rescaled Hamiltonian have come sufficiently close to their limiting values at either the dense or dilute disordered sink. We then count the number of iterations required to meet this cutoff condition for a given initial Hamiltonian. Fig. 5-5 shows the results as contour diagrams, plotted in terms of temperature vs. chemical potential and temperature vs. electron density. There are two clear regions in Fig. 5-5(a) where the number of iterations blows up at low temperatures. The region for μ/J approximately between -0.5 and 1.6 flows to the τ phase quasifixed point. When expressed in terms of electron density in Fig. 5-5(b), this region is centered around a narrow range of densities near $\langle n_i \rangle = 0.65$, which is where the τ phase actually emerges for finite t_z/t_{xy}. The low-temperature region for $\mu/J \gtrsim 1.6$ flows to an antiferromagnetic quasifixed point, but does not appear in the electron density contour diagram because the entire region is mapped to $\langle n_i \rangle$ infinitesimally close to 1. This is similar to what we see in the anisotropic model for low t_z/t_{xy}, where the antiferromagnetic region is stable to only very small hole doping away from $\langle n_i \rangle = 1$, but gradually spreads to larger doping values as the interplane coupling is increased. Fig. 5-6 shows the quasifixed point behavior in another way, by plotting the number of renormalization-group iterations as a function of temperature, for two different $\langle n_i \rangle$. For $\langle n_i \rangle = 0.65$, in the τ phase range, the number of iterations diverges as temperature is decreased. In contrast, for $\langle n_i \rangle = 0.75$, not in the τ phase range, the number is nearly constant at all temperatures. In summary, we see that the $d = 2$ results are compatible with the small t_z/t_{xy} limit of the anisotropic model. A weak interplane coupling stabilizes both

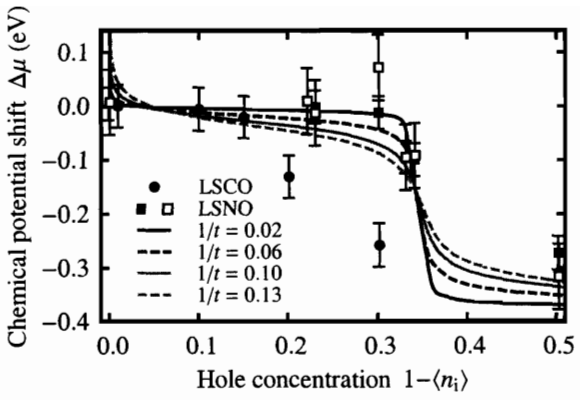

Figure 5-7: The calculated chemical potential shift $\Delta\mu$ is plotted as a function of hole concentration $1-\langle n_i\rangle$ for the isotropic $d = 2\,tJ$ model, at four different temperatures. For comparison with experimental results, the energy scale $\tilde{t} = 0.1$ eV is chosen. With this scale, the temperatures $1/t = 0.02$, 0.06, 0.10 and 0.13 correspond to 23, 70, 116, and 151 K respectively. Experimental values for $\Delta\mu$ determined from x-ray photoemission spectra at $\sim$ 80 K are shown for the cuprate $La_{2-x}Sr_xCuO_4$ (LSCO, filled circles) [22] and the nickelate $La_{2-x}Sr_xNiO_4$ (LSNO, filled squares) [23]. For LSNO we also show another experimental estimate based on ultraviolet photoemission spectra (open squares), taken at 150 K, except for the datapoint at zero hole concentration, which was taken at 230 K [23].

the τ and antiferromagnetic phases, yielding finite transition temperatures.

We mentioned earlier that the lamellar structure of A and D phases which appears in the anisotropic tJ phase diagram for hole dopings up to the τ phase might be an indicator of incommensurate ordering. It could be a reflection of stripe formation, the segregation of the holes on a microscopic scale into D-like stripes where the hole kinetic energy is minimized, alternating with A-like stripes of antiferromagnetic order. The appearance of stripes is associated with the suppression of the chemical potential shift when the parent insulating system is doped with holes. For example, in the cuprate superconductor $La_{2-x}Sr_xCuO_4$ (LSCO), photoemission measurements of core levels have shown that the chemical potential shifts by a small amount (< 0.2 eV/hole) in the underdoped region, $\delta \equiv 1 - \langle n_i\rangle \lesssim 0.15$, compared to a large shift ($\sim$ 1.5 eV/hole) in the overdoped region, $\delta \gtrsim 0.15$, an observation which has been interpreted as a possible signature of stripes [22]. In non-superconducting systems where the existence of stripes is clearly established, like the nickelate $La_{2-x}Sr_xNiO_4$

(LSNO), we see a qualitatively similar behavior, with the chemical potential shifting significantly only for high-doping ($\delta \gtrsim 0.33$ for LSNO) [23]. For the tJ model, we take the chemical potential shift as $\Delta\mu = \tilde{\mu} - \tilde{\mu}_0$, where $\tilde{\mu}_0$ is the chemical potential below which $\langle n_i \rangle$ begins to the decrease noticeably from 1 in the low temperature limit. Fig. 5-7 shows our calculated $\Delta\mu$ vs. hole concentration for the $d = 2$ tJ model at four different temperatures. In order to compare with the experimental data for LSCO and LSNO, we choose an energy scale $\tilde{t} = 0.1$ eV. For the low-doping region, where interplane coupling generates a lamellar structure of A and D phases, the slope of the $\Delta\mu$ curve remains small. On the other hand, for high-doping, in the range of densities corresponding to the τ phase, $\Delta\mu$ turns steeply downward. The similarities between this behavior and the experimental data supports the idea of stripe formation in the low-doping region.

References

[1] E. Dagotto, Rev. Mod. Phys. **66**, 763 (1994).

[2] M. Imada, A. Fujimori, and Y. Tokura, Rev. Mod. Phys. **70**, 1039 (1998).

[3] S. Chakravarty, H.-Y. Kee, and K. Völker, Nature **428**, 53 (2004).

[4] A. Falicov and A.N. Berker, Phys. Rev. B **51**, 12458 (1995).

[5] A. Falicov and A.N. Berker, Turk. J. Phys. **19**, 127 (1995).

[6] M. Hinczewski and A.N. Berker, cond-mat/0503226.

[7] M. Hinczewski and A.N. Berker, cond-mat/0503631.

[8] A. Erbaş, A. Tuncer, B. Yücesoy, and A.N. Berker, ITU-MIT-Gürsey preprint (2005).

[9] A.A. Migdal, Zh. Eksp. Teor. Fiz. **69**, 1457 (1975) [Sov. Phys. JETP **42**, 743 (1976)].

[10] L.P. Kadanoff, Ann. Phys. (N.Y.) **100**, 359 (1976).

[11] A.N. Berker and S. Ostlund, J. Phys. C **12** 4961 (1979).

[12] R.B. Griffiths and M. Kaufman, Phys. Rev. B **26**, 5022 (1982).

[13] M. Suzuki and H. Takano, Phys. Lett. A **69**, 426 (1979).

[14] H. Takano and M. Suzuki, J. Stat. Phys. **26**, 635 (1981).

[15] A.N. Berker, S. Ostlund, and F.A. Putnam, Phys. Rev. B **17**, 3650 (1978).

[16] R. Shankar and V.A. Singh, Phys. Rev. B **43**, 5616 (1991).

[17] C. Bernhard, J.L. Tallon, T. Blasius, A. Golnik, and C. Niedermayer, Phys. Rev. Lett. **86**, 1614 (2001).

[18] A.V. Puchkov, P. Fournier, T. Timusk, and N.N. Kolesnikov, Phys. Rev. Lett. **77**, 1853 (1996).

[19] N.D. Mermin and H. Wagner, Phys. Rev. Lett. **17**, 1133 (1966).

[20] J.V. José, L.P. Kadanoff, S. Kirkpatrick, and D.R. Nelson, Phys. Rev. B **16**, 1217 (1977).

[21] A.N. Berker and D.R. Nelson, Phys. Rev. B **19**, 2488 (1979).

[22] A. Ino, T. Mizokawa, A. Fujimori, K. Tamasaku, H. Eisaki, S. Uchida, T. Kimura, T. Sasagawa, and K. Kishio, Phys. Rev. Lett. **79**, 2101 (1997).

[23] M. Satake, K. Kobayashi, T. Mizokawa, A. Fujimori, T. Tanabe, T. Katsufuji, and Y. Tokura, Phys. Rev. B **61**, 15515 (2000).

Chapter 6

Adding Disorder, Part I: Hierarchical-Lattice Ising Spin-Glasses

6.1 Introduction

The final element we would like to incorporate into our lattice fermion models is quenched randomness, to simulate the effect of substituting impurities like Zn or Ni for the copper atoms in the CuO_2 planes of high-temperature superconductors. Dealing with randomness through a position-space renormalization-group transformation poses substantial new challenges, because the quantity we focus on is not an individual set of interaction constants in the Hamiltonian, but the probability distribution describing those constants. Since this entails a completely different framework for implementing the renormalization-group transformation, it is useful to start with a much simpler, yet of high current interest, classical system like the Ising spin-glass, to gain fluency in the techniques that will be necessary to tackle the more complex problem of randomness in a quantum lattice conduction model.

A recent conjecture by Takeda, Sasamoto, and Nishimori [1] provides the perfect opportunity to demonstrate the power and versatility of position-space renormalization-

group methods applied to random systems. The conjecture relates the locations of multicritical points in Ising spin-glasses for pairs of mutually dual lattices. For most lattice types it is impossible to get precise information about spin-glass phase diagram properties, but our renormalization-group approach is actually exact for hierarchical lattices, so we can carefully test the conjecture on dual pairs of such lattices. In the three cases we look at, we find the conjecture is only approximately satisfied. The following section presents the details of our calculation, where the basic procedure—the bond-moving and decimation convolutions, the binning of the probability distributions—will be later extended to the quenched random tJ model in Chapter 7.

6.2 Multicritical Point Relations in Three Dual Pairs of Hierarchical-Lattice Ising Spin-Glasses

Michael Hinczewski and A. Nihat Berker
Department of Physics, Istanbul Technical University,
Maslak 34469, Istanbul, Turkey,
Department of Physics, Massachusetts Institute of Technology,
Cambridge, Massachusetts 02139, U.S.A.,
Feza Gürsey Research Institute, TÜBITAK - Bosphorus University,
Çengelköy 81220, Istanbul, Turkey

Abstract

The Ising spin-glasses are investigated on three dual pairs of hierarchical lattices, using exact renormalization-group transformation of the quenched bond probability distribution. The goal is to investigate a recent conjecture which relates, on such pairs of dual lattices, the locations of the multicritical points, which occur on the Nishimori symmetry line. Towards this end we precisely determine the global phase diagrams for these six hierarchical spin-glasses, using up to 2.5×10^9 probability bins to represent the quenched distribution subjected to an exact renormalization-group transformation. We find in all three cases that the conjecture is realized to a very good approximation, even when the mutually dual models belong to different spatial dimensionalities d and have different phase diagram topologies at the multicritical points of the conjecture and even though the contributions to the conjecture from each lattice of the dual pair are strongly asymmetric. In all six phase diagrams, we find reentrance near the multicritical point. In the models with $d = 2$ or 1.5, the spin-glass phase does not occur and the phase boundary between the ferromagnetic and paramagnetic phases is second order with a strong violation of universality.

PACS numbers: 75.10.Nr, 64.60.Kw, 05.45.Df, 05.10.Cc

arXiv: cond-mat/0507293

6.2.1 Introduction

The phase diagram structure of spin-glasses remains an open field of inquiry, since most approaches to the problem rely on approximations. Any exact analytical result in this area is thus very valuable, both for the direct information it provides and as a test for approximation methods. Over the last few years striking progress has been made combining the replica method, duality, and symmetry arguments [2, 3, 4, 5, 1], an approach which has yielded the exact locations of the multicritical points in the Ising and Potts spin-glasses on the square lattice and in the four-dimensional random-plaquette gauge model. The most recent result in this series [1] is a general conjecture relating the multicritical point locations of any spin-glasses on a pair of mutually dual lattices. In support of the conjecture, estimates based on Monte Carlo simulations were given for Ising spin-glasses, in $d = 2$, on the dual pairs of triangular and hexagonal lattices and, in $d = 3$, on the dual pairs of bilinear and lattice-gauge interactions on the cubic lattice. In both cases, within the numerical limitations, the conjecture is approximately satisfied.

We propose here to extensively test the conjecture in an alternative fashion using hierarchical lattices [6, 7, 8], by looking at Ising spin-glasses on mutually dual pairs [9, 10, 11, 12] of such lattices. These constitute ideal testing grounds, since an exact renormalization-group transformation for the quenched bond probability distribution can be constructed for such lattices, yielding global phase diagrams and critical properties. Accordingly, the location of the phase boundaries and of the multicritical points are precisely determined. We thus investigate three pairs of hierarchical lattices, and in the end find that the conjecture is very nearly satisfied for all of them.

6.2.2 The Conjecture

The Ising spin-glass is given by the Hamiltonian

$$-\beta H = \sum_{\langle ij \rangle} J_{ij} s_i s_j \,, \tag{6.1}$$

where $s_i = \pm 1$ at each site i, $\langle ij \rangle$ denotes a sum over nearest-neighbor pairs of sites, and the bond strengths J_{ij} are equal to $+J$ with probability $1-p$ and $-J$ with probability p. The limits $p = 0$ and $p = 1$ correspond to purely ferromagnetic and purely antiferromagnetic systems respectively.

To give a brief overview of the conjecture, let us consider the model on an arbitrary lattice, and treat the randomness through the replica method, where the system is replicated n times and the $n \to 0$ limit is eventually taken, in order to get results for the physical system. The partition function of the n-replicated system after averaging over randomness, Z_n, can be expressed entirely as a function of $n+1$ "averaged" combinations of edge Boltzmann factors, $e^{\pm J}$, associated with nearest-neighbor bonds [4, 5]. These averaged Boltzmann factors, $x_k(p, J)$, $k = 0, \ldots, n$, have the form

$$x_k(p, J) = pe^{-(n-k)J}e^{kJ} + (1-p)e^{(n-k)J}e^{-kJ}\,, \tag{6.2}$$

where the kth factor corresponds to a configuration with a parallel-spin bond in $n-k$ replicas and an antiparallel-spin bond in k replicas [1]. Thus,

$$Z_n = Z_n(x_0(p, J),\, x_1(p, J),\, \ldots,\, x_n(p, J))\,. \tag{6.3}$$

The partition function on the dual lattice, Z_n^*, can be expressed in a similar form,

$$Z_n^* = Z_n^*(x_0^*(p, J),\, x_1^*(p, J),\, \ldots,\, x_n^*(p, J))\,, \tag{6.4}$$

with the dual counterparts to the averaged Boltzmann factors given by

$$\begin{aligned} x_{2k}^*(p, J) &= \left(\frac{e^{-J}+e^{J}}{\sqrt{2}}\right)^{n-2k}\left(\frac{e^{-J}-e^{J}}{\sqrt{2}}\right)^{2k}\,, \\ x_{2k+1}^*(p, J) &= (2p-1)\left(\frac{e^{-J}+e^{J}}{\sqrt{2}}\right)^{n-2k-1}\left(\frac{e^{-J}-e^{J}}{\sqrt{2}}\right)^{2k+1}\,, \end{aligned} \tag{6.5}$$

for $0 \le 2k < 2k+1 \le n$. Z_n and Z_n^* are related as [1]

$$Z_n(x_0(p, J),\, \ldots,\, x_n(p, J)) = 2^a Z_n^*(x_0^*(p, J),\, \ldots,\, x_n^*(p, J))\,, \tag{6.6}$$

where a is a constant, which can be eliminated by using Eq. (6.6) evaluated at two different sets of parameters, (p_1, J_1) and (p_2, J_2), giving a relationship of the form

$$\begin{aligned} &Z_n(x_0(p_1, J_1), \ldots, x_n(p_1, J_1)) Z_n^*(x_0(p_2, J_2), \ldots, x_n(p_2, J_2)) \\ &= Z_n^*(x_0^*(p_1, J_1), \ldots, x_n^*(p_1, J_1)) Z_n(x_0^*(p_2, J_2), \ldots, x_n^*(p_2, J_2)) \,. \end{aligned} \tag{6.7}$$

The individual partition functions Z_n can be rewritten by extracting x_0, the averaged Boltzmann factor corresponding to an all-parallel spin state, thus effectively measuring the energy of the system relative to this state [4]:

$$Z_n(x_0, x_1, \ldots, x_n) = x_0^{N_B} \mathcal{Z}_n(u_1, u_2, \ldots, u_n) \,, \tag{6.8}$$

where N_B is the number of bonds in the lattice, and the reduced variables are $u_i \equiv x_i/x_0$. Eq. (6.7) becomes

$$\begin{aligned} &[x_0(p_1, J_1) x_0(p_2, J_2)]^{N_B} \mathcal{Z}_n(u_1(p_1, J_1), \ldots, u_n(p_1, J_1)) \mathcal{Z}_n^*(u_1(p_2, J_2), \ldots, u_n(p_2, J_2)) \\ &= [x_0^*(p_1, J_1) x_0^*(p_2, J_2)]^{N_B} \mathcal{Z}_n^*(u_1^*(p_1, J_1), \ldots, u_n^*(p_1, J_1)) \mathcal{Z}_n(u_1^*(p_2, J_2), \ldots, u_n^*(p_2, J_2)) \,. \end{aligned} \tag{6.9}$$

In general, the form of Eq. (6.9) is too complicated to yield useful information relating the locations of phase transitions. However, the multicritical points in both original and dual systems are expected to lie [13, 14, 15] on the Nishimori line [2], which simplifies the relation. Furthermore, the conjecture advanced in Ref. [1] states that, for the multicritical points (p_{1m}, J_{1m}) of the original system and (p_{2m}, J_{2m}) of its dual, Eq. (6.9) is satisfied when the leading Boltzmann factors x_0 from each side are equal,

$$x_0(p_{1m}, J_{1m}) x_0(p_{2m}, J_{2m}) = x_0^*(p_{1m}, J_{1m}) x_0^*(p_{2m}, J_{2m}) \,. \tag{6.10}$$

Since (p_{1m}, J_{1m}) and (p_{2m}, J_{2m}) lie on the Nishimori line,

$$e^{2J_{1m}} = \frac{1 - p_{1m}}{p_{1m}} \,, \qquad e^{2J_{2m}} = \frac{1 - p_{2m}}{p_{2m}} \,. \tag{6.11}$$

From Eqs. (6.2) and (6.5), Eq. (6.10) gives

$$(p_{1m}^{n+1} + (1 - p_{1m})^{n+1})(p_{2m}^{n+1} + (1 - p_{2m})^{n+1}) = 2^{-n} . \tag{6.12}$$

Finally taking the limit, $n \to 0$, one obtains the condition

$$H(p_{1m}) + H(p_{2m}) = 1 , \tag{6.13}$$

where $H(p) \equiv -p \log_2 p - (1-p) \log_2 (1-p)$. As expressed in Eq. (6.13), the conjecture is asserted to hold for multicritical points of Ising spin-glasses on any pair of mutually dual lattices [1].

6.2.3 The Multitude of Ising Spin-Glasses on Hierarchical Lattices

Hierarchical lattices [6, 7, 8] are constructed by replacing every single bond, in a connected cluster of bonds, with the connected cluster of bonds itself, and repeating this step an infinite number of times. These provide models exactly solvable by renormalization group, with which complex problems have been studied and understood. For example, frustrated [16], spin-glass [17], random-bond [18] and random-field [19], Schrödinger equation [20], lattice-vibration [21], dynamic scaling [22], aperiodic magnet [23], complex phase diagram [24], and directed-path [25] systems, etc., have been solved on hierarchical lattices.

To test the conjecture of Eq. (6.13), we study Ising spin-glasses on the dual pairs of hierarchical lattices, depicted in Figs. 6-1, 6-2, and 6-3. Each lattice in a given pair is the dual of the other. These particular choice of lattices are motivated by their properties under renormalization-group transformation as related to physical lattices. The hierarchical lattices of Fig. 6-1(a) and (b) yield the two variants of the Migdal-Kadanoff recursion relations [26, 27] for dimension $d = 2$ with length rescaling factor $b = 3$. Similarly, the lattice in Fig. 6-2(a) yields a Migdal-Kadanoff recursion relation for $d = 3$, $b = 3$. Its dual lattice in Fig. 6-2(b) has $d = 1.5, b = 9$. (The two variants

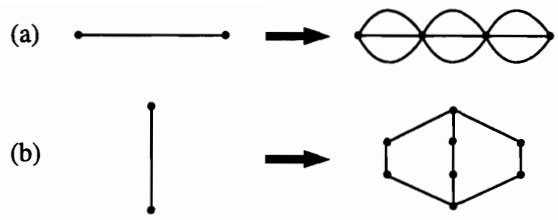

Figure 6-1: The pair of mutually dual hierarchical lattices on which the $d = 2$, $b = 3$ Migdal-Kadanoff recursion relations are exact.

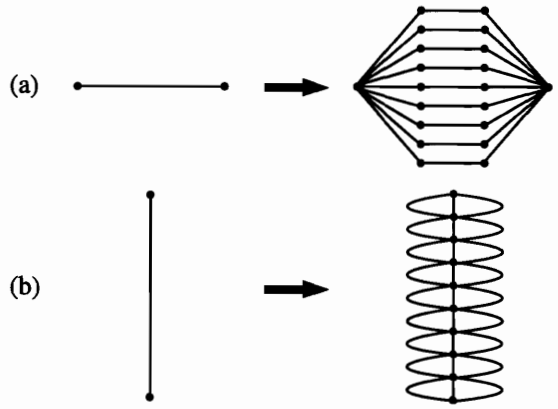

Figure 6-2: Another pair of mutually dual hierarchical lattices. The Migdal-Kadanoff recursion relations are exact for lattice (a) with $d = 3$, $b = 3$. Its dual lattice, in (b), has $d = 1.5$, $b = 9$.

of the Migdal-Kadanoff recursion relations correspond to mutually dual hierarchical lattices only in $d = 2$.) Lastly, the hybrid lattice in Fig. 6-3(a) is interesting because it has been shown to give very accurate results for the critical temperatures of the $d = 3$ isotropic and anisotropic Ising model [28]. This lattice has $d = 3, b = 3$, while its dual in Fig. 6-3(b) has $d = 1.5, b = 9$.

6.2.4 Exact Renormalization-Group Transformation of Hierarchical Spin-Glasses

For a pure system, the renormalization-group transformation on a hierarchical lattice consists of a decimation by summing over the internal sites in each of the connected clusters making up the lattice (the right-hand sides of Figs. 6-1-6-3). Thus, the hierarchical lattice construction process is reversed, as each connected cluster is replaced

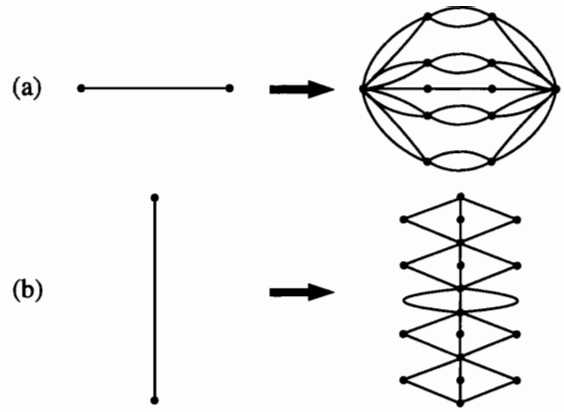

Figure 6-3: Another pair of mutually dual hierarchical lattices, with $d = 3$, $b = 3$ and $d = 1.5$, $b = 9$ respectively.

by a single renormalized bond. The decimation can be expressed as a mapping,

$$J'_{i'j'} = R(\{J_{ij}\}) \,, \tag{6.14}$$

where the set $\{J_{ij}\}$ are all the bonds within the connected cluster of the original system and $J'_{i'j'}$ is the renormalized bond between sites i' and j' of the rescaled system. In the pure case, all J_{ij} bonds are independent for ij, and the implementation of Eq. (6.14) is straightforward.

When quenched randomness is added to the system, the renormalization-group transformation is expressed in terms of quenched probability distributions [18], where the quenched probability distribution $\mathcal{P}'(J'_{i'j'})$ in the rescaled system is calculated from $\mathcal{P}(J_{ij})$ in the original system through the convolution

$$\mathcal{P}'(J'_{i'j'}) = \int \left[\prod_{ij}^{i'j'} dJ_{ij}\, \mathcal{P}(J_{ij}) \right] \delta \left(J'_{i'j'} - R(\{J_{ij}\}) \right) \,. \tag{6.15}$$

Here the product runs over all the bonds ij in the connected cluster of the original system between sites i' and j'.

The recursion of the quenched probability distribution, Eq. (6.15), is implemented numerically. The probability distribution is represented by histograms, each histogram being specified by a bond strength and an associated probability. Thus, for

the spin-glass problem, the starting distribution consists of two histograms, one at J with probability $1-p$, and one at $-J$ with probability p. Eq. (6.15) dictates the convolution of 9 probability distributions for the lattices of Fig. 6-1, and the convolution of 27 distributions for the lattices of Figs. 6-2 and 6-3. In this task, computational storage limits can be maximally exploited by factorizing Eq. (6.15) into an equivalent series of pairwise convolutions, each of which involves only two distributions convoluted using an appropriate R function. The types of pairwise convolutions needed are a "bond-moving" convolution, with

$$R_{\rm bm}(J_{i_1 j_1}, J_{i_2 j_2}) = J_{i_1 j_1} + J_{i_2 j_2}\,, \tag{6.16}$$

and a decimation convolution, with

$$R_{\rm dc}(J_{i_1 j_1}, J_{i_2 j_2}) = \frac{1}{2}\ln\left[\frac{\cosh(J_{i_1 j_1} + J_{i_2 j_2})}{\cosh(J_{i_1 j_1} - J_{i_2 j_2})}\right]\,, \tag{6.17}$$

which is just the standard decimation transformation for a two-bond Ising segment.

Consider the hierarchical lattice in Fig. 6-1(a). If $\mathcal{P}_{\rm init}$ is the initial probability distribution, a series of pairwise convolutions which yields the total convolution of Eq. (6.15) for this lattice is: (i) a bond-moving convolution of $\mathcal{P}_{\rm init}$ with itself, yielding $\mathcal{P}_1$; (ii) a bond-moving convolution of $\mathcal{P}_1$ with $\mathcal{P}_{\rm init}$, yielding $\mathcal{P}_2$; (iii) a decimation convolution of $\mathcal{P}_2$ with itself, yielding $\mathcal{P}_3$; (iv) a decimation convolution of $\mathcal{P}_3$ with $\mathcal{P}_2$, yielding $\mathcal{P}_{\rm final}$. For the lattice in Fig. 6-2(a), the series is: (i) a decimation convolution of $\mathcal{P}_{\rm init}$ with itself, yielding $\mathcal{P}_1$; (ii) a decimation convolution of $\mathcal{P}_1$ with $\mathcal{P}_{\rm init}$, yielding $\mathcal{P}_2$; (iii) a bond-moving convolution of $\mathcal{P}_2$ with itself, yielding $\mathcal{P}_3$; (iv) a bond-moving convolution of $\mathcal{P}_3$ with itself, yielding $\mathcal{P}_4$; (v) a bond-moving convolution of $\mathcal{P}_4$ with itself, yielding $\mathcal{P}_5$; (vi) a bond-moving convolution of $\mathcal{P}_5$ with $\mathcal{P}_2$, yielding $\mathcal{P}_{\rm final}$. For the lattice in Fig. 6-3(a), the series is: (i) a bond-moving convolution of $\mathcal{P}_{\rm init}$ with itself, yielding $\mathcal{P}_1$; (ii) a decimation convolution of $\mathcal{P}_1$ with itself, yielding $\mathcal{P}_2$; (iii) a decimation convolution of $\mathcal{P}_2$ with $\mathcal{P}_1$, yielding $\mathcal{P}_3$; (iv) a bond-moving convolution of $\mathcal{P}_3$ with itself, yielding $\mathcal{P}_4$; (v) a bond-moving convolution of $\mathcal{P}_4$ with itself, yielding $\mathcal{P}_5$; (vi) a decimation convolution of $\mathcal{P}_{\rm init}$ with itself, yielding $\mathcal{P}_6$; (vii) a decimation

convolution of $\mathcal{P}_6$ with $\mathcal{P}_{\text{init}}$, yielding $\mathcal{P}_7$; (viii) a bond-moving convolution of $\mathcal{P}_7$ with $\mathcal{P}_5$, yielding $\mathcal{P}_{\text{final}}$. As for the dual lattices in Figs. 6-1(b), 6-2(b), and 6-3(b), the series of pairwise convolutions are identical to their counterparts above, except that each bond-moving is replaced by a decimation, and vice versa.

Since the number of histograms that constitute the probability distribution increases rapidly with each renormalization iteration, a binning procedure is used when the desired (large, namely up to 2.5×10^9) number of histograms is reached: Before every pairwise convolution, the histograms are placed on a grid, and all histograms falling into the same grid cell are combined into a single histogram in such a way that the average and the standard deviation of the probability distribution are preserved. Histograms falling outside the grid, representing a negligible part of the total probability, are similarly combined into a single histogram. Any histogram within a small neighborhood of a cell boundary is proportionately shared between the adjacent cells. In the current study, the binning procedure is done separately for $J > 0$ and $J < 0$. After the convolution, the original number of histograms is reattained.

In the current study, 40,000 bins are generally used, representing the renormalization-group flows of 80,000 variables, requiring the calculation of 40,000 local renormalization-group transformations at each renormalization-group iteration. The numerical results converge rapidly with increasing bin number. For maximal accuracy in determining the exact locations of the multicritical points, in the immediate vicinity of these points we used at least 1,000,000 histograms, representing the renormalization-group flows of 2,000,000 variables, requiring the calculation of 1,000,000 local renormalization-group transformations at each renormalization-group iteration. It should thus be noted that our analysis is an exact numerical solution of Ising spin-glasses on hierarchical lattices.

6.2.5 Results

Global phase diagrams for the various hierarchical lattices are obtained from the renormalization-group flows of the probability distributions. Each phase has a corresponding sink, namely a completely stable fixed distribution. The boundaries between phases flow to unstable fixed distributions, analysis of which yields the order of the

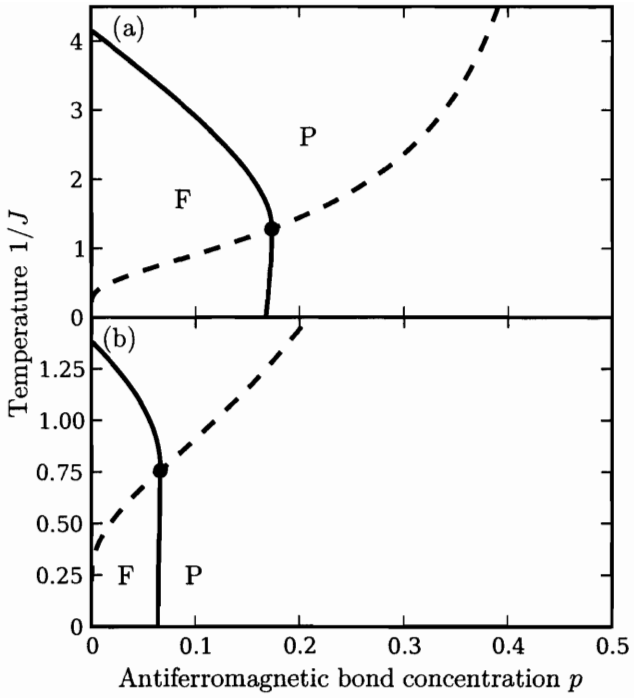

Figure 6-4: Phase diagrams for the two hierarchical lattices in Fig. 6-1, with the solid lines indicating second-order phase transitions between the ferromagnetic (F) and paramagnetic (P) phases. In each diagram the multicritical point, separating two different types of second-order boundary, is marked by a dot, and the Nishimori symmetry line is drawn dashed. The phase diagrams were calculated with 40,000 probability bins, except for the vicinity of the multicritical points, where for higher precision 1,000,000 probability bins were used.

phase transition and the values of the critical exponents of second- and higher-order transitions. All the phase diagrams are plotted in terms antiferromagnetic bond concentration p versus temperature $1/J$. The diagrams are symmetric around $p = 1/2$, with the ferromagnetic phase in the $p < 1/2$ half-space mapping onto the antiferromagnetic phase in the $p > 1/2$ half-space. Thus in the figures only the $p < 1/2$ portions are shown.

Fig. 6-4(a) and (b) show the phase diagrams for the dual pair of hierarchical lattices in Fig. 6-1(a) and (b) respectively. The phase structure of both diagrams is topologically identical to that of the $d = 2$ Ising spin-glass on a square lattice, which is only natural considering that the $d = 2$, $b = 3$ Migdal-Kadanoff recursion relations

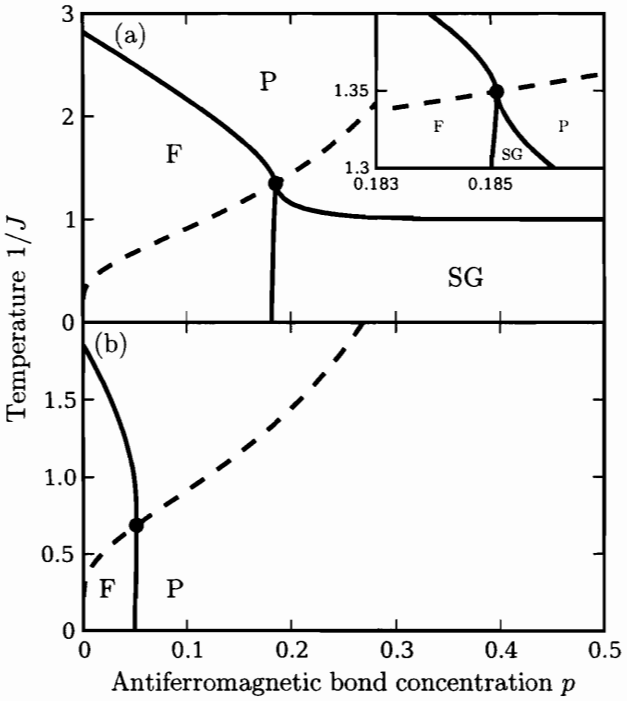

Figure 6-5: Phase diagrams for the two hierarchical lattices in Fig. 6-2, with the solid lines indicating second-order phase transitions between the ferromagnetic (F), paramagnetic (P), and spin-glass (SG) phases. In each diagram the multicritical point is marked by a dot, and the Nishimori symmetry line is drawn dashed. The phase diagrams were calculated with 40,000 probability bins (250,000 bins for the inset in the top figure), except for the vicinity of the multicritical points, where for higher precision 10^6 and 2.5×10^9 probability bins were used in (a) and (b) respectively.

are exact on these hierarchical lattices.[6] The $p = 0$ transition temperatures of the two models are related by the duality algebra [29]

$$\sinh(2J_{1c}) \sinh(2J_{2c}) = 1, \tag{6.18}$$

which is also true for the two other pairs of mutually dual hierarchical models. Furthermore, the $p = 1$ transition temperatures in Fig. 6-4(a) and (b) are related [10] by

$$J_{1c}^{-1} = b^{d-1} J_{2c}^{-1}, \tag{6.19}$$

since the mappings of the interaction constant in the repetition of renormalization-

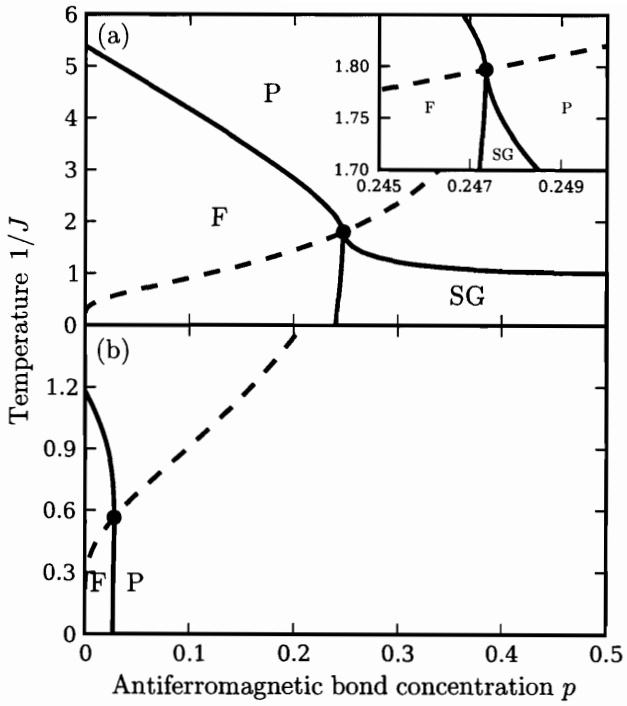

Figure 6-6: Phase diagrams for the two hierarchical lattices in Fig. 6-3, with the solid lines indicating second-order phase transitions between the ferromagnetic (F), paramagnetic (P), and spin-glass (SG) phases. In each diagram the multicritical point is marked by a dot, and the Nishimori symmetry line is drawn dashed. The phase diagrams were calculated with 40,000 probability bins (250,000 bins for the inset in the top figure), except for the vicinity of the multicritical points, where for higher precision 2.5×10^7 and 2.25×10^8 probability bins were used in (a) and (b) respectively.

group transformations differs only by an initial bond strengthening by a factor of b^{d-1}; note that Eq. (6.19) does not apply to $0 < p < 1$, since there the bond-moving is not a mere multiplicative strengthening, but a (b^{d-1})-fold convolution of the probability distributions that alters this distribution in a non-simple way. Eq. (6.19) is also not applicable to the two other pairs of mutually dual models, since the repetition of renormalization-group transformations are not differentiated by only a preliminary bond-moving.

In each of Fig. 6-4(a) and (b), a ferromagnetic phase at low temperatures and low p is separated from the disordered paramagnetic phase by two second-order phase boundaries, meeting at a multicritical point. (In a narrow neighborhood of

Figure	p_{1m}, J_{1m}^{-1}	J_{1N}^{-1}	p_{2m}, J_{2m}^{-1}	J_{2N}^{-1}	$H(p_{1m})$	$H(p_{2m})$	$H(p_{1m}) + H(p_{2m})$
Fig. 6-4	0.1735, 1.2810	1.2810	0.06620, 0.7557	0.7557	0.6656	0.3516	1.0172
Fig. 6-5	0.1851, 1.3494	1.3494	0.05128, 0.68546	0.68545	0.6911	0.2918	0.9829
Fig. 6-6	0.2473, 1.7973	1.7973	0.02796, 0.5636	0.5636	0.8070	0.1840	0.9911

Table 6.1: Locations of the multicritical points in the phase diagrams of Figs. 6-4–6-6 (corresponding to the hierarchical lattices of Figs. 6-1–6-3). J_{iN}^{-1} is the value calculated from p_{im} using Eq. (6.11) for the Nishimori line and turns out equal to J_{im}^{-1}, for both $i = 1$ and 2. The quantities $H(p_{im})$ that enter the conjecture and their sums are also given.

all multicritical points in our results, reentrance is observed: paramagnetic, then ferromagnetic, then paramagnetic or spin-glass phases are encountered as temperature is lowered.) The two second-order boundaries flow to distinct unstable probability distributions with different critical exponents, constituting a strong violation of universality [17] and consistent with the prediction, generally, of the absence of first-order transition under quenched randomness in $d = 2$. [30] As expected from symmetry considerations, the multicritical points fall [13, 14, 15] precisely on the Nishimori line [2] as seen in Table 6.1. As also seen in Table 6.1, $H(p_{1m}) + H(p_{2m}) = 1.0172$, so that the conjecture is realized to a very good approximation.

Fig. 6-5 shows the phase diagrams for the dual pair of hierarchical lattices in Fig. 6-2. While Fig. 6-5(b) has the same phase topology as the diagrams in Fig. 6-4, being at $d = 1.5$ below the spin-glass lower-critical dimension, a different structure occurs in Fig. 6-5(a). Here the $d = 3$, $b = 3$ Migdal-Kadanoff relations are exact on the hierarchical lattice, and for low temperatures in the vicinity of $p = 1/2$ there exists a spin-glass phase. The multicritical point occurs where the ferromagnetic, paramagnetic, and spin-glass phases meet. As expected both multicritical points lie directly on the Nishimori line. From Table 6.1 we see that $H(p_{1m}) + H(p_{2m}) = 0.9829$, so that the conjecture is realized to a very good approximation, even when the mutually dual models belong to different dimensionalities d and have different phase diagram topologies at the multicritical points of the conjecture.

The phase diagram structures in Fig. 6-6, corresponding to the dual pair of hierarchical lattices in Fig. 6-3, are similar to those of Fig. 6-5, illustrating dimensions above and below the spin-glass lower-critical dimension. Again the multicritical points for

both cases lie directly on the Nishimori line. In this case $H(p_{1m}) + H(p_{2m}) = 0.9911$, and the conjecture is realized to a very good approximation, again for mutually dual models belonging to different dimensionalities d and having different phase diagram topologies at the multicritical points of the conjecture.

Thus, we find that for all three mutually dual pairs of hierarchical lattices, the conjecture relating the locations of the multicritical points is satisfied to a very good approximation. This is all the more remarkable, since, as seen in Table 6.1, the contributions of $H(p_{1m})$ and $H(p_{2m})$ to the conjecture are strongly asymmetric. However, it should be noted that (1.0172, 0.9829, 0.9911), while being very close to 1, are different from integer 1. In our numerical implementation of the convolutions of the probability distributions, the results have converged to the precision of the digits shown in Table 6.1. Further increase of the already very large number of probability bins does not change the entries in the table. Further tests of the conjecture, using other systems, would be very useful.

References

[1] K. Takeda, T. Sasamoto, and H. Nishimori, J. Phys. A: Math. Gen. **38**, 3751 (2005).

[2] H. Nishimori, Prog. Theor. Phys. **66**, 1169 (1981).

[3] H. Nishimori and K. Nemoto, J. Phys. Soc. Japan **71**, 1198 (2002).

[4] J.-M. Maillard, K. Nemoto, and H. Nishimori, J. Phys. A: Math. Gen. **36**, 9799 (2003).

[5] K. Takeda and H. Nishimori, Nucl. Phys. B **686**, 377 (2004).

[6] A.N. Berker and S. Ostlund, J. Phys. C **12**, 4961 (1979).

[7] M. Kaufman and R.B. Griffiths, Phys. Rev. B **24**, 496 (1981).

[8] M. Kaufman and R.B. Griffiths, Phys. Rev. B **30**, 244 (1984).

[9] M. Kaufman and D. Andelman, Phys. Rev. B **29**, 4010 (1984).

[10] M. Kaufman, Phys. Rev. B **30**, 413 (1984).

[11] C. Itzykson and J.M. Luck, Proceedings of the Brasov International Summer School (1984).

[12] H. Ottavi and G. Albinet, J. Phys. A **20**, 2961 (1987).

[13] P. Le Doussal and A. Georges, Yale University Report No. YCTP-P1-88 (1988).

[14] P. Le Doussal and A.B. Harris, Phys. Rev. Lett. **61**, 625 (1988).

[15] E.J. Hartford and S.R. McKay, J. Appl. Phys. **70**, 6068 (1991).

[16] S.R. McKay, A.N. Berker, and S. Kirkpatrick, Phys. Rev. Lett. **48**, 767 (1982).

[17] G. Migliorini and A.N. Berker, Phys. Rev. B **57**, 426 (1998).

[18] D. Andelman and A.N. Berker, Phys. Rev. B **29**, 2630 (1984).

[19] A. Falicov, A.N. Berker, and S.R. McKay, Phys. Rev. B **51**, 8266 (1995).

[20] E. Domany, S. Alexander, D. Bensimon, and L.P. Kadanoff, Phys. Rev. B **28**, 3110 (1983).

[21] J.-M. Langlois, A.-M.S. Tremblay, and B.W. Southern, Phys. Rev. B **28**, 218 (1983).

[22] R.B. Stinchcombe and A.C. Maggs, J. Phys. A **19**, 1949 (1986).

[23] T.A.S. Haddad, S.T.R. Pinho, and S.R. Salinas, Phys. Rev. E **61**, 3330 (2000).

[24] J.-X. Le and Z.R. Yang, Phys. Rev. E **69**, 066107 (2004).

[25] R.A. da Silveira and J.-P. Bouchaud, Phys. Rev. Lett. **93**, 015901 (2004).

[26] A.A. Migdal, Zh. Eksp. Teor. Fiz. **69**, 1457 (1975) [Sov. Phys. JETP **42**, 743 (1976)].

[27] L.P. Kadanoff, Ann. Phys. (N.Y.) **100**, 359 (1976).

[28] A. Erbaş, A. Tuncer, B. Yücesoy, and A.N. Berker, Phys. Rev. E **72**, in press (2005).

[29] I. Syozi, in Phase Transitions and Critical Phenomena, C. Domb and M.S. Green, eds. (Academic, London, 1972), vol.1, pp.270-329.

[30] K. Hui and A.N. Berker, Phys. Rev. Lett. **62**, 2507 (1989).

Chapter 7

Adding Disorder, Part II: Quenched Random tJ Model

7.1 Introduction

The electronic properties and phase diagram of high-T_c materials are particularly sensititive to dilute impurities—substitution of $3d$ transition elements (Zn, Ni, Co, Fe), or other metals (Al, Ga), for the Cu atoms of the CuO_2 planes [1]. The interplay between disorder, strong antiferromagnetic correlations in the parent compound, and doped charge carriers, offers a window onto the nature of both the superconducting phase and the normal state above T_c. In the present chapter we focus on the case of a nonmagnetic (spin $S = 0$) impurity like Zn^{2+}, which can be simulated in the tJ model by introducing static vacancies onto the lattice.

The most pronounced effect of Zn substitution in cuprates is the rapid destruction of the superconducting phase [1, 2]; for example in $YBa_2Cu_3O_{7-y}$ the transition temperature is reduced at a rate of $\sim$ 15K/at.% of impurities, so that it takes Zn concentrations of only $\sim$ 6% to entirely eliminate superconductivity [2]. The effects in the metallic region above T_c are equally surprising: nuclear magnetic resonance experiments have found that Zn atoms induce local magnetic moments at nearest-neighbor Cu sites [3], and enhance antiferromagnetic correlations for several lattice spacings around the impurity [4, 5].

As for the antiferromagnetic insulator near half-filling, it is remarkably robust against dilution of the Cu spins. In the half-filled compound $La_2Cu_{1-z}Zn_zO_4$, Zn concentrations of $z \sim 0.4$ are required to reduce the Néel temperature to zero [6], while for lightly hole-doped $La_{2-x}Sr_xCu_{1-z}Zn_zO_4$ (with $x = 0.017$) the Néel temperature actually *increases* with the addition of Zn up to $z = 0.05$, before turning downwards again at higher z [7]. Since the mobile holes introduced by Sr doping are extremely effective at destroying long-range antiferromagnetic order (it only takes $x \sim 0.02$), apparently small amounts of Zn impurities counteract this influence by reducing hole mobility. Of course, at larger concentrations the beneficial role of Zn is outweighed by its negative effect through spin dilution.

We will seek out parallels to these empirical observations in the $d = 3$ tJ model with a quenched random distribution of chemical potentials. We have already done the groundwork for this study in earlier parts of the thesis. Chapter 5 derived the recursion relations for a tJ Hamiltonian with non-uniform bond strengths, and Chapter 6 showed how to construct a renormalization-group transformation for a quenched probability distribution. The calculation in the present chapter is a direct application of these ideas.

7.2 tJ Hamiltonian with Quenched Randomness

The Hamiltonian for our model, expressed as a single lattice summation, is

$$\begin{aligned} -\beta H &= \sum_{\langle ij \rangle} P \left[-t \sum_{\sigma} \left(c^{\dagger}_{i\sigma} c_{j\sigma} + c^{\dagger}_{j\sigma} c_{i\sigma} \right) - J \mathbf{S}_i \cdot \mathbf{S}_j + V n_i n_j + \mu_{ij} (n_i + n_j) \right] P \\ &\equiv \sum_{\langle ij \rangle} \{ -\beta H(i,j) \} , \end{aligned} \tag{7.1}$$

where $P = \prod_i (1 - n_{i\downarrow} n_{i\uparrow})$ is a projection operator prohibiting double occupation of sites. The notation is the same as that of Section 4.2.2, with the only difference being that here the chemical potential μ_{ij} can vary between different pairs of nearest-neighbor sites. To represent the effect of nonmagnetic impurities, the chemi-

cal potentials have a quenched distribution where $\mu_{ij} = \mu$ with probability $1-p$, and $\mu_{ij} = \mu_{\rm imp}$ with probability p. The impurity potential is set to $\mu_{\rm imp}/J = -1000$, and the values of μ/J we explore to calculate phase diagrams satisfy $|\mu/J| \ll |\mu_{\rm imp}/J|$. Thus the strongly repulsive impurity potentials have the effect of creating static vacancies along a fraction p of the bonds in the system.

7.3 Renormalization-Group Transformation

The renormalization-group transformation described below, which involves decimating segments of two consecutive bonds that may have different chemical potentials, will map the initial Hamiltonian of Eq. (7.1) onto a generalized Hamiltonian of the same form as Eq. (5.14),

$$\begin{aligned} -\beta H(i,j) = P\Bigg[& -t_{ij} \sum_{\sigma} \left(c^{\dagger}_{i\sigma} c_{j\sigma} + c^{\dagger}_{j\sigma} c_{i\sigma} \right) - J_{ij} \mathbf{S}_i \cdot \mathbf{S}_j + V_{ij} n_i n_j \\ & + \mu_{ij}(n_i + n_j) + \nu_{ij}(n_i - n_j) + G_{ij} \Bigg] P \,, \end{aligned} \tag{7.2}$$

where now all the bond interaction constants $\mathbf{K}_{ij} \equiv (t_{ij}, J_{ij}, V_{ij}, \mu_{ij}, \nu_{ij})$ are nonuniform, and distributed with a joint probability $\mathcal{P}(\mathbf{K}_{ij})$.

In order to express the renormalization-group transformation in terms of this quenched probability distribution, we adopt the procedure outlined in Chapter 6. We employ the $d = 3$, $b = 2$ Migdal-Kadanoff approximation—a decimation followed by a fourfold bond moving. The resulting recursion relations are exactly realized on the hierarchical lattice shown in Fig. 7-1. The renormalization-group transformation on such a lattice consists of replacing every connected cluster of the kind depicted on the right-hand side of Fig. 7-1 with a single bond, a mapping

$$\mathbf{K}'_{i'j'} = \mathbf{R}(\{\mathbf{K}_{ij}\}) \,, \tag{7.3}$$

where $\{\mathbf{K}_{ij}\}$ is the set of interactions in the connected cluster, and $\mathbf{K}'_{i'j'}$ are the renormalized interactions between sites i' and j' of the rescaled system.

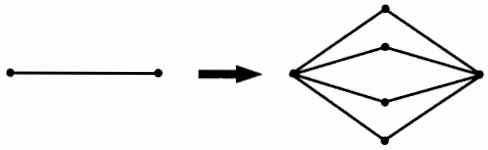

Figure 7-1: Hierarchical lattice on which the $d = 3$, $b = 2$ Migdal-Kadanoff recursion relations are exact.

The probability distribution $\mathcal{P}'(\mathbf{K}'_{i'j'})$ of the renormalized interactions is obtained from the convolution,

$$\mathcal{P}'(\mathbf{K}'_{i'j'}) = \int \left[\prod_{ij}^{i'j'} d\mathbf{K}_{ij}\, \mathcal{P}(\mathbf{K}_{ij}) \right] \delta\left(\mathbf{K}'_{i'j'} - \mathbf{R}(\{\mathbf{K}_{ij}\}) \right) . \tag{7.4}$$

The product inside the integral runs over the eight interactions ij in the connected cluster of the original system between sites i' and j'.

In order to numerically implement the convolution, the probability distributions are represented by histograms, where each histogram is a set of interaction constants (t, J, V, μ, ν) and an associated probability. The full convolution of eight probability distributions in Eq. (7.4) is accomplished through an equivalent series of three pairwise convolutions, each involving only two probability distributions at a time. These pairwise convolutions come in two varieties, distinguished by the $\mathbf{R}$ function used in the integral. The "bond-moving" convolution has

$$\mathbf{R}_{\mathrm{bm}}(\mathbf{K}_{i_1 j_1}, \mathbf{K}_{i_2 j_2}) = \mathbf{K}_{i_1 j_1} + \mathbf{K}_{i_2 j_2} , \tag{7.5}$$

while the decimation convolution function $\mathbf{R}_{\mathrm{dc}}(\mathbf{K}_{i_1 j_1}, \mathbf{K}_{i_2 j_2})$ is identical to the $\mathbf{R}$ function of Eq. (5.16), which is the decimation of a non-uniform two-bond segment defined through Eqs. (5.12)–(5.15). If $\mathcal{P}_{\mathrm{init}}$ is the initial probability distribution, the series of three pairwise convolutions is as follows: (i) a decimation convolution of $\mathcal{P}_{\mathrm{init}}$ with itself, yielding $\mathcal{P}_1$; (ii) a bond-moving convolution of $\mathcal{P}_1$ with itself, yielding $\mathcal{P}_2$; (iii) a bond-moving convolution of $\mathcal{P}_2$ with itself, yielding $\mathcal{P}_{\mathrm{final}}$.

As in Chapter 6, the probability distributions are binned before every pairwise convolution, to ensure that there is an upper bound on the number of histograms

as we iterate the renormalization-group transformation. However, unlike the Ising-type decimation used for the hierarchical-lattice spin-glasses, calculating $\mathbf{R}_{dc}$ for the tJ system is computationally expensive, particularly since the arithmetic must be done at large precision in order to get accurate results when the interaction constants blow up near a phase sink. For efficiency, we use a coarser grid in the binning procedure, partitioning each of the five axes in our interaction space into four regions, for a total of $4^5 = 1024$ grid cells. In principle we would then have to evaluate $\mathbf{R}_{dc}$ up to $1024^2 \approx 10^6$ times at each renormalization-group step. The number of such steps needed for the interaction constants in the renormalized system to clearly approach one of the phase sinks is on the order of 10. And to draw a detailed phase diagram typically requires determining the phases of at least 5000 points. Thus if every evaluation of $\mathbf{R}_{dc}$ takes about 0.01 s on a Pentium 4 processor, we have to expend a staggering 17 years of computation time to get a single phase diagram.

Fortunately, most of the weight of the probability distributions is carried by a small fraction of the histograms. We follow up the binning procedure by culling the histograms: the ones with the 100 largest probabilities are kept, while the others are collapsed into a single histogram in such a way that the average and standard deviation of the probability distribution are unchanged. This culling is only done before the decimation convolution, since the computational costs for the bond-moving convolutions are negligible. We now need to evaluate 10^4 local renormalization-group transformations at every step, so generating a phase diagram takes weeks, not years. The diagrams presented in the next section were calculated using eight processors of a Pentium 4 cluster at the TÜBİTAK Feza Gürsey Research Institute.

7.4 Results

We looked at small concentrations of impurity bonds, $p = 0.01$, 0.02, and 0.03, for the tJ Hamiltonian of Eq. (7.1) with $J/t = 0.444$ and $V/J = 0.25$. Phase diagrams in terms of chemical potential μ/J versus temperature $1/t$ are shown in Figs. 7-2(b)–(d). For comparison, Fig. 7-2(a) shows the phase diagram of the pure ($p = 0$) system.

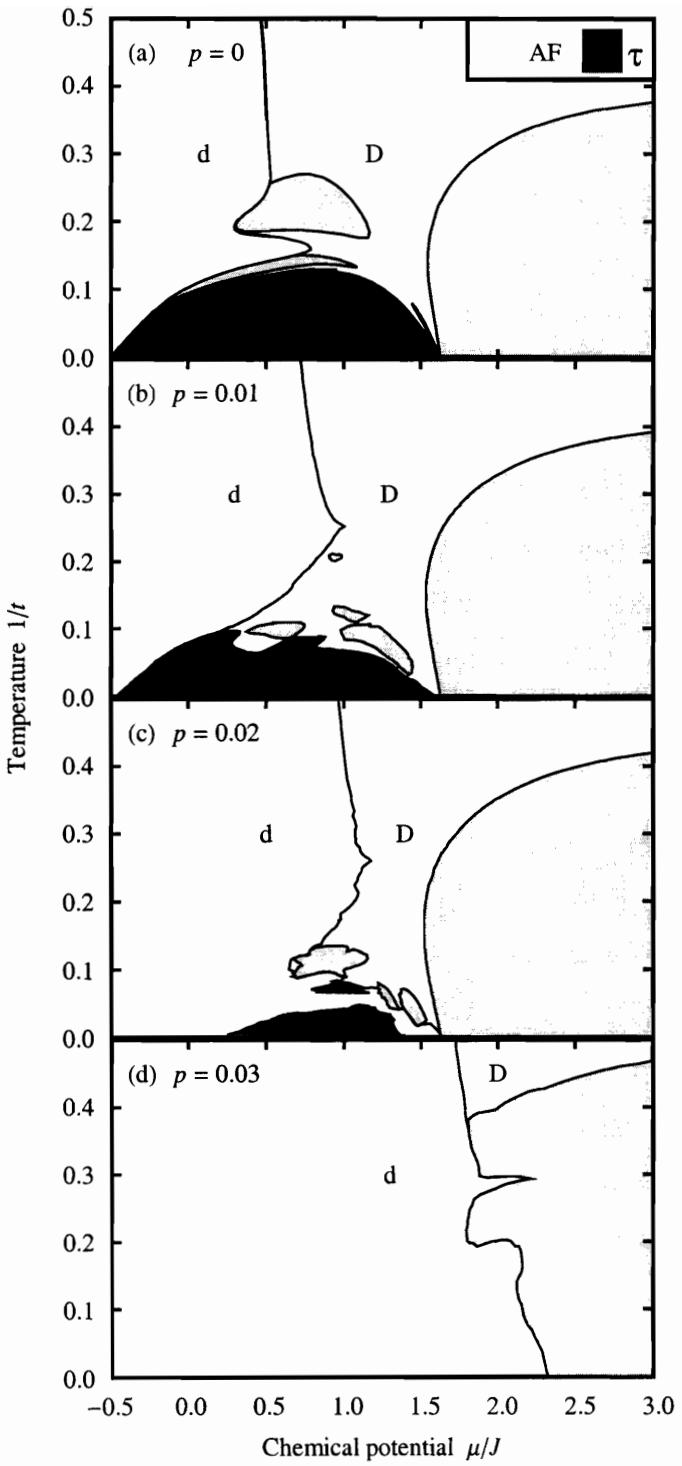

Figure 7-2: Phase diagrams of the $d = 3$ tJ model for small values of the impurity concentration p, plotted in terms of chemical potential μ/J versus temperature $1/t$. Fig. 7-2(a) shows the pure ($p = 0$) system for comparison. The curves in these diagrams are boundaries between basins of attraction for sinks of the renormalization-group flows—as such they can represent either first- or second-order phase transitions, or disorder lines. The phases depicted in the figures are: dilute disordered (d); dense disordered (D), antiferromagnetic (AF), and τ.

The curves in the diagrams represent boundaries between basins of attraction for the various phase sinks, which can be either first-order, second-order, or disorder lines. The four phases found in the pure $d = 3$ system—dilute disordered (d), dense disordered (D), antiferromagnetic (AF), and τ—are also present in the quenched random model. The characteristics of these phases are summarized in Section 4.2.4.

The evolution of the system with impurity concentration is marked by two salient features. The first is the rapid suppression of the τ phase, which has vanished entirely by $p = 0.03$. Since the parallels between the τ phase and the superconducting phase in cuprates have been noted in previous chapters, it is significant that the rate at which the τ phase disappears is comparable to the T_c reduction with Zn impurities mentioned above. The second feature is the increase in the antiferromagnetic transition temperatures with p, at least at these small concentrations. Of course the dilute disordered phase gradually takes up a larger portion of the phase diagram, and at higher p the antiferromagnetic phase vanishes from the chemical potential range shown in the figures. We already described in the introduction observations of enhanced Néel temperature T_N for lightly holed doped $La_{2-x}Sr_xCu_{1-z}Zn_zO_4$, and it is worth noting that a similar, though smaller, effect has been found even at larger hole dopings of $x = 0.115$ and 0.13, with the T_N increasing up to $z = 0.0075$ [8]. In the case of $x = 0.13$, there is even no long-range antiferromagnetic order for the Cu spins in the Zn-free compound; it appears for $z > 0.0025$. Whatever the mechanism behind these effects—whether localization of holes or the pinning of dynamical stripe correlations—our calculation exhibits the surprising role that small concentrations of nonmagnetic impurities have in stabilizing antiferromagnetism.

The phase diagrams shown here are the preliminary results in a more extensive, ongoing investigation of quenched randomness in the tJ model. In the near future we plan to modify the renormalization-group transformation to allow for site (as opposed to bond) disorder, as well as to examine the effect of magnetic ($S \neq 0$) impurities.

References

[1] G. Xiao, M.Z. Cieplak, J.Q. Xiao, and C.L. Chien, Phys. Rev. B **42**, 8752 (1990).

[2] B. Jayaram, S.K. Agarwal, C.V. Narasimha Rao, and A.V. Narlikar, Phys. Rev. B **38**, 2903 (1988).

[3] A.V. Mahajan, H. Alloul, G. Collin, and J.-F. Marucco, Phys. Rev. Lett. **72**, 3100 (1994).

[4] M.-H. Julien, T. Fehér, M. Horvatić, C. Berthier, O.N. Bakharev, P. Ségransan, G. Collin, and J.-F. Marucco, Phys. Rev. Lett. **84**, 3422 (2000).

[5] S. Ouazi, J. Bobroff, H. Alloul, and W.A. MacFarlane, Phys. Rev. B **70**, 104515 (2004).

[6] O.P. Vajk, P.K. Mang, M. Greven, P.M. Gehring, and J.W. Lynn, Science **295**, 1691 (2002).

[7] M. Hücker, V. Kataev, J. Pommer, J. Harraß, A. Hosni, C. Pflitsch, R. Gross, and B. Büchner, Phys. Rev. B **59**, 725 (1999).

[8] I. Watanabe, T. Adachi, K. Takahashi, S. Yairi, Y. Koike, and K. Nagamine, Phys. Rev. B **65**, 180516 (2002).

Chapter 8

Conclusion

Throughout the thesis, we have focused on the Hubbard and tJ models because of their relevance to high-T_c materials, and their almost totemic status in the the condensed matter community. They are examples of the perfectly posed physics riddle: at once intuitively simple and stubbornly resistant to rigorous understanding. Having reached a ubiquity whose only precedent may be the Ising model in an earlier generation, these strongly correlated systems are still waiting for their Onsager—or perhaps a computational revolution that will make clever analytical solutions moot. Position-space renormalization-group techniques played a role in demystifying another once elusive area—phase transitions and critical phenomena in classical models—and our current approach has tried to extend that success to quantum systems. While we have confined our attention to the tJ and Hubbard Hamiltonians, the procedure outlined in the previous chapters is quite general: so long as we can numerically manipulate the Hamiltonian matrix for the small cluster we are decimating, we can derive quantum recursion relations and calculate a phase diagram.

This opens up a variety of directions for future research. Moving beyond one-band descriptions of correlated electrons, we can consider more complicated tight-banding lattice models involving several types of orbitals. We have already mentioned the d-p model for the CuO_2 planes in cuprates, but perhaps the most intriguing candidates come from the field of heavy fermion physics. Here the main goal has been to understand the interactions between localized electrons in narrow f bands

and the conduction electrons in broader s, p, or d bands. The basic models for these interactions—the periodic Anderson and Kondo lattice Hamiltonians—are amenable to our renormalization-group techniques. To get a global, finite-temperature phase diagram beyond mean-field theory for a realistic case, for example the Kondo lattice model in three dimensions, would be a significant contribution.

In the latter half of the thesis we have also tried to bring some complexities from real-world materials into the simplified models that were our starting points. The effects of randomness on interacting electrons is one of the crucial issues raised here, and it touches on far wider questions than just the role of impurities in high-temperature superconductors. Like Coulomb repulsion, disorder can lead to electron localization and drive metal-insulator transitions. A complete understanding of its influence will only come through exploring systems where impurity and Coulomb interactions coexist. Among these is the Anderson-Hubbard model, which supplements the standard Hubbard Hamiltonian with random local potentials. The renormalization-group transformation for quenched probability distributions can be readily extended to this system, though it presents an even more formidable computational challenge than the random tJ model of Chapter 7.

However much theorists may strive to bridge the gap between their models and the real world, it is very possible that in the next few years this gap will be bridged from the other direction: by direct experimental realizations of the Hubbard model and other idealized condensed matter systems. The prospect of studying ultracold fermions in lattices created from crossed standing laser waves is immensely exciting. Already great progress has been made for bosons in optical lattices, with important observations like the the superfluid-insulator transition at zero temperature. For those of us used to working at least two removes from reality—laboring over approximations to approximations—it will be nice that one day the Hubbard or tJ model may be a tangible object in someone's laboratory, easily tunable and possessing definite, falsifiable physical properties. Of course there is always the chance that thousands of theoretical papers, including this very thesis, may be rendered obsolete by such a development. But this inherent risk, after all, is what keeps physics interesting.

Appendix A

Numerical Methods for Implementing the Renormalization-Group Transformation

In order to accurately follow the renormalization-group flows even when the interaction constants tend to $\pm\infty$, special measures need to be taken in evaluating the recursion relations. The first, and most basic, step is to use arbitrary precision numbers in the calculations. This is done natively in Mathematica, where most of the work in this thesis was implemented. For the quenched random tJ model of Chapter 7, we switched to C++ for speed, and here the GMP and MPFR packages allow for arbitrary precision floating-point arithmetic. The actual number of digits varied with application, but a typical calculation used at least 125-digit precision.

Unfortunately this by itself is not enough to ensure reasonable numerical results under all circumstances. The main problem arises from the need to exponentiate or take logarithms of matrices. The elements of these matrices are linear combinations of the interaction constants, which often blow up after a few iterations. Simply exponentiating such matrices will generate overflow errors. To overcome this, we

structure the program so that we never have to take the exponent of a large number.

Consider a real, symmetric matrix M, a block in the larger three-site Hamiltonian matrix $-\beta H(i,j) - \beta H(j,k)$, whose elements we determine at the beginning of the calculation from the interaction constants. Standard eigenvalue routines can be used to find the orthogonal matrix S and diagonal matrix D satisfying $M = S^T D S$. Here S has the normalized eigenvectors of M in the columns, so that $S_{ij} = v_i^{(j)}$, where $\vec{v}^{(j)}$ is the jth eigenvector. D has the eigenvalues of M along the diagonal, $D_{ij} = \lambda_i \delta_{ij}$. When used with arbitrary precision numbers, eigenvalue routines are fairly robust, and the only precaution necessary is to set a threshold for eigenvector components in S that should be strictly zero but get a finite value due to roundoff. For example, when using 125-digit precision, we set to zero any components smaller than a threshold $\delta = 10^{-100}$. The exponent of M is equal to

$$e^M = S^T e^D S\,, \tag{A.1}$$

so that every element of e^M can be expressed in the following form,

$$(e^M)_{ij} = \sum_k v_k^{(i)} v_k^{(j)}\, e^{\lambda_k}\,. \tag{A.2}$$

The way we store $(e^M)_{ij}$ for further manipulation is as a list of ordered pairs $\{(v_k^{(i)} v_k^{(j)}, \lambda_k)\}$. From this point on in the calculation, all basic arithmetic operations on the $(e^M)_{ij}$ are expressed in terms of these lists. The γ_i which enter the recursion relations are linear combinations of $(e^M)_{ij}$ from different Hamiltonian matrix blocks M, so in the end we have a list representing each of the γ_i. These lists have the form $\{(x_k, y_k)\}$, where the corresponding numerical value would be $\sum_k x_k e^{y_k}$.

The recursion relations, defining the renormalized interaction constants, involve taking the logarithms either of the γ_i directly or some combination of the γ_i that can also be expressed as a list. We find the logarithm of a list $\{(x_k, y_k)\}$ by selecting the

largest exponent $y_{\max}$ from the list, and calculating

$$\log\{(x_k, y_k)\} \equiv y_{\max} + \log\left(\sum_k x_k e^{y_k - y_{\max}}\right) . \tag{A.3}$$

The only complication arises if there are two or more ordered pairs in the list sharing the largest exponent $y_{\max}$ that nearly cancel each other out. For example, consider two pairs (x_i, y_i) and (x_j, y_j), where $|y_i - y_j| < \delta$, $|x_i + x_j| < \delta$, and y_i, y_j are the largest exponents in list. Here δ is the threshold value mentioned earlier. In this case, we assume the cancellation would be exact except for roundoff error, so we simply delete these two pairs and take the logarithm of the remaining list.

Carefully designing the numerical algorithms in this vein is the only way to guarantee that the renormalization-group transformation can be iterated as many times as necessary to reach a phase sink, or get convergent thermodynamic densities from products of the recursion matrices.

Vita

Michael Hinczewski was born in Łódź, Poland on August 3, 1979, the son of Wojciech and Cecilia Hinczewski. He moved with his family to the United States in 1984, where they have been living since. He studied at Simon's Rock College of Bard from 1995 through 1997, and then transferred to Yale University, where he graduated with a Bachelor of Science in Physics in 1999. From the autumn of that year through the summer of 2005, Michael has been a graduate student in the Physics Department at the Massachusetts Institute of Technology. He divides his time between Boston and Istanbul, Turkey, where his wife, Durşen Saygın Hinczewski, is a physics graduate student at Istanbul Technical University. At this point in time, they have not yet acquired any children or pets, but did once try to raise a tomato plant on the balcony of their apartment, with tragic consequences.